

NEAR-INFRARED STUDIES OF EMBEDDED STAR CLUSTERS

Chan Park
Gyeongbuk, Rep of Korea

B.S., Kyungpook National University, 1996
M.S., Seoul National University, 1999
M.S., University of Virginia, 2004

A Dissertation Presented to the Graduate
Faculty of the University of Virginia
in Candidacy for the Degree of
Doctor of Philosophy

Department of Astronomy

University of Virginia
May, 2010

Michael F. Skrutskie

Zhi-Yun Li

Robert W. O'Connell

Bradley B. Cox

Abstract

The Fan Mountain Near-Infrared Camera, *FanCam*, features an $8.7' \times 8.7'$ field of view on a 1024×1024 Teledyne Imaging Sensors HAWAII-1 detector array. The instrument mounts at the $f/15.5$ focus of the 31 inch telescope. Its seeing-limited optical design, optimized for the *JHK* atmospheric bands, includes a field stop at the telescope focus, a doublet collimator, two 8-position filterwheels straddling a Lyot stop, and a doublet reimager. The $0.51'' \text{pixel}^{-1}$ plate scale leads to a slightly oversampled point spread function for the typical seeing of $1.5''$. The entire optical train is encased in a cryogenic dewar cooled by a closed-loop cooling system. Chapter 2 describes the camera design and some early results of camera performance test.

Long term near-infrared, *J*, *H*, and *K_s*, photometric monitoring of the embedded cluster NGC 1333 is presented in Chapter 3. We employ the Stetson variability index and reduced χ^2 to identify variable objects. Color-magnitude and color-color diagrams demonstrate that NGC 1333 is extremely young and highly extincted. Light curves in all three bands are well correlated. The spatial distribution of variable stars shows a strong correlation with the peak of the extinction map while non-variable stars are evenly spread over the whole field of view. *Spitzer*-2MASS-identified IR excess YSOs and *Chandra* X-ray sources were compared with our variable stars. A total of 25 previously-unknown member candidates are presented, with 15 objects in the mass range of brown dwarfs. The IMF and mass distribution of the cluster are presented. We discuss the implication of *K_s* vs. *H-K_s* color-magnitude diagram slope statistics in view of the evolutionary sequence of young star-forming embedded clusters.

Another long term near-infrared, *J*, *H*, and *K_s*, photometric monitoring performed with *FanCam* for the embedded cluster NGC 7129 is presented in Chapter 4.

NEAR-INFRARED STUDIES OF EMBEDDED STAR CLUSTERS

Chan Park
Gyeongbuk, Rep of Korea

B.S., Kyungpook National University, 1996
M.S., Seoul National University, 1999
M.S., University of Virginia, 2004

A Dissertation Presented to the Graduate
Faculty of the University of Virginia
in Candidacy for the Degree of
Doctor of Philosophy

Department of Astronomy

University of Virginia
May, 2010



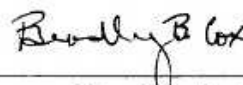
Michael F. Skrutskie



Zhi-Yun Li



Robert W. O'Connell



Bradley B. Cox

Acknowledgements

In the very first line of my acknowledgements, I want to thank my thesis advisor, Mike Skrutskie, who has allowed me to do my graduate training in the Virginia Astronomical Instrumentation Laboratory established and led by him. It has been a great pleasure to work with him over the whole period of my graduate life. It would not have been possible for me to fulfill this dissertation project without his patience and encouragement throughout the years. I would like to express my deep appreciation for his painstaking efforts to help me improve my writing and presentations. My gratitude also goes to my thesis committee members: Brad Cox, Bob O'Connell, and Zhi-Yun Li, who has offered me guidance and insightful suggestions to support this work. I have always enjoyed working with Srikrishna Kanneganti for instrumentation, course work at classes, and every other activities we have done together. I appreciate Ori Fox who has helped me a lot to proofread my manuscript. I would like to thank John Wilson and Matt Nelson for being with me and providing me their excellent knowledge on infrared instrumentation.

My special gratitude goes to Mike Meyer who allowed me his object information for my observation project, Rob Gutermuth who kindly provided me his Classification data even before them published, Armin Rest who helped me with his DIMM information, and Bruce Wilking who told me his research tip for my variability project. And many many more helps that I missed to describe here have made this work possible. People at the Department of Astronomy have helped me and my family settle well down in Charlottesville and enjoy all throughout our staying in the town. Many thanks for all of them. My classmates: Ricardo Munoz, Rick Mellon, Marios Chatzikos, and Jeff Carlin, I have had great fun of time with you guys for several years.

Finally, I wish to express my special gratitude to my colleagues and seniors in Korea Astronomy and Space Science Institute: In-Soo Yuk, Moo-Young Chun, Sungho Lee, Heeyoung Oh, and Byeong-Gon Park, who have supported me with their time and spiritual encouragement.

Dedication

*To **Younghee**, my bosom friend.*

Table of Contents

Abstract	ii
Acknowledgements	iv
Dedication	vi
List of Figures	xviii
List of Tables	xix
1 General Introduction	1
1.1 Embedded Clusters and Variability	2
1.2 Instrumental Development	7
1.3 Characterization of the Site: Fan Mountain Observatory	10
1.4 Contents of the Thesis and Work Apportionment	18
2 <i>FanCam</i> – A Near-Infrared Camera for the Fan Mountain Observa-	20
tory	
2.1 Introduction	22
2.2 Optical Design	22
2.3 Mechanical Design	28
2.4 Cryogenic Design	39
2.5 Electronics	42
2.6 Camera Performance	44
2.6.1 Detector	44
2.6.2 Photometry and Sensitivity	44
2.6.3 Astrometry	46
2.6.4 Mechanical Performance	47
2.7 Upgrades	51
3 Near-Infrared Variability of Young Stellar Objects in the Embedded	
Cluster NGC 1333	52
3.1 Introduction	54

3.2	Data	57
3.2.1	Observations	58
3.2.2	Data Reduction	58
3.2.3	Point Source List	60
3.2.4	Photometric Integrity	61
3.3	Results	72
3.3.1	Identification of Variable Stars	72
3.3.2	Mean Colors and Magnitudes	76
3.3.3	Light Curves and Color Variations	80
3.3.4	Spatial Distribution of Variable Stars	86
3.3.5	Cluster Membership	88
3.3.6	Literature Cluster Members	88
3.3.7	New Members	89
3.3.8	Brown Dwarfs	91
3.3.9	Mass Spectrum of Cluster Members	93
3.4	Discussion	97
3.4.1	Origin of the Variability	97
3.4.2	Characteristics of the Variability: An Evolutionary Sequence?	99
3.5	Conclusions	106
4	Preliminary Results of the Near-Infrared Variability Study in the Embedded Cluster NGC 7129	117
4.1	Introduction	119
4.2	Data	119
4.2.1	Observations	120
4.2.2	Data Reduction	121
4.2.3	Point Source List	122
4.2.4	Photometric Integrity	123
4.3	Results	128
4.3.1	Identification of Variable Stars	128
4.3.2	Mean Colors and Magnitudes	130
4.3.3	Light Curves and Color Variations	133
4.4	Discussion	138
5	Summary and Conclusions	158
A.	A Hand-held NIR Spectrograph for Earth Observations from Space	161
B.	Feasibility of an Infrared Parallax Program using the Fan Mountain Tinsley reflector	164
C.	Theoretical Estimate of FanCam Sensitivity	167

D. FanCam Photometric Image Processing	172
E. More Examples of Light Curves and Color-magnitude Variabilities	175
References	210

List of Figures

1.1	<i>Chandra</i> X-ray detection fraction of the IC 348 cluster ($d \sim 300\text{pc}$) members as a function of spectral type (Preibisch & Zinnecker 2001a). Spectral type M4 corresponds to $M_* \sim 0.2M_\odot$ for age $\sim 1\text{Myr}$	4
1.2	An example of single epoch photometry for a variable star with misleading results. In this case, $\Delta(H-K_s)$ color difference is ~ 0.2 mag, which may cause significant error in estimating various quantities such as color excess, mass, or membership determination.	5
1.3	A synopsis of <i>FanCam</i> and the 31 inch telescope upgrade project. . .	9
1.4	An aerial view of the Fan Mountain Station in 1960s. The station administration building on the left and the domes for the 10 inch astrophotograph and the 32 inch Tinsley Cassegrain reflector telescope on the right are seen. The mountain top area was supporting a thriving apple orchard then (Birney 1966).	13
1.5	The Meade LX-200 DIMM Telescope equipped with an aperture mask. One aperture is installed with a $1'$ BK-7 wedge prism and the other is an empty opening.	14
1.6	DIMM aperture mask drawing. One aperture is installed with a $1'$ BK-7 wedge prism and the other is an empty opening.	15
1.7	A typical seeing measurement with the custom UVa DIMM at the Fan Mountain Observatory. A wider or wilder fluctuation of the image separation in the upper panel yields larger seeing at the lower panel.	16
1.8	Statistics of the seeing evaluation campaign at Fan Mountain Observatory.	17
2.1	(<i>top left</i>) Field curvature and distortion for the optical design. The plots run from the center to the corner of the FOV. (<i>top right</i>) En-squared energy plot for the different field positions the design was weighted with. (<i>bottom left</i>) The positions on the detector weighted in the optical design. (<i>bottom right</i>) Spot diagram for JHK_s bands combined. The box is two pixels on a side. The tight combined psfs imply that there is no noticeable change in plate scale or distortion across the filters.	27

2.2	Snapshots of <i>FanCam</i> at various stages of its mechanical design. (<i>top left</i>) The optical design, with the optical path folded up in accordance with the requirements of the mechanical design. (<i>top right</i>) Computer-generated model of the camera where detailed mechanical parts are assembled with the optics. (<i>bottom left</i>) Precision-machined parts assembled without the optics. Thinned G-10 posts hold the optical bench in place. The coiled cylinder rising up from the bottom of the dewar is the cryogenic cold-head. Flexible copper straps and braids connect the tip of the cryocooler with different locations on the optical bench (not shown). (<i>bottom right</i>) The fully assembled (and uncovered) camera.	33
2.3	(<i>top left</i>) The camera closed up and cold, ready for first-light. Notice the light-weighting and the stiffeners installed subsequently. (<i>top right</i>) <i>FanCam</i> on the telescope. Notice the small tail-piece of the telescope. The cables connected to <i>FanCam</i> are transporting the refrigerant keeping the dewar cold. (<i>bottom</i>) A typical cooldown of <i>FanCam</i> . The chaotic behavior of the cold-head temperatures at around 120K is due to a phase-transitional instability at these temperatures inherent to the proprietary gas mixture PT-13 used by the Cryotiger cooling system.	34
2.4	An example of CAD drawing: Optical Bench. Precision optical bench design does not require extra alignment of optics mounts on the plate.	35
2.5	An example of CAD drawing: Filterwheel. Filter-holding surface is tilted 7° from the wheel axis.	36
2.6	An example of CAD drawing: Collimator Lens Mount. No radial preload is applied to the lenses.	37
2.7	An example of CAD drawing: Detector Box Base. HAWAII-1 focal plane array is housed above the base with 4 standoffs at each corner.	38
2.8	(<i>top left</i>) The magnitude comparison between the 2MASS and <i>FanCam</i> . No systematic nonlinearities are seen. (<i>top right</i>) The error analysis of FanCam magnitudes and comparison with 2MASS. The exposure time for the FanCam magnitudes is 10 minutes in each filter. (<i>bottom left</i>) A comparison of the variation in magnitude, in one hundred 60-s frames, of 44 stars and the error estimated by our IRAF scripts. The true error estimate is 0.004 mag higher than the IRAF estimate. (<i>bottom right</i>) The histogram of internal variations is of the measurements of distances of 43 stars to a single star in 100 60 s <i>J</i> -band frames. The second, broader, histogram is of the difference between the 2MASS positions and positions in a <i>FanCam J</i> -band image with 10 minutes of cumulative exposure.	49

- 2.9 (top left) A composite of the Orion Nebula with 1 minute exposures in JHK_s bands. (top right) A stacked image of NGC 2420 in J band with a cumulative exposure time of 10 minutes. (bottom left) A 30 minute K_s -band image of an extragalactic supernova Type II_n 2005ip in NGC 2906 (Fox et al. 2009). (bottom right) Mon R2 in H band with an inset of the same from 2MASS. *FanCam* sees deeper than 2MASS in this 5 minute exposure. *FanCam*'s plate scale of $0.51'' \text{ pixel}^{-1}$ also improves upon the $2'' \text{ pixel}^{-1}$ plate scale of 2MASS. 50
- 3.1 The boundaries of two observed fields marked over the 2MASS K_s image of NGC 1333. The northern field is centered at R.A. (J2000.0) = $3^h29^m11^s$, Dec. (J2000.0) = $+31^\circ23'38''$ and the southern field is centered at R.A. (J2000.0) = $3^h28^m52^s$, Dec. (J2000.0) = $+31^\circ17'10''$. Each square covers about $8.7' \times 8.7'$ field of view. 62
- 3.2 Color-mosaic image of NGC 1333 north cluster composed of *FanCam* J , H , and K_s – blue, green, and red colors were assigned respectively. The total integration time is ~ 4 hours in each band. Coordinates of the central point are R.A.(J2000.0) = $3^h29^m11^s$ and Dec.(J2000.0) = $+31^\circ23'38''$. The array plate scale is $0.51'' \text{ pixel}^{-1}$. The sky seeing spans from $1.2''$ to $2.5''$. Blue diffuse features are dust-scattered light in J band, and red ones are from hot dust and/or shocked molecular hydrogen line emission in K_s band. 63
- 3.3 Visible RGB color image of the same region of NGC 1333 north cluster for comparison. Credit & Copyright: Stephen Leshin (From Astronomy Picture of the Day 2009 April 18) 64
- 3.4 Color-mosaic image of NGC 1333 south cluster composed of *FanCam* J , H , and K_s – blue, green, and red colors were assigned respectively. The total integration time is ~ 3 hours in each band. Coordinates of the central point are R.A.(J2000.0) = $3^h28^m52^s$, Dec.(J2000.0) = $+31^\circ17'10''$. The array plate scale is $0.51'' \text{ pixel}^{-1}$. The sky seeing spans from $1.2''$ to $2.5''$. Blue diffuse features are dust-scattered light in J band, and red ones are from hot dust and/or shocked molecular hydrogen line emission in K_s band. 65
- 3.5 Visible RGB color image of the same region of NGC 1333 south cluster for comparison. Credit & Copyright: Stephen Leshin (From Astronomy Picture of the Day 2009 April 18) 66

3.6	Magnitude differences between 2MASS and <i>FanCam</i> PSF photometry (northern field). Instead of observing independent standard stars, a statistical method with 2MASS point-source catalog was used to determine the instrumental offsets of each filter system. General dispersions likely come from stellar variability itself. The broader faint-end scatterings originate from 2MASS magnitude uncertainties near its survey sensitivity limits.	67
3.7	Magnitude differences between 2MASS and <i>FanCam</i> PSF photometry (southern field). Instead of observing independent standard stars, a statistical method with 2MASS point-source catalog was used to determine the instrumental offsets of each filter system. General dispersions likely come from stellar variability itself. The broader faint-end scatterings originate from 2MASS magnitude uncertainties near its survey sensitivity limits.	68
3.8	Photometric uncertainty; <i>FanCam</i> north data (solid) and 2MASS archive (open) for comparison. <i>FanCam</i> photometry in this study reaches up to 18.7, 17.5, and 16.7 mag for <i>J</i> , <i>H</i> , and <i>K_s</i> , respectively with signal-to-noise ratio 10, which is ~ 2 mag deeper than 2MASS survey. . . .	69
3.9	Photometric uncertainty; <i>FanCam</i> south data (solid) and 2MASS archive (open) for comparison. <i>FanCam</i> photometry in this study reaches up to 18.5, 17.1, and 16.5 mag for <i>J</i> , <i>H</i> , and <i>K_s</i> , respectively with signal-to-noise ratio 10, which is ~ 2 mag deeper than 2MASS survey. . . .	70
3.10	Observed photometric RMS for variables (solid) and non-variables (open). RMS of the ensemble measurements was computed to estimate the signal-to-noise ratio in our photometry. The observed RMS ranges from ~ 0.015 mag for bright stars to ~ 0.10 for stars near the sensitivity limits of this study. The values correspond to SNRs of ~ 70 and ~ 10 , respectively. We interpret the RMS bottomline 0.015 mag as the photometric repeatability of our data set.	71
3.11	Stetson variability index (Stetson 1996) of NGC 1333 point sources. Non-variable stars tend to scatter around the parallel zero line symmetrically while true variables show some positive offsets. Inset is the Stetson index plot of another embedded cluster NGC 7129 for reference (Park et al. in prep). We identify a point source with $S \geq 1$ as a variable star.	75

- 3.12 K_s vs. $H-K_s$ color-magnitude diagram for all point sources; 110 variables with small filled circles and 88 non-variables with asterisks. Infrared excess sources (Gutermuth et al. 2008) Class I (triangles) and Class II (open circles) YSOs are marked over. *Chandra*-identified X-ray sources (Getman et al. 2002) are displayed with crosses. Squares are for the brown dwarf candidates selected by Wilking et al. (2004) and Scholz et al. (2009) (bigger squares). The upper solid line is 1 Myr isochrone of the NextGen model (Baraffe et al. 1998) covering mass from $0.02 M_\odot$ to $1.4 M_\odot$, the dashed line is 1 Myr isochrone for the DUSTY model (Chabrier et al. 2000) covering mass from $0.005 M_\odot$ to $0.1 M_\odot$, and the lower solid line is 1 Myr age line for the COND model (Baraffe et al. 2003) covering the same mass range as the dashed line. The dotted diagonal lines represent the direction and magnitude of the reddening vector (Cohen et al. 1981); the slope is 1.35. The rhombi along the reddening lines are marked for the visual extinction A_V of 10 interval. 78
- 3.13 $J-H$ vs. $H-K_s$ color-color diagram. Symbols represent for the same contents as Figure 3.12 but the lower dot-dashed lines show the Classical T Tauri star locus as described in Meyer et al. (1997) 79
- 3.14 Example of J , H , and K_s light curves of a Class II pre-main-sequence star; FMO 135, also known as MBO 47 by Wilking et al. (2004), LAL 163 by Lada et al. (1996), and ID 71 by Gutermuth et al. (2008). Fluctuations are apparently non-periodic but well correlated in all three bands. 82
- 3.15 Example of J , H , and K_s light curves of a Class II pre-main-sequence object; FMO 197, also known as MBO 118 by Wilking et al. (2004), LAL 246 by Lada et al. (1996), and ID 102 by Gutermuth et al. (2008). Fluctuations are apparently non-periodic but well correlated in all three bands. The mass of FMO 197 is derived to $\sim 0.03 M_\odot$ based on 1 Myr model isochrones (Baraffe et al. 1998). 83
- 3.16 Color variability of a Class II pre-main-sequence star; FMO 135. The upper panels are color-magnitude correlations between K_s vs. $H-K_s$ and J vs. $J-H$. The lowers are time-variations of $H-K_s$ and $J-H$ colors. The K_s vs. $H-K_s$ color-magnitude diagram shows a positive linear-regression slope, implying the color becomes redder as the K_s gets fainter. 84
- 3.17 Color variability of a Class II pre-main-sequence star; FMO 197. Each panel represents the same as Figure 3.16. It is an example of a star that becomes redder when it lights up, producing a negative slope in K_s vs. $H-K_s$ relation. The dashed line represents the Classical T Tauri star locus (Meyer et al. 1997), characteristic of disk activity in pre-main-sequence stars. 85

- 3.18 Spatial distribution of all *FanCam* point sources in two observed regions; 110 variable stars (filled circles) and 88 non-variable stars (asterisks). Various symbols represent the same as Figure 3.12 – i.e., Class I (triangles) and Class II (open circles) YSOs by Gutermuth et al. (2008), *Chandra* X-ray sources (crosses) by Getman et al. (2002), and BD candidates (squares) of Wilking et al. (2004) + Scholz et al. (2009) (bigger squares). The background contour is the extinction distribution of $A_V=18, 16, 14, 12, 10, 8, 6, 4$ (Gutermuth et al. 2008). Variable stars and IR excess sources are well connected with the extinction map while non-variable stars are fairly randomly scattered throughout the observed area. 87
- 3.19 Mass function for variable stars (solid histogram) and all point sources (dashed histogram) detected with *FanCam* in NGC 1333. Long-dashed line represents the best-fit power-law mass spectrum for low-mass stellar regime ($0.1M_\odot \leq M_* \leq 2M_\odot$), where $\alpha = 2.27$. The error bars are computed by combining \sqrt{N} counting statistics and uncertainty in masses. The dotted vertical line indicates hydrogen-burning limit ($0.075M_\odot$) and the dot-dashed vertical line for deuterium-burning limit ($0.012M_\odot$). 96
- 3.20 Light curves and the phase-shifted magnitude variation of a periodic variable star; FMO 250. The best fit period is 10.952 days. Two full cycles of the phase are plotted for better display of the periodicity. The color and magnitude variability ranges are consistent with cool starspot models investigated by Carpenter et al. (2001). 102
- 3.21 Histograms of the slopes derived from the K_s vs. $H-K_s$ diagrams in NGC 1333 (this paper), NGC 7129 (Park et al. in prep), ρ Ophiuchi (Alves de Oliveira & Casali 2008), and the Trapezium in Orion (Carpenter et al. 2001). The currently available samples for the color-magnitude slope statistics are limited in these four clusters only. Accretion disk models can account for the negative slope color variability, and variable extinction models can explain positive slopes, in general. The histogram morphological difference between the clusters maybe reflects the evolutionary stage of very young star-forming clusters. . . . 103
- 3.22 Color variability of a variable star; FMO 120. Each panel represents the same as Figure 3.16. It is an example of stars that show slopes close to zero ($-10^\circ < \theta < 10^\circ$), or no magnitude change in K_s band while $H-K_s$ color varies significantly. 104

3.23	Correlation between the slope (K_s vs. $H-K_s$) and the X-ray strength measured by <i>Chandra</i> (Getman et al. 2002). Most of the strongest X-ray sources have slopes between -30° and 0° . The single mode distribution around -20° of the NGC 1333 slope histogram (Figure 3.21) seems to have something to do with strong magnetic activities of very young cluster members.	105
4.1	Color-mosaic image of the embedded cluster NGC 7129, composed of <i>FanCam</i> J , H , and K_s – blue, green, and red colors were assigned respectively. The total integration time is ~ 2.5 hours in each band. Coordinates of the central point are R.A.(J2000.0)= $21^h42^m58^s$ and Dec.(J2000.0)= $+66^\circ06'35''$. The array plate scale is $0.51''\text{pixel}^{-1}$. The sky seeing spans from $1.2''$ to $2.5''$	124
4.2	Magnitude differences between 2MASS and <i>FanCam</i> PSF photometry NGC 7129. Instead of observing independent standard stars, a statistical method with 2MASS point-source catalog was used to determine the instrumental offsets of each filter system. General dispersions likely come from stellar variability itself. The broader faint-end scatterings originate from 2MASS magnitude uncertainties near its survey sensitivity limits.	125
4.3	Photometric uncertainty; <i>FanCam</i> NGC 7129 (lower) and 2MASS archive (upper) for comparison. <i>FanCam</i> photometry in this study reaches up to 18.7, 17.1, and 16.3 mag for J , H , and K_s , respectively with signal-to-noise ratio 10, which is ~ 2 mag deeper than 2MASS survey. . . .	126
4.4	Observed photometric RMS for variables (solid) and non-variables (open). RMS of the ensemble measurements was computed to estimate the signal-to-noise ratio in our photometry. The observed RMS ranges from ~ 0.015 mag for bright stars to ~ 0.10 for stars near the sensitivity limits of this study. The values correspond to SNRs of ~ 70 and ~ 10 , respectively. We interpret the RMS bottomline 0.015 mag as the photometric repeatability of our data set.	127
4.5	Stetson variability index (Stetson 1996) of NGC 7129 point sources. Non-variable stars tend to scatter around the parallel zero line symmetrically while true variables show some positive offsets. We identify a point source with $S \geq 1$ as a variable star.	129

- 4.6 K_s vs. $H-K_s$ color-magnitude diagram for all point sources; 166 variable stars with small filled circles and 314 non-variables with asterisks. Infrared excess sources (Gutermuth et al. 2004) 5 Class I (triangles) and 34 Class II (open circles) YSOs are marked over. The lower solid line is 3 Myr isochrone of the NextGen model (Baraffe et al. 1998) covering mass from $0.03 M_\odot$ to $1.4 M_\odot$, the upper solid line is 3 Myr isochrone of the Padova group (Marigo et al. 2008) covering mass from $1.4 M_\odot$ to $7 M_\odot$. The upper dashed line is 1 Myr isochrone of the NextGen model covering mass from $0.03 M_\odot$ to $1.4 M_\odot$, the lower dashed line is 10 Myr isochrone of the same model and same mass coverage. The dotted diagonal lines represent the direction and magnitude of the reddening vector (Cohen et al. 1981); the slope is 1.35. The rhombi along the reddening lines are marked for the visual extinction A_V of 10 interval. 131
- 4.7 $J-H$ vs. $H-K_s$ color-color diagram for all point sources; 166 variable stars with small filled circles and 314 non-variables with asterisks. Infrared excess sources (Gutermuth et al. 2004) 5 Class I (triangles) and 34 Class II (open circles) YSOs are marked over. Several variable sources are unseen in the C-C diagram due to their unmeasured J band brightness. The lower left corner solid line is 3 Myr isochrone of the NextGen model (Baraffe et al. 1998) covering mass from $0.075 M_\odot$ to $0.5 M_\odot$. The dotted diagonal lines represent the direction and magnitude of the reddening vector (Cohen et al. 1981); the slope is 1.35. The rhombi along the reddening lines are marked for the visual extinction A_V of 10 interval. 132
- 4.8 Example of J , H , and K_s light curves of a Class II pre-main-sequence star; FMO 366 in NGC 7129. Fluctuations are apparently non-periodic but well correlated in all three bands. 134
- 4.9 Example of J , H , and K_s light curves of a Class II pre-main-sequence object; FMO 270 in NGC 7129. Fluctuations are apparently non-periodic but well correlated in all three bands. 135
- 4.10 Color variability of a Class II pre-main-sequence star; FMO 366 in NGC 7129. The upper panels are color-magnitude correlations between K_s vs. $H-K_s$ and J vs. $J-H$. The lowers are time-variations of $H-K_s$ and $J-H$ colors. The K_s vs. $H-K_s$ color-magnitude diagram shows a positive linear-regression slope, or the color becomes redder as the K_s gets fainter, which is consistent with extinction dominant variability. The isochrones in the color-magnitude diagrams are for 3 Myr tracks from Baraffe et al. (1998). 136

4.11	Color variability of a Class II pre-main-sequence star; FMO 270 in NGC 7129. Each panel represents the same as Figure 4.10. It is an example of a star that becomes redder when it lights up, producing a negative slope in K_s vs. $H-K_s$ relation. The dashed line represents the Classical T Tauri star locus (Meyer et al. 1997), characteristic of disk activity in pre-main-sequence stars.	137
4.12	Histograms of the slopes derived from the K_s vs. $H-K_s$ diagrams in NGC 7129.	140
A..1	A summary of the Hand-held NIR Spectrograph project (Kanneganti et al. 2006). The poster was presented in SPIE 2006 at Orlando Florida.	163
B..1	A quick summary of the infrared parallax feasibility study with <i>FanCam</i> (Bartlett et al. 2010a). The poster was presented in AAS 215th 2010 January at Washington DC.	166
C..1	Equivalent noise electrons in 10 minutes exposure for <i>FanCam</i> . Lower dashed curve is for sky background, upper one is for telescope thermal noise, and the solid line is for the sum of 2 thermal components and readout noise. Dots with wavelength ranges represent airglow components, which is dominant in J and H bands. In K band, airglow is competing with the sum of other components.	171
D..1	<i>FanCam</i> photometric data reduction procedure. (<i>top left</i>) Raw image. (<i>top right</i>) Median-combined sky image. (<i>bottom left</i>) Raw image subtracted by the median-combined sky frame. (<i>bottom right</i>) Master object frame, combined 10 individual reduced object image, ready for photometry.	174
E..1	Light curves and color-magnitude correlations for the variable star FMO 44 in NGC 1333.	176
E..2	Light curves and color-magnitude correlations for the variable star FMO 54 in NGC 7129.	189

List of Tables

1.1	Briefs of Embedded Clusters NGC 1333 and NGC 7129	6
2.1	Principal Parameters of the Optical Design (Theoretical)	26
2.2	Prescription for the Optical Design (in mm, at room temperature) . .	26
3.1	Log of Observations of NGC 1333	108
3.2	Point-Source List of NGC 1333	109
3.2	Point-Source List of NGC 1333	110
3.2	Point-Source List of NGC 1333	111
3.2	Point-Source List of NGC 1333	112
3.2	Point-Source List of NGC 1333	113
3.3	<i>FanCam</i> -identified Variable Stars & Substellar Objects	114
3.3	<i>FanCam</i> -identified Variable Stars & Substellar Objects	115
3.3	<i>FanCam</i> -identified Variable Stars & Substellar Objects	116
4.1	Log of Observations of NGC 7129	141
4.2	Point-Source List of NGC 7129	142
4.2	Point-Source List of NGC 7129	143
4.2	Point-Source List of NGC 7129	144
4.2	Point-Source List of NGC 7129	145
4.2	Point-Source List of NGC 7129	146
4.2	Point-Source List of NGC 7129	147
4.2	Point-Source List of NGC 7129	148
4.2	Point-Source List of NGC 7129	149
4.2	Point-Source List of NGC 7129	150
4.2	Point-Source List of NGC 7129	151
4.2	Point-Source List of NGC 7129	152
4.2	Point-Source List of NGC 7129	153
4.3	<i>FanCam</i> -identified Variable Stars in NGC 7129	154
4.3	<i>FanCam</i> -identified Variable Stars in NGC 7129	155
4.3	<i>FanCam</i> -identified Variable Stars in NGC 7129	156
4.3	<i>FanCam</i> -identified Variable Stars in NGC 7129	157

Chapter 1

General Introduction

Human endeavor has long sought to unravel the nature of stars by studying star clusters. Given that all members of a cluster form at the virtually same time with similar metallicity, unlike individual field stars, observations of cluster stars provide a direct constraint for testing stellar evolution theory by examining differences between cluster members as well as trends characteristic of the cluster population as a whole. Star clusters also represent a fundamental link to the origins of our Solar System since most present-day isolated stars formed long ago in now-dispersed star clusters.

Of all stars born in Giant Molecular Clouds, huge complexes of dense interstellar gas and dust with masses ranging 10^4 - $10^6 M_{\odot}$, 70-90% are found within embedded clusters (Lada & Lada 2003). These embedded clusters are dense associations of hundreds to thousands of newly formed ($\lesssim 1$ Myr old) stars. The manner in which these stars form has direct implications on the formation of the extrasolar systems and exoplanets around the stars.

Like main-sequence clusters, studying young embedded clusters provides insight into the star formation and the accretion process of planetary disk. The obscuring nature of the gas and dust in embedded clusters, however, makes observations at

optical wavelengths difficult. Infrared observations are less prone to extinction effects from the cloud gas and dust. In this thesis, I introduce my infrared observational astronomical journey through two selected embedded clusters, NGC 1333 and NGC 7129, to place a “building block” upon the “house” of human endeavor.

1.1 Embedded Clusters and Variability

Observing clusters of young stellar and substellar objects generally guarantees homogeneity among the age of its members, which is ideal for the statistical study of stellar formation and evolution. Specific criteria exist to identify members in a stellar cluster. Traditionally, pre-main-sequence (PMS) stars in young clusters have been identified by several techniques, including H_α emission line spectroscopy or narrow-band photometry, X-ray observations, near-infrared (J, H, K (L)) observations, and multi-color optical photometry (V, R, I), as well as some statistical approaches (e.g., Sung et al. 2004; Ramírez et al. 2004).

Among these probing tools, only X-ray and infrared methods are useful for deeply embedded young clusters due to the heavily obscuring nature of gas and dust in natal molecular clouds. However, the infrared excess method is insufficient for members with no significant disk. The X-ray method also has sharp detection limit for low-mass stellar regime (cf. Figure 1.1; see also § 3.1).

Variability studies in embedded clusters provide several advantages over the previously mentioned techniques. Since photometric variation at visible and near-infrared wavelengths is a hallmark of pre-main-sequence stars, it can serve as evidence for membership in young star-forming clusters. Monitoring photometric variability over a reasonable period of time provides both mean magnitude and RMS values for each cluster member star. Typically, the RMS values are several times larger than the

conventional photometric uncertainty of contemporary facilities, which is significant and non-negligible.

A single epoch observation can deliver misleading results due to miscorrelated variations between different photometric bands (e.g., see Figure 1.2). This thesis will show that the statistics of a color-magnitude variability pattern (especially the K_s vs. $H-K_s$ gradient) can be used as a tool to constrain the ages of young embedded clusters. Most of all, these variability studies will lead to a better understanding of YSOs in embedded clusters. Various mechanisms behind luminosity variations in YSOs can be diagnosed by using the variability information obtained from sequential observations of the objects (in § 3.4.1).

Lada & Lada (2003) compiled a list of 76 nearby embedded clusters from various available literature. Of these, I selected two for variability studies with the criteria that, 1) The cluster has more than 100 members, 2) The cluster's angular size is comparable to my instrument, and 3) The cluster is observable during winter season in my planned observing location since the sky thermal background is significantly reduced. The latter point is important for ground-based infrared observations. Table 1.1 lists the estimated parameters for the two embedded clusters NGC 1333 and NGC 7129.

To conduct this variability study successfully, the observing instrument must meet several requirements. First, the instrument must be an infrared device sensitive enough to penetrate obscuring circumstellar/circumcluster material. Second, its field of view must cover the angular spread of typical nearby embedded clusters. Third, we need easy access to the instrument throughout the yearlong monitoring program. Fourth, the system must yield good quality of astrometric data consistently throughout the observing campaign.

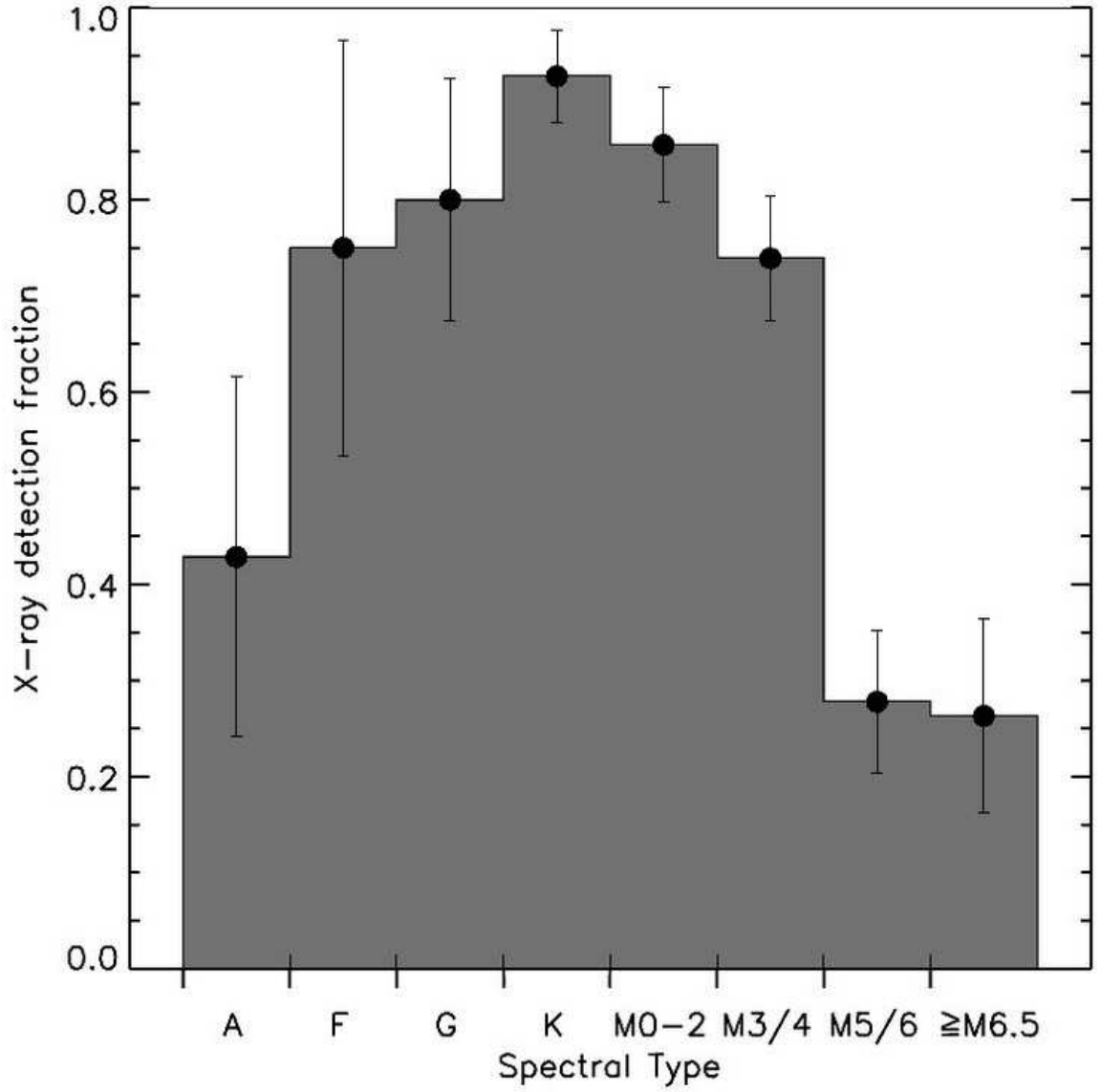


Fig. 1.1.— *Chandra* X-ray detection fraction of the IC 348 cluster ($d \sim 300$ pc) members as a function of spectral type (Preibisch & Zinnecker 2001a). Spectral type M4 corresponds to $M_* \sim 0.2M_\odot$ for age ~ 1 Myr.

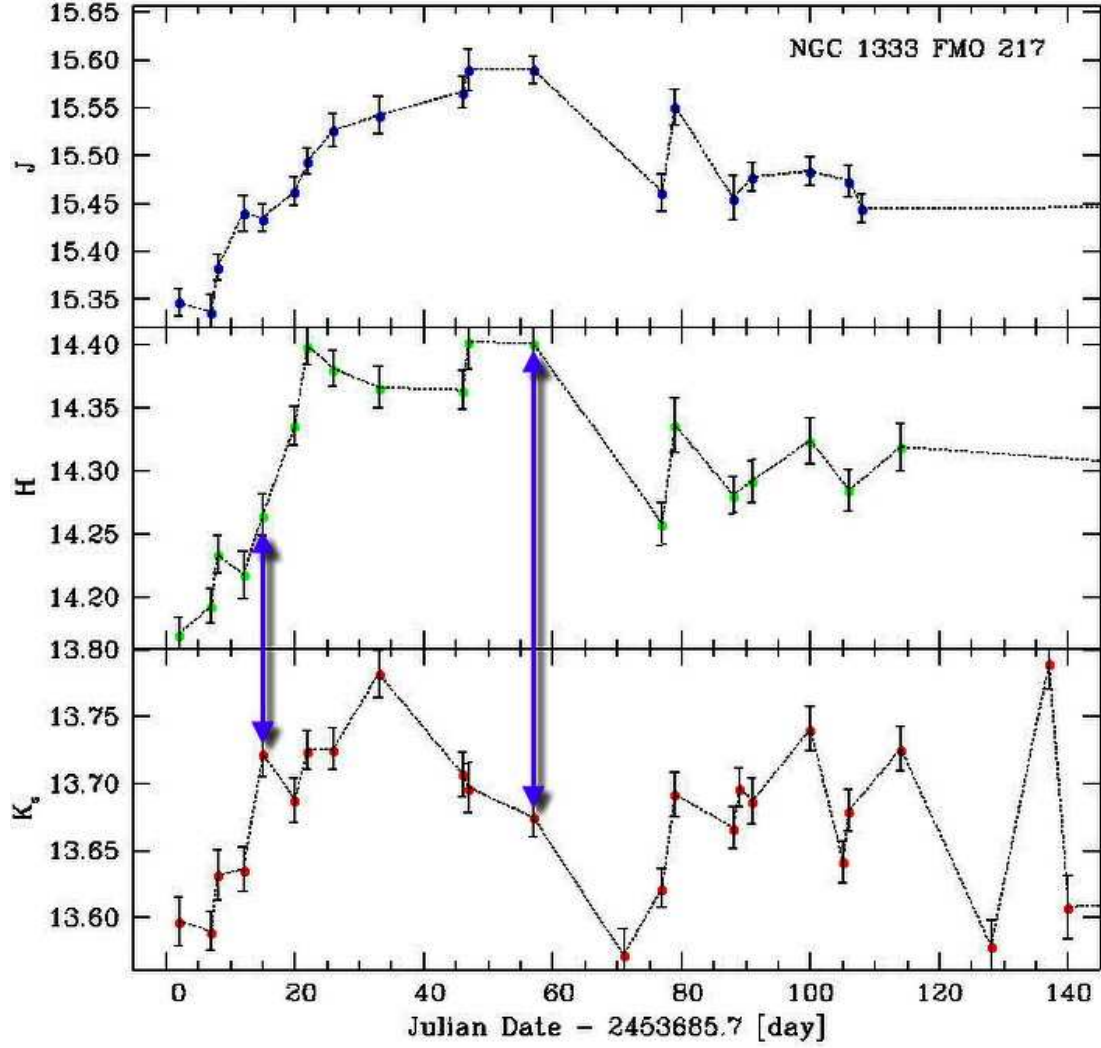


Fig. 1.2.— An example of single epoch photometry for a variable star with misleading results. In this case, $\Delta(H-K_s)$ color difference is ~ 0.2 mag, which may cause significant error in estimating various quantities such as color excess, mass, or membership determination.

Table 1.1. Briefs of Embedded Clusters NGC 1333 and NGC 7129

Name	RA (J2000)	Dec (J2000)	Distance (pc)	Size (pc)	N _*	K (limit)	Mass M_{\odot}	References
NGC 1333	03:32:08.1	+31:31:03	318	0.49	143	14.5	79	1
NGC 7129	21:43:02.2	+66:06:29	1000	...	139	17.0	76	2

Note. — Table extracted from Lada & Lada (2003).
References: 1 Lada et al. (1996), 2 Hodapp (1994)

1.2 Instrumental Development

An instrument to fulfill the requirements of the variability study described in the previous section was originally conceived by Prof. Skrutskie, PI of the 2MASS near-infrared survey project (Skrutskie et al. 2006), and the proposed device was accepted by the Major Research Instrumentation (MRI) program of the National Science Foundation (NSF).

The instrument was to be designed, fabricated, constructed, and commissioned “in-house” around a state of the art Teledyne (then, Rockwell Scientific) HgCdTe Astronomical Wide Area Infrared Imaging (HAWAII) 1024×1024 array. The host facility was the 31 inch Tinsley Laboratories reflector telescope at Fan Mountain Observatory ($78^{\circ}41'6''$ E, $37^{\circ}52'7''$ N, 556 m elevation) located only in 30 minutes from the University of Virginia main “Ground” in Charlottesville. The telescope had a good history of stability (e.g., Birney 1966) although it was not actively used for decades once the 40 inch reflector telescope was built in the site¹.

The primary goal of the project was to train next generation astronomical instrumentalists by inspiring students in the end-to-end development and implementation of a major instrument. Fortunately, I was able to capitalize on the newly established Virginia Astronomical Instrumentation Laboratory (VAIL), which, in conjunction with the dark site at Fan Mountain, provided me the amazing opportunity to conduct productive research on embedded clusters.

The essential components in developing an astronomical infrared camera or spectrograph are the optics, cryostat, mechanical/optomechanical design, controller electronics, and software. The design and implementation of each component was done

¹The feasibility of an astrometric study with the 31 inch telescope has been convinced after *FanCam* was commissioned (Bartlett et al. 2010, cf. Appendix B.).

by a close collaboration between an instrumentation team of graduate and undergraduate students of the University of Virginia. A more detailed review of the work is given in § 1.4. The project PI scrutinized and evaluated the student's decisions in each step, but he encouraged students to make their own decision as much as possible throughout the project.

A more detailed description of the instrument is given in Chapter 2. The data reduction procedure is presented in Appendix D., describing a series of semi-automatic IRAF scripts I wrote for the FITS imaging. The instrument and its initial testing performance are summarized in the following symposium poster (Figure 1.3).



Fig. 1.3.— A synopsis of *FanCam* and the 31 inch telescope upgrade project.

1.3 Characterization of the Site: Fan Mountain Observatory

The University of Virginia has a long history of astronomical, particularly astrometric, research centered around the 26 inch refractor at Leander McCormick Observatory on the “Grounds” of the University of Virginia in Charlottesville. When more modern (and less light-polluted) facilities were required in the early 1960s, the Astronomy department established the Fan Mountain Station of the Leander McCormick observatory on a mountaintop 15 miles southwest of Charlottesville. Fan Mountain has a modest peak of 1825 ft. (556 m) and is located on the eastern foothills of the Blue Ridge mountains. It was considered by the U.S. Naval Observatory as a site for its relocation in the 1950s (Figure 1.4, Birney 1966), and it still remains one of the least light-polluted but readily accessible locations in the eastern United States. Today the mountain hosts a 40 inch astrometric reflector, a 24 inch rapid-response remote reflector, a 10 inch astrograph refractor, and the 31 inch Tinsley Laboratories reflector which supports the infrared camera discussed in this thesis.

Development of the Fan Mountain Near-infrared Camera (described in Chapter 2) was supported by a MRI grant from the NSF. The grant proposal stipulated that the camera design would mainly be performed by the graduate students supported by the grant and thus many parameters of the system were undetermined at the outset of the project. The most important of these was the pixel scale of the camera, which ultimately should account for the astronomical seeing at the observing site.

The camera design effort began with a yearlong site seeing evaluation at Fan Mountain using a Differential Image Motion Monitor (DIMM) fashioned out of an 8 inch Schmidt-Cassegrain telescope (Meade LX-200) and an SBIG STV CCD camera

with no filter installed. The DIMM and a sample observation are shown in Figure 1.5. The study relied extensively on Tokovinin (2002) for the design of the DIMM, observations, and analysis.

Our monitor has two apertures of 2.3 inch diameter each, their centers 5.6 inch apart (Figure 1.6). One of the apertures has a BK-7 prism wedge ($1'$ angle) that deviates its light by $30''$. Images are taken with an SBIG STV camera. The two apertures create two pictures in each image frame of the star at which the telescope is pointed. The spots are defocused to enhance positional accuracy. The variation in the separation of the two spots is converted into an estimation of seeing following Tokovinin (2002). The observations were performed close to the 31 inch telescope location, but in a direction and distance at which the dome structure does not affect the observations much. The DIMM survey revealed a median seeing estimate of $1.52'' \pm 0.47''$ in the H band² (Figure 1.8). Near-simultaneous observations with the DIMM and the 31 inch telescope have shown no noticeable degradation in image quality due to dome seeing.

Infrared observations at wavelengths longer than $3 \mu\text{m}$ can only be conducted from high altitude dry sites due to significant water vapor absorption even at the band centers of astronomical filters. However, the astronomical J , H and K_s bands are virtually unaffected by water vapor, and in these bands the measured opacity contribution of water vapor, even at wet low-altitude sites like Fan Mountain, tends to be less than $0.1 \text{ mag airmass}^{-1}$, permitting high precision photometric observations (cf. Skrutskie et al. 1996). Data gathered from the National Weather Service suggests about 100 nights a year at the Fan Mountain Observatory are usable for photometric

²According to the equation (5) of Tokovinin (2002), $\text{FWHM} = 0.98 \left(\frac{D}{\lambda}\right)^{0.2} \left(\frac{\sigma^2}{K}\right)^{0.6}$, where D is the diameter of subapertures, σ is standard deviation of the fluctuating image separations, and K is a constant (in our case 3.0×10^{-10}). We converted from visual-band $\lambda=0.55\mu\text{m}$ to H -band $1.7\mu\text{m}$ with this relation.

observations and a review of observations with *FanCam* supports this estimate.



Fig. 1.4.— An aerial view of the Fan Mountain Station in 1960s. The station administration building on the left and the domes for the 10 inch astrograph and the 32 inch Tinsley Cassegrain reflector telescope on the right are seen. The mountain top area was supporting a thriving apple orchard then (Birney 1966).



Fig. 1.5.— The Meade LX-200 DIMM Telescope equipped with an aperture mask. One aperture is installed with a 1' BK-7 wedge prism and the other is an empty opening.

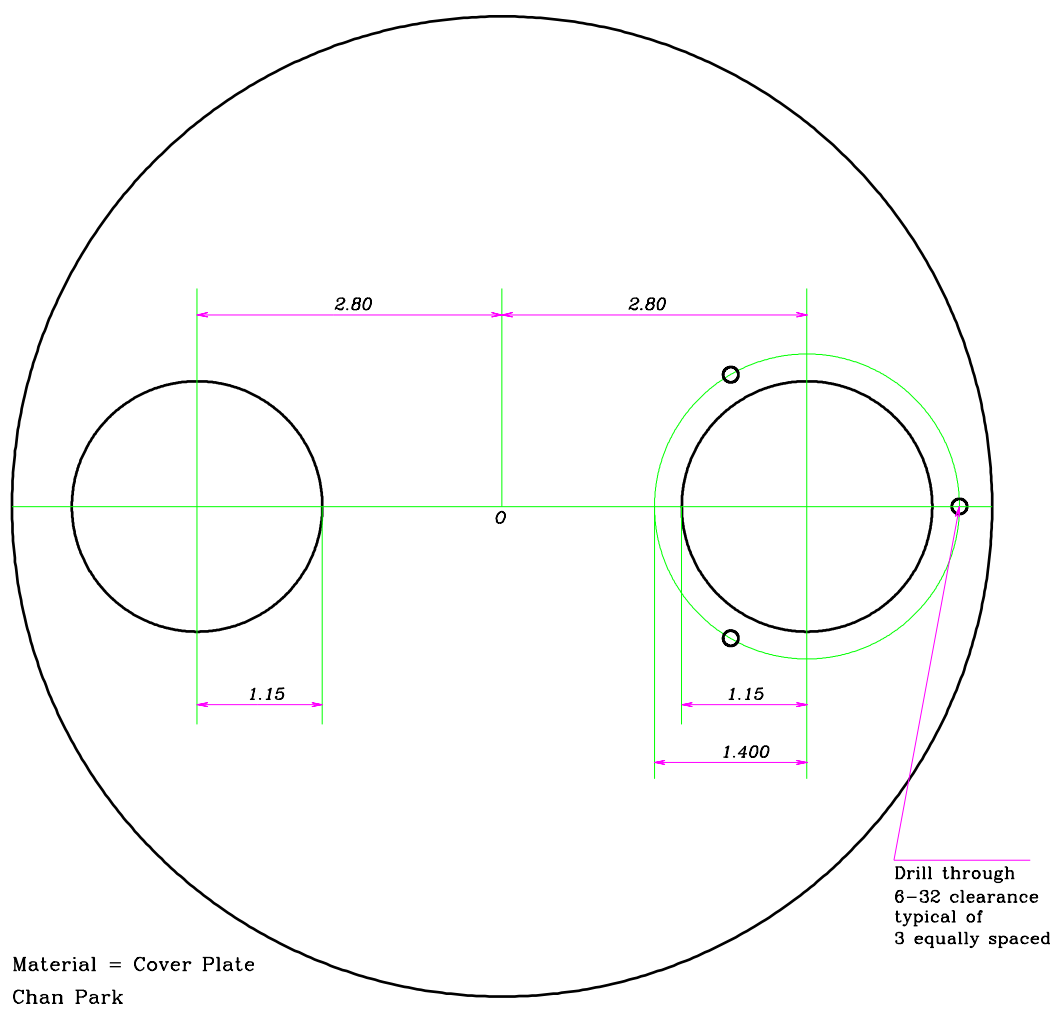


Fig. 1.6.— DIMM aperture mask drawing. One aperture is installed with a 1' BK-7 wedge prism and the other is an empty opening.

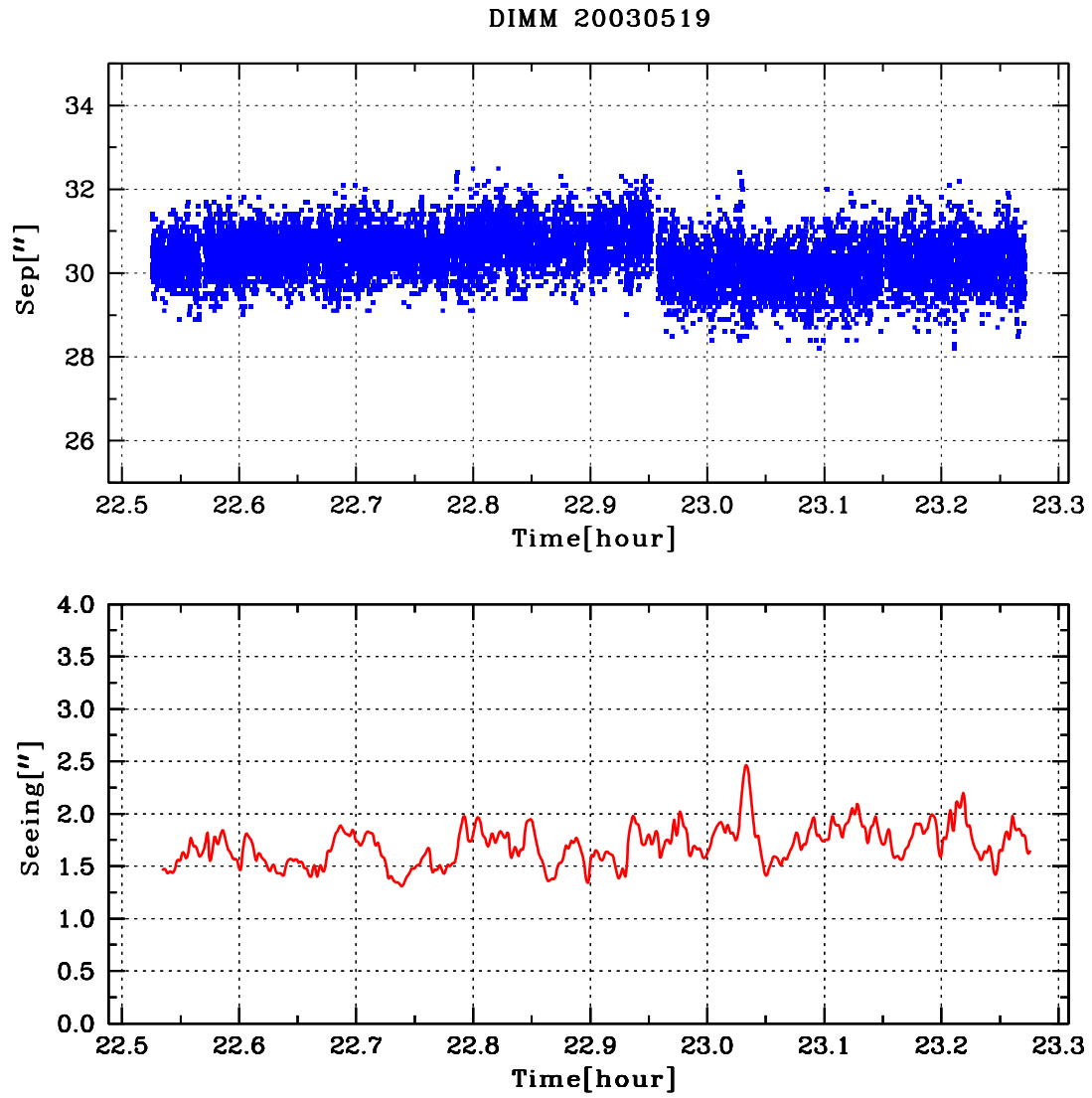


Fig. 1.7.— A typical seeing measurement with the custom UVa DIMM at the Fan Mountain Observatory. A wider or wilder fluctuation of the image separation in the upper panel yields larger seeing at the lower panel.

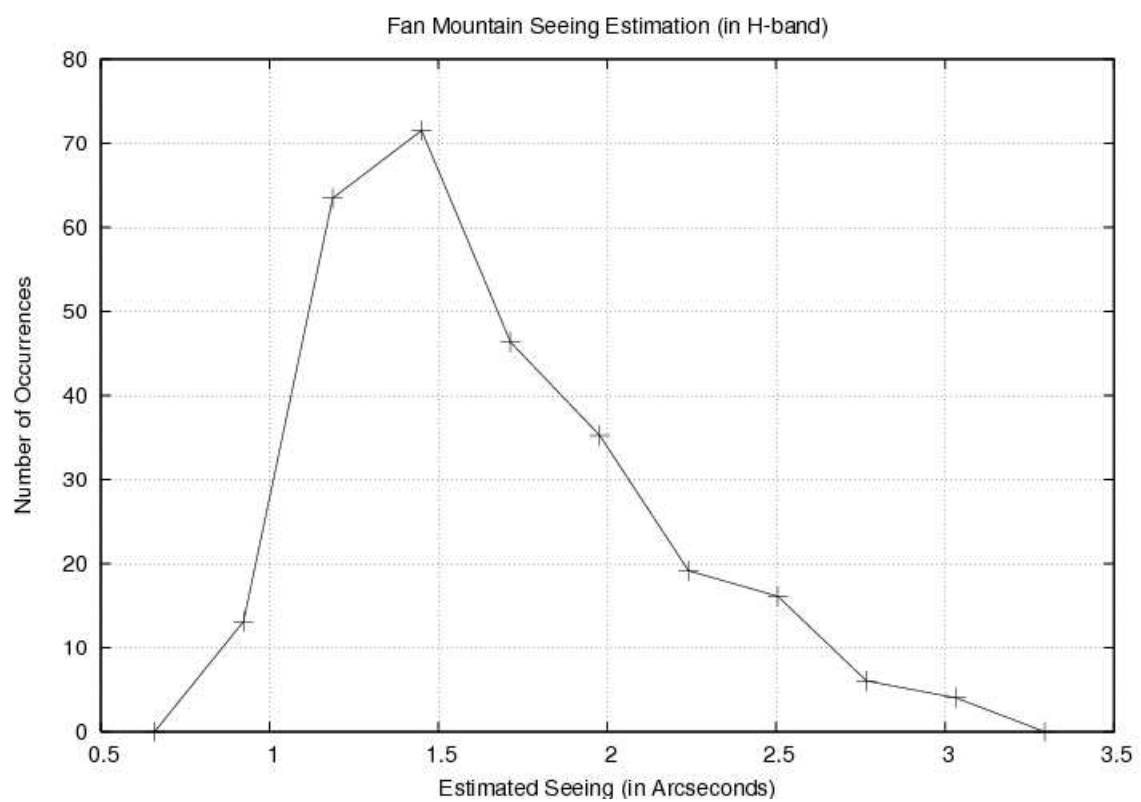


Fig. 1.8.— Statistics of the seeing evaluation campaign at Fan Mountain Observatory.

1.4 Contents of the Thesis and Work Apportionment

In Chapter 2, the detailed description of the instrument, *FanCam*, is presented. We explain optical design, mechanical design, cryogenic design, controller electronics, and initial results of camera performance test in each section. The warm and cold camera optics design, the tolerance analysis of the design, and the procurement process of all the optical elements were conducted by Srikrishna Kanneganti, a Virginia Astronomy graduate student. I was in charge of the mechanical and cryostat design, fabrication, and the examination of all the machined parts. The machining tasks were performed at UVa in-house shops.

The controller electronics and a custom Linux driver for the PCI card were provided by Astronomical Research Cameras Inc. (See § 2.5 for more details). The early version of user interface and data acquisition software of *FanCam* was developed by a Virginia undergraduate student Aaron Smith. The readout software was upgraded later by Dr. Matthew Nelson. The optomechanical work was done by an inseparable collaboration between optical designer (Kanneganti) and mechanical designer (Park) by the nature of the job. In every important step, we consulted Dr. John Wilson as well as Prof. Skrutskie. The contents of Chapter 2 was published in 2009 August in the *Publications of the Astronomical Society of the Pacific*, 121:885-896.

In Chapter 3, the long term near-infrared photometric variability study of the embedded cluster NGC 1333 is described. The observation and data reduction procedure are given in § 3.2. The results of variability identification, the analysis of the mean colors and magnitudes, the spatial distribution of variable objects, and the statistical study of stellar/substellar masses and color-magnitude correlations are

presented in § 3.3. Chapter 4 has a similar structure as Chapter 3, but focuses on another embedded cluster, NGC 7129, which is also very young but ~ 3 times further away than NGC 1333. The article of Chapter 3 is being submitted in 2010 May in the *Astronomical Journal*, and Chapter 4 is in preparation state to be published.

The variability study of the two selected embedded clusters were proposed originally for the scientific application of *FanCam* as a part of my Ph.D. thesis. I planned the optimized observational strategy and conducted most of the observations for myself. I was also responsible for the development of the data reduction software and the astronomical interpretation of the reduced data of NGC 1333 and NGC 7129. S. Kaneganti and Prof. Skrutskie have been the best consultant and advisor throughout all the activities of my campaign.

Finally, in Appendices A. and B., I introduce two more collaborative work. The hand-held near-infrared spectrograph project in which I worked for its mechanical design was presented in the SPIE conference of May 2006 and published in the *Proceedings of SPIE* 6265:62653W, 2006 July. The parallax feasibility study with *FanCam* was presented in the AAS 215th conference 2010 January and published in *New Astronomy* 15:547-553, 2010. In this astrometry program, I helped Jennifer Bartlett observe the test cluster NGC 2420 and process the obtained FITS images. The miscellaneous items are presented in the rest of Appendices for future reference.

Chapter 2

FanCam – A Near-Infrared Camera for the Fan Mountain Observatory

Article appears in PASP 121:885–896, 2009 August

Authors¹: Kanneganti, Park, Skrutskie, Wilson, Nelson, Smith, & Lam

Abstract

The Fan Mountain Near-Infrared Camera, *FanCam*, provides the University of Virginia's 31 inch telescope with a near-infrared observing capability that is relatively unique among small-aperture telescopes. *FanCam* features an $8.7' \times 8.7'$ field of view on a 1024×1024 Teledyne Imaging Sensors HAWAII-1 detector array. The instrument mounts at the $f/15.5$ focus of the 31 inch telescope. Its seeing-limited optical design, optimized for the *JHK* atmospheric bands, includes a field stop at the telescope focus, a doublet collimator, two 8-position filterwheels straddling a Lyot stop, and a doublet reimager. Four fold mirrors wrap the optical path onto a compact optical bench.

¹The first and second authors have contributed equally to the work presented in this article.

The $0.51''\text{pixel}^{-1}$ plate scale leads to a slightly oversampled point spread function for the typical seeing of $1.5''$. The entire optical train is encased in a cryogenic dewar cooled by a closed-loop cooling system. This Chapter describes the optical, mechanical, cryogenic and electronic design of the camera as well as some early results that illustrate the camera's capabilities.

2.1 Introduction

The introduction of infrared array detector technology beginning in the mid-1980's revolutionized ground and space-based observational research. Today, a large-format near-infrared camera/spectrograph is a staple of nearly every major observatory. Modern arrays and the instruments that contain them are, however, costly and while observatories with telescopes of 2-m apertures and larger can sometimes afford such instruments, 1-m aperture and smaller telescopes can rarely support such expensive equipment. Since smaller telescopes are far more available for long-term synoptic observations, small telescopes with infrared instrumentation can exploit scientific niches prohibitive at larger facilities. The University of Virginia has undertaken the development of a facility infrared camera for its 31 inch telescope at Fan Mountain Observatory 15 miles southwest of Charlottesville, Virginia to fulfill such a scientific niche and to provide students training in the basic concepts of camera and cryogenic design. The camera design and assembly has been primarily performed by graduate students. In this Chapter we describes the resulting design as well as its execution and commissioning at Fan Mountain Observatory.

2.2 Optical Design

The measured median seeing of around $1.5''$ with occasional excursions below $1''$ established a design goal of $0.5'' \text{ pixel}^{-1}$ for the camera optics. The array available for this project was a Rockwell (now Teledyne Imaging Sensors) 1024×1024 HAWAII-1 array (Hodapp et al. 1995). At $0.5'' \text{ pixel}^{-1}$ this array would cover a field of view of $8.5' \times 8.5'$.

Background suppression in an infrared system requires the formation of a conj-

gate pupil image where a coincident cold Lyot stop blocks thermal radiation coming from surfaces other than the telescope mirrors (e.g., Persson et al. 1992, 2002). In practice this configuration is achieved by collimating a portion of the optical path such that a conjugate image of the telescope pupil is formed within the collimated space and placing at that location a cold optical mask that blocks everything other than the pupil image.

The optical design was optimized using the commercial design software ZEMAX. A doublet collimator and a doublet reimager with a field flattener near the detector was chosen as the desired optical configuration. Elements were paired based on multiple combinations of standard low-cost materials chosen from well documented optimal near-infrared achromat combinations (Ren & Allington-Smith 1999; Oliva & Gennari 1995, 1998). For convenience of assembly and disassembly, the corrector was required to be at least 30 mm away from the detector. The design software allowed weighted preferences on the optical quality and physical dimensions to guide iterative optimization of the design. The design preferences included a common focus for J , H , and K_s filters to allow the switching between any filters without the need for refocusing, a Lyot stop located in the collimated space, a plate scale of around $0.5''$ pixel⁻¹, an RMS PSF less than 2 pixels in diameter, and a field distortion of less than 0.1% across the field to ease mosaicing and enable precision astrometry.

Design requirements also included upper limits on doublet focal lengths, lens sizes and curvatures to reduce the cost of the optics and the bulk of the instrument. The design was driven towards small lenses with low radii of curvature to reduce cost, to ease assembly, and to minimize optical aberrations. As the design progressed, the optimization process forced the corrector element to lose much of its optical power and it was then removed from the design. The doublets were designed as separated

rather than cemented doublets to avoid the added thermal stress present in cemented lens assemblies in a cryogenic instrument. The performance of the optical design at different locations on the field of view (FOV) was weighted in the optimization based on the area covered and the importance of location (the center being more important than the corners). The plate scale was allowed to evolve slightly during design progress in an effort to minimize aberrations. As the design evolved, various material pairings were eliminated until only the BaF₂-Infrasil pairing remained. The design was made for a temperature of 77 K and when all the constraints in the design had been met, the configuration was modified slightly to match the test plates of three vendors at room temperatures and re-optimized. The optical performance of all three designs was indistinguishable. Optics For Research, Inc was chosen to fabricate the optical elements. The final warm design parameters are given in Table 2.1. The theoretical performance of the final optical design is presented in Figure 2.1, and its optical prescription in Table 2.2. Four bare-gold fold mirrors were added to make the mechanical layout compact (see §2.3). In the wavelength range of 1.0-2.4 μm , all four mirrors have better than 98% reflection, the window has better than 98% transmission and all four lenses have better than 98.5% single surface transmission, resulting in a cumulative camera throughput of about 80%. This estimate does not include detector quantum efficiency and filter throughput.

Two filterwheels straddle the Lyot Stop. Each wheel has 8 positions. The filter slots are machined with a 7° tilt away from the optical path to avoid ghosts created by filters. Currently, the first filterwheel holds Y, *J*, *H*, *K_s*, H₂ and Br- γ filters and a blocker while the second filterwheel holds K, Pa- β & Fe-II filters and two Wollaston Prism Polarizers offset by a 45-degree rotation (Oliva et al. 1997; Oliva 1997; McDavid et al. 2006). One position in each filterwheel must remain empty

for independent operation, leaving two positions in the second filterwheel to be filled by gratings at a future date. The optical setup includes an aperture wheel located at the telescope's Cassegrain focal plane. The aperture wheel has four positions. One position supplies a field stop for the camera in the imaging mode, and is undersized to prevent stray light from spraying in from the edges of the detector substrate. Another position will contain a multiple-slit aperture mask for use with gratings to enable long slit spectroscopy, while a third position has a blocker in place for testing purposes and the fourth position is empty.

Table 2.1: Principal Parameters of the Optical Design (Theoretical)

Design Parameters	Values
Field of View (FOV)	$8.7' \times 8.7'$
Pixel Plate-scale	$0.51'' \text{ pixel}^{-1}$
Field Curvature	$< 50 \mu\text{m}$, maximum at the edge of the FOV, causing a blur of $< 0.25 \text{ pixel}$
Distortion	$< 0.1 \text{ pixels}$ on 90% of the FOV, $< 0.5 \text{ pixels}$ at the corners of the FOV
Sharpest Optical Ghosts	$> 400 \text{ pixels}$ across and 9 mag fainter
Focus shift (secondary mirror)	$\sim 20 \mu\text{m}$ from K_s to H, confocal from H to J
Elemental Position Tolerances	$< 12'$ in Tilt $< 200 \mu\text{m}$ in Decenter $< 200 \mu\text{m}$ in Axial Position

Table 2.2: Prescription for the Optical Design (in mm, at room temperature)

Surf	Surface Title	Radius	Thickness	Glass	Diameter
Obj	Telescope focus	∞	236.44	Field Stop	31.47×31.47
2	Collimator 1	176.66	10.00	BaF ₂	76.20
3	...	149.00	5.00	...	76.20
4	Collimator 2	-96.37	5.00	Infrasil	76.20
5	...	129.30	220.00	...	76.20
6	Lyot Stop	∞	60.00	...	13.70
7	Reimager 1	84.82	5.00	Infrasil	50.80
8	...	-58.91	23.00	...	50.80
9	Reimager 2	153.00	10.00	BaF ₂	50.80
10	...	77.09	131.32	...	50.80
Ima	Image	∞	...	Detector	18.94×18.94

Note: Positive radii indicate convex and negative radii indicate concave exterior surfaces.

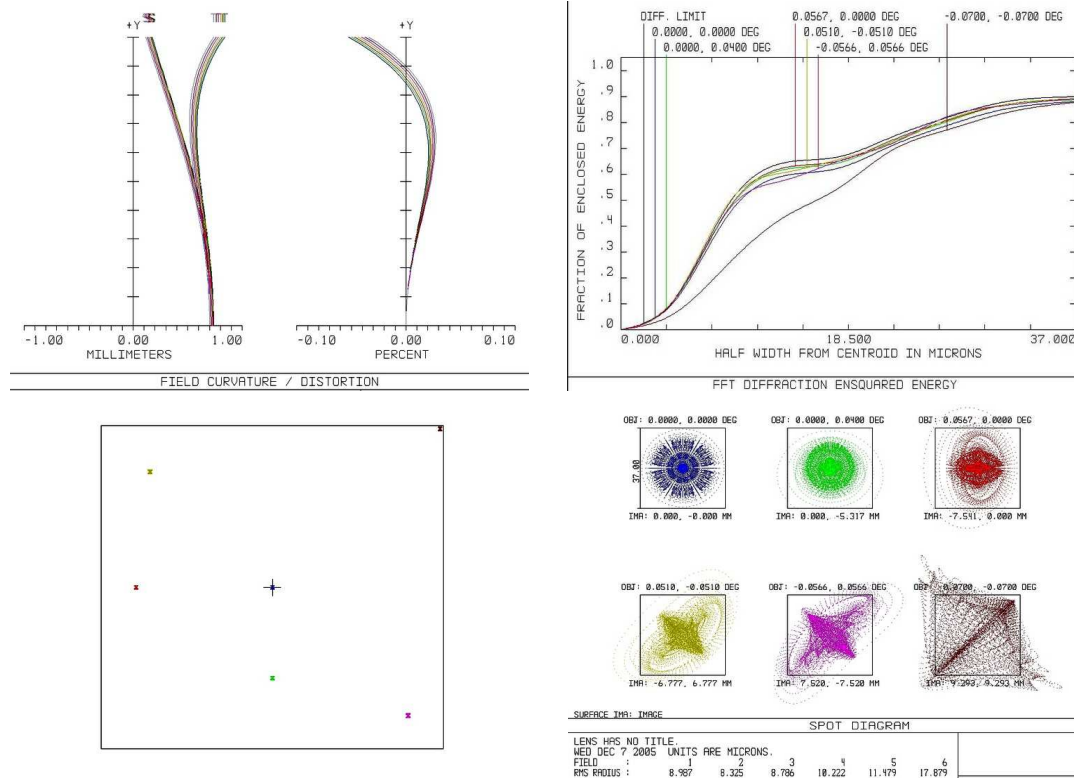


Fig. 2.1.— (*top left*) Field curvature and distortion for the optical design. The plots run from the center to the corner of the FOV. (*top right*) Ensquared energy plot for the different field positions the design was weighted with. (*bottom left*) The positions on the detector weighted in the optical design. (*bottom right*) Spot diagram for JHK_s bands combined. The box is two pixels on a side. The tight combined psfs imply that there is no noticeable change in plate scale or distortion across the filters.

2.3 Mechanical Design

The German equatorial configuration of the 31 inch telescope constrains the overall dimensions of the instrument which must fit behind the tube of the telescope and clear the floor when the telescope is pointed at the zenith. This leads to a maximum-size requirement of $40 \times 40 \times 40$ inches for the dewar. The distance from the telescope focal plane, 4 inch from the back of the telescope, to the detector focal plane is about 28 inch. Four gold first-surface fold mirrors are used to package the optical path after the telescope focal plane into a compact open rectangle as shown in Figure 2.2 (*top left*). This configuration permitted the mounting of all fold mirrors and optical components on a single 18×10 inch rectangular optical bench perpendicular to the optical axis of the telescope, as shown in Figure 2.2 (*top right*). The optical bench is covered by a 5-sided $18 \times 10 \times 6$ inch rectangular radiation shield with a circular opening at the top for the optical path. Four hollow cylindrical G-10 fiberglass posts support the optical bench from underneath and in turn stand on a 20×12 inch “bottom plate” that forms the back of the vacuum dewar. The bottom plate, and an identically sized “top plate” sit on either end of a rectangular shell to make up the $20 \times 12 \times 11$ inch dewar. The four sides of the shell are welded together and the top and bottom plates are sealed with O-rings in rectangular grooves all around the rims.

The bottom plate supports all physical connections into the dewar, consisting of the four G-10 support posts, a pressure sensor, the vacuum port, the electronic connections to the detector, the temperature sensors attached to various locations in the dewar, the cold-head and three motor shafts that drive the filterwheels and the aperture wheel. The top plate holds a 3 inch circular Zinc Selenide optical window with a 2.25 inch clear aperture seated on an O-ring and need rarely be disturbed. The other four sides of the dewar are bare. This allows the top plate to be handled

together with the four walls of the dewar as a single cover that sits on the rectangular O-ring on the bottom plate. Four legs on the underside of the bottom plate act as a stand when the camera is in the lab and as protection for all the connections on the back of the dewar when it is on the telescope. This configuration makes the system very easy to open, requiring only the removal of the 5-sided dewar shell and the 5-sided radiation shield to gain access to all the components in the dewar. The dewar shell was light-weighted on all five sides in an effort to decrease the overall system mass. The thinning of the vacuum shell was overly aggressive, resulting in sufficient deformation under vacuum to compromise the O-ring seal. Bracing was added on two sides to stiffen the shell and the system has demonstrated good vacuum integrity from then on. The complete system (not including electronics) is $20 \times 12 \times 11$ inches and weighs 80 lb. The camera is shown in the lab and on the telescope in Figure 2.3.

The optics were positioned on the optical bench using two dowel pins per mount. The optical design has a loose tolerance for tilt and decenter of the lenses (see Table 2.1) so the barrels for the lenses were oversized by 0.005 inch per inch of lens diameter. This allows for differential thermal contraction between the aluminum barrels and the lenses while keeping maximum decenters of the lenses within the allowed limits. The axial positioning of the lenses was achieved by using simple aluminum ring spacers with their surfaces bevelled to match the curvatures of the lens faces they press against. The spacers have the same outer diameter as the lenses and have an inner diameter 0.25 inch smaller. Rings made of 0.010 inch nylon sheets act as low-friction non-abrasive contacts between the lenses and their spacers. Three spring plungers push the lens and spacer assembly against a machined cardinal surface on the lens mount to provide repeatable axial and tilt positioning. The spring plungers apply a force of 4 lbf on the 3 inch collimator lenses and 2 lbf on the 2 inch reimager lenses.

No radial pre-load is applied to the lenses.

The gold front-surface fold mirrors are positioned on three nylon-tipped set-screws on the front surface and constrained radially by three more on the circumference. A spring plunger centered on the back of the mirror provides pressure to hold the mirror against the front set screws. The spring plungers apply a force of 2 lbf on the 0.1-lb 2 inch mirror, 4 lbf on the 0.4-lb 3 inch mirrors. All the mirrors are made of quartz, and no degrading effect of these pre-loads has been noticed on the optical performance. Figure 2.2 shows the mechanical design and assembly. The detector is mounted on a fanout board (discussed in §2.5) which is encased in a light-tight box with an aperture protected by a light baffle. The box is mounted on a frame that stands vertical on the optical bench. The detector box is free-positioned on the frame along both the axes of the detector array to adjust its position relative to the field stop. The frame can be positioned freely along the optical path to adjust focus. While this setup is not absolutely repeatable, very good success with detector positioning was seen on three different instances by using measurements from the edges of the optical bench to the detector mount.

The filterwheels and the aperture wheel have been machined with a spur gear on their rims to form a natural driven gear. The aperture wheel is positioned parallel to the optical bench and has a straight-through gear shaft from the dewar exterior to the aperture wheel. The gear shaft has multiple breaks in it for flexure and thermal insulation. The two filterwheels are positioned perpendicular to the optical bench. They have spur gear connections to secondary shafts parallel to their axis, which in turn use miter gears to connect to the shafts that emerge above the optical bench from the dewar exterior. All these shafts are well aligned and constrained radially, but are allowed some freedom axially to accommodate differential thermal contraction. The

gear train for the aperture wheel contains a flex coupling where it emerges above the optical bench. This ensures that any misalignment due to flexure or contraction will not hamper the functioning of the aperture wheel control. The two filter wheel trains do not have a flex coupling as the miter gears in them form a natural break in the axis. All the gear interlockings in these gear trains have calibrated offsets at room temperature that settle into well meshed gear trains when they cool to 100 K.

FanCam contains some baffling to keep stray light from reaching the detector. Following the optical path from the dewar entrance to the detector, the first baffle encountered is the dewar window cover. The cover has a knife-edge bevel facing the detector to minimise scattered light. The open hole beneath the window in the dewar top plate has a deep-threaded barrel. The entrance to the radiation shield has an extended baffle that protrudes from just above the aperture wheel to just below the dewar window. The barrel of this baffle is deep-threaded in a similar manner to the entrance of the dewar. The radiation shield itself acts as a significant protection against stray light and thermal emission from the warm dewar shell, and is seated on a step around the optical bench to prevent a light leak. The aperture mask acts as another primary stray light blocker. A large flat baffle with an aperture just large enough for the expanding optical beam is positioned between the aperture wheel and the first mirror to further protect against scattered light from the dewar window. There are no more baffles until the light path passes through the first filterwheel.

The Lyot stop, sized to be the exact size of the pupil image at 13.7 mm, is an excellent baffle that blocks stray and scattered light from the telescope. The reimaging optics and the final mirror are placed inside a small box with protruding threaded barrels at the entrance and the exit of the optical path through the box. The detector is encased in a light-tight box with a threaded barrel that protrudes and enshrouds

the barrel from the reimaging optics. A mylar sheet is wrapped around these two barrels to prevent light scattering in between them. All the surfaces described here, with the exception of the threaded dewar entrance and the inside of the detector box, are painted with Aeroglaze Z-306 black paint. The two filterwheels and the aperture wheel are also painted black. All the painted surfaces are colder than 120K and act as excellent absorbing surfaces for stray and thermal light. Overall stray light is only detected at two orders of magnitude or more fainter than the broadband backgrounds.

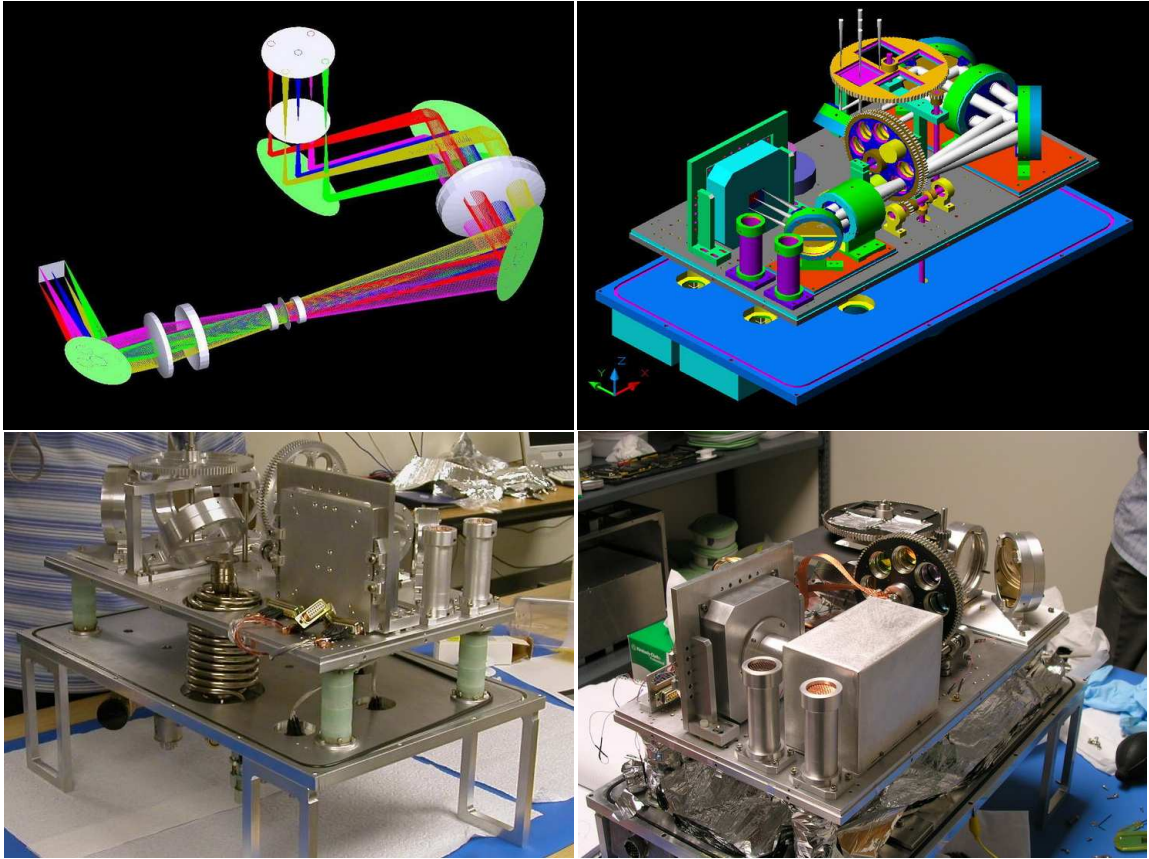


Fig. 2.2.— Snapshots of *FanCam* at various stages of its mechanical design. (*top left*) The optical design, with the optical path folded up in accordance with the requirements of the mechanical design. (*top right*) Computer-generated model of the camera where detailed mechanical parts are assembled with the optics. (*bottom left*) Precision-machined parts assembled without the optics. Thinned G-10 posts hold the optical bench in place. The coiled cylinder rising up from the bottom of the dewar is the cryogenic cold-head. Flexible copper straps and braids connect the tip of the cryocooler with different locations on the optical bench (not shown). (*bottom right*) The fully assembled (and uncovered) camera.

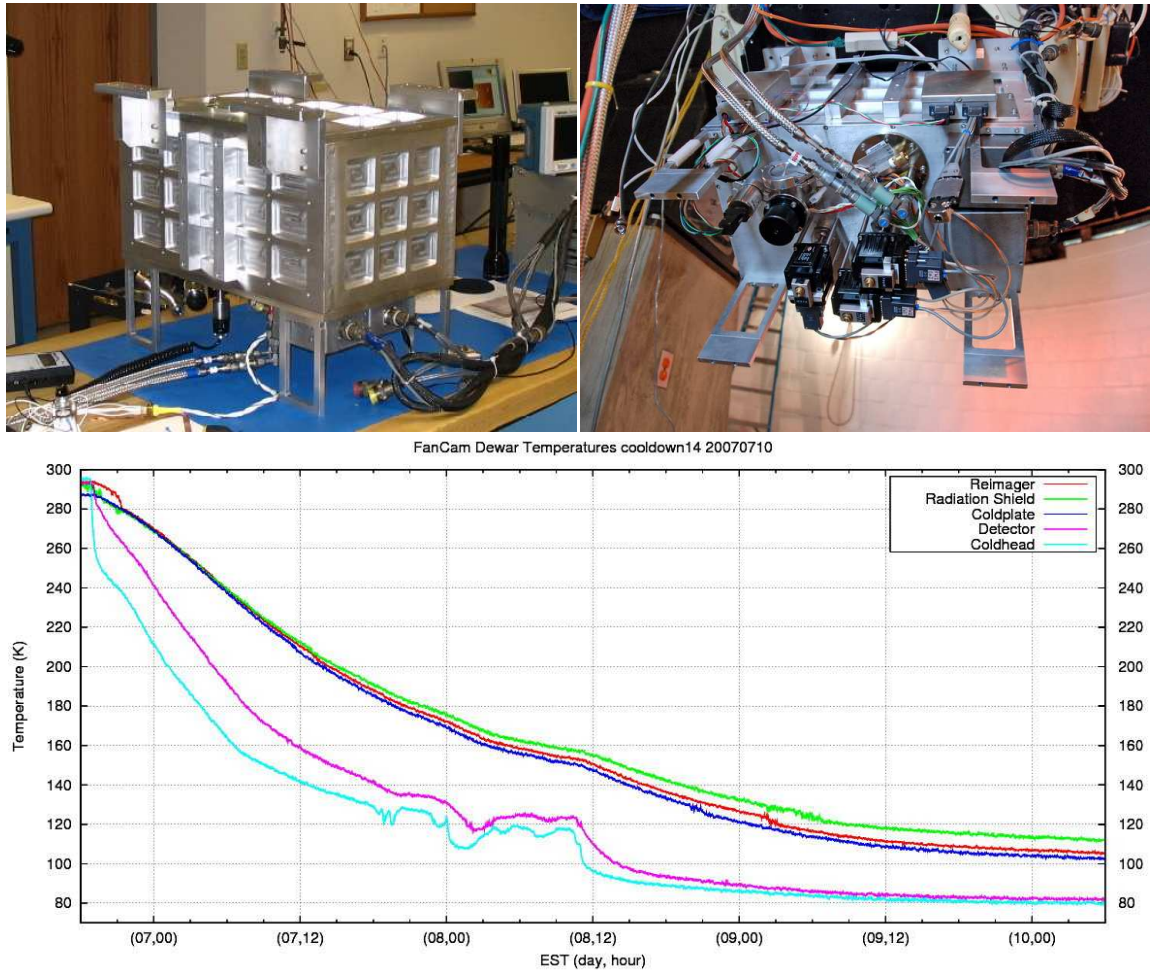


Fig. 2.3.— (*top left*) The camera closed up and cold, ready for first-light. Notice the light-weighting and the stiffeners installed subsequently. (*top right*) *FanCam* on the telescope. Notice the small tail-piece of the telescope. The cables connected to *FanCam* are transporting the refrigerant keeping the dewar cold. (*bottom*) A typical cooldown of *FanCam*. The chaotic behavior of the cold-head temperatures at around 120K is due to a phase-transitional instability at these temperatures inherent to the proprietary gas mixture PT-13 used by the Cryotiger cooling system.

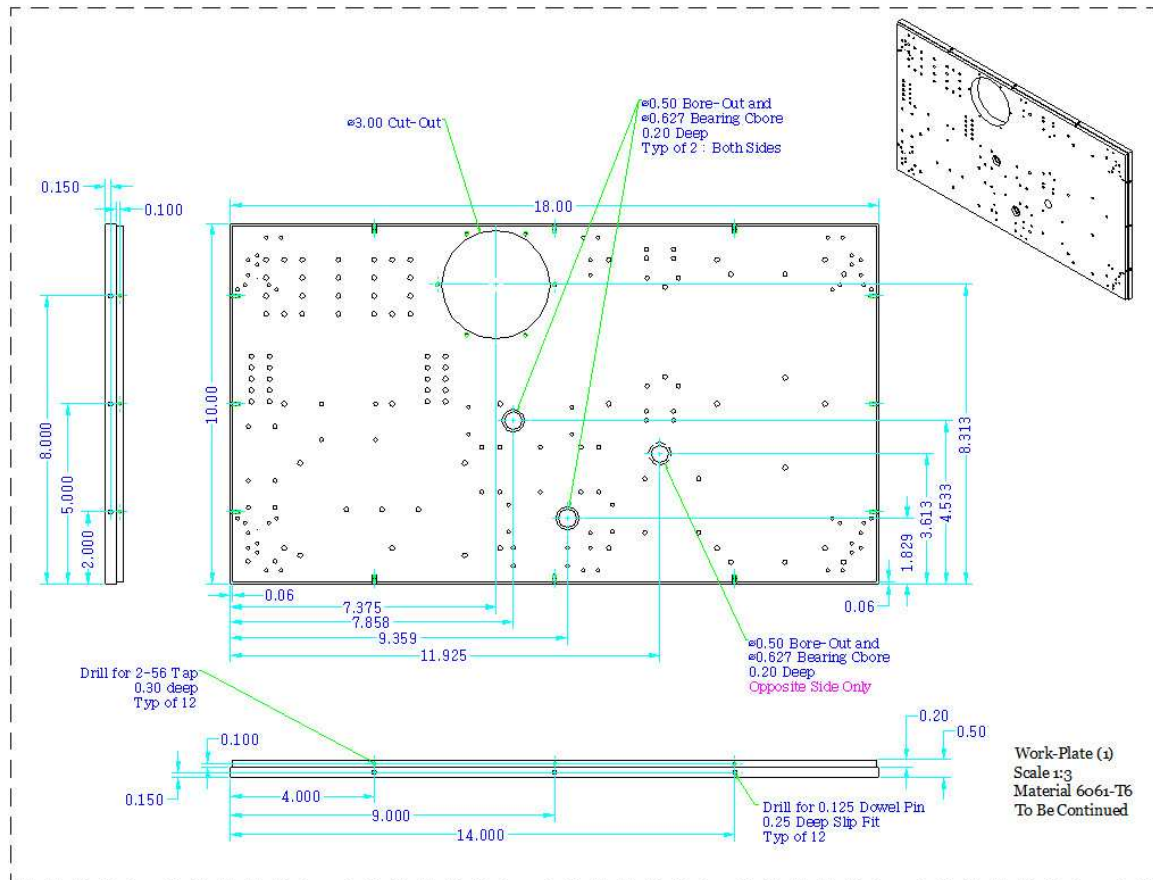


Fig. 2.4.— An example of CAD drawing: Optical Bench. Precision optical bench design does not require extra alignment of optics mounts on the plate.

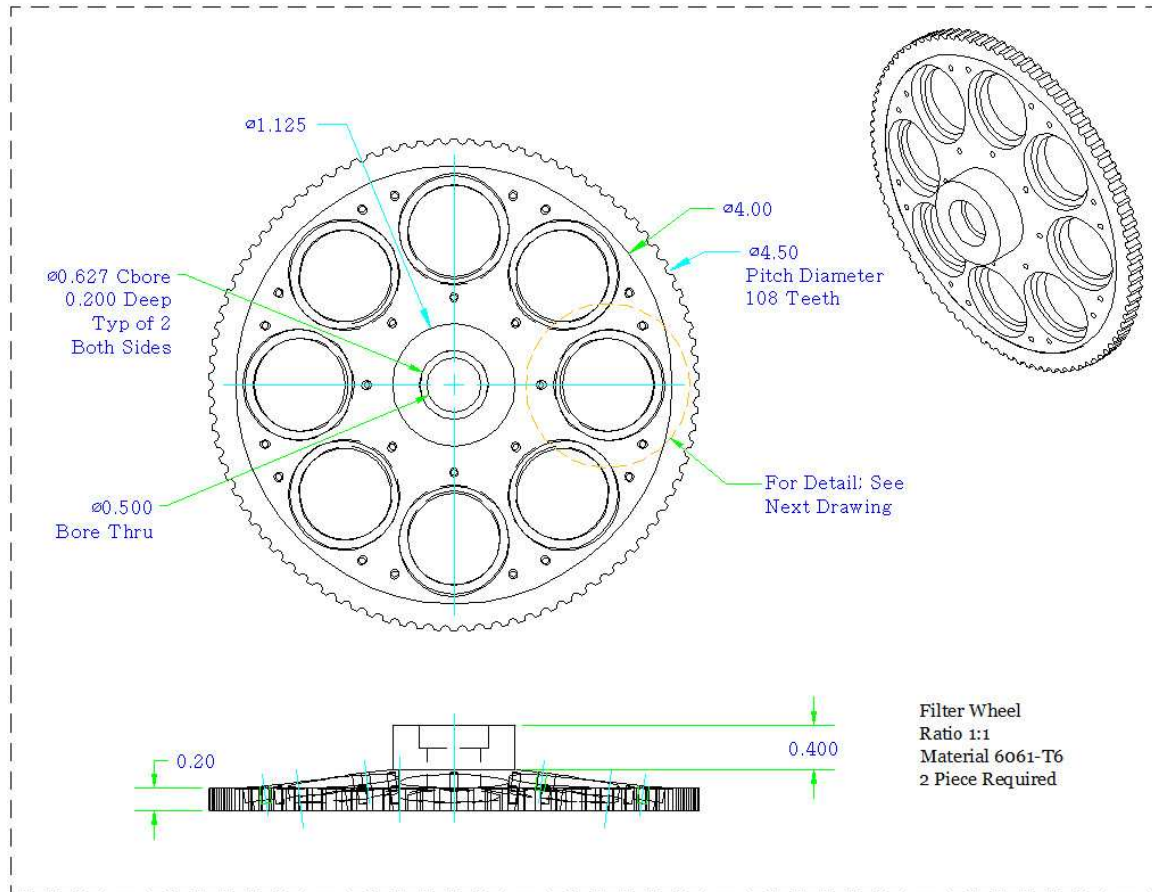


Fig. 2.5.— An example of CAD drawing: Filterwheel. Filter-holding surface is tilted 7° from the wheel axis.

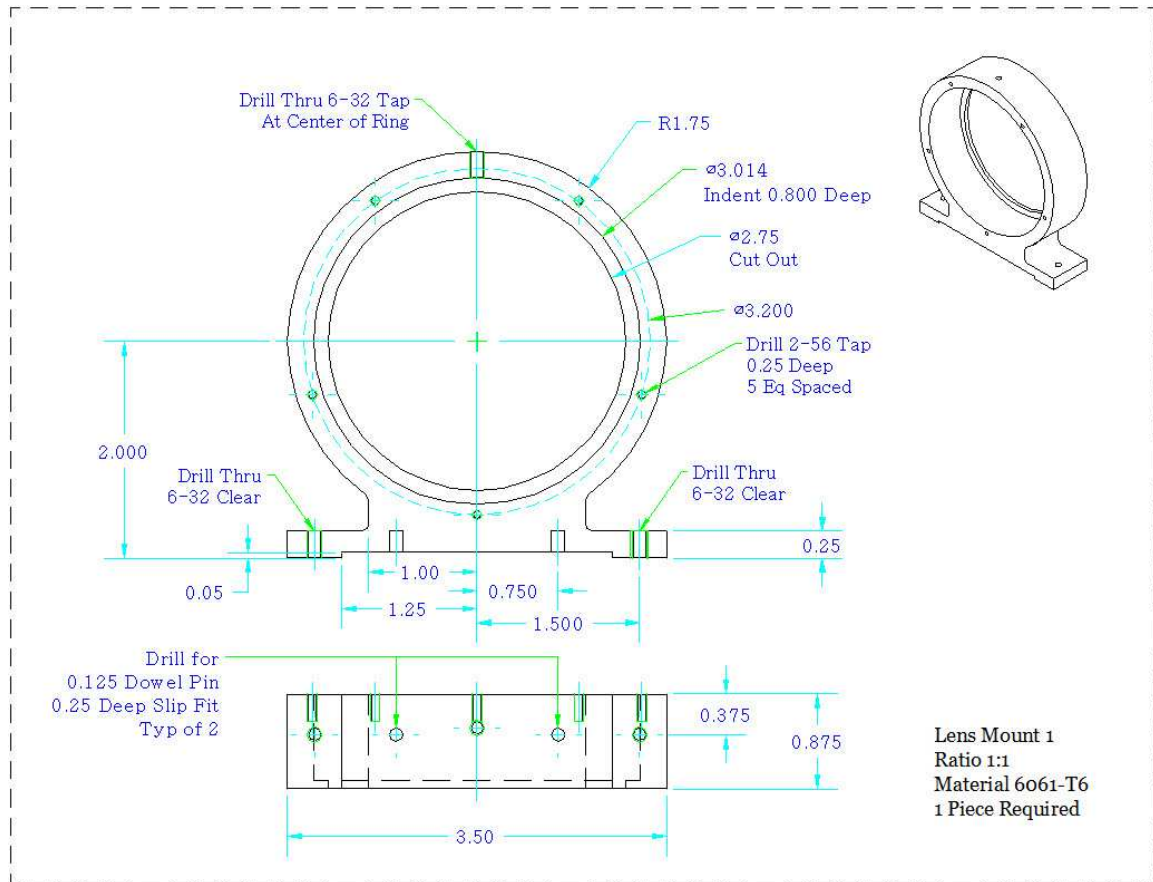


Fig. 2.6.— An example of CAD drawing: Collimator Lens Mount. No radial pre-load is applied to the lenses.

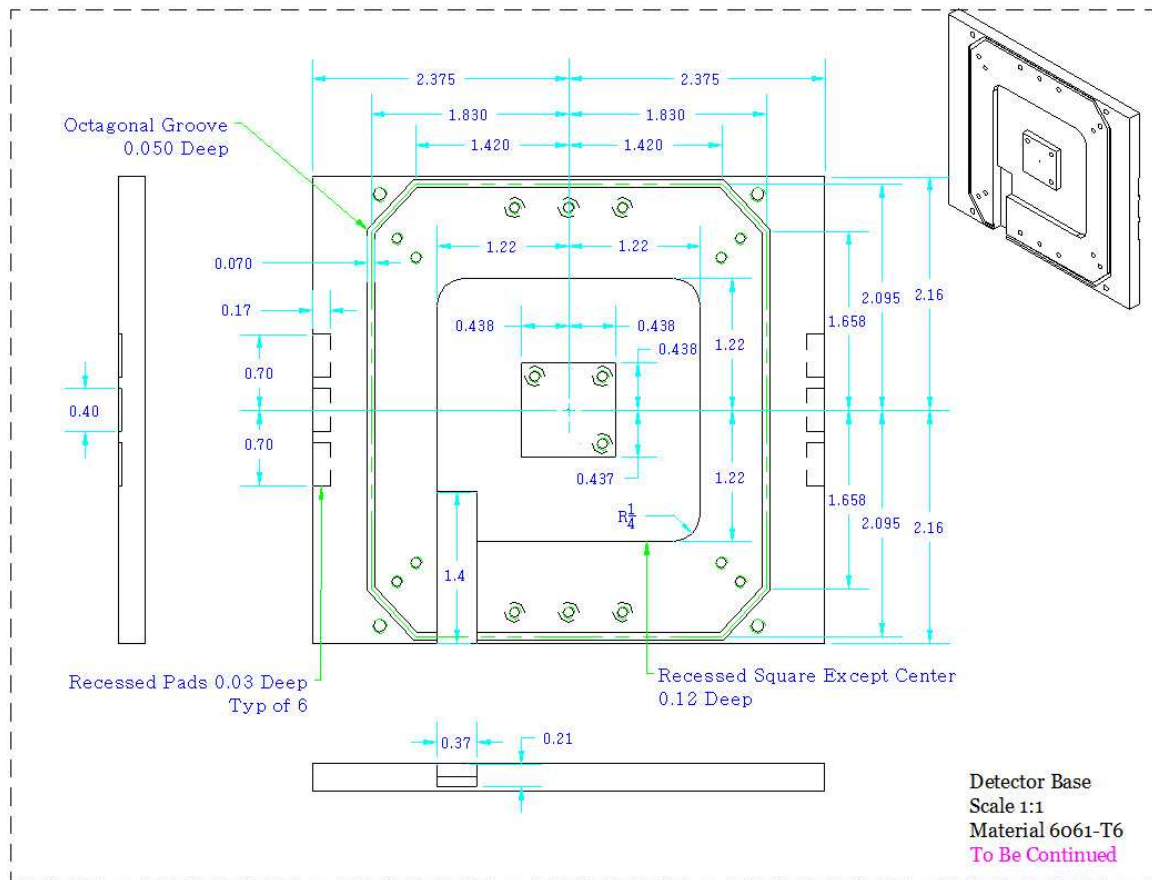


Fig. 2.7.— An example of CAD drawing: Detector Box Base. HAWAII-1 focal plane array is housed above the base with 4 standoffs at each corner.

2.4 Cryogenic Design

Fan Mountain Observatory does not maintain any personnel at the site and thus, to increase the ease of maintenance and observing, the system uses a closed-cycle cryogenic refrigeration system manufactured by IGC Polycold. This “Cryotiger” system can dissipate 5 Watts of heat load at a cold-head temperature of 80 K and about 4.3 Watts at 77 K. The cold-head is compact, with the working cold tip of the cold-head less than 6 inches from its base which stays at room temperature and outside the dewar. The compressor and cold-head are connected via 50 feet of refrigerant supply and return lines, permitting the compressor to reside in a temperature controlled environment and providing sufficient cable slack to permit pointing of the telescope, particularly “flipping” over the German mount. While the Cryotiger system has helped create a camera system with a minimal work load during normal operations, its low cooling capacity was also the most demanding constraint on the cryogenic design.

The optical bench is supported by four thin-walled cylindrical G-10 posts from the dewar bottom plate. The G-10 posts are 1 inch diameter, 2.75 inch long cylinders with 0.032 inch thick walls. Small aluminum bases are epoxied at both ends of the G-10 posts, and are bolted to the optical bench and the bottom plate. The optical bench was expected to cool to 100 K and the G-10 posts were estimated to create a combined heat load of 0.40 W on it. The steel shafts that drive the filter wheels and the aperture wheel are converted to G-10 upon entry into the dewar and revert back to steel upon reaching the optical bench. The G-10 conversion is done by slipping a hollow G-10 shaft onto an undersized end of the steel shaft and using a bolt to constrain it rotationally. The bolt also provided some axial compliance in case of an axial misalignment between the G-10 and steel shafts. All shafting is 0.25 inches

in diameter. The three G-10 shafts are estimated to create a maximum combined heat load of 0.12 W on the optical bench. The electrical wiring (discussed in §2.5) lays a conductive thermal load of 0.55 W on the optical bench. The residual gas pressure in the dewar, typically 1×10^{-4} Torr, is estimated to create a gas conduction heat transfer load of 1.4 W (Flynn 2005). The radiation shield and the back of the optical bench are covered by about 20 layers of one-sided aluminized-mylar insulation. Heat absorption by multilayer insulations depend on the residual gas pressure. At a pressure of 1×10^{-4} Torr the thermal load from the insulation is about 1.7 W (Scurlock & Saull 1976; Stochl 1974; Shu et al. 1986). The cumulative thermal load on the cooling system is estimated at 4.17 W.

Attention must also be given to differential thermal contraction in cryogenic system design. All machined parts in the camera, except for the thermal isolators described above, are made of aluminum in an effort to mitigate problems associated with differential contraction. The optical positioning of all the lenses and mirrors takes into account thermal contraction of the various materials between 298 K and 100 K. The only metal parts on the cold space that are not made of aluminum are the stainless steel shafts and bearings. Bearings used in *FanCam* have a diameter of 0.500 inch or 0.625 inch and cryogenic tests have shown that when mounted in “slip-fit” slots oversized in diameter by 0.0005 inch, these bearings function smoothly at 77 K. Thus, all bearings are mounted in slots sized to this specification. Shaft collars are used with all bearings to ensure that they do not slip out of their slots. The design of the gear trains that use these shafts takes into account the difference between the build and operating temperatures (see §2.3).

The thermal link between the cold-head and the rest of the system is formed by a bundle of eight, 0.030 inch thick, 1 inch wide copper straps anchored by small pads of

metallic Indium at one end on the optical bench, in the middle at the cold-head tip and at the other end on the detector mount box. The detector mount box is insulated from the optical bench by G-10 washers and nylon bolts. This helps keep the detector colder than the rest of the system. The strength of the thermal connection between the cold-head and optical bench, and the cold-head and detector, is determined by the length of copper straps between these three locations. The final lengths were determined by experimentation over multiple cooldowns. In the final configuration, the Cryotiger cold-head reaches a temperature of 77 K, cools the detector to 80 K, the rest of the optical bench to 100 K, and the radiation shield to 120 K. Cooling the optics to <140 K is sufficient to suppress the thermal background for operation out to a wavelength of $2.4\text{ }\mu\text{m}$. Given the large thermal mass of the system and the ability of the cryogenic refrigerator to dissipate no more than 10 Watts, the time required to reach operating temperature is approximately 3 days. Once cold, the system can remain in that state as long as the vacuum is well maintained.

In practice, O-ring diffusion coupled with the marginally extra cooling capacity of the Cryotiger leads to shorter periods of cryogenic sustainability during warmer months of the year. In an effort to retain a better vacuum for longer duration and counter the effects of O-ring diffusion, getter materials have been placed in the dewar. The two small towers seen in the foreground in Figure 2.2 (top right and bottom right) contain Zeolite 5A and activated charcoal. The charcoal adsorbs most vapours and gases at cryogenic temperatures and releases them when warmed to room temperature or higher, while Zeolite adsorbs high quantities of water at room and cryogenic temperatures and will release it when baked at around 300°C . A release of up to 100 mTorr of gases has been noted when *FanCam* is warmed after staying cold for 3 months, indicating the very good vacuum integrity of the dewar. The system stays

cold for about 5 weeks at a stretch in the summer and up to 5 months during the winter.

2.5 Electronics

A custom fanout board designed by the University of Hawaii provides the mount for the HAWAII-1 array and distributes the chip carrier's input and output lines to solder connections for low thermal conductivity cabling. To eliminate amplifier glow from the on-chip output JFET, the fanout board includes a J270 JFET per quadrant configured as a source follower. The fanout separates the input digital clock lines from the analog output signals and biases, which interface with the dewar via separate connectors. An Astronomical Research Cameras (ARC) controller provides clock and bias voltages and samples the outputs at three microseconds per pixel dwell time. At this rate the entire chip can be read in 0.7 s, setting the minimum frame integration time. The clock and bias signals enter the dewar through independently powered buffer circuitry that conditions and electrically isolates the input lines.

Similarly, the output signals from the quadrant source followers are amplified, offset, and isolated by independent circuitry prior to entering the ARC electronics. The ARC controller used with the camera was a spare unit for the Two Micron All Sky Survey project. The 2MASS controller firmware was specialized for the short readout time and frame triggering unique to 2MASS. Independent firmware and timing code was developed for the *FanCam* application. As is standard with ARC controllers the digitized frame results emerge from the controller via a fiber optic line which connects to a custom PCI receiver card inside, in this case, a Linux PC. ARC provided the Linux driver for the PCI card. The Linux driver was modified in-house for compatibility with the current Linux kernel. Both an in-house user interface

as well as the ARC-supplied “voodoo” interface have been used at the telescope to configure the camera, retrieve data, and record frames in FITS format. The in-house user interface, written in Java, includes functionality to dither the telescope position between frames and to buffer prior frames for subtraction from incoming frames. Recorded frames are correlated double-sampled, i.e., the difference between a readout of the array immediately following reset and one at the end of the requested integration time.

The four video lines that carry the signals are connected through 32 AWG coaxial copper cables with shields connected to the fanout board ground. The cables are all connected to a single DB-25 connector. The complementary DB-25 connector, mounted on the optical bench, is in turn connected to a 19-pin circular hermetic connector on the bottom plate of the dewar. The clock and bias lines are all connected through eight 32 AWG copper coaxial cables and two 30 AWG copper wires to a second DB-25 connector, the complement of which, mounted on the optical bench, is connected to an 18-pin circular hermetic connector mounted on the bottom plate of the dewar. Auxiliary wiring used for temperature sensors and the detector heater is connected to a DB-9 connector. The filterwheel position sensors are connected to a DB-15 connector. The counterparts to these two connectors are connected by nine twisted pairs of 32 AWG constantan wires, two 30 AWG copper wires, one 32 AWG constantan wire and one 32 AWG copper coaxial cable between them to a 26-pin circular hermetic connector on the bottom plate of the dewar. The thermal load from the electronic wiring is addressed in §2.4.

2.6 Camera Performance

2.6.1 Detector

The detector in *FanCam* is a 1024×1024 element HAWAII-1 detector array with $18.5 \mu\text{m}$ pixels from Teledyne Imaging Sensors (formerly Rockwell Scientific). The usable pixels exceed 99.5% of the entire array. The gain is $4.6 e^- \text{ADU}^{-1}$ and the read noise $17 e^- \text{rms}$ in a correlated double sample. At an operating temperature of 80 K, a small (but in practice negligible) light leak dominates the dark current signal from the HAWAII-1 detector. The measured dark current from the vendor for this detector is $0.050 e^- \text{s}^{-1}$. In practice, through broad and even narrowband filters, airglow and thermal background render any observation with exposure time longer than 10 s background limited.

2.6.2 Photometry and Sensitivity

Most of the analysis detailed in this section has been performed on a dataset obtained on 19 November 2005 of the core of the open cluster NGC 2420. The observations were made in the three primary filters in use with *FanCam*—broadband J , H and K_s . The data consist of 60 dithered 10 s frames of NGC 2420 in each band, 10 10 s dark frames, 10 10 s frames of uncrowded sky in the middle of the on-target frames in each band and 10 10 s frames of unsaturated twilight sky flats in each of the bands. The dataset has background counts of $1000 \text{ ADU minute}^{-1}$ in J , $6000 \text{ ADU minute}^{-1}$ in H and $5500 \text{ ADU minute}^{-1}$ in K_s bands. These backgrounds are typical for a good photometric night at Fan Mountain, and as the detector saturation is at around 25000 ADU, exposure time on individual frames is limited to about 2 minutes. The actual operational limit, however, on exposures for all observations is

one minute because the 31 inch telescope does not have a guiding apparatus. Neither of these exposure limits compromise the observations because the high backgrounds determine the signal-to-noise ratio of the final data, and the only overhead caused by the exposure time limit is the effort that must be expended on frame combination to create images with long exposure times.

After processing the data through standard IRAF reduction techniques, flattened, sky and dark corrected and combined images of NGC 2420 were obtained in each of the three bands. The analysis presented here is based on these images. The Point Spread Function (PSF) of point sources in these images is 2.5 pixels ($1.25''$). The PSF on a typical night usually has a range of 2-4 pixels ($1''$ - $2''$). On occasion a PSF of 1.8 pixels ($\sim 0.9''$) FWHM has been obtained with no evidence of variation in the shape of the PSF across the FOV or residual aberrations. A signal detection limit of 10σ is achieved at a magnitude of 19.0 in J band, 18.0 in H band and 17.0 in K_s band in 10 minutes of integration (see Figure 2.8, top right). No systematic deviation from 2MASS has been detected in *FanCam* photometry (see Figure 2.8, top left). The observations at Fan Mountain are always background-limited and the limiting magnitudes mentioned here are thus subject to change based on the background values, which have been known to reach as high as $8000 \text{ ADU minute}^{-1}$ in J , $12000 \text{ ADU minute}^{-1}$ in H and $13000 \text{ ADU minute}^{-1}$ in K_s bands.

To estimate systematic errors in *FanCam* observing and data reduction techniques, data was obtained on 14 October 2007 of the core of the open cluster NGC 2420. The dataset consisted of 100 60 s frames of the core of NGC 2420 in J band, 10 10 s dark frames and 10 10 s frames of unsaturated twilight sky flats in J band. The dataset was processed in a manner identical to the dataset described above. Photometry was performed independently on each of the 100 data frames. True photometric error

was estimated for 44 stars as the standard deviation in the estimated magnitudes for that star in the 100 frames. The systematic error was then calculated for each star as the difference between true error and the average of the IRAF-generated error estimates for that star in the 100 frames. The systematic error in photometry has been estimated at 0.004 mag (See Figure 2.8, bottom left) and needs to be added to the IRAF-generated errors to derive the true error estimates in *FanCam* photometry.

The design performance of the optics calls for ghost-free images and no ghosts caused by the optics have been detected. However, well-focused ghosts of bright sources occur in *J*-band images when using a filter originally used in the 2MASS prototype camera (Beichman et al. 1998). These ghosts are 5.5 magnitudes fainter than the sources, as was the case in the 2MASS prototype survey, and separated by 17.5". This *J*-band filter has since been replaced with one that has already been demonstrated to be ghost-free.

2.6.3 Astrometry

The astrometric capabilities of *FanCam* have been tested using the same set of observations of NGC 2420 used for the photometric quality testing. For astrometric comparison with 2MASS, the *FanCam* images with 10 minutes cumulative exposure time were used. The *FanCam* astrometric coordinates were determined by a WCS solution using 2MASS coordinates of six stars randomly selected from the field (the field is shown in Figure 2.9 top-right). The coordinates of all the stars in the field were then extracted from the *FanCam* image. For astrometric comparison, stars with good 2MASS astrometry (less than 70 mas error), i.e., stars with magnitudes between 10 and 14 in all bands were selected. The 2MASS and *FanCam* coordinates of these 85 stars were then compared. A histogram of the scatter of *FanCam* positions around

the 2MASS positions is shown in Figure 2.8 (bottom-right).

The internal repeatability of *FanCam* astrometry has been estimated using a set of 100 60 s *J*-band images. Positions of 44 bright stars were extracted in the pixel coordinates of each individual frame. The reference for each frame was calculated from an average of the coordinates of six randomly selected stars. The scatter in the position of a star in all the 100 frames was used to estimate the internal error of those star coordinates. A histogram of the internal errors for these 44 stars is shown in Figure 2.8 (bottom-right). The histograms point to an accuracy of $0.035''$ in *J*-band astrometry with *FanCam*.

2.6.4 Mechanical Performance

The mounting systems for the lenses and mirrors in *FanCam* have withstood repeated thermal cycling, disassemblies and some unexpected mechanical shocks with no noticeable detriment to the optical performance. Positioning of the filters and polarizers has been repeatable to within $40\text{ }\mu\text{m}$ or 0.06° as measured by the positioning of the polarizers at the Lyot stop. The aperture wheel gears have suffered intermittent misalignment that permitted its rotation in only one direction. It is suspected that this is caused by an inflexible axial coupling used to connect the two shafts for turning the aperture wheel (See §2.4). The shafts and bearings have been resilient through multiple thermal cycles and continue to work well. Apart from the initial shell flexure issues, there have been no flexure/rigidity problems with the mechanical design of *FanCam*. The cooling capacity of the Cryotiger cooling system has been only marginally adequate to sustain the temperatures needed inside the dewar, and has lead to unplanned warmups of the system during particularly hot and humid times in summer. At these instances, the dewar usually warms up to a cold-head temperature

of around 120 K, where the Cryotiger system has a higher heat load capacity (see Figure 2.3).

FanCam was originally assembled with a temporary ZnSe window that was available prior to the delivery of the Infrasil window prescribed by the optical design. When the ZnSe window was eventually replaced by an Infrasil window, condensation was noticed on the window during periods of high humidity. It has been surmised that radiative thermal coupling of the window with the cold interior at $10\text{ }\mu\text{m}$ lead to condensation on the Infrasil window. The ZnSe window fared better because its transparency extends past $15\text{ }\mu\text{m}$ and its thermal conductivity ($k_{\text{ZnSe}}=18\text{ Wm}^{-1}\text{K}^{-1}$) is nearly 12 times that of Infrasil, thereby coupling it well with the warm exterior and poorly with the cold interior. The cooling of a window is dominantly caused by the radiative at its inside surface ($P_{rad} = A\varepsilon\sigma T^4$, where A is window surface area, ε is emissivity of the window, σ is Stefan-Boltzmann constant, and T is window temperature), and conduction plays a major role in heating of the window ($H = kA_c\Delta T x^{-1}$, where k is thermal conductivity of the window, A_c is heat flow total cross-section area, ΔT is temperature difference between the window and the dewar outside, and x is the radius of window in this case). By equating the heating and cooling energy transfer rate, we can get the equilibrium temperature at the ceter of the window. It tells that a 3 inch diameter Infrasil window reaches ~ 10 degree lower temperature than environment, while ZnSe stays within 1 degree lower. A new ZnSe window has since been procured and installed, with no recurrence of condensation. The swapping of the windows should change the astigmatism and increase the spot radius on the scale of less than $1\text{ }\mu\text{m}$ at the detector and, consistent with this, no change in optical performance has been noticed.

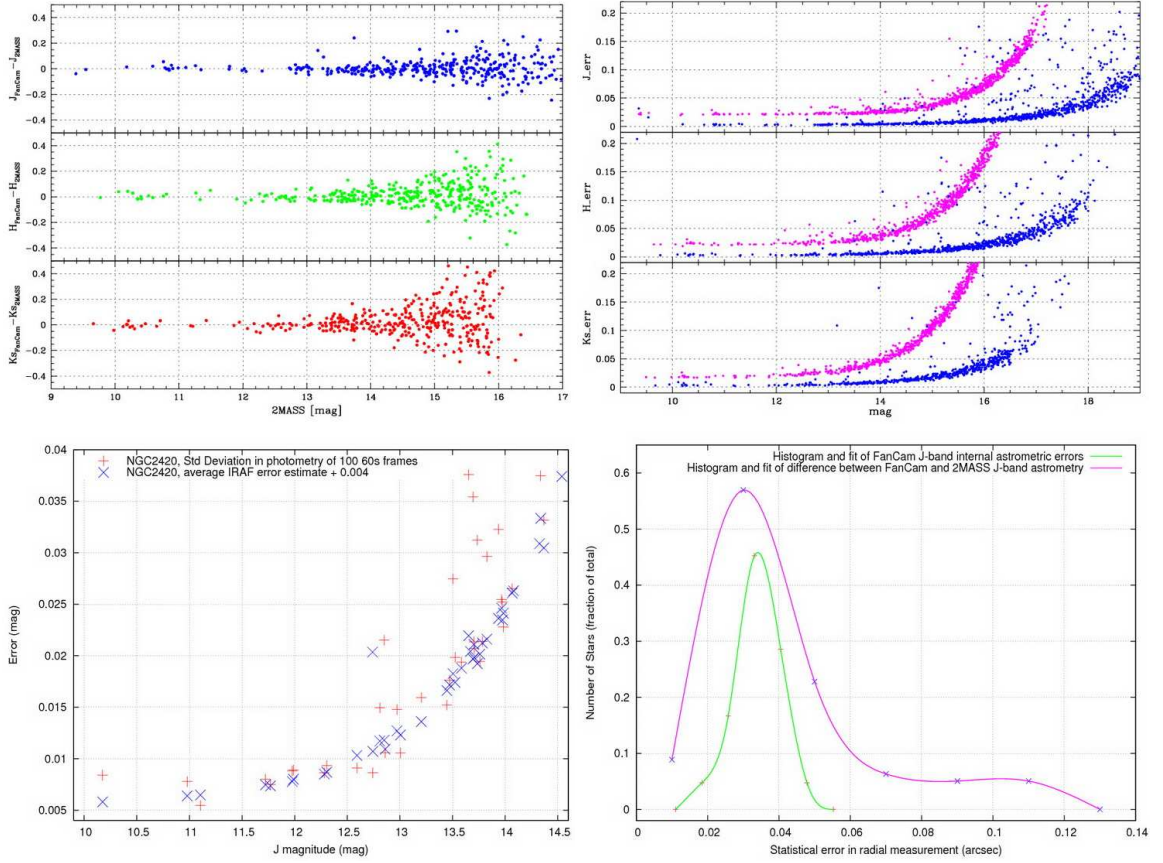


Fig. 2.8.— (*top left*) The magnitude comparison between the 2MASS and *FanCam*. No systematic nonlinearities are seen. (*top right*) The error analysis of *FanCam* magnitudes and comparison with 2MASS. The exposure time for the *FanCam* magnitudes is 10 minutes in each filter. (*bottom left*) A comparison of the variation in magnitude, in one hundred 60-s frames, of 44 stars and the error estimated by our IRAF scripts. The true error estimate is 0.004 mag higher than the IRAF estimate. (*bottom right*) The histogram of internal variations is of the measurements of distances of 43 stars to a single star in 100 60 s *J*-band frames. The second, broader, histogram is of the difference between the 2MASS positions and positions in a *FanCam* *J*-band image with 10 minutes of cumulative exposure.

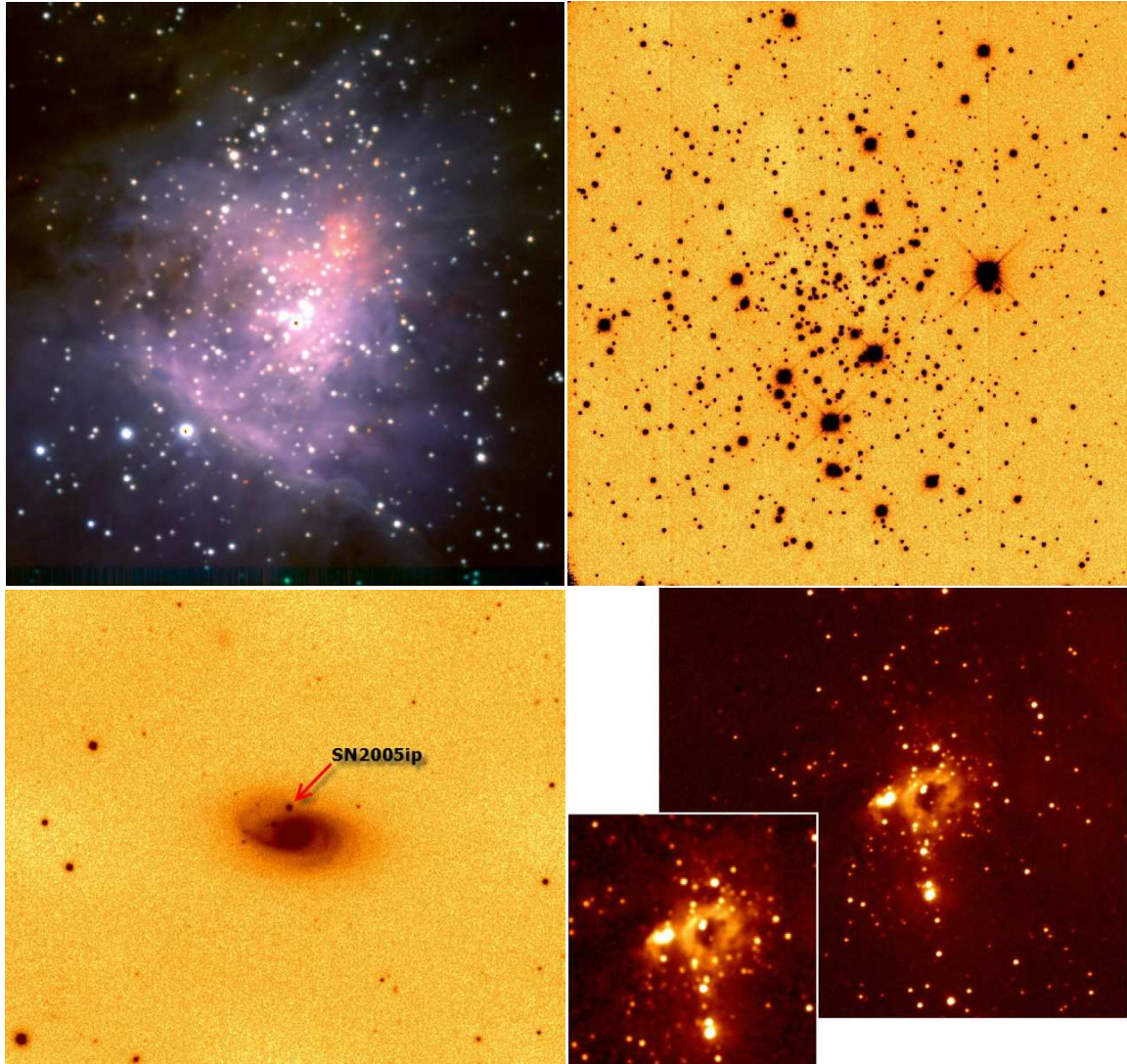


Fig. 2.9.— (*top left*) A composite of the Orion Nebula with 1 minute exposures in JHK_s bands. (*top right*) A stacked image of NGC 2420 in J band with a cumulative exposure time of 10 minutes. (*bottom left*) A 30 minute K_s -band image of an extragalactic supernova Type II_n 2005ip in NGC 2906 (Fox et al. 2009). (*bottom right*) Mon R2 in H band with an inset of the same from 2MASS. *FanCam* sees deeper than 2MASS in this 5 minute exposure. *FanCam*'s plate scale of $0.51'' \text{ pixel}^{-1}$ also improves upon the $2'' \text{ pixel}^{-1}$ plate scale of 2MASS.

2.7 Upgrades

Future upgrades of the system include installing one or more gratings in the filter wheels to facilitate spectroscopic measurements of resolutions $R \sim 200\text{-}500$ in conjunction with the broadband filters. A slit mask for spectroscopy is also to be installed in the aperture wheel. The filter wheels and the aperture wheel are at present turned manually, and are positioned with the help of mechanical shaft encoders. A flex coupling will be used to replace a rigid shaft coupling in the aperture wheel gear-shaft train to remedy the intermittent misalignment of gears discussed in §2.6.4. In the near future, Hall-effect position sensors will be mounted on the filter wheels and computer-controlled encoded motors mounted on the shafts entering the dewar to allow computerized operation of the filter wheels and the aperture wheel. There are concerns about vacuum leaks due to the use of single o-ring shaft feedthroughs and these will be replaced with ferrofluidic feedthroughs. Due to the issues with cooling capacity mentioned in §2.6.4 the cold-head in *FanCam* will be replaced with a high-performance version to insure against further unplanned warmups of *FanCam*.

Chapter 3

Near-Infrared Variability of Young Stellar Objects in the Embedded Cluster NGC 1333

Article submitting to AJ, 2010 May

Authors: Park, Skrutskie, & Kanneganti

Abstract

Long term near-infrared, J , H , and K_s , photometric monitoring of the embedded cluster NGC 1333 is presented in this Chapter. The data were obtained with *FanCam*, a near-infrared camera at Fan Mountain Observatory near Charlottesville, VA, from November 2005 to October 2007, including 33 epochs for the northern cluster and 31 epochs for the southern. We employ the Stetson variability index and reduced chi-square to identify variable stars. More than 50% of the detected point sources, 110 out of 198, are variable, which is unusually high compared with previous cluster variability

studies (e.g., the Orion Nebula cluster, Chamaeleon I cluster, ρ Ophiuchi cluster, NGC 7129), suggesting that NGC 1333 is much younger and/or our observed field of view contains few field stars. Color-magnitude and color-color diagrams demonstrate that NGC 1333 is extremely young and highly extincted. Light curves in all three bands are well correlated. No periodicities are evident. Based on color-magnitude variability trends, accretion-driven variability predominates over extinction-driven variability; $\sim 80\%$ (62 of 78) of the stars become bluer as they fade, showing negative slopes in the K_s vs. $H-K_s$ diagram. The spatial distribution of variable stars shows a strong correlation with the peak of the extinction map while non-variable stars are evenly spread over the whole field of view. 64 out of 72 *Spitzer*-2MASS-identified IR excess YSOs, 89%, are variable, including 13 Class I and 51 Class II stars. 41 of 42 *Chandra* X-ray sources are identified with variable stars; virtually 100%. A total of 25 previously-unknown member candidates are presented, with 15 objects in the mass range of brown dwarfs. We present the first Initial Mass Function of NGC 1333 covering the majority of stellar and substellar members in North and South clusters. The general IMF pattern is similar to that of other embedded clusters. The computed substellar-to-stellar mass ratio in NGC 1333 ($R_{ss} = 0.34 \pm 0.07$) is very well matched with other clusters, although there exist some exceptional cases. We discuss the implication of K_s vs. $H-K_s$ color-magnitude diagram slope statistics in view of the evolutionary sequence of young star-forming embedded clusters.

3.1 Introduction

The young stellar cluster NGC 1333 is named for an optical reflection nebula lying in the active star-forming complex Perseus OB2 and is physically related to the dark cloud Lynds 1450 (Strom et al. 1976; Sargent 1979; Lynds 1969). It is known as an ongoing star formation site via collision of clouds (Loren 1976). While the apparently-nearby Per OB1 association, including η & χ Per, belongs to the Galactic Perseus Arm whose distance is at least ~ 2 kpc (Kolesnik & Metreveli 1985; Xu et al. 2006), the Per OB2 association and NGC 1333 are located inside the Local Spur, or Orion Arm. *Hipparcos* parallactic studies establish a distance to the Per OB2 association of ~ 300 pc (de Zeeuw et al. 1999; Belikov et al. 2002), settling the controversy in earlier studies that suggested a distance between 100 and 500 pc (e.g., Rydgren 1971; Strom et al. 1974; Cernis 1990). Lada et al. (1996) estimated the age of the NGC 1333 embedded cluster to be no more than 1-2 Myrs by interpreting the high fraction of infrared excess sources and by modeling the infrared luminosity function in K band. This age estimate is consistent with the kinematic or expansion age of the Per OB2 association, 1.3 Myrs, derived from proper motion measurements (Lesh 1969).

Strom et al. (1976) first surveyed the NGC 1333 region at near-infrared wavelengths. They found 25 near-infrared sources above a 3σ detection limit of $K=10$ mag. Subsequent near-infrared observations established the existence of two subclusters separated by about $5'$, or 0.5 pc (Aspin et al. 1994; Lada et al. 1996; Wilking et al. 2004; Oasa et al. 2008). Gutermuth et al. (2008) confirmed the double-clustered spatial distribution using *Spitzer* mid-infrared observations and 2MASS near-infrared data. The younger populations, Class I protostars, are found more consistently along the filamentary structures of the submillimeter dust continuum emission (Sandell & Knee 2001; Hatchell et al. 2005). Along the ridge of the dust continuum emission

contours, there exist many indications of star formation in progress, which includes numerous Herbig-Haro objects (e.g., Herbig & Jones 1983; Bally et al. 1996; Bally & Reipurth 2001) and several *IRAS* sources harboring extremely young Class 0 protostars (e.g., Sandell et al. 1991, 1994; Bachiller et al. 1998; Looney et al. 2000; Chini et al. 2001; Choi et al. 2006; Walsh et al. 2007). A profusion of protostellar outflows from the violent turmoil of forming stars must be producing shock waves throughout the molecular complex. These shocks may induce collapse of nearby molecular cloud cores (Preibisch & Zinnecker 2001b). Some of the collapsed cores will generate their own protostellar outflows, and they will drive other cloud cores into collapse. This positive feedback may augment the star formation rate in the region. NGC 1333 and the related molecular cloud complex is an excellent example of self-triggering by shock waves from protostellar outflows (Knee & Sandell 2000).

Time variability is a hallmark of young forming stars, and can provide insight into the processes occurring on scales less than 1 AU. The presence of many infrared excess sources (Lada et al. 1996; Gutermuth et al. 2008) and X-ray sources (Getman et al. 2002; Preibisch 2003) in this cluster offers an interesting chance to correlate these properties with variability. By monitoring daily, weekly, and monthly near-infrared photometric variations, we can distinguish various classes of time variability in the embedded young populations (Skrutskie et al. 1996; Carpenter et al. 2001). Using a state of the art infrared camera, *FanCam* (Kanneganti et al. 2009), at a small (0.8 m) local telescope provides a nearly unique opportunity to perform this long-term monitoring campaign. Infrared observations are well suited to detect disk thermal variations and deeply extincted populations. The large field of view of the moderate-sized telescope is well matched to the wide angular distribution of the star cluster. Despite its small size, an 0.8-meter telescope can detect sources as faint as

$K=17$. Membership identification is one of the important goals of this work. Near-infrared variability is an effective tool for separating YSOs from field stars in a deeply obscured region. K -band variability is particularly useful since dust obscuration is more significant at shorter wavelengths (Kaas 1999).

X-ray emission is another good indicator of cluster membership, notably for diskless or weak-disk pre-main-sequence populations. Getman et al. (2002) and Preibisch (2003) observed the NGC 1333 region using *Chandra* and *XMM-Newton*. However, Preibisch & Zinnecker (2001a) showed the X-ray detection fraction for spectral types later than M4 (or, $M_* \lesssim 0.2 M_\odot$)¹ sharply drops below 30% in their X-ray imaging study of the embedded cluster IC 348 which is also located in the Perseus molecular cloud complex ($d \sim 300$ pc). This low-mass and substellar pre-main-sequence detection gap in the contemporary X-ray observations can be well covered with infrared variability study; no other previous infrared monitoring data have shown such a discontinuous drop on the detection frequency near and/or below the spectral type M4, at least for clusters up to 1 kpc away (e.g., Carpenter et al. 2001, 2002; Alves de Oliveira & Casali 2008; Park et al. in prep).

Near-infrared time variability of young stellar objects originally was investigated with individually-targeted aperture photometry (e.g., Cohen & Schwartz 1976; Rydgren & Vrba 1983; Skrutskie et al. 1996). Owing to the dramatic advance in the near-infrared array technology during last decades, the variability monitoring of entire star clusters has become the preferred method. For example, Carpenter et al. (2001, 2002) presented detailed analyses of J , H , and K_s time-series photometry for the Orion Nebula cluster and the Chamaeleon I star-forming region using the

¹The stellar mass corresponding to the spectral type M4 has some spread depending on the stellar evolutionary model adopted. Taking $T_{\text{eff}} = 3270\text{K}$ for the intermediate temperature scale of M4 (Luhman 1999), the corresponding mass ranges for the age of 10 to 1 Myr; $0.21\text{--}0.30M_\odot$ (Baraffe et al. 1998), $0.15\text{--}0.08M_\odot$ (Burrows et al. 1997), and $0.23\text{--}0.19M_\odot$ (D’Antona & Mazzitelli 1997, 1998). Considering the typical uncertainty of the models, however, the differences are insignificant.

2MASS south camera. Also, Alves de Oliveira & Casali (2008) examined the deep near-infrared variability of young stellar objects in the ρ Ophiuchi embedded cluster with WFCAM IR imager on the UK Infrared Telescope. Such monitoring campaigns require a substantial investment of observing time – time that is not often available on large aperture telescopes. Here we describe a near-infrared variability monitoring program using an 0.8-meter telescope. In § 2, we describe our data set including the observations and the data reduction procedures. In § 3, we explain the identification of variable stars from the multiband photometry and analyze the properties of colors and magnitudes of the variables, and we also deal with cluster membership in § 3. Section 4 discusses the characteristics and origins of the variability. The summary and conclusions are given in § 5.

3.2 Data

All data were obtained with *FanCam*, a near-infrared camera based on a 1024×1024 Teledyne Imaging Sensors (formerly Rockwell Scientific) HAWAII-1 $2.5\text{-}\mu\text{m}$ cutoff HgCdTe array. The camera features $8.7' \times 8.7'$ field of view and $0.51''\text{pixel}^{-1}$ plate scale. The average system gain and the read noise are measured to be $4.6\text{ e}^- \text{ADU}^{-1}$ and $17\text{ e}^- \text{rms}$. Typical flux limits for a point source detection in 10σ 15 minutes integration time are 61, 98, and $160\text{ }\mu\text{Jy}$ (or, 18.5, 17.5, and 16.5 mag) in J , H , and K_s bands, respectively. The detailed description of the instrument is provided by Kanneganti et al. (2009). *FanCam* is operated by the University of Virginia on the 31-inch Tinsley reflector telescope at Fan Mountain Observatory.

3.2.1 Observations

Observations of NGC 1333 were conducted from November 12, 2005 through October 30, 2007. The northern field is centered at R.A. (J2000.0) = $3^h29^m11^s$, Dec. (J2000.0) = $+31^\circ23'38''$ and the southern field is centered at R.A. (J2000.0) = $3^h28^m52^s$, Dec. (J2000.0) = $+31^\circ17'10''$. The boundaries of the observed areas are displayed over the 2MASS K_s -band image in Figure 3.1, and each of the stacked *FanCam* images is shown in Figure 3.2 and Figure 3.4. Each night's observation consisted of 15 minutes of on-source integration in each of the two fields divided into individual 30 or 60 second exposures. Flat field observations consisted of exposures on twilight sky. Flats were obtained either at dusk or dawn every observing night when conditions permitted. Median filtered spatially dithered observations of a field approximately $30'$ from the cluster provided sky images for background subtraction. These reference fields are free from nebulosity and bright sources. Five minutes of sky data were collected between each set of integrations on the cluster in order to minimize the time between source and sky observation. Most of the sky frames were taken within 10 minutes of object observation. Dithering on target permitted the replacement of bad pixels with good data. The frame to frame dither was $\sim 20''$, several times the FWHM. In total, the northern field data were obtained on 33 nights and the southern field was observed on 31 nights. Table 3.1 provides the observation log.

3.2.2 Data Reduction

For each night the J -, H -, and K_s -band images were reduced independently by band with a series of standard Image Reduction and Analysis Facility (IRAF) procedures (e.g., McLean 1997). Five 60 sec or ten 30 sec dithered sky images were median-combined to establish a single master sky background frame. We then subtracted this

sky background from each object image, which corrects non-uniform background level and fringe patterns generated by airglow emission through the optics system. The sky-subtracted object images were then divided by the normalized flat image. The master flat image was made by combining eight twilight flat frames, and subtracting a master dark image to cancel out the dark current component, although it is only a few counts, compared with typical 6000 counts of sky background at H and K_s bands and 1000 counts at J band. *FanCam* saturation is $\sim 30,000$ ADU. A single master image was produced for each J , H , and K_s band per night, by combining 15 or 30 object frames with “average” as the type of combine operation. Dithered images were shifted into a reference frame using interpolation type “drizzle”, formally known as Variable-Pixel Linear Reconstruction algorithm (Fruchter & Hook 2002), with the pixel fraction parameter [0.5] for both of x and y directions. If pixels are undersampled, drizzle works to improve the image resolution via combining multiple dithered images. For *FanCam* images, which are well sampled, drizzle just maintains spatial resolution while shifting an image. Outlying pixels were rejected from the image combine using the sigma clipping algorithm with 3σ lower and upper limits. One or two of the worst images, for example due to bad tracking, were excluded from the stacking procedure.

Photometric magnitudes and uncertainties were extracted with Point Spread Function (PSF) photometry in the IRAF/DAOPHOT package. The photometric system of *FanCam* is almost identical with 2MASS system, which is based on the calibrated spectrum of Vega (Cohen et al. 1992). Zero magnitude fluxes of the 2MASS J , H , and K_s bands are 1594 ± 27.8 , 1024 ± 20.0 , and 666.7 ± 12.6 Jy, respectively (Cohen et al. 2003). We use 2MASS magnitudes of non-variable stars to perform the instrumental zero-point correction for *FanCam* photometry. The source match radius

0.5'' was used. Figure 3.6 shows the differences between *FanCam* and 2MASS magnitudes. Dispersion in these plots most likely arises from photometric variability. However, the broader faint-end dispersions originate from 2MASS uncertainties since the 2MASS data reaches its limiting magnitude ~ 2 mag earlier than *FanCam*. Stars between 11 mag and 15 mag are used for the calibration. The bright end of this range avoids saturation in the *FanCam* data while the faint end avoids significant uncertainty in the 2MASS magnitudes. All nights were referenced, photometrically, to a single epoch – 2005 November 19 for the northern cluster and 2005 November 12 for the southern. The southern field has similar statistics to the north.

3.2.3 Point Source List

This *FanCam* data set was obtained in various observing conditions, different seeing and different sky background level. Typical seeing disk sizes span from 1.2'' to 2.5''. Most of the data were observed during winter season which provides lowest near-infrared thermal background. The limiting magnitudes of a typical night were estimated at 18.7, 17.5, and 16.7 mag at 10σ detection level for J , H , and K_s bands, respectively (Figure 3.8). At the 10σ level or above, a total of 155 preliminary point sources from the northern field and 127 from the southern field were extracted at J , H , or K_s from the reference master images. Seventy of these sources were subsequently removed as they proved to be filter glints, persistence, extragalactic extended sources, unresolved double stars, etc. Some bright sources were also excluded because they are close to the saturation limit of the camera system. We also found that 14 stars were counted twice in the overlapped area between the north and the south fields. Those overlapping star's magnitudes and colors are the average of both the northern and southern data. Table 3.2 gives the photometric properties of the final

198 objects, brighter than the defined 10σ limiting magnitudes in at least one band. The magnitudes in the table are the average values of all the observed epochs for each source. The RMS of the ensemble measurements are listed in the neighboring columns – in many cases inflated by source variability. We discuss the observed RMS in the following section.

3.2.4 Photometric Integrity

The observed RMS in our time-series photometry was derived from the individual magnitudes (m_i) and photometric uncertainties (σ_i) with the relation of

$$\sigma_{obs}^2 = \frac{n \sum_{i=1}^n (m_i - \bar{m})^2 / \sigma_i^2}{(n - 1) \sum_{i=1}^n 1 / \sigma_i^2}, \quad (3.1)$$

where n is the number of observation for each star in each band. The photometric uncertainty of an individual star originates from random fluctuations due to the photon statistics of the sky, which dominates to the read-noise of the detector. We estimate the empirical signal-to-noise ratio of the photometry using the computed observed RMS. Figure 3.10 shows the distribution of the observed RMS as a function of magnitude. The individual outstanding points above the main body of the distribution are due to intrinsic variability. The observed RMS values range from a minimum of ~ 0.015 mag for bright stars, dominated by photometric systematics, to ~ 0.10 for stars near the sensitivity limits described above. The observed RMS floor of 0.015 mag for bright stars is interpreted as the minimum photometric repeatability for our data set, and consequently a minimum photometric uncertainty of 0.015 mag has been imposed on all of the photometric measurements.

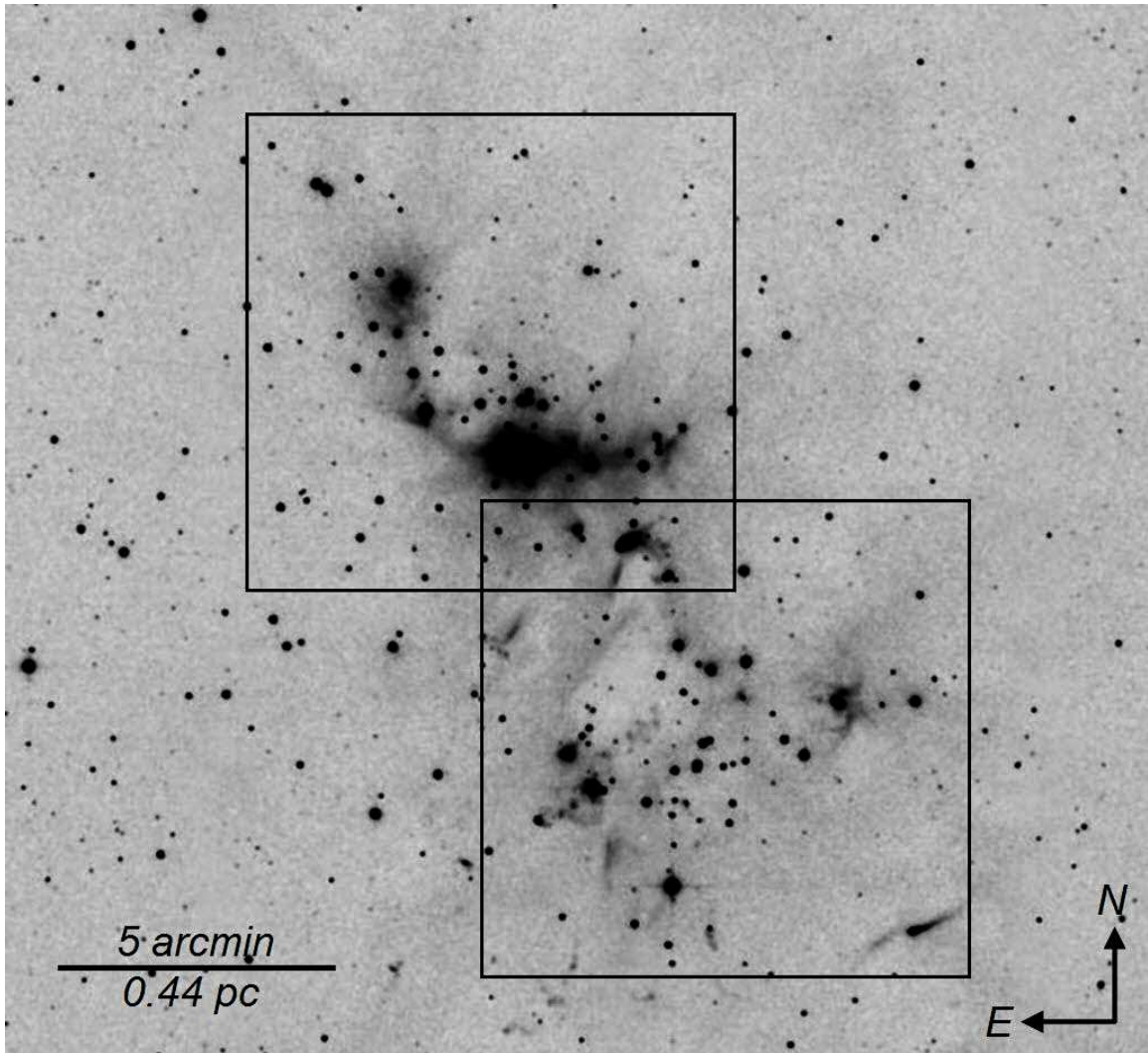


Fig. 3.1.— The boundaries of two observed fields marked over the 2MASS K_s image of NGC 1333. The northern field is centered at R.A. (J2000.0) = $3^h29^m11^s$, Dec. (J2000.0) = $+31^\circ23'38''$ and the southern field is centered at R.A. (J2000.0) = $3^h28^m52^s$, Dec. (J2000.0) = $+31^\circ17'10''$. Each square covers about $8.7' \times 8.7'$ field of view.



Fig. 3.2.— Color-mosaic image of NGC 1333 north cluster composed of *FanCam J*, *H*, and *K_s* – blue, green, and red colors were assigned respectively. The total integration time is ~ 4 hours in each band. Coordinates of the central point are R.A.(J2000.0) = $3^h 29^m 11^s$ and Dec.(J2000.0) = $+31^\circ 23' 38''$. The array plate scale is $0.51''\text{pixel}^{-1}$. The sky seeing spans from $1.2''$ to $2.5''$. Blue diffuse features are dust-scattered light in *J* band, and red ones are from hot dust and/or shocked molecular hydrogen line emission in *K_s* band.



Fig. 3.3.— Visible RGB color image of the same region of NGC 1333 north cluster for comparison. Credit & Copyright: Stephen Leshin (From Astronomy Picture of the Day 2009 April 18)



Fig. 3.4.— Color-mosaic image of NGC 1333 south cluster composed of *FanCam* J , H , and K_s – blue, green, and red colors were assigned respectively. The total integration time is ~ 3 hours in each band. Coordinates of the central point are R.A.(J2000.0) = $3^h 28^m 52^s$, Dec.(J2000.0) = $+31^\circ 17' 10''$. The array plate scale is $0.51''\text{pixel}^{-1}$. The sky seeing spans from $1.2''$ to $2.5''$. Blue diffuse features are dust-scattered light in J band, and red ones are from hot dust and/or shocked molecular hydrogen line emission in K_s band.



Fig. 3.5.— Visible RGB color image of the same region of NGC 1333 south cluster for comparison. Credit & Copyright: Stephen Leshin (From Astronomy Picture of the Day 2009 April 18)

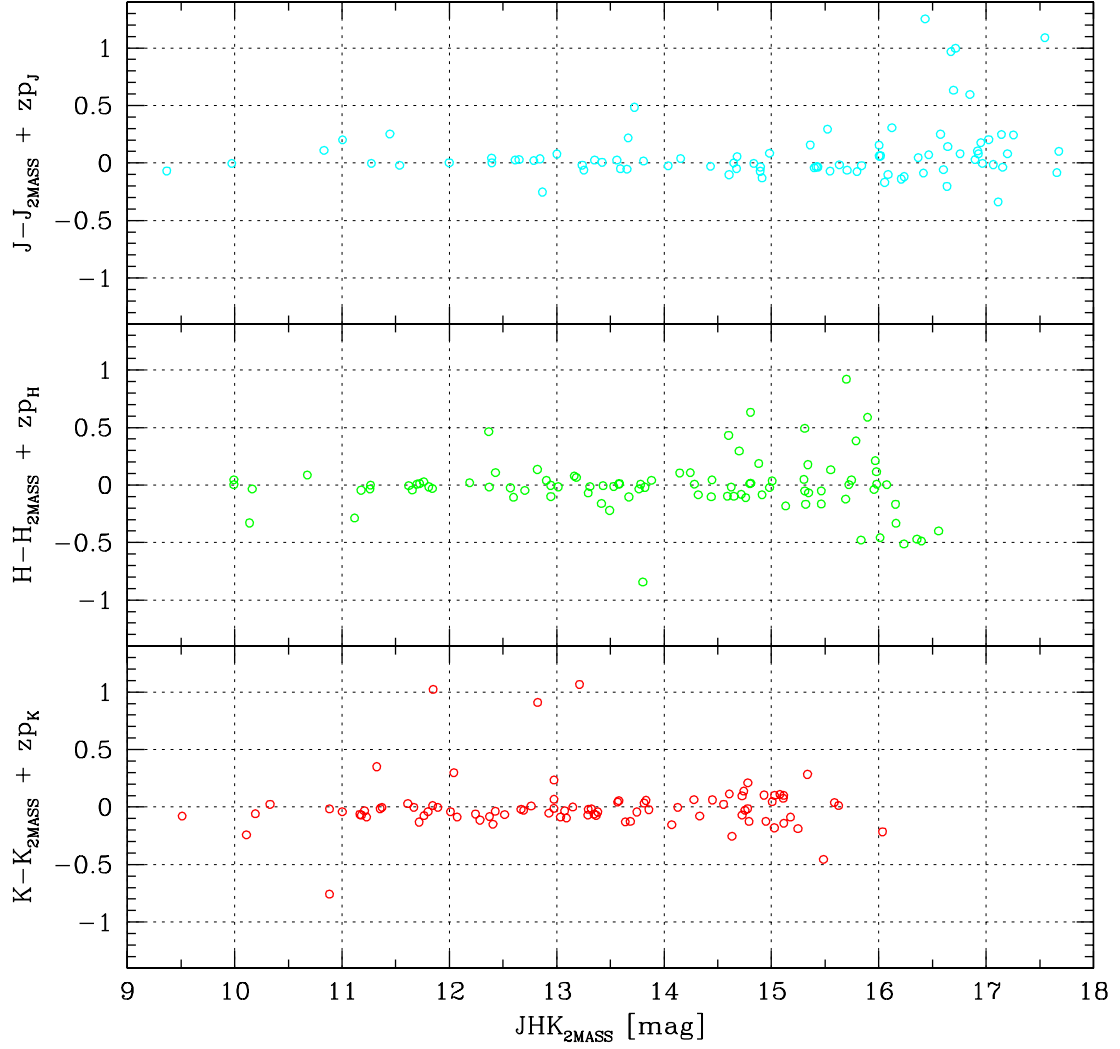


Fig. 3.6.— Magnitude differences between 2MASS and *FanCam* PSF photometry (northern field). Instead of observing independent standard stars, a statistical method with 2MASS point-source catalog was used to determine the instrumental offsets of each filter system. General dispersions likely come from stellar variability itself. The broader faint-end scatterings originate from 2MASS magnitude uncertainties near its survey sensitivity limits.

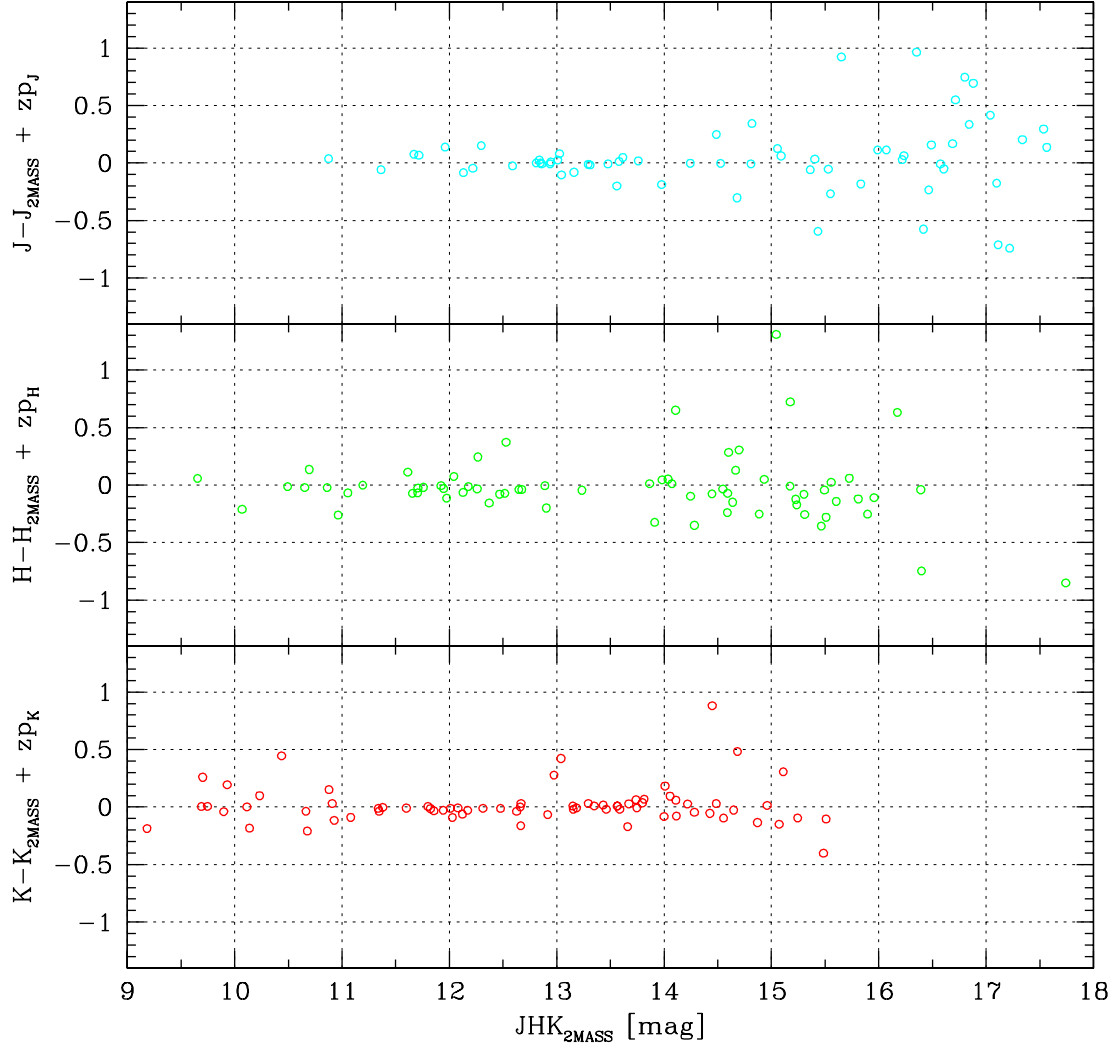


Fig. 3.7.— Magnitude differences between 2MASS and *FanCam* PSF photometry (southern field). Instead of observing independent standard stars, a statistical method with 2MASS point-source catalog was used to determine the instrumental offsets of each filter system. General dispersions likely come from stellar variability itself. The broader faint-end scatterings originate from 2MASS magnitude uncertainties near its survey sensitivity limits.

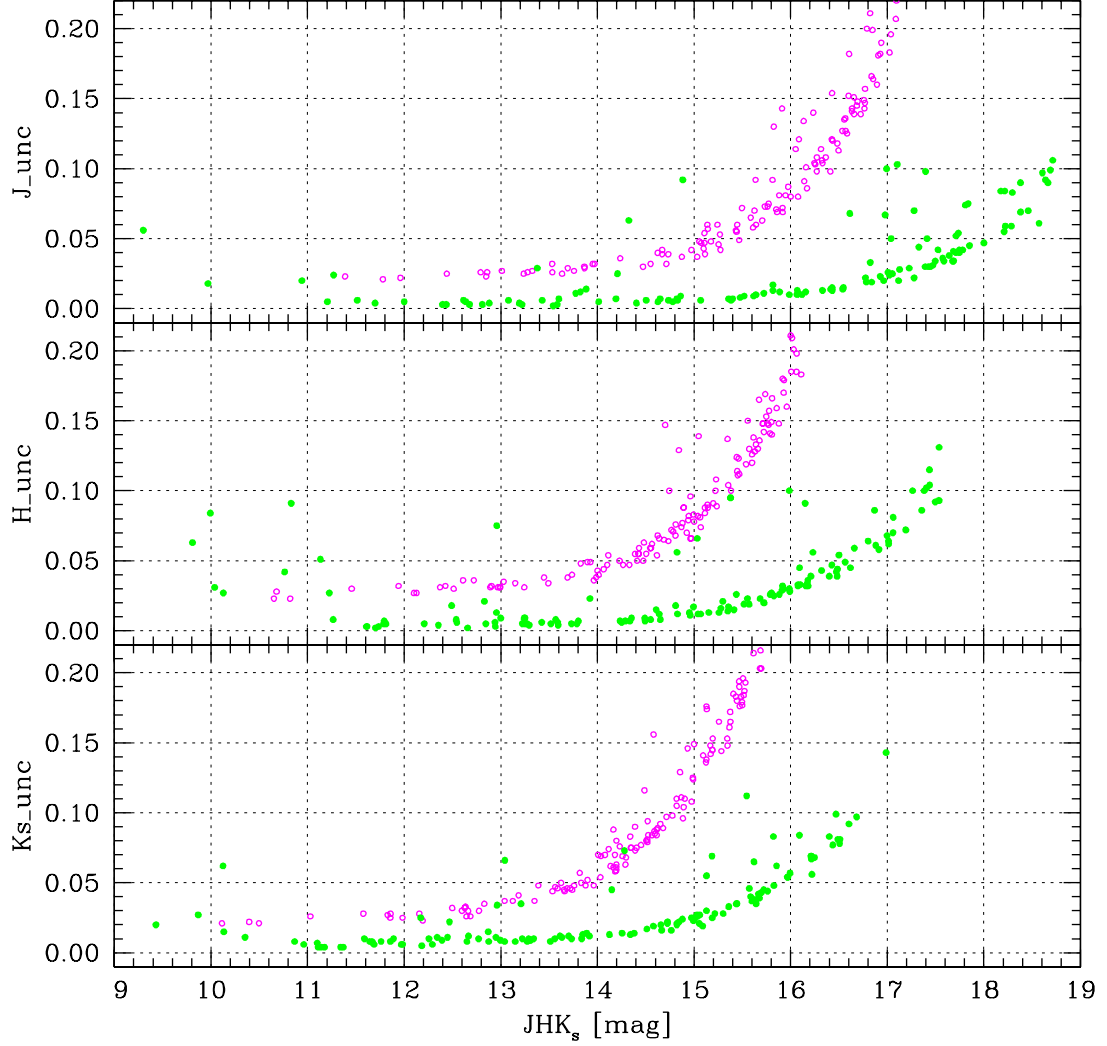


Fig. 3.8.— Photometric uncertainty; *FanCam* north data (solid) and 2MASS archive (open) for comparison. *FanCam* photometry in this study reaches up to 18.7, 17.5, and 16.7 mag for J , H , and K_s , respectively with signal-to-noise ratio 10, which is ~ 2 mag deeper than 2MASS survey.

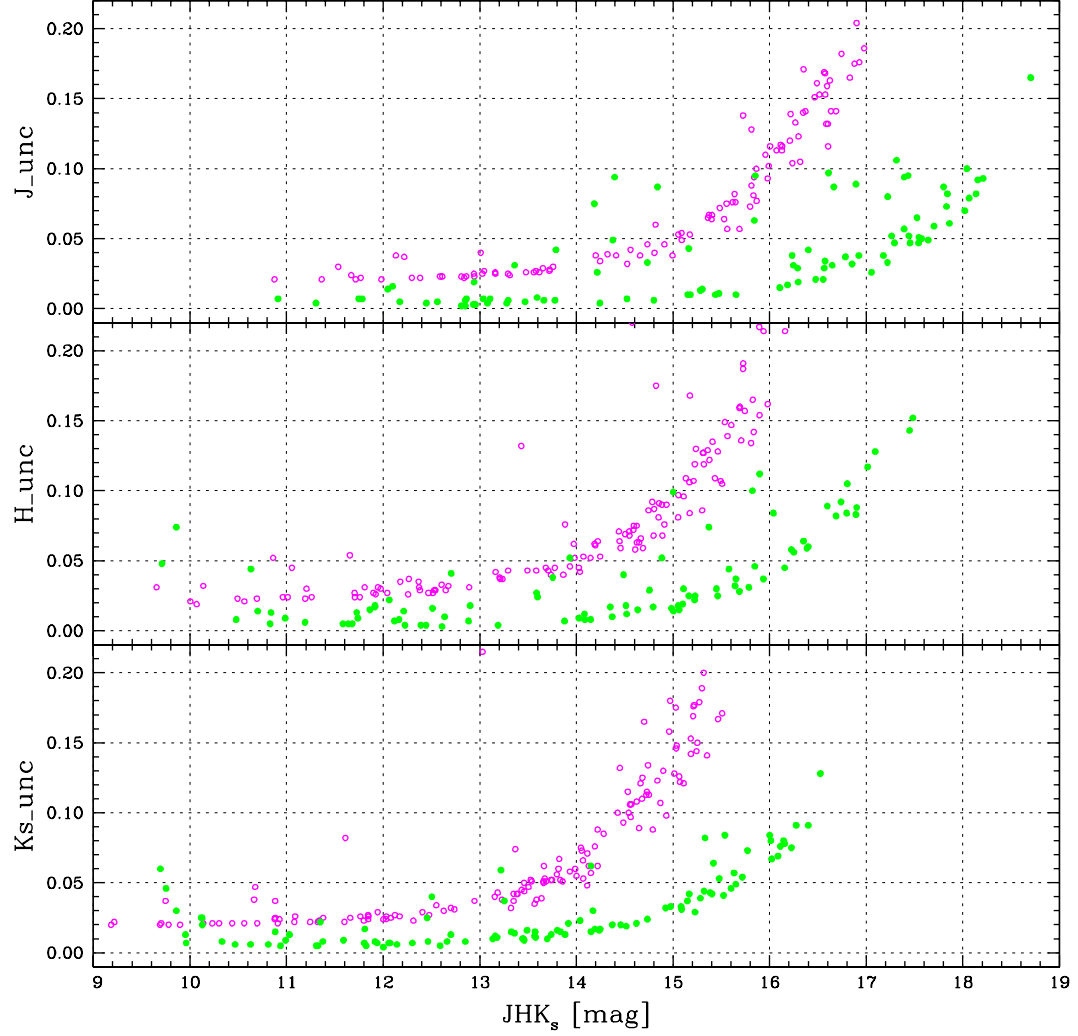


Fig. 3.9.— Photometric uncertainty; *FanCam* south data (solid) and 2MASS archive (open) for comparison. *FanCam* photometry in this study reaches up to 18.5, 17.1, and 16.5 mag for J , H , and K_s , respectively with signal-to-noise ratio 10, which is ~ 2 mag deeper than 2MASS survey.

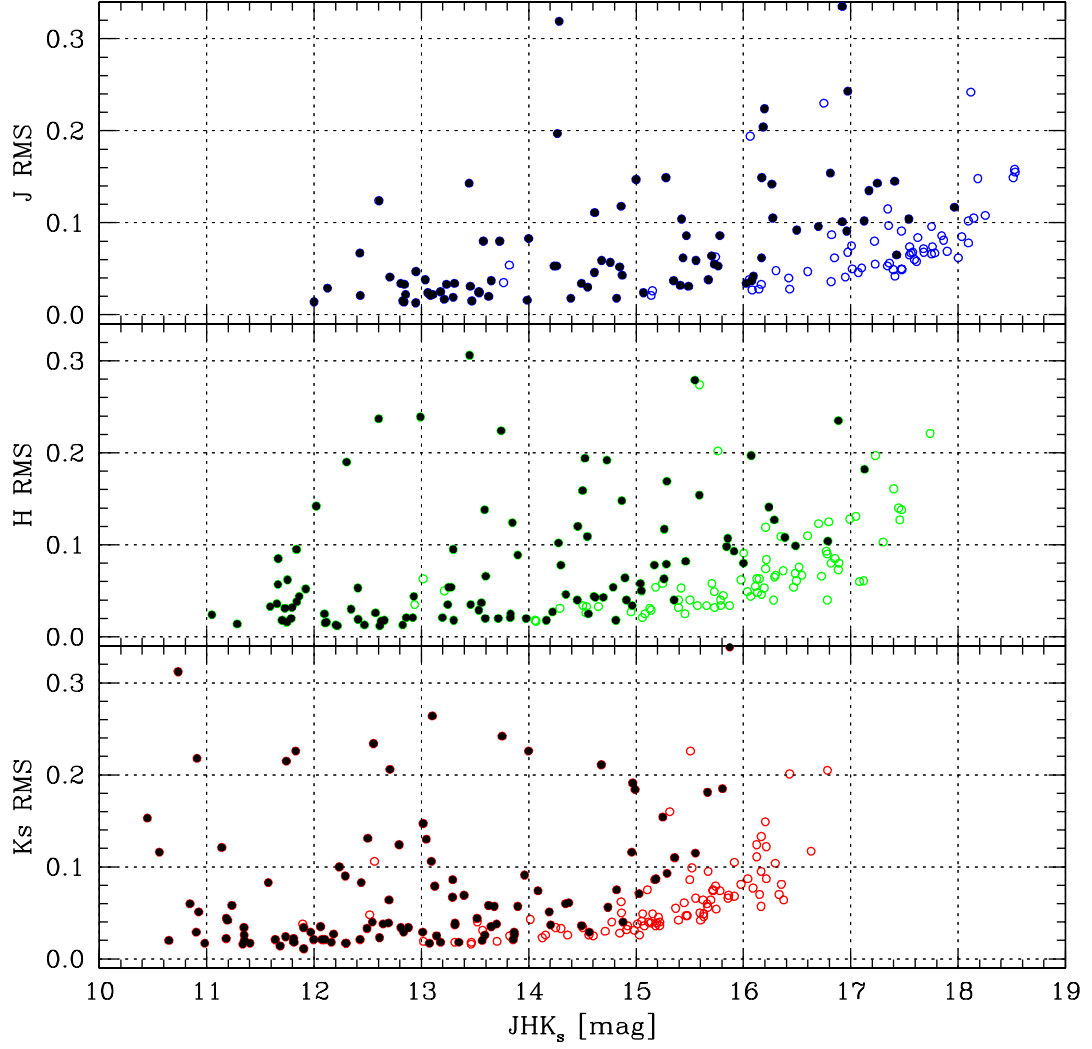


Fig. 3.10.— Observed photometric RMS for variables (solid) and non-variables (open). RMS of the ensemble measurements was computed to estimate the signal-to-noise ratio in our photometry. The observed RMS ranges from ~ 0.015 mag for bright stars to ~ 0.10 for stars near the sensitivity limits of this study. The values correspond to SNRs of ~ 70 and ~ 10 , respectively. We interpret the RMS bottomline 0.015 mag as the photometric repeatability of our data set.

3.3 Results

3.3.1 Identification of Variable Stars

Following the arguments in Carpenter et al. (2001), we use the Stetson variability index (Stetson 1996), S , as the primary statistical tool for variable source selection. Since the Stetson statistic correlates photometric fluctuation in multiband photometry, it has two major advantages over simple RMS-based methods. First, the Stetson statistic will mitigate the significance of a single-band outlying measurement. Second, it multiplies the common-mode signal between bands enhancing the detectability of low-amplitude variables. For each star the index, S , was computed with the following,

$$S = \frac{\sum_{i=1}^p g_i \operatorname{sgn}(P_i) \sqrt{|P_i|}}{\sum_{i=1}^p g_i}, \quad (3.2)$$

where p is the number of all pairs of observations for a given star, a pair $P_i = \delta_{bt}\delta_{b't}$ is the product of the normalized residuals of two observations, the subscripts b and b' mean one of the observed bands J , H , or K_s , and g_i is the weight assigned to each pair of the normalized residuals. The normalized residual for a given band, δ_{bt} , is defined as

$$\delta_{bt} = \sqrt{\frac{n}{n-1}} \left(\frac{m_{bt} - \bar{m}_b}{\sigma_{bt}} \right), \quad (3.3)$$

where n is the number of measurements used to compute the mean magnitude \bar{m}_b and σ_{bt} is the photometric uncertainty in band b at a given observational epoch. The subscript t in the equation traces the observed time, or, epoch. If the magnitude scattering were due to purely random noise, the expectation value $\langle \delta_{bt}\delta_{b't} \rangle$ would be zero; thus the index S tends to zero for a non-variable star, while it will tend toward a positive value for a substantially variable star. The magnitude of the positive number

depends on the amount of the variability, i.e., the larger the variability the larger the value. In the case of only a single band measurement in an epoch, the expectation value $\langle \delta_{bt}^2 \rangle$ is unity for purely random noise. Therefore, this offset is subtracted so that the product of the normalized residuals is zero;

$$P_i = \begin{cases} \delta_{bt}\delta_{b't}, & \text{for } b \neq b' \\ \delta_{bt}^2 - 1, & \text{for } b = b' \end{cases}. \quad (3.4)$$

The weights, g_i , can either be $\frac{2}{3}$ or 1. For three band detections at an epoch, a weight of $\frac{2}{3}$ is assigned for all three available pairs, while a weight of 1 is assigned for the case of one- or two-band detections.

Figure 3.11 presents the Stetson variability index, S , for all the stars in the point-source list as a function of H magnitude. Non-variable stars will scatter symmetrically around zero, while true physical variables show some positive offset depending on their degree of variability. NGC 1333, however, contains few non-variable stars, rendering it difficult to determine the optimum minimum value of S for variable selection. Similar observations of NGC 7129 (upper-right inset in Figure 3.11, Park et al. in prep) provide a better estimate of the threshold. The width of the distribution for non-variable stars should depend on the typical uncertainty of a single observation and the total number of observational epochs used to compute the indices. The NGC 7129 observation was done by *FanCam* in parallel with the observation of NGC 1333 and the total number of epochs, 30, is almost same as this study. Accordingly, we define variable stars as objects showing Stetson index $S \geq 1$. There are 96 variable sources meeting this criterion.

As a secondary variability indicator, we employ the reduced chi-square, χ_ν^2 (Bevington & Robinson 2003). Since the Stetson statistic correlates the fluctuations in

multiband photometry, it dilutes any variability dominated by a single band. Therefore, the reduced chi-square for each band photometry provides a complementary variability index;

$$\chi_\nu^2 = \frac{1}{\nu} \sum_{i=1}^n \frac{(m_i - \bar{m})^2}{\sigma_i^2}, \quad (3.5)$$

where n is the number of photometric measurements and $\nu = n - 1$. σ_i is the photometric uncertainty of the measurement m_i . This reduced chi-square is 1 for a gaussian random distribution. Visual examination of stars with large reduced chi-square ($\gtrsim 15$ in J , H , or K_s) revealed 14 additional variables giving a total of 110 variable stars. These were single band dominated variables and excluded due to the Stetson statistic property discussed above. Table 3.3 summarizes the properties of each variable star. The 25 variables are newly identified cluster members, 15 of which are likely brown dwarfs (see § 3.3.7).

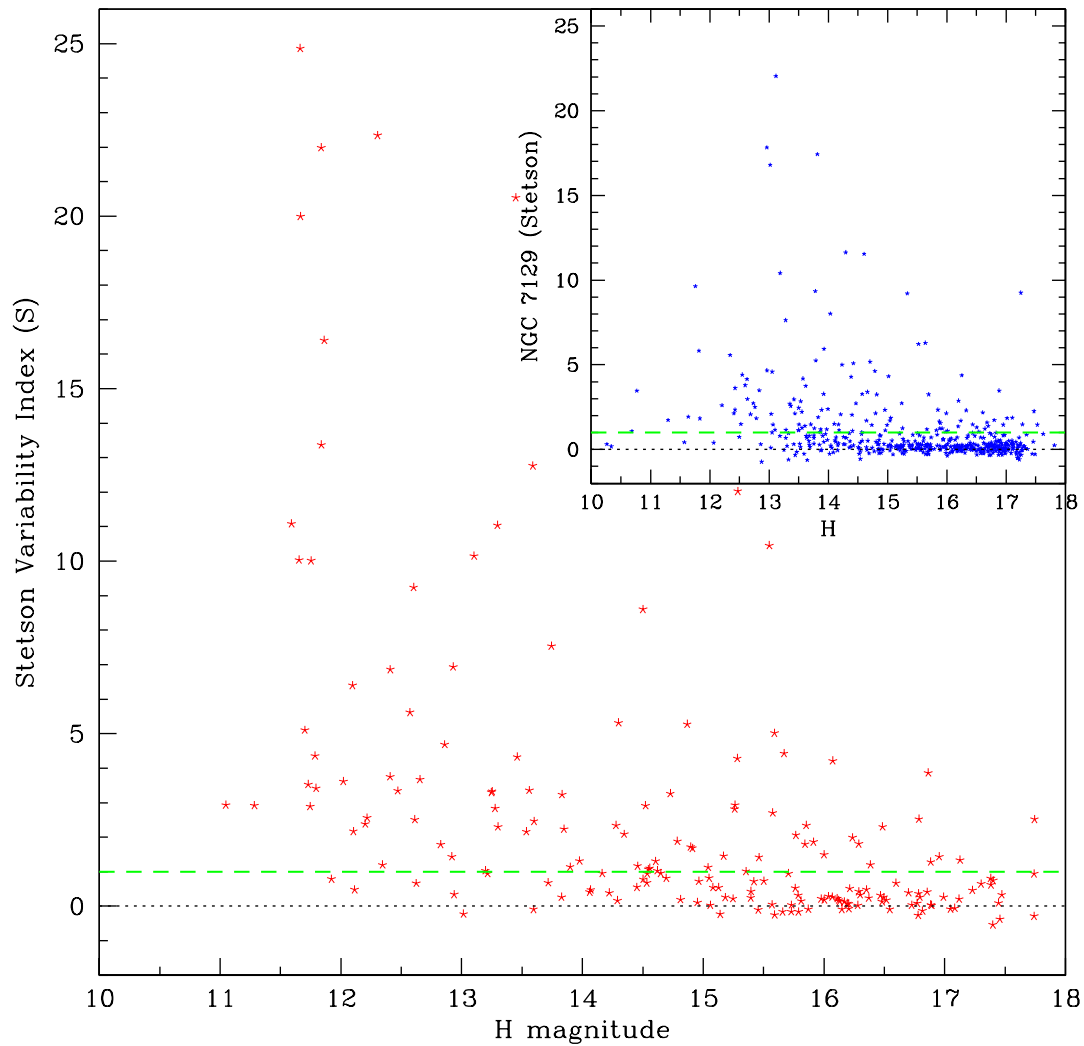


Fig. 3.11.— Stetson variability index (Stetson 1996) of NGC 1333 point sources. Non-variable stars tend to scatter around the parallel zero line symmetrically while true variables show some positive offsets. Inset is the Stetson index plot of another embedded cluster NGC 7129 for reference (Park et al. in prep). We identify a point source with $S \geq 1$ as a variable star.

3.3.2 Mean Colors and Magnitudes

The average colors and magnitudes of the variable and non-variable stars are displayed in a color-magnitude diagram (Figure 3.12) and a color-color diagram (Figure 3.13). These diagrams provide insight into the mass and age of the observed cluster and its members. In the K_s vs. $H-K_s$ color-magnitude diagram, the filled circles and the star symbols represent 110 variable and 88 non-variable stars, respectively. Lada et al. (1996) suggested that NGC 1333 is an extremely young embedded cluster, no more than 1-2 Myr old, from their analyses of the fraction of infrared excess sources and the comparison of K -band luminosity functions (KLFs) with the Trapezium cluster in Orion and the IC 348 young open cluster. The upper solid line is drawn for the 1 Myr isochrone from the Lyon group's NextGen model (Baraffe et al. 1998) covering from $0.02 M_\odot$ to $1.4 M_\odot$, the dashed line is for the 1 Myr isochrone of DUSTY model (Chabrier et al. 2000) covering from $0.005 M_\odot$ to $0.1 M_\odot$, and the lower solid line displays the COND model 1 Myr age line (Baraffe et al. 2003) covering the same mass range as the dashed line. The isochrones were shifted to 300 pc adopted from the study of *Hipparcos* data for NGC 1333 (de Zeeuw et al. 1999; Belikov et al. 2002).

The dotted diagonal parallel lines represent the direction and magnitude of the reddening vector (Cohen et al. 1981) converted to the 2MASS photometric system following the transformation relations of Carpenter (2001); the slope is 1.35. *FanCam* transformations are nearly identical to 2MASS (Kanneganti et al. 2009). The diamond symbols on the reddening vector lines are marked at intervals of 10 magnitudes of visual extinction. The calculated A_V for each star is given in Table 3.2. For variable stars, the extinctions were derived from the separations between the stars and the model-averaged 1 Myr isochrone along the reddening vector lines. Deviations away

from the 2MASS field star main sequence² were used for the non-variable star's A_V estimate. Stars in the non-variable group tend to be fainter than stars in the variable group, consistent with the fact that most of the non-variable stars are reddened background stars. The infrared excess sources classified by Gutermuth et al. (2008) are identified in the diagram; the triangles are Class I young stellar objects and the open circles are Class II YSOs. 13 of the 15 (87%) Class I stars are variable, and 51 of the 57 (89%) Class II stars are identified as variables. The crosses in Figure 3.12 represent the *Chandra*-identified X-ray sources adopted from Getman et al. (2002) (see § 3.3.6 for detail). Spectroscopically studied brown dwarf candidates of Wilking et al. (2004) and Scholz et al. (2009) are plotted with open squares (see § 3.3.8 for more). A pentagon is marked for the confirmed low-mass stellar member by Scholz et al. (FMO 120). Small solid squares on the left hand side represent a mid-age open cluster NGC 2420. It is ~ 2 Gyr old and visual extinction is less than 0.02 mag, therefore we plot it for a reference distribution of an unreddened ZAMS (Lee et al. 1999).

The color-color diagram of $J-H$ vs. $H-K_s$ is plotted in Figure 3.13. The solid line in the lower-left corner of the graph illustrates the 1 Myr isochrone from the NextGen stellar evolution model of Baraffe et al. (1998) encompassing the mass range from $0.075 M_\odot$ to $1.4 M_\odot$. Symbols in Figure 3.13 are the same as in Figure 3.12. The dot-dashed reference lines are included to show the Classical T Tauri star locus as described in Meyer et al. (1997).

²All the 2MASS point source catalog data within the distance range of $30'$ to $40'$ from the center of NGC 1333 were plotted on the K_s vs. $H-K_s$ C-M diagram to extract the first-order field star main-sequence track. The data-collected area (i.e., $30' < r < 40'$) is known as relatively clean region in the Perseus molecular cloud complex through the $850\mu\text{m}$ survey and $\text{C}^{18}\text{O}(1-0)$ intensity map (e.g., Hatchell et al. 2005).

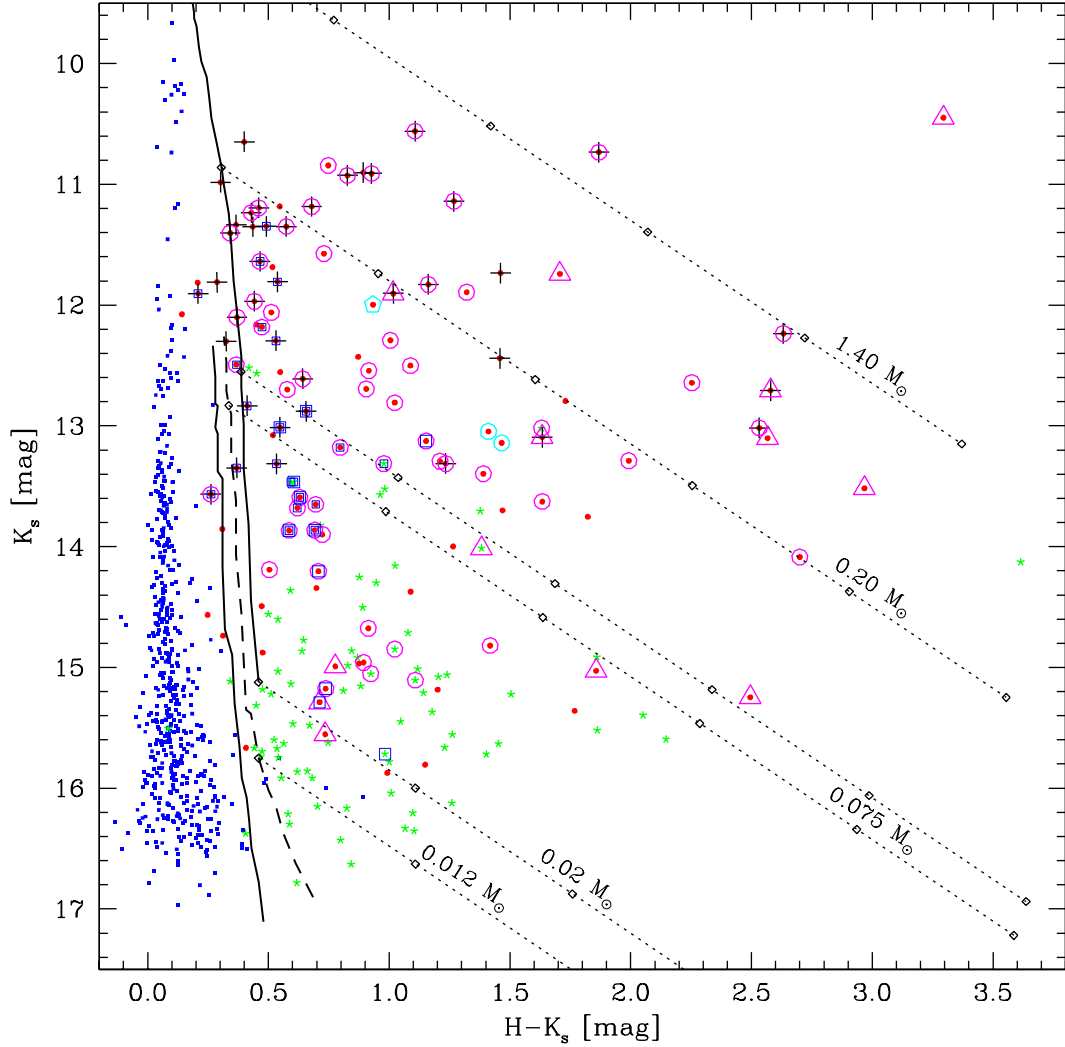


Fig. 3.12.— K_s vs. $H-K_s$ color-magnitude diagram for all point sources; 110 variables with small filled circles and 88 non-variables with asterisks. Infrared excess sources (Gutermuth et al. 2008) Class I (triangles) and Class II (open circles) YSOs are marked over. *Chandra*-identified X-ray sources (Getman et al. 2002) are displayed with crosses. Squares are for the brown dwarf candidates selected by Wilking et al. (2004) and Scholz et al. (2009) (bigger squares). The upper solid line is 1 Myr isochrone of the NextGen model (Baraffe et al. 1998) covering mass from $0.02 M_\odot$ to $1.4 M_\odot$, the dashed line is 1 Myr isochrone for the DUSTY model (Chabrier et al. 2000) covering mass from $0.005 M_\odot$ to $0.1 M_\odot$, and the lower solid line is 1 Myr age line for the COND model (Baraffe et al. 2003) covering the same mass range as the dashed line. The dotted diagonal lines represent the direction and magnitude of the reddening vector (Cohen et al. 1981); the slope is 1.35. The rhombi along the reddening lines are marked for the visual extinction A_V of 10 interval.

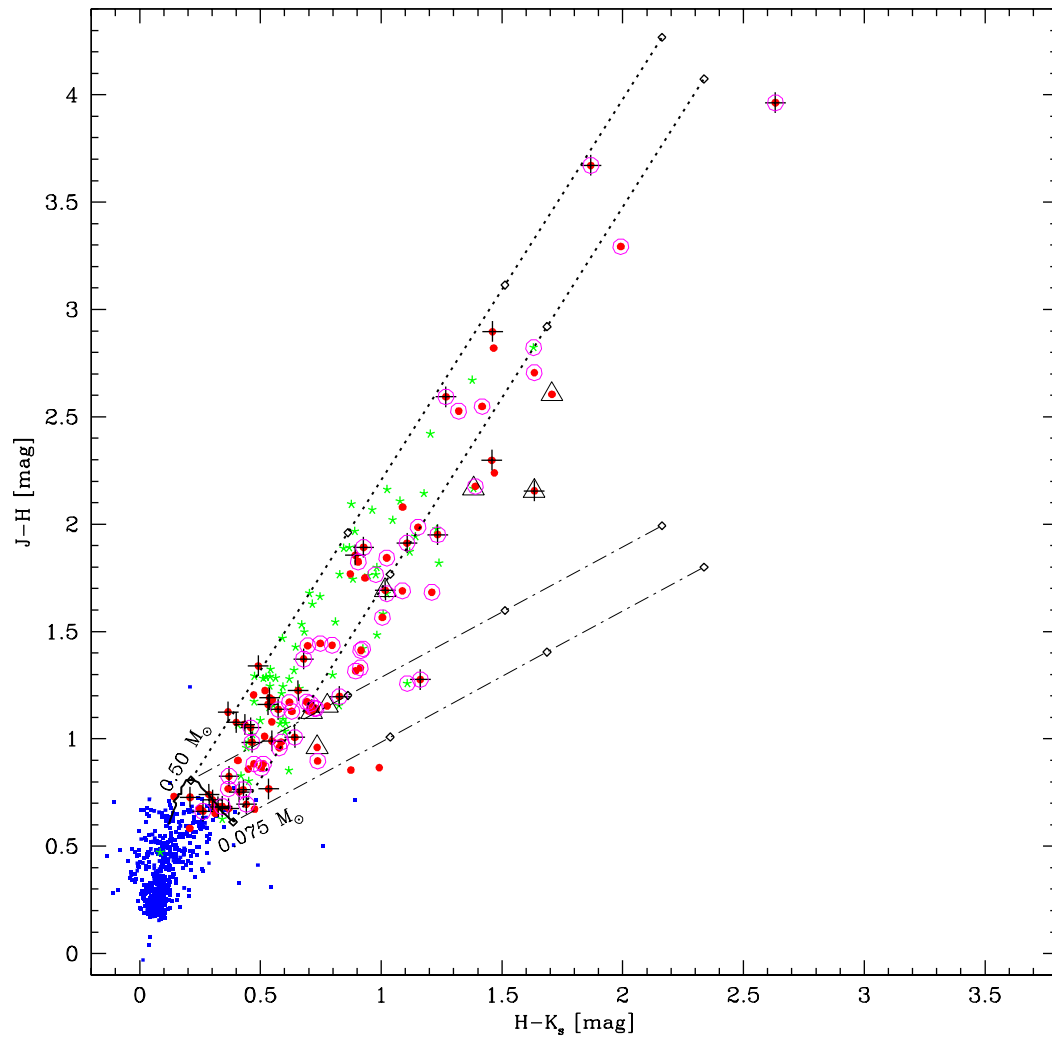


Fig. 3.13.— $J-H$ vs. $H-K_s$ color-color diagram. Symbols represent for the same contents as Figure 3.12 but the lower dot-dashed lines show the Classical T Tauri star locus as described in Meyer et al. (1997)

3.3.3 Light Curves and Color Variations

Figure 3.14 shows J -, H -, and K_s -band time-series photometry for star 135, one of the 110 variable stars identified in this study, which is also known as MBO 47 (Willing et al. 2004) and LAL 163 (Lada et al. 1996). Gutermuth et al. (2008) classified this star (their ID 71) as a Class II YSO. The abscissa represents the elapsed time since the first day of this monitoring campaign (2005 Nov 11 UT, or, JD 2453685.5). We assumed all the observations of each night were done at midnight local time, allowing ± 0.15 days uncertainty. The full x-axis data (718 days) will be available in the electronic form of this paper, while we use in this figure only first 5 months for the sake of clarity. The plots show non-periodic fluctuations that are well correlated in all three bands. The J and H plots are better correlated with each other than with the K_s light curve, which is consistent with the view that the origin of K_s -band variability is more sensitive to accretion luminosity than the J and H bands. Figure 3.15 shows another example of JHK_s light curves. The object FMO 197 is classified as a Class II YSO and a variable point source with an isochrone-estimated mass of $\sim 0.03 M_\odot$. Accordingly we identify the object as a new brown dwarf candidate in NGC 1333 (cf. Table 3.3). We do not see any characteristic difference between light curves of Class I and Class II pre-main-sequence objects.

Dust with ISM characteristics will obscure more light at shorter wavelengths according to the standard reddening law. Extinction variation will make sources redder as they dim. Luminosity added by accretion-disk activity is expected to have its peak at $\lambda \sim 2 \mu m$ or longer wavelength because the typical maximum disk temperature T_D is $\sim 1500 K$. Accretion variation will thus produce redder colors when a source brightens due to an increase in accretion rate through the inner disk. The different causes of the variability will be evident in the color-magnitude diagrams. In Figure

3.16 and 3.17, correlations between K_s vs. $H-K_s$ and J vs. $J-H$ and time-variations of $J-H$ and $H-K_s$ colors are presented to show the two different variability trends described above. The oblique dashed line in the upper-left color-magnitude diagram represents the locus of the Classical T Tauri stars in K_s vs. $H-K_s$ graph. The slope, -1.68 or -59° , is derived by combining information³ from Meyer et al. (1997) and López-Chico & Salas (2007). The followings are two illustrative examples (See Appendix E. for more):

- FMO 135 (Figure 3.16): This Class II YSO shows the variability dominated by extinction. In the upper-left panel of the figure, the $H-K_s$ color increases as the K_s magnitude increases; becoming redder as the star dims. The linear-regression fit line has a similar slope to the reddening vector, suggesting that circumstellar extinction drives the photometric variability rather than accretion-disk activity. The J vs. $J-H$ variability (upper-right panel) shows the same trend as the K_s vs. $H-K_s$ variability.
- FMO 197 (Figure 3.17): This Class II YSO shows variability more consistent with changes in accretion rate. The best regression fitting line of the K_s vs. $H-K_s$ correlation has a negative slope. The $H-K_s$ color becomes redder as the star brightens, which is a good indication of the existence of disk activity (Carpenter et al. 2001). The upper-right panel the J vs. $J-H$ diagram, however, shows the opposite color vs. flux correlation, becoming redder when faint. The seeming contradiction most likely arises because disk accretion dominates K_s variability while extinction is more important at shorter wavelengths. J band flux is presumably not affected by the existing disk activity in this case.

³Meyer et al. (1997) provides the relation of $(J - H) = a(H - K)$, and López-Chico & Salas (2007) $K = b(J - K)$. Putting them together, we get $K = c(H - K)$ where $c = b(1 + a)$. Then, converted the CIT system into the 2MASS system.

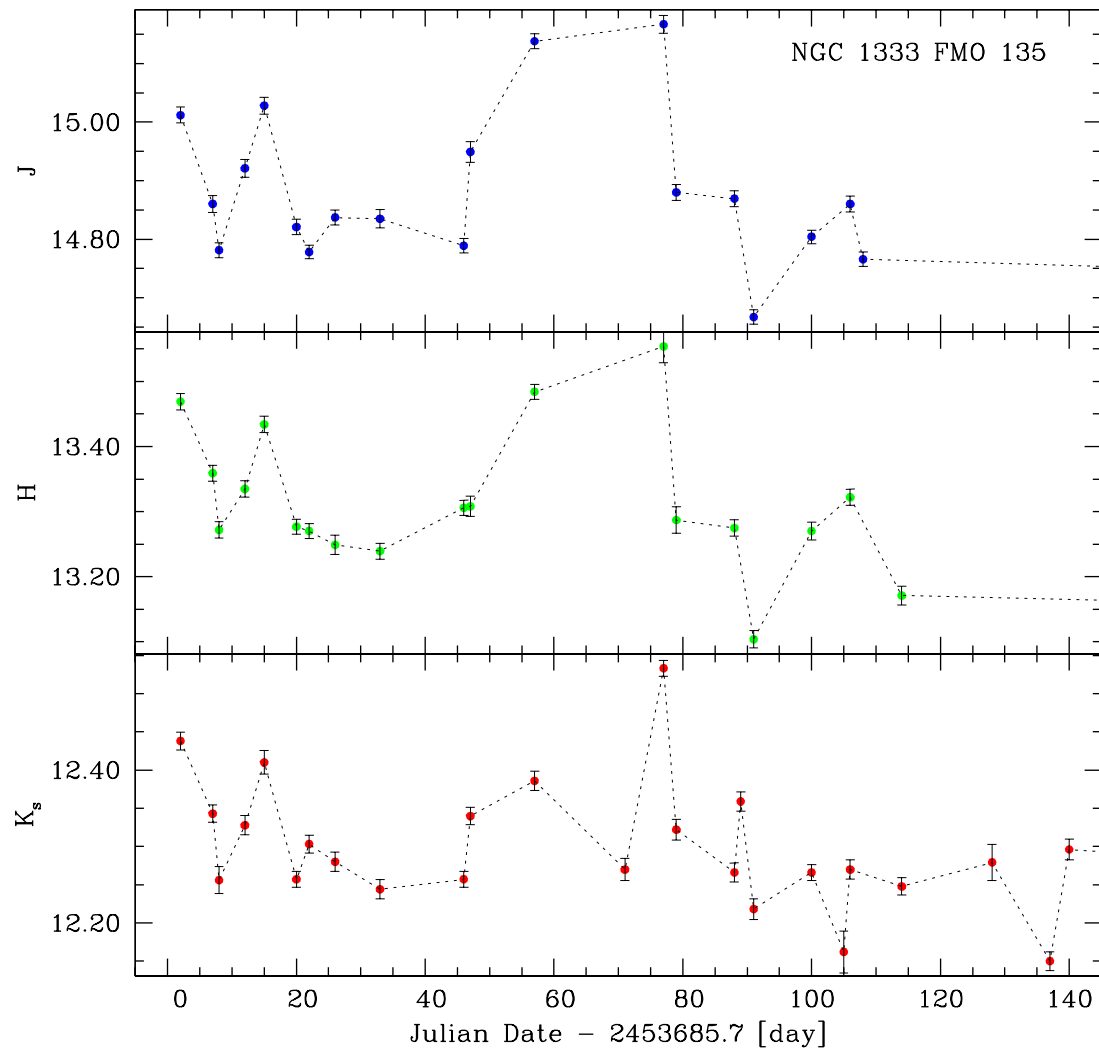


Fig. 3.14.— Example of J , H , and K_s light curves of a Class II pre-main-sequence star; FMO 135, also known as MBO 47 by Wilking et al. (2004), LAL 163 by Lada et al. (1996), and ID 71 by Gutermuth et al. (2008). Fluctuations are apparently non-periodic but well correlated in all three bands.

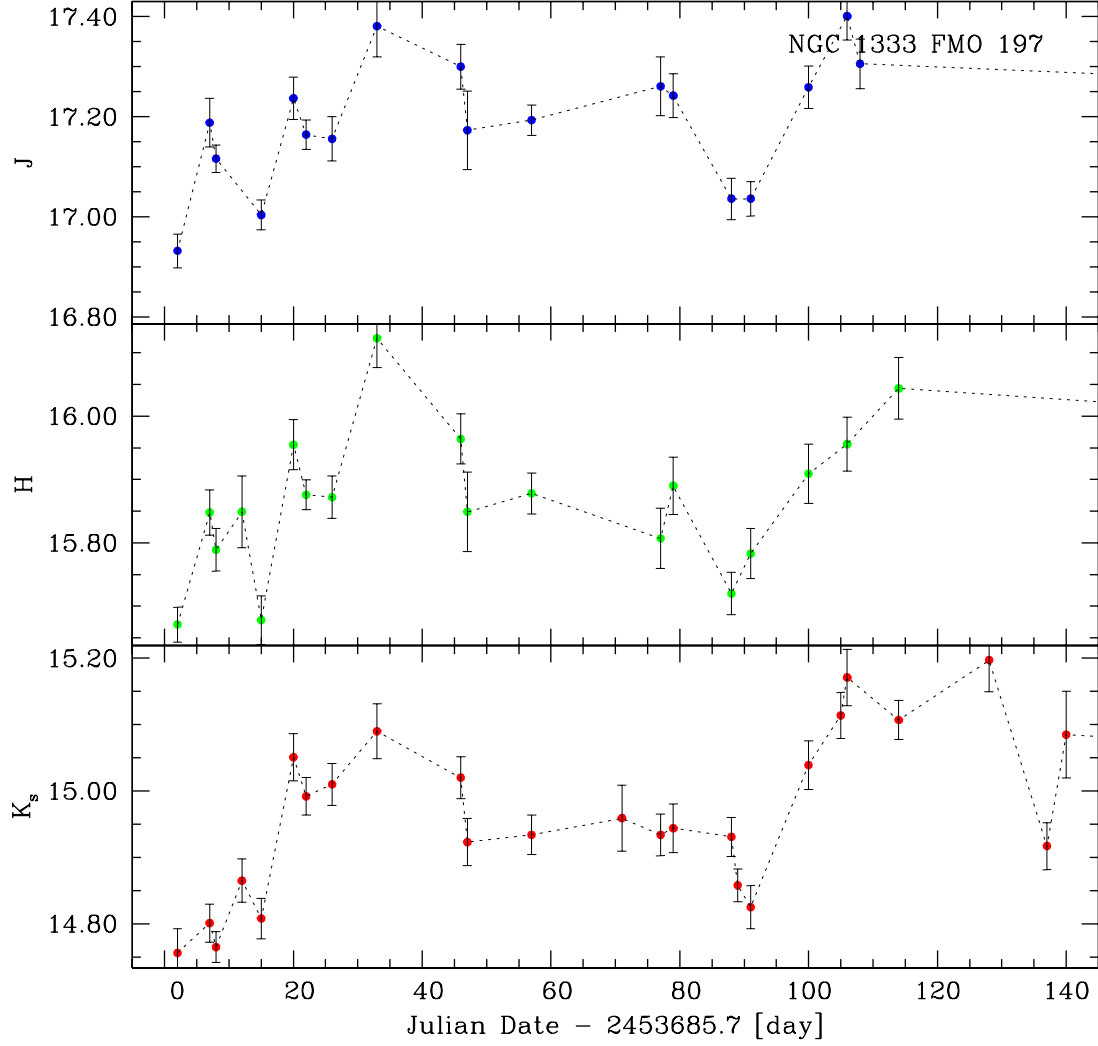


Fig. 3.15.— Example of J , H , and K_s light curves of a Class II pre-main-sequence object; FMO 197, also known as MBO 118 by Wilking et al. (2004), LAL 246 by Lada et al. (1996), and ID 102 by Gutermuth et al. (2008). Fluctuations are apparently non-periodic but well correlated in all three bands. The mass of FMO 197 is derived to $\sim 0.03 M_{\odot}$ based on 1 Myr model isochrones (Baraffe et al. 1998).

NGC 1333 FMO 135

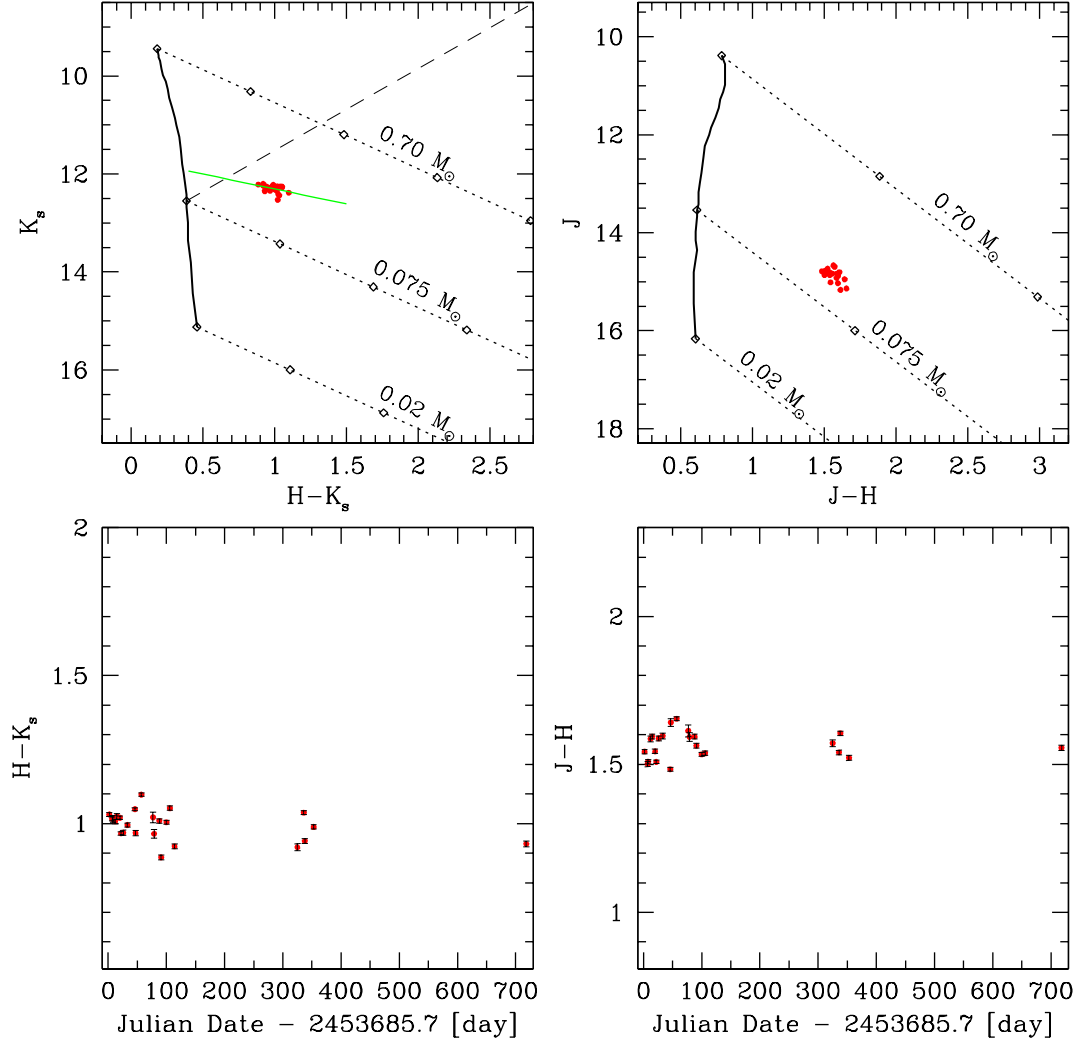


Fig. 3.16.— Color variability of a Class II pre-main-sequence star; FMO 135. The upper panels are color-magnitude correlations between K_s vs. $H-K_s$ and J vs. $J-H$. The lowers are time-variations of $H-K_s$ and $J-H$ colors. The K_s vs. $H-K_s$ color-magnitude diagram shows a positive linear-regression slope, implying the color becomes redder as the K_s gets fainter.

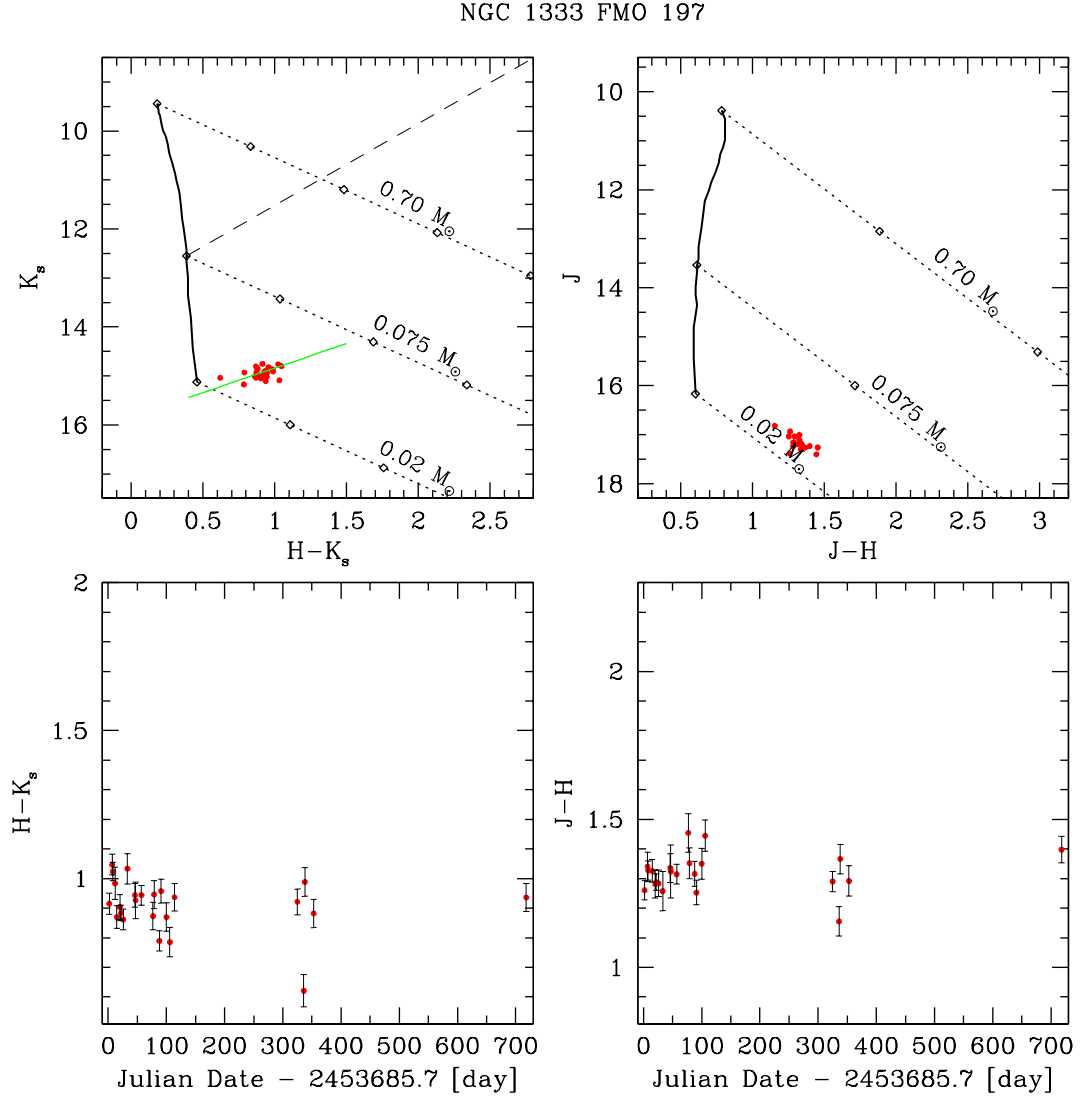


Fig. 3.17.— Color variability of a Class II pre-main-sequence star; FMO 197. Each panel represents the same as Figure 3.16. It is an example of a star that becomes redder when it lights up, producing a negative slope in K_s vs. $H-K_s$ relation. The dashed line represents the Classical T Tauri star locus (Meyer et al. 1997), characteristic of disk activity in pre-main-sequence stars.

3.3.4 Spatial Distribution of Variable Stars

The spatial distribution of the variable stars (filled circles) and non-variable stars (asterisks) is presented in Figure 3.18. The overlaid dotted contours show the extinction distribution derived from the 2MASS data covering a region larger than our observed area (Fig. 5 of Gutermuth et al. (2008)). The highest contour value is A_V of 18 and the outer contours decrease in steps of 2 mag. The peak extinction reaches $A_V \sim 50$ and is well matched with the densest region of the $C^{18}O(1-0)$ integrated intensity map obtained at FCRAO (Hatchell et al. 2005; Wilking et al. 2004). The triangles, open circles, crosses, and squares represent the Class I and Class II young stellar objects (Gutermuth et al. 2008), the *Chandra*-identified X-ray sources (Getman et al. 2002), and the brown dwarf candidates of Wilking et al. (2004) + Scholz et al. (2009), respectively. Virtually all of the X-ray sources match variable stars. The distribution of non-variable stars is fairly uniform throughout the observed area; it does not show any apparent correlation with the cluster center or the extinction map. Few of non-variable stars are seen through the highest extinction area. In contrast, the surface density of variable stars and infrared excess objects is highest toward the extinction peak, implying these objects have direct affiliation with the molecular cloud.

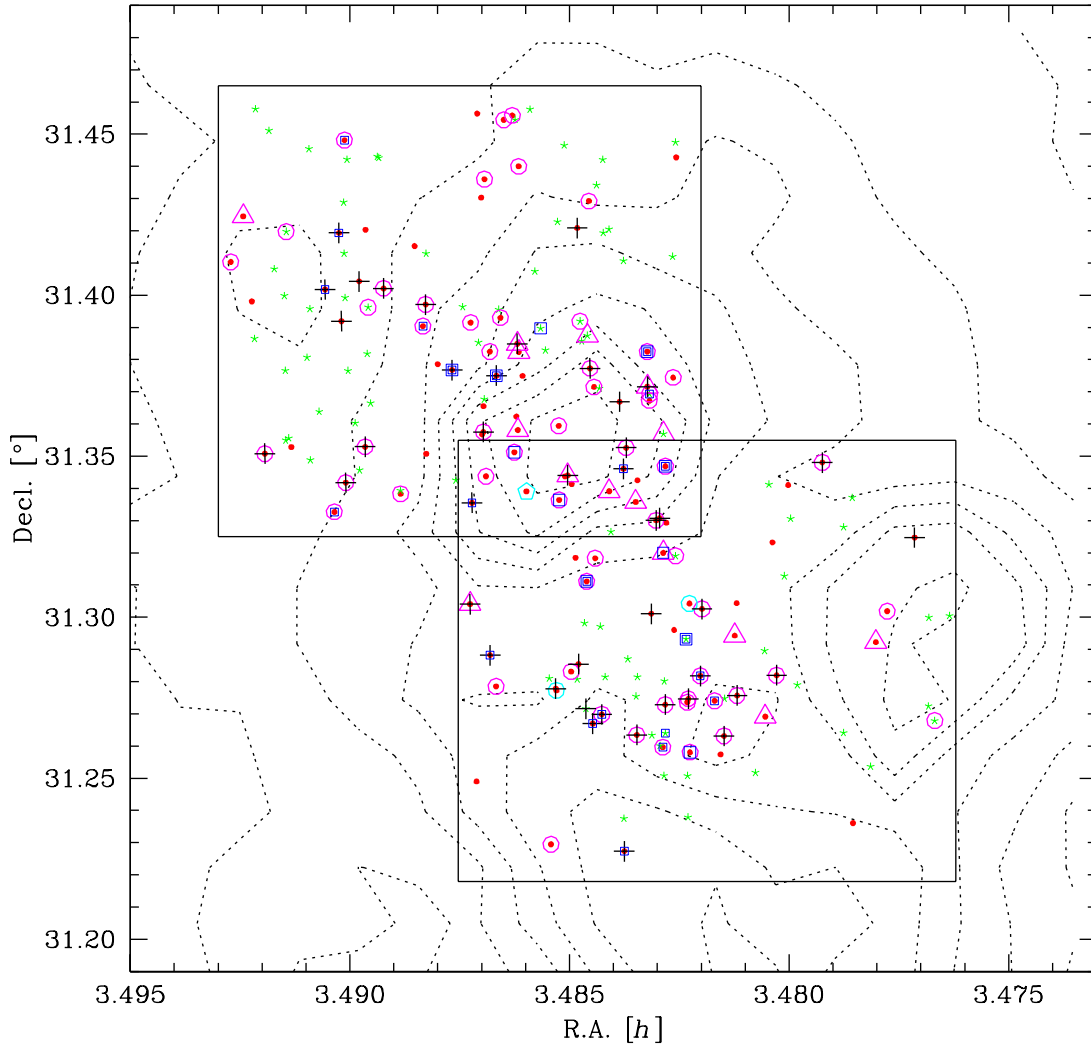


Fig. 3.18.— Spatial distribution of all *FanCam* point sources in two observed regions; 110 variable stars (filled circles) and 88 non-variable stars (asterisks). Various symbols represent the same as Figure 3.12 – i.e., Class I (triangles) and Class II (open circles) YSOs by Gutermuth et al. (2008), *Chandra* X-ray sources (crosses) by Getman et al. (2002), and BD candidates (squares) of Wilking et al. (2004) + Scholz et al. (2009) (bigger squares). The background contour is the extinction distribution of $A_V=18, 16, 14, 12, 10, 8, 6, 4$ (Gutermuth et al. 2008). Variable stars and IR excess sources are well connected with the extinction map while non-variable stars are fairly randomly scattered throughout the observed area.

3.3.5 Cluster Membership

Infrared excess has provided a traditional means of selecting membership of deeply embedded clusters (e.g., Aspin et al. 1994; Lada et al. 1996; Wilking et al. 2004; Gutermuth et al. 2008). This method, however, provides incomplete results given members which lack significant disks. X-ray observations have been used as a powerful independent method to discriminate cluster members from background or foreground contamination, since X-rays select for elevated magnetic activity instead of disk thermal activity (e.g., Feigelson et al. 1993; Getman et al. 2002; Preibisch 2003). The X-ray method should be particularly efficient for the census of young stellar clusters such as NGC 1333 (~ 1 Myr), given that X-ray luminosities are 10–10,000 times higher than those of main-sequence stars during all the stages of pre-main-sequence evolution (Feigelson & Montmerle 1999; Getman et al. 2002). X-ray emission from pre-main-sequence stars depends strongly on stellar mass, rendering the X-ray detection rate of low-mass stars and brown dwarfs relatively low (e.g., Preibisch & Zinnecker 2001a; Feigelson et al. 2002). In this section, we compare our variable stars with previously known cluster members and highlight the unmatched variable stars as candidates for new cluster membership which can reinforce X-ray and infrared excess selection.

3.3.6 Literature Cluster Members

Lada et al. (1996) performed a near-infrared imaging survey covering the entire region (432 square arcminutes) of the NGC 1333 cluster and estimated that 143 stars are physically associated with the molecular cloud. Since then several authors have made extensive contributions to establishing a concrete and unequivocal membership census of the cluster population. The recent work of Gutermuth et al. (2008) integrated

Spitzer IRAC and MIPS mid-infrared photometry with the 2MASS near-infrared archive data in order to identify a total of 137 bona fide cluster members using empirically derived infrared excess source detection methods. Their catalog includes 39 Class I protostars, 94 Class II sources, and 4 transition/debris disks. Even more recently, Oasa et al. (2008) presented deep ($K_s \leq 18.1$) near-infrared survey results in the southern 25 square arcminute area centered on the well-known YSO, SVS 13 (Strom et al. 1976). They classified 44 Class I and II YSOs from their 76 point sources.

X-ray survey data in this region are available. Getman et al. (2002) detected 127 X-ray sources in about $17' \times 17'$ field of view toward NGC 1333 region and identified 95 sources with known cluster members. *XMM-Newton* X-ray sources published by Preibisch (2003) matches *Chandra* data for almost all of its detected sources. Therefore, we do not deal with these X-ray observations separately. For earlier spectral type objects than M4 (or, $M_* \gtrsim 0.2 M_\odot$), 61% (14/23) of probable cluster members were detected in X-ray. For later spectral type objects than M4 (or, $M_* \lesssim 0.2 M_\odot$), only 32% (27/85) detected (cf. Figure 3.12 and Table 3.3). These X-ray detection fractions as a function of spectral type are well consistent with the result of the *Chandra* observation of the nearby young star-forming cluster IC 348 performed by Preibisch & Zinnecker (2001a).

3.3.7 New Members

We assume that the 110 variable stars identified here are cluster members and compare with previously confirmed members. Of the 137 cluster members identified by Gutermuth et al. (2008) 110 stars lie within the observed area depicted in Figure 3.1, and 72 of the 110 have *FanCam* counterparts (15 Class I and 57 Class II). Guter-

muth et al. took advantage of the lower extinction at mid-infrared wavelengths to identify more YSOs than this study. 64 of the 72 matched sources are variable with 13 being Class I and 51 Class II YSOs, thus 89% of the IR excess sources identified by Gutermuth et al. are variable.

The *Chandra* survey area of Getman et al. (2002) is about 2 times larger than the *FanCam* observation. 42 of 110 *Chandra* X-ray sources in their Tables 1 and 2 matched *FanCam* sources to within $1''$, and 41 of 42 (98%) are variable, a much higher rate than the IR excess sources. The only exception is star 101, located just north of the complex outflow source SVS 13 where the photometric uncertainty is very high because of the complicated background. This source is detected only in K_s band in our *FanCam* survey. The Stetson method tends to produce a non-variable result when the photometric uncertainty of a source is high.

Twenty-three sources match both IR excess YSOs and X-ray sources. Oasa et al. (2008) identified two additional Class II members that overlap our variable sources; FMO 116, 117. Scholz et al. (2009) added a spectroscopically confirmed star into the cluster membership list; FMO 120. Greissl et al. (2007) *HST* near-infrared grism data yielded no additional matches. Overall, 85 stars were identified with literature cluster members. The other 25 variables are probable new cluster members.

The possibility of the contamination from the extragalactic variable sources such as Active Galactic Nuclei and the background galactic variable stars is very low. Alves de Oliveira & Casali (2008) used AGN cumulative flux distribution (Treister et al. 2006) and their 2-band cross-correlation index simulations to estimate the number of extragalactic AGN contaminants in the 0.8 sq. degree ρ Ophiuchi field. They predicted about 9 AGNs with detectable IR variability in their ρ Ophiuchi area which is ~ 20 times larger than the NGC 1333 field of this study. Furthermore, more than

95% of those AGNs lie within $16 \leq K_s \leq 18$, whereas our K_s limiting magnitude is 16.5 mag. Therefore, the number of possible variable AGN contaminants in the field of view of our observation is likely zero.

Similarly, using the detailed Galactic infrared point source model (Wainscoat et al. 1992) and the DENIS and ISOGAL Galactic bulge surveys (Schultheis et al. 2000), Alves de Oliveira & Casali (2008) predicted that the ρ Ophiuchi field should contain less than one AGB variable star. The Wainscoat et al. (1992) model predicts the AGB column density toward NGC 1333 ($l=158.3^\circ$, $b=-20.5^\circ$) is almost the same as that toward ρ Ophiuchi ($l=353.7^\circ$, $b=+17.7^\circ$) since both fields are located in high galactic latitude, $|b| \sim 20^\circ$. Therefore, the chance of finding even a single AGB star in the NGC 1333 field is $\lesssim 5\%$ and insignificant in this study.

Given these estimates of background variable contamination, all of the 25 previously-identified variable sources are likely new NGC 1333 members. From the color-magnitude diagram of Figure 3.12, considering the theoretical stellar evolutionary models and interstellar reddening law, 15 of the 25 new members are brown dwarfs ($M < 0.075 M_\odot$). The other 11 stars are also very low-mass stars ($0.075 < M < 0.20 M_\odot$).

3.3.8 Brown Dwarfs

A significant amount of effort has been made in recent years to inventory very low-mass stars and brown dwarfs in NGC 1333 (e.g., Wilking et al. 2004; Greissl et al. 2007; Winston et al. 2009; Scholz et al. 2009). Wilking et al. selected 25 brown dwarf candidates based on broadband near-infrared colors. They defined the water vapor index (Q) in low-resolution near-infrared spectra, and derived detailed subclass spectral types from M2.3 to M8.2 for all their BD candidates. We can identify 22 of

these 25 stars in our field of view. 19 of these 22 sources are variable and 3 are detected as non-variable (LAL 142, 153, 164, or FMO 56, 67, 134). Six of the candidates were above the hydrogen burning limit in the analysis here, compatible with Wilking et al.’s labeling of these objects as “bd?”. Five are close to the hydrogen burning limit depending on the isochrone model adopted. The other 8 candidates are substellar according to both *FanCam* and Wilking et al.⁴ (cf. Table 3.3).

Scholz et al. presented 19 probable brown dwarf members and 9 possible stellar members in NGC 1333 with their near-infrared spectroscopic confirmation. Within our targeted regions, 11 of their 19 brown dwarf candidates were identified. 2 of them are determined as non-variables and one is tentatively belong to the stellar mass group. One of the 2 non-variable BD candidates (FMO 171) shows pretty big flux variability. However, it was excluded from the variable group due to its faintness and high photometric uncertainties around the extinction peak area. 6 of the 11 overlap with the BD samples of Wilking et al. (2004). Our *FanCam* result eventually supports 2~4 confirmed BD members in NGC 1333 additionally from the spectroscopy of Scholz et al. (2009).

From their 9 stellar mass member candidates, Scholz et al. suggested that 2 of them (23 and 26, or FMO 95 and 217 respectively) likely be background objects owing to their apparent discrepancy between spectroscopic temperatures and spectral types. Both of them, however, show strong variability nature in our *FanCam* monitoring. FMO 217 is a variable substellar object ($M \sim 0.04$) well correlated in all 3 bands, a *Spitzer*-classified infrared excess source, and one of the BD candidates of Wilking et al. (2004). FMO 95 is also a variable substellar object ($M \sim 0.05$) of which *J*-band variability stronger than the other 2 bands, a *Spitzer* excess source, and a candidate

⁴Wilking et al. (2004) assigned 3 of the 8 objects spectral types slightly earlier than the hydrogen-burning limit (M6) — M4.2, M2.5, and M2.6 for LAL 184, 279, and 313, respectively.

BD of Wilking et al., too. Moreover, FMO 95 is a *Chandra*-detected X-ray source and does not show any amount of extinction; i.e., $A_V=0$.

In addition to the previously proved brown dwarfs, we present here 15 unknown probable substellar members in NGC 1333. They are summarized in Table 3.3.

3.3.9 Mass Spectrum of Cluster Members

The mass of stellar/substellar objects is one of the fundamental quantities we pursue. Initial mass distribution function in star clusters plays an essential role in building a “natural” star-formation/stellar-evolution model on which finding the mass of an individual star depends iteratively. An exclusive advantage of studying the mass function of a youngest stellar colony, like NGC 1333, is that the observed mass spectrum can directly be an initial mass function, IMF, itself.

The position of a pre-main-sequence star on a near-infrared color-magnitude diagram (or, Hertzsprung-Russell diagram) is a function of its age, extinction, and circumstellar-disk effect, as well as its mass. Even if we take the assumption of a coeval star formation and the universal reddening law, pinning-down the mass is not yet definitive owing to the amount of infrared excess caused by disk activity. Noticing this additional possibility of uncertainty, we derived the masses of all the variable stars based on the intrinsic colors (1 Myr isochrones of Baraffe et al. (1998) and Chabrier et al. (2000) models) and extinction correction in the K_s vs. $H-K_s$ color-magnitude diagram.

The individual mass values are presented in Table 3.3, and the counting statistics of the cluster IMF is plotted in Figure 3.19 with the form of $\log(\frac{\Delta N}{\Delta M})$ vs. $\log(\frac{M}{M_\odot})$ ⁵.

⁵We plot the number density instead of just number in a mass bin to make the effect of bin-size minimized. The mass interval is chosen with $\Delta\log(\frac{M}{M_\odot})=0.2$, and the actual plotted relation is; $\log(\frac{\Delta N}{\Delta M}) = \log(\frac{\Delta N}{M_c}) + \log(\frac{\log e}{\Delta\log(M/M_\odot)}) \pm \log e \sqrt{1/N + \varepsilon_M^2}$, where M_c is the central mass of a bin,

The error bars in the histogram correspond to \sqrt{N} counting statistics combined with the roughly estimated mass uncertainty originated from various factors. A typical of 30% error in our mass estimate is employed here. A mass spectral index $\alpha = 2.27$, defined with $dN/dM = k * M^{-\alpha}$, is derived toward the very low-mass stellar regime ($0.1M_{\odot} \leq M_* \leq 2M_{\odot}$), suggesting Salpeter type mass function slope (Salpeter 1955). It flattens at around the hydrogen-burning limit and slowly drops beyond the point. If we assume all the faint sources were cluster members, the mass function remains flat all through the brown dwarf mass regime (dashed-line histogram).

The mass distribution pattern seems rather different from the previous study of Oasa et al. (2008) in a smaller southern field ($5' \times 5'$) of NGC 1333, which has shown $\alpha \approx 1.6$ covering from $1M_{\odot}$ to almost the deuterium burning limit ($0.012M_{\odot}$, or $13M_{Jup}$) with no peak or bump. It is also significantly steeper than that of pre-stellar dust clump mass spectrum in NGC 1333 in the similar mass regime ($\alpha = 1.4$, Sandell & Knee 2001). On the other hand, the overall behavior of our NGC 1333 IMF is in surprising agreement with some of the previous studies in other young clusters. Many authors found their mass functions increasing with a Salpeter type slope before reaching a peak or a flat top at $\sim 0.1\text{--}0.2M_{\odot}$, and declining toward brown dwarf regime (e.g., Luhman et al. 1998; Hillenbrand & Carpenter 2000; Muench et al. 2002; Slesnick et al. 2004; Sung et al. 2004; Levine et al. 2006). Moreover, our NGC 1333 IMF shows the possibility of a secondary peak at $\sim 0.05M_{\odot}$, being consistent with the reveal of Muench et al. (2002) and Slesnick et al. (2004) in Trapezium Cluster and of Levine et al. (2006) in NGC 2024, although the exact peak positions are slightly misaligned each other.

To compare different IMFs obtained from diverse samples and investigate the properties of low-mass stars and brown dwarfs in various star-forming regions, authors

ϵ_M is fractional uncertainty in mass (0.3 in this plot).

used to define the ratio of the numbers of substellar to stellar objects in a cluster as follows (e.g., Briceño et al. 2002; Luhman et al. 2003; Slesnick et al. 2004; Levine et al. 2006);

$$R_{ss} = \frac{N(0.02 \leq M/M_{\odot} \leq 0.08)}{N(0.08 < M/M_{\odot} \leq 10)}. \quad (3.6)$$

Because it counts the total numbers of each subgroup, the ratio itself is little affected by the detailed ups and downs of mass function shape. In our variability-based membership mass function of NGC 1333, there are 31 objects with masses $0.02 \leq M/M_{\odot} \leq 0.08$ and 78 objects with masses $0.08 < M/M_{\odot} \leq 10$. We count 12 more bright sources beyond our *FanCam* 60-second saturation limit into the stellar mass group of the cluster members ⁶. This yields a value of $R_{ss} = 31/(78+12)$ or 0.34 ± 0.07 , with errors again from the \sqrt{N} counting statistics. The substellar-to-stellar mass ratio in NGC 1333 is very similar to several previous works including in NGC 2024 (0.30 ± 0.05 , Levine et al. 2006), in Trapezium (≈ 0.30 , Slesnick et al. 2004 and the recomputation of Levine et al. 2006), and in Taurus (0.24 ± 0.05 , Guieu et al. 2006). It seems, however, too early to conclude that the fraction of brown dwarf formation is universal and independent of the local star-forming environment, as some of other exemplary clusters are not in a good agreement (e.g., IC 348, $R_{ss}=0.12 \pm 0.03$; Luhman et al. 2003), waiting better understanding in the future.

⁶There are 20 saturated stars in our field of view, but 8 of them are considered Galactic foreground stars by employing the statistical star count models (Wainscoat et al. 1992).

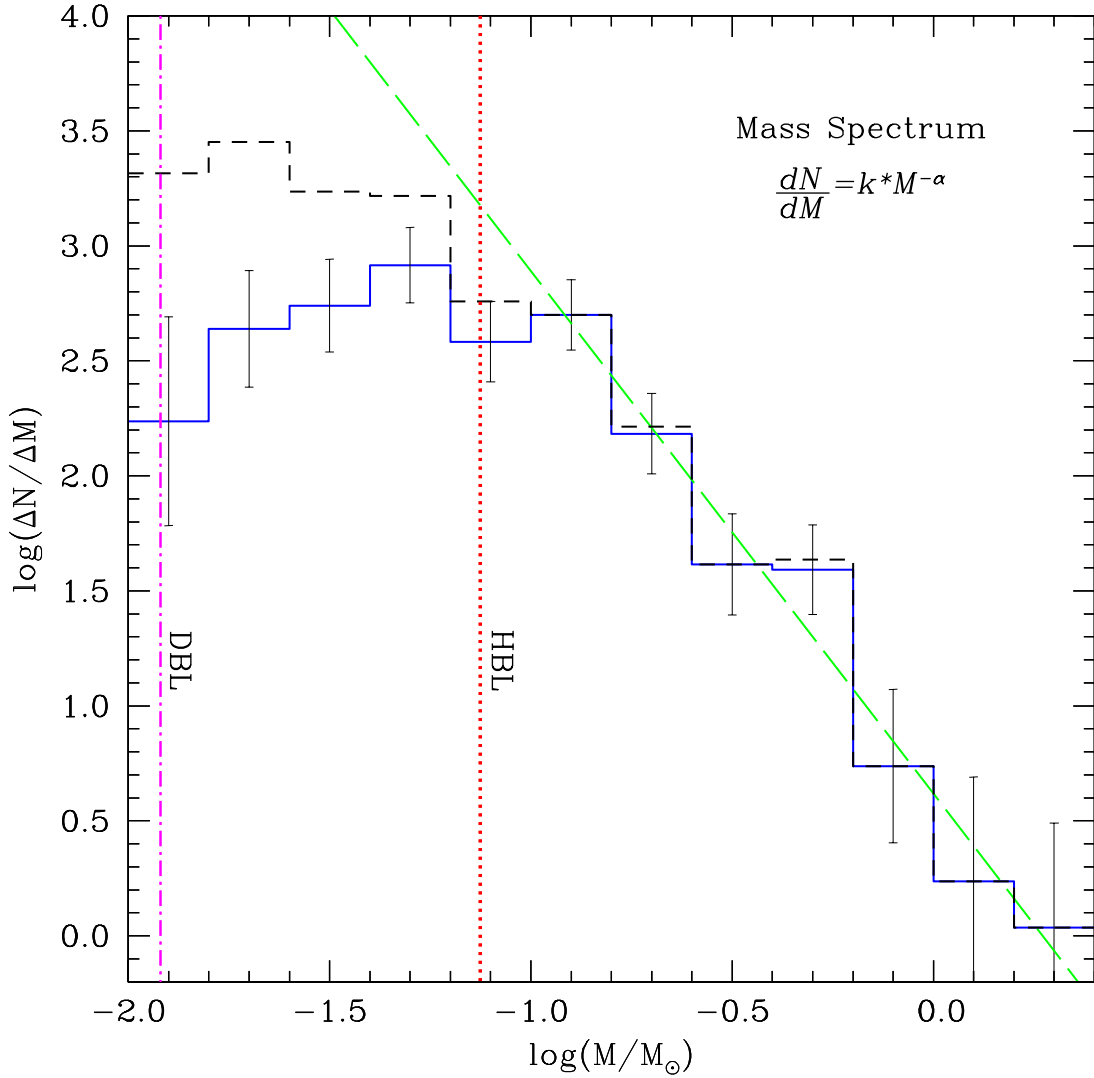


Fig. 3.19.— Mass function for variable stars (solid histogram) and all point sources (dashed histogram) detected with *FanCam* in NGC 1333. Long-dashed line represents the best-fit power-law mass spectrum for low-mass stellar regime ($0.1M_{\odot} \leq M_* \leq 2M_{\odot}$), where $\alpha = 2.27$. The error bars are computed by combining \sqrt{N} counting statistics and uncertainty in masses. The dotted vertical line indicates hydrogen-burning limit ($0.075M_{\odot}$) and the dot-dashed vertical line for deuterium-burning limit ($0.012M_{\odot}$).

3.4 Discussion

3.4.1 Origin of the Variability

The near-infrared photometric monitoring data can be used to discern the possible physical origins of the stellar flux variability. The contributions of many previous studies on young stellar object variability, including both visible and infrared wavelengths, established several plausible causes of variation (e.g., Herbst et al. 1994; Rydgren & Vrba 1983; Liseau et al. 1992; Kenyon et al. 1994; Skrutskie et al. 1996; Carpenter et al. 2001). The most common and effective explanations are fourfold: rotationally modulated cool starspots, existence of hot starspots on the rotating stellar surface, changes in the line-of-sight extinction due to the inhomogeneity of circumstellar material, and variations in accretion disk thermal activity due to irregular mass accretion rates. Skrutskie et al. (1996) pointed out that the accretion disk effects can produce substantially more variability at near-infrared wavelengths compared with visible wavelengths while the infrared variations due to starspots and dust extinction will have smaller amplitudes than simultaneous visible wavelength variations. Carpenter et al. (2001) used the detailed models for each case and compared their observations with the models. In this section, we interpret our observations in the context of the near-infrared variability models following the arguments in Carpenter et al. (2001) and references therein.

The short-term timescales of observed variable stars (daily, weekly, or monthly) suggest that the origin of the variability is associated with the stellar photosphere or the inner circumstellar environment. Models show that cool starspots will produce peak-to-peak variability amplitudes less than 0.4 mag in J , H , and K_s bands, and less than 0.03 mag in $J-H$ and $H-K_s$ colors. We use a conservative upper limit of color

change 0.05 mag given the simplicity of the starspot models to inspect our data set. Five variables out of 110 were identified within this range of colors and magnitudes (FMO 44, 45, 60, 238, and 250). None of these stars explicitly exhibit periodic variation. We applied the Discrete Fourier Transform numerical scheme of Scargle (1989) to search for periodicities. For FMO 250, a period, 10.952 days, was extracted. For the other cool starspot candidates, the periodicity search was unsuccessful. The light curves of FMO 250 and the phase-adjusted magnitude variations are shown in Figure 3.20.

To see how many variables are affected by hot starspots, we adopt the criteria of near-infrared magnitude peak-to-peak amplitudes less than 0.4 mag and peak-to-peak colors between 0.05 - 0.12, with a positive slope in K_s vs. $H-K_s$ diagram (Carpenter et al. 2001). A total of 23 variables satisfy these criteria but they all produce negative gradients in the CMD linear-regression fitting. None of them shows a clear periodicity. The negative slopes are not compatible with the prediction of hot starspot models. Therefore, the selected 23 stars cannot be purely hotspot-driven variables although they are met the color and magnitude criteria of the models, which suggests additional mechanisms may simultaneously be operating.

Dust extinction is prominent in young star-forming regions. Inhomogeneous line-of-sight dust extinction will produce a positive slope in a near-infrared color-magnitude diagram. Adopting the interstellar reddening law of Cohen et al. (1981) and transforming their CIT NIR photometric system into the *FanCam* system, extinction lines with a $+53^\circ$ tilt⁷ are drawn in the K_s vs. $H-K_s$ diagram (e.g., Figure 8, 12, 13). Of 110 variable sources, only one star (FMO 179) shows a slope greater than $+45^\circ$ in the K_s vs. $H-K_s$ diagram. The FMO 179 was identified as Class I by Gutermuth et al. (2008). Although there are several other stars with positive slopes, the slopes are

⁷Using the extinction law of Rieke & Lebofsky (1985), the slope is $+60^\circ$.

too shallow to be considered due dominantly to extinction.

The majority of the NGC 1333 variables have negative slopes in the K_s vs. $H-K_s$ diagram (Figure 3.21). When infalling/accreting material heats the circumstellar disk, the longer wavelength band, K_s , becomes brighter relative to the shorter bands, J or H , because the maximum accreting temperature of the heated material is $\lesssim 2000K$ (e.g., Bary et al. 2008). Increased K_s emission produces negative slopes in the color-magnitude diagram. For NGC 1333, however, we cannot simply claim that the observed stellar variability is driven by accretion exclusively since most of the slopes are distributed around -20° while the locus of classical T Tauri stars (disk activity dominant YSOs) predicts slopes of around -60° (see § 3.3.3). Possibly the accretion variability model of T Tauri stars is too simplistic. Very young objects could be dominated by infall in a different way than older T Tauri stars, leading to a different disk temperature structure and substantial extinction variation, which produces hybrid slopes in the CMD. Alternatively, active accretion in NGC 1333 may accompany extraordinarily strong accretion hotspots and higher accretion rates that could compromise the simplistic prediction of variability along the classical T Tauri star locus. Line emission variability may also contaminate the broadband fluxes especially for actively accreting pre-main-sequence objects (Bary et al. 2008), which is not included in the accretion disk variability models of Carpenter et al. (2001).

3.4.2 Characteristics of the Variability: An Evolutionary Sequence?

To search for any correlation between color change and magnitude variation, we investigated a plot of K_s vs. $H-K_s$ for each variable star and produced a histogram counting the slope statistics of linear-regression fit in Figure 3.21. The figure also in-

cludes three other cluster's histograms for comparison. The angle definition adopted is the same as in previous studies (Carpenter et al. 2001; Alves de Oliveira & Casali 2008), i.e., $\theta = \tan^{-1}(b)$, where $b = \frac{\Delta K_s}{\Delta(H-K_s)}$. Variability likely arises from a combination of various flux-changing sources, for example, starspots on the stellar surface, variable circumstellar extinction, and changes in accretion rate and/or geometry. The slopes in the color-magnitude diagram differentiate between those processes and can identify the dominant mechanism for an individual star as well as for the cluster as a whole.

Sixty-two stars out of the 110 variable stars in NGC 1333 have obvious negative slopes, with their colors becoming redder as they brighten, while 16 have positive slopes. Twenty-two variable stars show slopes close to zero, $-10^\circ < \theta < 10^\circ$, i.e., no change in K_s -band brightness as $H-K_s$ color varies (e.g., Figure 3.22). The remaining 9 objects were excluded from the statistics because any significant slope was not defined. For example, FMO 127 was detected only in K_s band, and stars 40 and 201 have extraordinarily large uncertainties in their slopes due to the scarcity of data. Others display fuzzy cluster shapes of dots in the color-magnitude diagram, producing large ambiguity in their slopes. The overall statistics of the K_s vs. $H-K_s$ slopes in NGC 1333, however, does not show the bimodal distribution as seen in ρ Ophiuchi (Alves de Oliveira & Casali 2008) and in the Trapezium in Orion A cloud (Carpenter et al. 2001). Instead, it shows a single mode distribution peaked at near -20° , characteristic of a stellar population dominated by accretion variability.

The correlation of the X-ray strength and the K_s vs. $H-K_s$ slope gives insight into the single peak around -20° in the NGC 1333 histogram. Figure 3.23 shows that most of the strongest X-ray sources have slopes between -30° and 0° . Young magnetically active stars produce strong X-ray emission. Therefore, the single peak around -20° of

the NGC 1333 histogram seems related to the extreme youth of the cluster relative to the other three clusters compared above. Although the age of the four embedded clusters presented in Figure 3.21 are known as one to a few million years, method to specify their relative youth/oldness is not well defined yet.

The morphological difference in the CMD slope histograms may reflect the evolutionary stage of the embedded star-forming clusters. As a cluster ages, the separation between the positive and the negative peaks becomes more and more distinctive and stars tend to move toward the extinction-driven group from the accretion-driven group resulting in the double-peak slope distribution. The underlying physics, however, is not clear. NGC 1333 is one of the least evolved embedded clusters known. It contains large numbers of protostars (Sandell & Knee 2001). The variations of colors and magnitudes in NGC 1333 likely originate from complicated mixtures of various variability sources. During the protostellar phase and early Class II stage, the IR variability might be represented by the blend of various agents. Then, as a star+disk system evolves into the late Class II and Class III phase, it maybe turns to be characterized by two different groups (strong vs. weak accretion), which produces bimodal peaks discussed above. The number of clusters investigated such near-infrared color-magnitude variability slope statistics is too sparse to illuminate the relationship between cluster evolution and variability mode yet although they show some tantalizing trends.

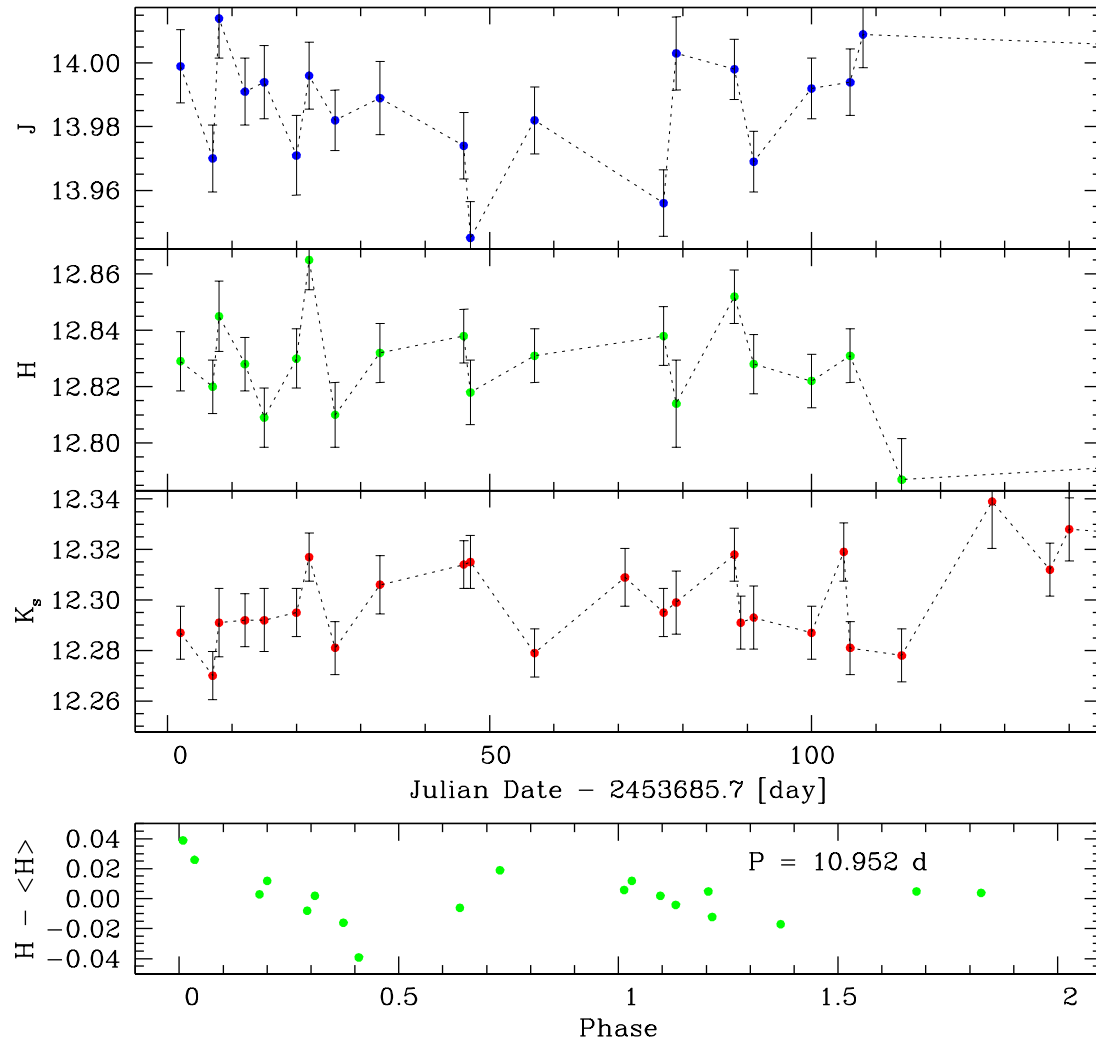


Fig. 3.20.— Light curves and the phase-shifted magnitude variation of a periodic variable star; FMO 250. The best fit period is 10.952 days. Two full cycles of the phase are plotted for better display of the periodicity. The color and magnitude variability ranges are consistent with cool starspot models investigated by Carpenter et al. (2001).

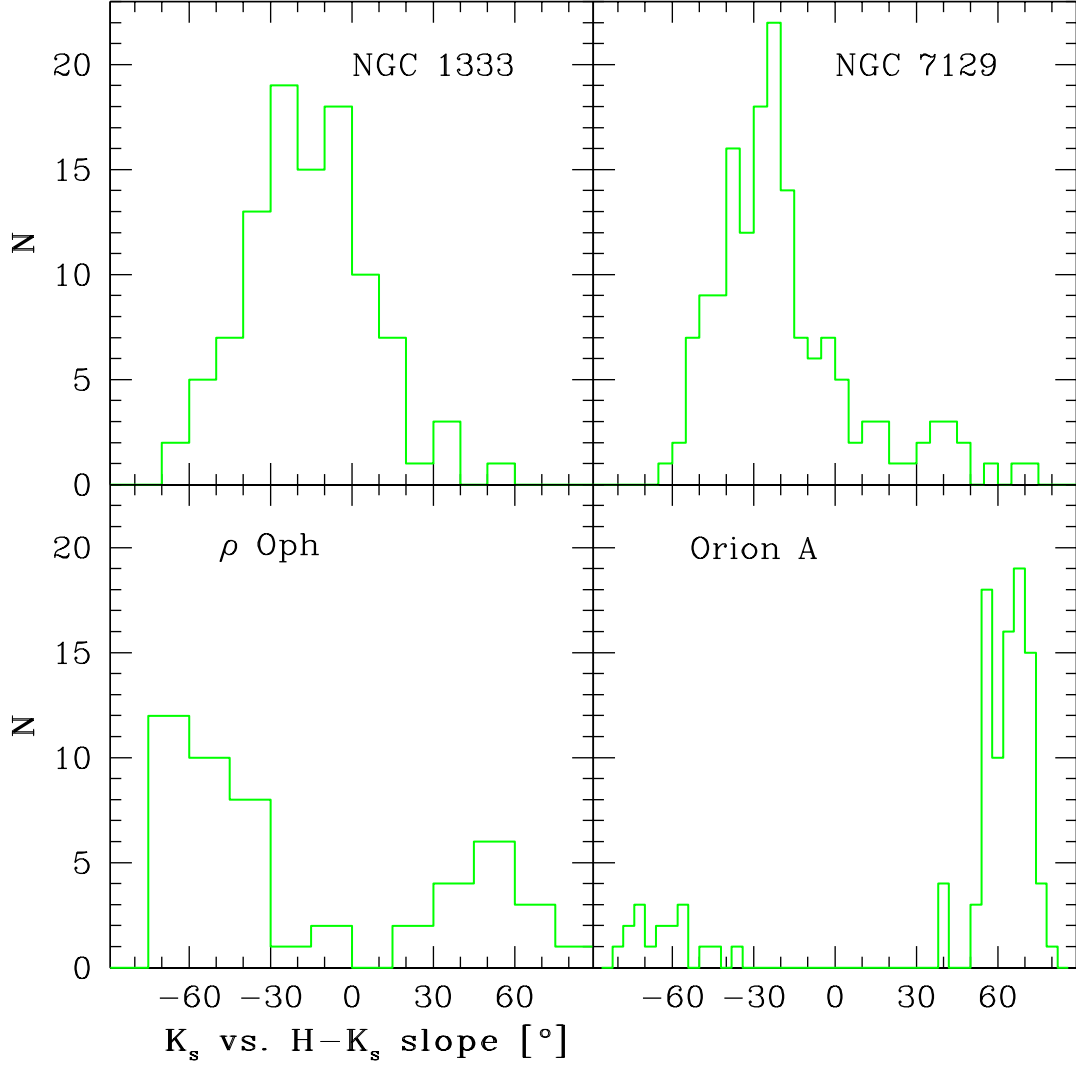


Fig. 3.21.— Histograms of the slopes derived from the K_s vs. $H-K_s$ diagrams in NGC 1333 (this paper), NGC 7129 (Park et al. in prep), ρ Ophiuchi (Alves de Oliveira & Casali 2008), and the Trapezium in Orion (Carpenter et al. 2001). The currently available samples for the color-magnitude slope statistics are limited in these four clusters only. Accretion disk models can account for the negative slope color variability, and variable extinction models can explain positive slopes, in general. The histogram morphological difference between the clusters maybe reflects the evolutionary stage of very young star-forming clusters.

NGC 1333 FMO 120

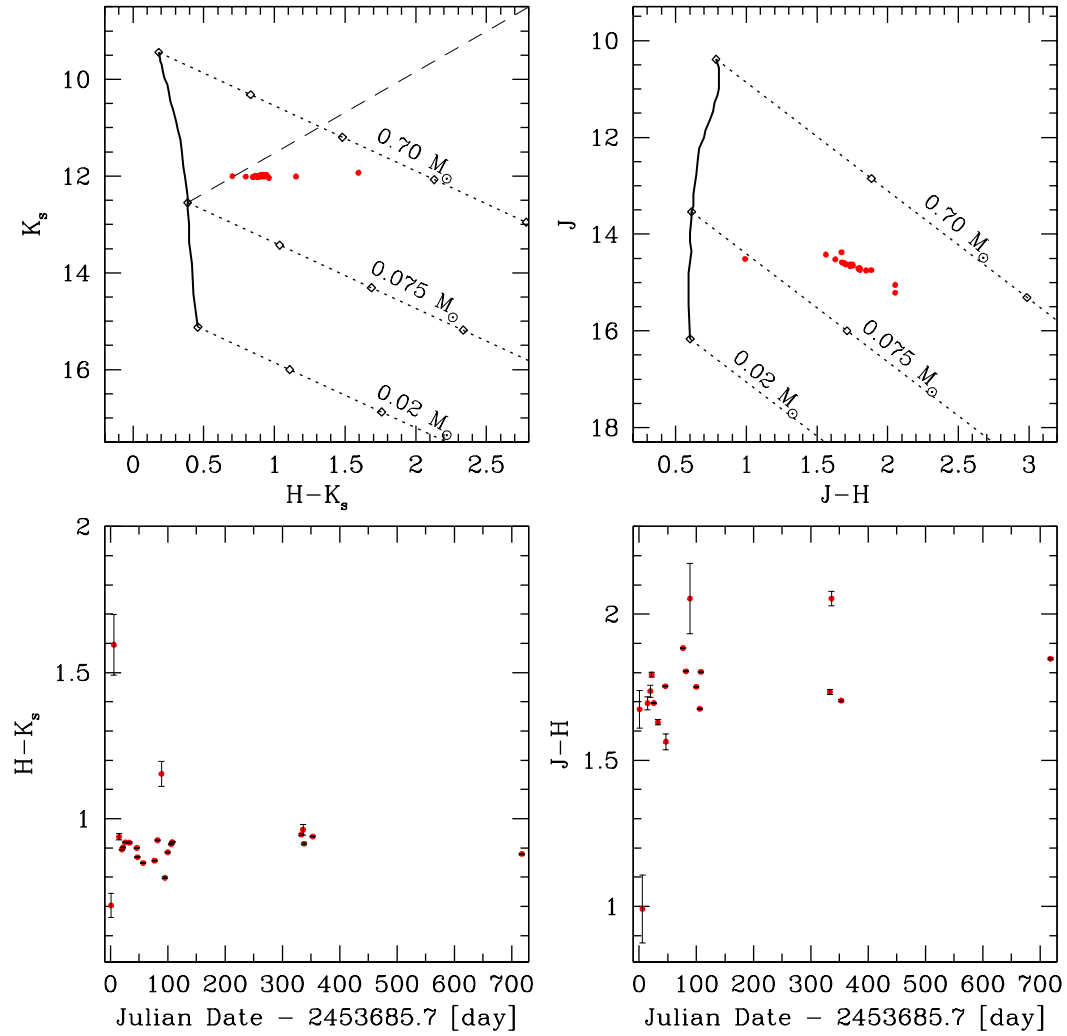


Fig. 3.22.— Color variability of a variable star; FMO 120. Each panel represents the same as Figure 3.16. It is an example of stars that show slopes close to zero ($-10^{\circ} < \theta < 10^{\circ}$), or no magnitude change in K_s band while $H-K_s$ color varies significantly.

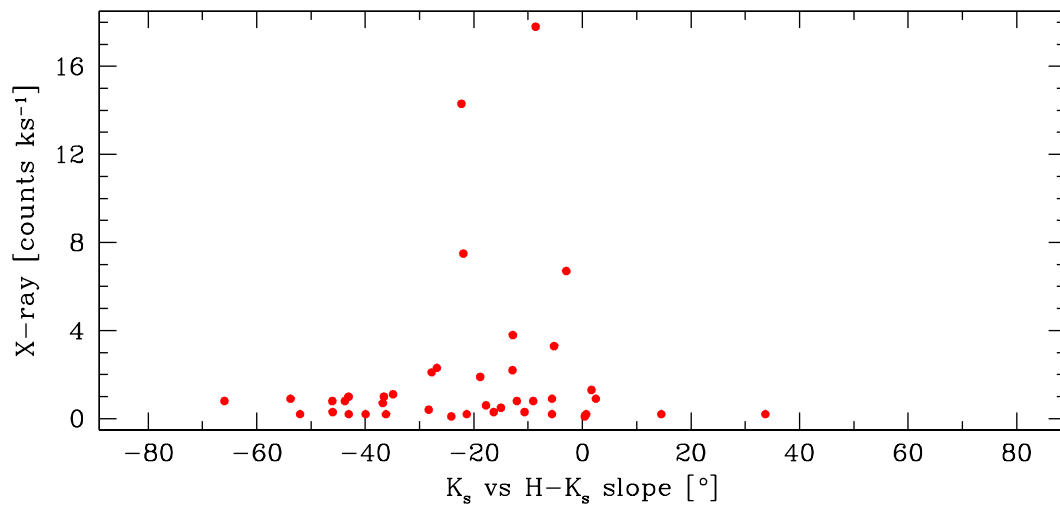


Fig. 3.23.— Correlation between the slope (K_s vs. $H-K_s$) and the X-ray strength measured by *Chandra* (Getman et al. 2002). Most of the strongest X-ray sources have slopes between -30° and 0° . The single mode distribution around -20° of the NGC 1333 slope histogram (Figure 3.21) seems to have something to do with strong magnetic activities of very young cluster members.

3.5 Conclusions

NGC 1333, a nearby embedded star-forming cluster in Perseus OB2 association, was photometrically monitored from November 2005 through October 2007 using a newly developed near-infrared camera, *FanCam*, at Fan Mountain Observatory near Charlottesville Virginia. Two separate fields were targeted with each covering $8.7' \times 8.7'$ field of view. Data sets were reduced and analyzed in the context of variability, cluster membership, and the evolutionary stage of the infant cluster.

Out of 198 established point sources, we identified 110 variable stars, 96 with the Stetson index statistic (Stetson 1996) and 14 with a conventional reduced- χ^2 method. Color-magnitude and color-color diagrams composed of J , H , and K_s confirm the ultimate youth of the cluster age and the highly extincted circumstellar environment. The three band light curves are displaying temporally well correlated variability for large fraction of the variable stars, although periodic properties are not determined for most of the sources. The spatial distribution densities of variable stars and IR excess YSOs are highest around the peak of the extinction map while non-variables do not show any concentration in the fields of view.

Out of 72 *Spitzer*-2MASS-identified IR excess YSOs (Gutermuth et al. 2008, a recent intensive near- to mid-IR investigation in this cluster), 64 stars are matched as variable stars, reading 89% variability rate. Out of 42 *Chandra*-identified X-ray sources (Getman et al. 2002), 41 turned out to be variables in our *FanCam* monitoring campaign, leading virtually 100% variability rate. A total of 25 variable stars are unidentified with any of literature cluster members. The chance of external contamination from Galactic or extragalactic variable sources is obviously insignificant. We present the 25 unmatched ones as new cluster member candidates, with 15 brown dwarfs ($M < 0.075M_{\odot}$) and 10 very low-mass stars ($0.075 < M < 0.20M_{\odot}$).

The general behavior of the Initial Mass Function of NGC 1333 is well consistent with the previous studies in other embedded clusters. It shows a Salpeter type increase in the low-mass stellar mass regime, reaches a peak at $\sim 0.1\text{--}0.2M_{\odot}$, and declines toward brown dwarf regime. The NGC 1333 IMF also shows a tentative secondary peak at $\sim 0.05M_{\odot}$, which was suggested by Muench et al. (2002) and Slesnick et al. (2004) in Trapezium Cluster and by Levine et al. (2006) in NGC 2024. We computed the substellar-to-stellar mass ratio in NGC 1333 ($R_{ss} = 0.34 \pm 0.07$). It is comparable to several previous works in other clusters within their error ranges but not consistent with all of them, which remains the universality of the brown dwarf formation fraction unresolved and requires more thorough study to make the issue clear.

The slope statistics in the K_s vs. $H-K_s$ color-magnitude diagram shows a single mode distribution peaked at near -20° , suggesting that accretion activity dominate the flux variation in the near-infrared bands. The strongest X-ray sources have the K_s vs. $H-K_s$ slopes between -30° and 0° , which is coincident with the angle of the single peak shown in NGC 1333 CMD slopes. From the comparison of four embedded clusters, we find a clue that the color-magnitude variability pattern may reflect the forming-stars' evolution history in its very early stage of cluster formation. If we could establish the method with larger number of sample clusters, it will be a sensitive and powerful age-determination tool to understand the early stage evolution of star-forming clusters.

Table 3.1. Log of Observations of NGC 1333

UT Date	J^N	H^N	K_s^N	J^S	H^S	K_s^S	JD-2453685.7 ^a
2005 Nov 12	X	X	X	1
2005 Nov 13	X	X	X	2
2005 Nov 17	X	X	X	6
2005 Nov 18	X	X	X	X	7
2005 Nov 19	X	X	X	8
2005 Nov 23	X	X	X	X	X	X	12
2005 Nov 26	X	X	X	X	X	X	15
2005 Dec 01	X	X	X	X	X	X	20
2005 Dec 03	X	X	X	X	X	X	22
2005 Dec 07	X	X	X	X	X	X	26
2005 Dec 14	X	X	X	X	X	X	33
2005 Dec 27	X	X	X	X	X	X	46
2005 Dec 28	X	X	X	X	X	X	47
2006 Jan 07	X	X	X	X	X	X	57
2006 Jan 21	X	71
2006 Jan 27	X	X	X	X	X	X	77
2006 Jan 29	X	X	X	79
2006 Feb 01	X	X	X	82
2006 Feb 07	X	X	X	88
2006 Feb 08	X	X	X	X	89
2006 Feb 10	X	X	X	91
2006 Feb 14	X	X	95
2006 Feb 19	X	X	X	X	X	X	100
2006 Feb 24	X	X	105
2006 Feb 25	X	X	X	X	X	X	106
2006 Feb 27	X	X	X	X	108
2006 Mar 05	...	X	X	114
2006 Mar 19	X	128
2006 Mar 28	X	X	137
2006 Mar 31	X	X	140
2006 Oct 02	X	X	X	325
2006 Oct 10	X	X	X	333
2006 Oct 13	X	X	X	X	X	X	336
2006 Oct 15	X	X	X	X	X	X	338
2006 Oct 26	X	349
2006 Oct 30	X	X	X	X	X	X	353
2007 Feb 05	X	X	451
2007 Feb 06	X	X	452
2007 Oct 30	X	X	X	X	X	X	718
Total Obs #	24	24	32	23	23	30	

^aThe Julian Date for 2005 November 11 05:00:00.0 UT is 2453685.70833.

^NThe northern field of NGC 1333

^SThe southern field of NGC 1333

Table 3.2. Point-Source List of NGC 1333

FMO ^a	R.A. (J2000.0)	Dec. (J2000.0)	J^b	σ_J^c	H^b	σ_H^c	K_s^b	$\sigma_{K_s}^c$	J	N_{obs}^d H	K_s	A_V^e
001	03:28:33.65	+31:18:01.5	17.594	0.060	15.706	0.058	14.861	0.062	05	05	06	9.92
002	03:28:34.85	+31:16:04.3	17.472	0.091	16.214	0.084	15.106	0.075	11	13	15	13.96
003	03:28:35.33	+31:17:59.6	16.303	0.048	14.504	0.034	13.522	0.040	15	15	20	12.03
004	03:28:35.36	+31:16:20.5	16.782	0.090	15.781	0.074	00	08	16	12.32
008	03:28:36.51	+31:19:28.9	12.838	0.014	12.097	0.025	11.810	0.022	17	15	21	0.00
011	03:28:38.75	+31:18:06.8	16.786	0.104	14.086	0.074	00	11	27	37.42
012	03:28:39.68	+31:17:32.0	16.486	0.099	13.518	0.044	00	18	29	41.97
013	03:28:40.10	+31:15:13.1	17.383	...	16.123	0.124	00	03	19	16.30
014	03:28:41.55	+31:14:09.7	16.386	0.108	15.185	0.087	00	17	30	12.93
015	03:28:41.63	+31:20:13.7	18.702	...	16.281	0.040	15.077	0.036	01	19	30	15.44
016	03:28:42.33	+31:19:40.7	17.613	0.058	16.289	0.065	15.747	0.054	19	21	25	5.26
017	03:28:42.34	+31:15:50.7	16.165	0.095	00	00	19	0.00
023	03:28:44.07	+31:20:52.9	14.259	0.053	13.252	0.054	12.610	0.023	19	20	28	5.17
025	03:28:46.10	+31:16:44.2	16.063	0.194	15.591	0.274	15.506	0.226	05	05	08	0.00
027	03:28:46.67	+31:19:50.1	17.578	0.068	15.812	0.045	14.984	0.031	19	22	30	9.66
028	03:28:46.87	+31:20:27.7	14.848	0.052	14.164	0.018	13.855	0.021	22	22	30	0.00
029	03:28:47.20	+31:18:46.0	17.446	0.140	15.395	0.042	00	08	28	28.47
030	03:28:47.82	+31:16:55.1	12.950	0.047	11.753	0.062	10.926	0.051	22	22	30	8.90
031	03:28:48.16	+31:19:23.5	15.488	0.031	14.812	0.018	14.564	0.029	22	22	29	0.00
032	03:28:48.44	+31:20:28.4	17.221	0.080	15.128	0.031	14.251	0.034	20	22	30	10.41
033	03:28:48.74	+31:16:08.8	16.885	0.235	15.028	0.071	00	09	29	23.50
034	03:28:48.80	+31:17:22.5	17.753	0.096	15.082	0.025	13.705	0.019	19	22	30	18.10
035	03:28:49.54	+31:15:06.2	17.740	0.221	15.594	0.050	00	04	28	29.93
039	03:28:51.05	+31:16:32.4	13.296	0.019	12.470	0.013	12.100	0.021	22	22	30	1.05
040	03:28:51.09	+31:18:15.6	14.284	0.319	13.103	0.455	12.554	0.234	20	06	09	3.70
042	03:28:51.25	+31:17:39.4	16.921	0.335	15.768	...	14.991	0.184	08	03	17	6.24
043	03:28:52.09	+31:16:29.2	16.166	0.033	14.538	0.033	13.823	0.025	22	22	30	7.92
044	03:28:52.13	+31:15:47.1	13.106	0.022	12.410	0.019	11.968	0.029	22	22	30	2.26
045	03:28:52.40	+31:15:26.4	12.948	0.013	12.217	0.012	12.075	0.021	22	22	30	0.00
046	03:28:52.90	+31:16:26.5	13.627	0.020	12.860	0.021	12.493	0.033	22	22	30	0.82
047	03:28:53.93	+31:18:09.2	15.001	0.147	12.408	0.053	11.140	0.121	19	21	29	15.86
048	03:28:54.07	+31:16:54.3	13.087	0.021	12.103	0.015	11.638	0.021	22	22	30	2.78
050	03:28:54.92	+31:15:29.0	16.076	0.037	14.911	0.040	14.204	0.037	21	22	30	5.48
051	03:28:54.96	+31:18:15.3	17.427	0.065	14.607	0.044	13.141	0.025	20	22	30	18.11
052	03:28:55.05	+31:16:28.8	13.578	0.080	11.666	0.085	10.559	0.116	22	22	30	13.54
053	03:28:55.07	+31:14:16.3	15.977	0.081	00	00	24	0.00
054	03:28:55.12	+31:15:02.6	16.124	0.111	00	00	17	0.00
055	03:28:55.13	+31:16:24.8	13.036	0.038	11.592	0.033	10.844	0.060	22	22	30	7.67
056	03:28:55.24	+31:17:35.3	15.141	0.021	14.069	0.017	13.464	0.016	22	22	30	6.23
059	03:28:56.10	+31:19:08.6	16.089	0.077	00	00	23	0.00
060	03:28:56.22	+31:17:45.7	13.471	0.015	12.612	0.012	12.162	0.018	22	22	30	2.30
065	03:28:56.86	+31:19:45.4	16.171	0.149	15.041	0.058	14.342	0.060	16	19	28	5.29

Table 3.2—Continued

FMO ^a	R.A. (J2000.0)	Dec. (J2000.0)	J^b	σ_J^c	H^b	σ_H^c	K_s^b	$\sigma_{K_s}^c$	J	N_{obs}^d H	K_s	A_V^e
066	03:28:56.94	+31:20:48.8	15.437	0.062	14.452	0.040	13.866	0.026	19	20	28	3.70
067	03:28:56.94	+31:15:50.3	15.152	0.026	14.060	0.018	13.466	0.018	22	22	30	6.06
068	03:28:56.94	+31:16:22.3	13.729	0.080	11.837	0.095	10.910	0.218	22	22	30	10.50
069	03:28:57.03	+31:16:48.6	17.102	0.051	16.068	0.044	15.467	0.047	21	20	28	6.16
070	03:28:57.04	+31:15:02.7	17.740	...	14.126	0.023	00	03	30	52.52
071	03:28:57.11	+31:19:12.0	17.125	0.102	16.001	0.080	15.289	0.093	22	21	29	5.06
072	03:28:57.15	+31:15:34.6	15.412	0.032	13.976	0.020	13.179	0.018	22	22	30	7.39
073	03:28:57.37	+31:15:36.1	18.034	0.085	16.371	0.072	15.624	0.064	15	20	27	8.41
074	03:28:57.41	+31:19:50.6	12.125	0.029	11.048	0.024	10.648	0.020	22	22	30	2.19
077	03:28:57.69	+31:19:48.2	13.060	0.024	11.923	0.052	11.349	0.026	22	22	30	4.65
078	03:28:58.05	+31:15:48.0	16.727	0.066	15.222	0.040	00	15	29	20.07
079	03:28:58.09	+31:18:03.8	12.827	0.015	11.702	0.018	11.336	0.016	22	22	30	1.33
080	03:28:59.22	+31:16:53.2	18.145	0.105	16.990	0.128	16.165	0.057	09	13	15	9.61
081	03:28:59.22	+31:20:33.0	16.698	0.096	15.844	0.098	14.969	0.191	20	20	27	7.82
082	03:28:59.27	+31:15:48.4	16.273	0.105	12.602	0.237	10.734	0.312	22	21	27	25.64
083	03:28:59.33	+31:16:31.5	17.361	0.056	15.394	0.032	14.503	0.034	21	22	30	10.63
085	03:28:59.37	+31:20:08.6	17.907	...	17.743	...	15.248	0.154	01	02	24	33.61
086	03:29:00.01	+31:17:13.3	18.096	0.102	16.598	0.110	15.916	0.105	08	19	23	7.41
087	03:29:00.14	+31:21:09.4	16.497	0.092	14.546	0.109	13.312	0.037	10	14	15	14.32
088	03:29:00.30	+31:13:38.3	13.178	0.025	11.838	0.038	11.347	0.034	15	16	21	3.33
089	03:29:00.34	+31:14:14.8	16.773	0.093	14.913	0.032	00	17	30	25.53
090	03:29:00.37	+31:20:45.8	13.536	0.025	12.345	0.030	11.807	0.019	19	20	28	3.87
092	03:29:01.39	+31:19:35.5	18.527	0.158	17.229	0.197	16.430	0.201	05	12	17	9.21
093	03:29:01.53	+31:20:20.8	13.743	0.224	10.448	0.153	00	20	27	48.61
094	03:29:01.87	+31:16:53.2	16.848	0.062	15.420	0.053	14.774	0.040	22	21	30	6.86
095	03:29:02.15	+31:16:11.4	14.491	0.034	13.828	0.021	13.566	0.020	22	22	30	0.00
096	03:29:02.26	+31:17:49.6	16.949	0.041	15.657	0.034	15.182	0.036	21	21	30	4.23
097	03:29:02.69	+31:19:05.6	17.966	0.117	15.260	0.063	13.626	0.058	15	22	30	20.58
098	03:29:02.88	+31:16:00.9	12.842	0.033	12.114	0.016	11.905	0.011	22	22	30	0.00
100	03:29:03.38	+31:18:40.0	15.728	0.055	14.556	0.025	13.864	0.029	22	22	30	5.39
101	03:29:03.46	+31:16:17.8	15.501	0.086	00	00	26	0.00
102	03:29:03.55	+31:17:53.3	18.532	0.155	16.854	0.085	16.151	0.070	14	15	19	7.73
104	03:29:04.06	+31:17:07.5	13.308	0.034	12.625	0.017	12.300	0.017	22	22	30	0.24
105	03:29:04.16	+31:16:50.6	17.344	0.115	15.182	0.054	14.157	0.026	20	22	30	12.69
107	03:29:04.30	+31:19:06.4	16.972	0.243	16.073	0.197	15.666	0.181	22	21	28	0.01
108	03:29:04.62	+31:20:29.0	17.409	0.145	15.170	0.078	13.701	0.038	16	21	30	17.90
109	03:29:04.66	+31:16:59.1	15.279	0.149	13.589	0.138	12.501	0.131	22	22	30	12.35
110	03:29:04.94	+31:20:38.6	16.883	...	14.728	0.192	13.094	0.106	01	17	27	20.82
112	03:29:05.17	+31:20:37.4	15.263	0.117	13.998	0.226	00	07	20	14.50
114	03:29:05.64	+31:20:10.8	16.810	0.154	15.913	0.093	15.176	0.086	22	22	29	5.51
116	03:29:05.86	+31:16:38.1	14.457	0.120	13.046	0.130	00	04	12	17.27
117	03:29:05.92	+31:16:40.1	16.196	0.224	13.898	0.089	12.440	0.083	06	06	18	18.30

Table 3.2—Continued

FMO ^a	R.A. (J2000.0)	Dec. (J2000.0)	J^b	σ_J^c	H^b	σ_H^c	K_s^b	$\sigma_{K_s}^c$	J	N_{obs}^d H	K_s	A_V^e
118	03:29:06.31	+31:13:46.1	14.897	0.064	12.644	0.038	00	19	25	30.93
119	03:29:06.45	+31:16:51.7	17.381	...	15.520	0.099	00	02	24	25.55
120	03:29:08.32	+31:20:20.4	14.679	0.059	12.930	0.044	11.997	0.021	20	22	29	10.10
121	03:29:09.32	+31:21:04.3	16.264	0.142	14.278	0.102	13.125	0.079	13	17	15	13.11
122	03:29:10.81	+31:16:42.5	16.185	0.204	14.502	0.159	13.292	0.086	18	19	26	13.94
123	03:29:11.30	+31:17:17.5	13.999	0.083	13.246	0.035	12.834	0.029	17	17	24	1.38
124	03:29:11.64	+31:20:37.5	15.424	0.104	13.599	0.066	12.694	0.039	15	14	23	9.34
125	03:29:12.41	+31:14:56.3	12.605	0.124	12.021	0.142	11.814	0.018	09	09	17	0.00
126	03:29:12.79	+31:20:07.9	14.615	0.111	13.848	0.124	13.314	0.039	09	08	17	3.12
127	03:29:12.95	+31:18:14.5	13.961	0.091	00	00	12	0.00
128	03:28:56.05	+31:26:34.1	16.169	0.062	14.964	0.034	14.492	0.036	20	19	26	1.59
129	03:28:56.10	+31:26:50.9	17.847	0.086	16.781	0.040	16.375	0.064	14	12	15	3.16
130	03:28:56.30	+31:22:27.9	15.742	0.063	13.215	0.050	11.894	0.038	21	23	30	17.24
131	03:28:56.33	+31:24:43.1	17.678	0.072	15.787	0.040	14.919	0.036	16	22	29	10.27
133	03:28:57.08	+31:21:24.9	16.167	0.133	00	00	18	0.00
134	03:28:58.23	+31:22:09.3	16.055	0.038	14.290	0.031	13.312	0.018	24	24	32	11.96
135	03:28:58.24	+31:22:02.1	14.861	0.118	13.296	0.095	12.291	0.090	24	24	32	11.12
137	03:28:58.41	+31:22:17.6	15.286	0.169	12.707	0.206	00	23	32	36.12
138	03:28:58.42	+31:22:56.7	15.350	0.037	14.222	0.027	13.592	0.026	24	24	32	4.53
144	03:29:00.37	+31:24:38.5	16.599	0.047	14.533	0.026	13.570	0.031	24	24	32	11.73
145	03:29:00.69	+31:22:00.8	16.093	0.042	13.196	0.021	11.735	0.024	24	24	32	18.67
147	03:29:01.57	+31:25:13.6	18.869	...	16.892	0.080	15.662	0.060	01	17	30	15.84
148	03:29:02.03	+31:25:09.7	18.689	...	16.546	0.067	15.369	0.055	03	21	31	15.03
149	03:29:02.07	+31:26:31.4	18.514	0.149	16.495	0.061	15.448	0.061	05	20	30	13.03
150	03:29:02.36	+31:22:15.8	18.254	0.108	17.401	0.161	16.783	0.205	06	06	07	6.43
151	03:29:02.59	+31:26:02.9	17.398	...	16.332	0.070	00	03	22	13.32
152	03:29:02.79	+31:22:17.3	16.963	0.091	14.787	0.054	13.397	0.069	23	23	32	16.78
153	03:29:03.11	+31:22:38.2	14.267	0.197	12.991	0.239	11.829	0.226	24	24	32	13.84
154	03:29:03.20	+31:25:45.1	15.764	0.053	14.621	0.043	13.898	0.057	24	24	32	5.87
156	03:29:03.32	+31:23:14.7	17.562	0.067	15.396	0.040	14.014	0.043	23	24	31	18.18
158	03:29:03.79	+31:23:08.7	17.898	0.069	15.790	0.034	14.712	0.030	16	24	31	13.50
160	03:29:03.93	+31:23:30.9	17.397	0.049	15.977	0.062	15.053	0.041	22	24	31	11.13
161	03:29:04.16	+31:25:15.0	13.651	0.037	11.795	0.032	10.902	0.029	24	24	32	9.96
166	03:29:05.23	+31:26:47.4	17.083	0.060	15.631	0.046	00	10	28	19.26
168	03:29:05.67	+31:21:33.8	18.575	...	15.282	0.079	13.290	0.067	02	23	32	26.46
169	03:29:05.78	+31:25:22.1	17.472	0.138	16.630	0.117	00	09	13	9.87
170	03:29:06.78	+31:22:58.5	17.007	0.075	15.246	0.058	14.300	0.033	22	24	31	11.47
171	03:29:07.15	+31:23:22.9	18.184	0.148	16.700	0.123	15.717	0.074	11	20	25	12.04
173	03:29:07.62	+31:24:26.7	17.781	0.067	16.037	0.049	15.154	0.049	20	24	32	10.50
176	03:29:08.04	+31:27:27.7	17.866	0.081	16.795	0.125	16.213	0.122	14	15	20	5.87
178	03:29:08.64	+31:22:29.6	17.541	0.104	15.462	0.082	14.373	0.061	18	24	32	11.51
179	03:29:08.94	+31:22:56.2	16.054	0.405	13.449	0.306	11.742	0.215	22	23	32	22.61

Table 3.2—Continued

FMO ^a	R.A. (J2000.0)	Dec. (J2000.0)	J^b	σ_J^c	H^b	σ_H^c	K_s^b	$\sigma_{K_s}^c$	J	N_{obs}^d H	K_s	A_V^e
180	03:29:08.97	+31:26:23.9	16.921	0.101	15.590	0.154	14.676	0.211	24	22	30	8.57
182	03:29:09.03	+31:21:29.2	15.669	0.343	13.102	0.264	00	11	28	35.74
183	03:29:09.07	+31:23:05.6	14.612	0.046	12.920	0.021	11.903	0.034	24	24	32	11.49
184	03:29:09.15	+31:21:44.4	14.523	0.194	12.793	0.124	00	16	29	22.49
185	03:29:09.24	+31:27:16.0	17.353	0.097	16.207	0.119	15.671	0.095	18	21	25	5.16
187	03:29:09.48	+31:27:20.8	14.236	0.053	13.277	0.054	12.699	0.064	22	22	26	4.10
190	03:29:10.18	+31:27:15.9	15.558	0.059	14.695	0.043	14.191	0.051	22	22	29	2.24
192	03:29:10.45	+31:23:34.8	15.674	0.038	13.831	0.025	12.808	0.034	24	24	32	11.17
193	03:29:10.61	+31:23:43.9	18.001	0.062	16.130	0.048	15.012	0.038	15	23	32	14.12
194	03:29:10.78	+31:22:30.1	14.760	0.057	13.535	0.029	12.879	0.034	24	24	32	5.27
195	03:29:11.32	+31:22:57.0	14.871	0.043	13.459	0.035	12.543	0.040	24	24	32	9.58
197	03:29:11.77	+31:26:09.5	17.170	0.135	15.854	0.107	14.960	0.116	23	24	32	8.12
198	03:29:11.77	+31:22:03.6	16.749	0.230	15.763	0.202	15.314	0.160	04	06	04	3.83
199	03:29:11.85	+31:21:55.8	15.575	...	13.753	0.242	00	02	26	23.53
200	03:29:11.86	+31:21:27.1	15.548	0.279	13.016	0.147	00	24	32	35.22
201	03:29:11.95	+31:21:24.3	17.730	...	16.864	0.418	15.872	0.339	02	08	14	9.28
202	03:29:12.03	+31:25:48.9	16.026	0.034	15.354	0.040	14.878	0.040	24	24	32	1.47
203	03:29:12.26	+31:23:07.0	18.119	0.242	16.300	0.067	15.061	0.049	13	20	32	15.98
204	03:29:12.37	+31:27:23.1	15.704	0.064	15.050	0.050	14.738	0.056	20	22	24	0.00
207	03:29:12.90	+31:23:29.3	13.456	0.031	12.573	0.026	12.061	0.035	24	24	32	3.34
210	03:29:13.54	+31:23:46.9	18.294	...	16.351	0.109	15.209	0.045	02	23	32	14.49
211	03:29:14.10	+31:20:33.2	16.082	0.027	15.456	0.025	15.114	0.040	24	24	32	2.18
212	03:29:14.42	+31:22:36.2	14.550	0.030	13.560	0.037	13.012	0.029	24	24	32	3.48
213	03:29:15.60	+31:22:42.7	16.954	...	15.805	0.185	00	03	17	11.82
214	03:29:16.54	+31:21:02.5	15.069	0.024	13.301	0.018	12.429	0.021	24	24	32	8.93
215	03:29:16.55	+31:24:46.4	16.972	0.068	15.729	0.049	15.136	0.039	22	24	32	6.04
216	03:29:16.59	+31:23:49.4	13.234	0.033	11.862	0.044	11.183	0.044	24	24	32	6.41
217	03:29:16.81	+31:23:25.2	15.469	0.086	14.299	0.078	13.679	0.057	24	24	32	4.33
218	03:29:17.50	+31:24:54.9	17.128	0.182	15.360	0.110	00	07	31	21.93
222	03:29:18.64	+31:20:21.5	17.120	0.061	15.718	0.075	00	14	31	18.49
223	03:29:18.65	+31:20:17.8	18.785	...	16.237	0.141	14.819	0.075	02	22	32	16.57
226	03:29:20.04	+31:24:07.6	18.830	...	14.867	0.148	12.235	0.100	01	24	32	37.18
227	03:29:20.42	+31:26:33.4	17.680	0.068	16.148	0.063	15.478	0.047	13	11	17	7.23
228	03:29:20.54	+31:26:35.0	16.822	0.087	15.503	0.040	14.864	0.050	15	14	21	6.75
231	03:29:21.10	+31:21:59.3	17.624	0.084	16.468	0.054	15.915	0.068	21	21	24	5.43
232	03:29:21.30	+31:23:46.4	17.472	0.050	14.649	0.033	13.018	0.019	22	24	32	22.01
233	03:29:21.38	+31:22:54.4	17.302	0.103	16.204	0.149	00	09	23	13.81
235	03:29:21.52	+31:25:12.9	13.213	0.017	12.202	0.013	11.685	0.014	24	24	32	3.59
236	03:29:21.54	+31:21:10.5	12.431	0.021	11.746	0.016	11.404	0.017	24	24	32	0.92
237	03:29:21.99	+31:20:44.4	17.342	0.053	16.169	0.046	15.695	0.064	20	23	30	4.21
238	03:29:22.04	+31:24:15.3	12.000	0.014	11.284	0.014	10.982	0.017	24	24	32	0.47
239	03:29:22.36	+31:21:36.9	17.752	0.066	16.518	0.076	15.857	0.066	22	22	30	7.09

Table 3.2—Continued

FMO ^a	R.A. (J2000.0)	Dec. (J2000.0)	J^b	σ_J^c	H^b	σ_H^c	K_s^b	$\sigma_{K_s}^c$	J	N_{obs}^d H	K_s	A_V^e
241	03:29:22.94	+31:22:35.5	17.070	0.046	16.111	0.055	15.669	0.056	22	24	30	3.72
242	03:29:23.03	+31:26:31.7	18.630	...	17.048	0.131	16.040	0.087	02	16	27	12.43
243	03:29:23.14	+31:20:30.4	12.427	0.067	11.664	0.057	11.235	0.058	24	24	32	2.39
244	03:29:23.19	+31:23:57.2	17.457	0.127	16.354	0.081	00	09	20	13.89
246	03:29:23.24	+31:26:53.2	13.538	0.024	12.655	0.018	12.182	0.027	22	22	30	2.66
247	03:29:23.26	+31:24:46.7	16.816	0.080	15.555	0.066	00	19	30	16.32
248	03:29:23.30	+31:25:43.7	16.213	0.087	00	00	21	0.00
249	03:29:23.49	+31:23:31.0	12.853	0.022	11.786	0.020	11.351	0.020	24	24	32	2.43
250	03:29:23.70	+31:25:09.6	13.986	0.016	12.826	0.013	12.295	0.017	24	24	32	3.53
252	03:29:24.07	+31:19:57.7	15.780	0.086	14.346	0.046	13.650	0.035	16	22	27	5.55
253	03:29:24.83	+31:24:06.3	14.392	0.018	13.717	0.020	13.348	0.018	24	24	32	0.46
254	03:29:25.31	+31:21:49.7	16.817	0.036	15.571	0.034	15.032	0.026	23	24	32	5.21
257	03:29:26.03	+31:20:55.7	17.014	0.050	15.732	0.032	15.220	0.036	23	23	31	4.80
258	03:29:26.08	+31:23:44.8	17.761	0.074	16.482	0.069	15.862	0.069	21	23	29	6.46
260	03:29:26.15	+31:26:43.5	13.766	0.035	12.938	0.035	12.519	0.048	22	21	29	3.36
262	03:29:26.32	+31:22:50.4	17.476	0.049	16.193	0.053	15.630	0.049	23	23	30	5.58
264	03:29:27.60	+31:21:10.0	14.819	0.018	13.595	0.020	13.076	0.017	24	24	29	2.99
265	03:29:27.83	+31:21:20.1	16.431	0.028	15.141	0.029	14.601	0.025	23	24	28	5.23
266	03:29:28.01	+31:25:11.0	17.547	0.065	15.871	0.034	14.848	0.028	19	23	28	12.66
267	03:29:28.06	+31:21:17.8	16.145	0.028	15.059	0.021	14.559	0.026	23	24	28	4.61
268	03:29:28.08	+31:22:35.7	18.096	0.078	16.885	0.073	16.297	0.104	12	18	15	5.96
269	03:29:28.17	+31:23:59.3	16.422	0.040	14.953	0.027	14.362	0.026	24	24	29	6.01
270	03:29:29.01	+31:24:29.2	17.411	0.042	16.123	0.063	15.600	0.042	22	23	27	4.96
271	03:29:29.42	+31:27:03.9	17.227	0.055	16.207	0.074	15.740	0.079	18	20	23	4.10
273	03:29:29.77	+31:21:02.7	12.706	0.041	11.654	0.036	11.194	0.042	24	24	27	2.90
274	03:29:30.54	+31:27:27.9	13.819	0.054	13.016	0.063	12.564	0.106	19	17	18	3.87
275	03:29:30.62	+31:23:11.4	17.548	0.074	16.003	0.091	15.193	0.039	19	22	22	9.38
276	03:29:30.84	+31:23:53.1	12.808	0.034	11.729	0.031	11.182	0.022	22	23	24	4.30
278	03:29:31.54	+31:25:27.9	17.248	0.143	16.288	0.127	15.553	0.115	14	11	17	5.31
279	03:29:32.56	+31:24:37.1	13.445	0.143	12.304	0.190	11.574	0.083	05	05	06	7.05

Note. — The right ascension units are hours, minutes, and seconds. The declination units are degrees, arcminutes, and arcseconds. The list is sorted by FMO identification numbers.

^aFan Fountain Observatory NGC 1333 infrared sources ID number.

^bAverage magnitudes over the total period of the monitoring campaign of this study.

^cObserved RMS.

^dNumber of detection in each band.

^eVisual extinction derived from the K_s vs. $H-K_s$ color-magnitude diagram with 1 Myr isochrones (Baraffe et al. 1998; Chabrier et al. 2000; Baraffe et al. 2003) and the interstellar reddening information from Cohen et al. (1981) (see Figure 3.12). A_V might be somewhat overestimated (≤ 2 mag) owing to the K_s excess emission by the existence of disk component which we did not take into account here.

Table 3.3. *FanCam*-identified Variable Stars & Substellar Objects

FMO ^a	R.A. (J2000.0)	Dec. (J2000.0)	K_s^b	$\sigma_{K_s}^c$	Mass ^d [M_\odot]	Class ^e	X-ray ^f [cnts ks ⁻¹]	BD ^g	Stetson Index	Slope ^h [deg]
008	03:28:36.51	+31:19:28.9	11.810	0.022	0.11	...	0.9	...	6.399	2.48
011	03:28:38.75	+31:18:06.8	14.086	0.074	0.21	II	2.524	-8.49
012	03:28:39.68	+31:17:32.0	13.518	0.044	0.51	I	2.301	-0.38
014	03:28:41.55	+31:14:09.7	15.185	0.087	0.04	P	1.201	-11.23
023	03:28:44.07	+31:20:52.9	12.610	0.023	0.09	II	0.2	...	3.326	0.70
028	03:28:46.87	+31:20:27.7	13.855	0.021	0.04	P	0.951	-33.46
030	03:28:47.82	+31:16:55.1	10.926	0.051	0.39	II	0.8	...	10.015	-9.06
031	03:28:48.16	+31:19:23.5	14.564	0.029	0.03	P	0.194	-41.36
033	03:28:48.74	+31:16:08.8	15.028	0.071	0.06	I	...	P	1.281	20.26
039	03:28:51.05	+31:16:32.4	12.100	0.021	0.10	II	0.3	...	3.345	-46.02
040	03:28:51.09	+31:18:15.6	12.554	0.234	0.09	10.149	...
042	03:28:51.25	+31:17:39.4	14.991	0.184	0.03	I	...	P	2.056	...
044	03:28:52.13	+31:15:47.1	11.968	0.029	0.11	II	0.2	...	6.861	...
045	03:28:52.40	+31:15:26.4	12.075	0.021	0.08	2.561	-23.43
046	03:28:52.90	+31:16:26.5	12.493	0.033	0.08	II	...	W	4.685	-51.43
047	03:28:53.93	+31:18:09.2	11.140	0.121	0.55	II	1.0	...	3.753	-43.09
048	03:28:54.07	+31:16:54.3	11.638	0.021	0.14	II	0.2	W	2.169	-43.06
050	03:28:54.92	+31:15:29.0	14.204	0.037	0.04	II	...	S,P	1.681	-20.12
051	03:28:54.96	+31:18:15.3	13.141	0.025	0.13	2	1.306	8.18
052	03:28:55.05	+31:16:28.8	10.559	0.116	0.74	II	0.9	...	19.990	-53.75
055	03:28:55.13	+31:16:24.8	10.844	0.060	0.38	II	11.084	-54.88
128	03:28:56.05	+31:26:34.1	14.492	0.036	0.03	P	0.725	-31.62
060	03:28:56.22	+31:17:45.7	12.162	0.018	0.10	2.508	-34.87
130	03:28:56.30	+31:22:27.9	11.894	0.038	0.30	II	0.946	-6.56
065	03:28:56.86	+31:19:45.4	14.342	0.060	0.04	P	1.125	6.23
066	03:28:56.94	+31:20:48.8	13.866	0.026	0.05	II	...	W,S,P	0.548	-18.07
068	03:28:56.94	+31:16:22.3	10.910	0.218	0.45	II	0.8	...	21.984	-65.94
071	03:28:57.11	+31:19:12.0	15.289	0.093	0.02	I	...	S,P	1.495	-32.45
072	03:28:57.15	+31:15:34.6	13.179	0.018	0.08	II,2	...	W	1.314	-9.36
074	03:28:57.41	+31:19:50.6	10.648	0.020	0.30	...	0.9	...	2.933	-5.61
077	03:28:57.69	+31:19:48.2	11.349	0.026	0.19	II	6.7	...	0.787	-2.98
079	03:28:58.09	+31:18:03.8	11.336	0.016	0.15	...	1.3	...	5.104	1.63
135	03:28:58.24	+31:22:02.1	12.291	0.090	0.14	II	11.041	31.31
137	03:28:58.41	+31:22:17.6	12.707	0.206	0.65	I	0.2	...	12.022	-36.18
138	03:28:58.42	+31:22:56.7	13.592	0.026	0.05	II	...	W,S,P	0.390	-20.05
081	03:28:59.22	+31:20:33.0	14.969	0.191	0.03	P	1.800	-23.79
082	03:28:59.27	+31:15:48.4	10.734	0.312	1.98	II,2	14.3	...	9.237	-22.28
085	03:28:59.37	+31:20:08.6	15.248	0.154	0.08	I	2.517	...
087	03:29:00.14	+31:21:09.4	13.312	0.037	0.10	II	0.1	...	1.065	0.40
088	03:29:00.30	+31:13:38.3	11.347	0.034	0.17	...	7.5	W	13.371	-21.90
090	03:29:00.37	+31:20:45.8	11.807	0.019	0.13	...	0.3	W	1.198	-10.65
145	03:29:00.69	+31:22:00.8	11.735	0.024	0.41	...	1.1	...	1.033	-34.87

Table 3.3—Continued

FMO ^a	R.A. (J2000.0)	Dec. (J2000.0)	K_s^b	$\sigma_{K_s}^c$	Mass ^d [M_\odot]	Class ^e	X-ray ^f [cnts ks ⁻¹]	BD ^g	Stetson Index	Slope ^h [deg]
093	03:29:01.53	+31:20:20.8	10.448	0.153	...	I	7.539	-16.93
095	03:29:02.15	+31:16:11.4	13.566	0.020	0.04	II	0.6	W,P	0.264	-17.75
097	03:29:02.69	+31:19:05.6	13.626	0.058	0.11	II	2.820	-5.49
152	03:29:02.79	+31:22:17.3	13.397	0.069	0.10	II	1.880	-32.06
098	03:29:02.88	+31:16:00.9	11.905	0.011	0.10	...	2.3	W	0.477	-26.78
153	03:29:03.11	+31:22:38.2	11.829	0.226	0.26	II	0.2	...	42.716	-5.57
154	03:29:03.20	+31:25:45.1	13.898	0.057	0.05	II	...	P	1.032	-21.41
100	03:29:03.38	+31:18:40.0	13.864	0.029	0.05	II,2	...	W,S,P	1.102	-28.74
104	03:29:04.06	+31:17:07.5	12.300	0.017	0.09	...	0.5	...	0.665	-15.03
161	03:29:04.16	+31:25:15.0	10.902	0.029	0.43	...	1.0	...	3.419	-36.54
107	03:29:04.30	+31:19:06.4	15.666	0.181	0.01	P	4.211	...
108	03:29:04.62	+31:20:29.0	13.701	0.038	0.09	1.453	9.25
109	03:29:04.66	+31:16:59.1	12.501	0.131	0.14	II,2	12.763	...
110	03:29:04.94	+31:20:38.6	13.094	0.106	0.15	I	0.2	...	3.266	14.50
112	03:29:05.17	+31:20:37.4	13.998	0.226	0.07	P	2.932	-0.95
114	03:29:05.64	+31:20:10.8	15.176	0.086	0.03	II	...	S,P	1.859	-11.44
168	03:29:05.67	+31:21:33.8	13.290	0.067	0.18	II	4.283	17.93
116	03:29:05.86	+31:16:38.1	13.046	0.130	0.13	2	1.163	7.96
117	03:29:05.92	+31:16:40.1	12.440	0.083	0.21	2	2.1	...	1.135	-27.77
118	03:29:06.31	+31:13:46.1	12.644	0.038	0.47	II	1.719	-3.26
120	03:29:08.32	+31:20:20.4	11.997	0.021	0.16	6.935	-4.77
178	03:29:08.64	+31:22:29.6	14.373	0.061	0.05	P	1.418	-14.88
179	03:29:08.94	+31:22:56.2	11.742	0.215	0.54	I	20.535	55.27
180	03:29:08.97	+31:26:23.9	14.676	0.211	0.04	II	...	P	5.019	-63.70
182	03:29:09.03	+31:21:29.2	13.102	0.264	0.46	I	4.426	-15.47
183	03:29:09.07	+31:23:05.6	11.903	0.034	0.19	I	0.2	...	1.436	-39.96
184	03:29:09.15	+31:21:44.4	12.793	0.124	0.21	2.917	17.75
121	03:29:09.32	+31:21:04.3	13.125	0.079	0.10	II	...	S	2.342	1.33
187	03:29:09.48	+31:27:20.8	12.699	0.064	0.08	II	2.834	-23.27
190	03:29:10.18	+31:27:15.9	14.191	0.051	0.04	II	...	P	0.810	-34.03
192	03:29:10.45	+31:23:34.8	12.808	0.034	0.11	II	3.236	-50.16
194	03:29:10.78	+31:22:30.1	12.879	0.034	0.08	...	0.7	W,S	2.161	-36.78
122	03:29:10.81	+31:16:42.5	13.292	0.086	0.10	II,2	8.604	18.28
123	03:29:11.30	+31:17:17.5	12.834	0.029	0.07	...	3.8	W,P	3.298	-12.83
195	03:29:11.32	+31:22:57.0	12.543	0.040	0.12	II	4.326	-53.76
124	03:29:11.64	+31:20:37.5	12.694	0.039	0.11	II	2.464	-12.10
197	03:29:11.77	+31:26:09.5	14.960	0.116	0.03	II	...	P	2.344	-24.76
199	03:29:11.85	+31:21:55.8	13.753	0.242	0.12	2.705	...
200	03:29:11.86	+31:21:27.1	13.016	0.147	0.47	II	0.2	...	10.454	33.74
201	03:29:11.95	+31:21:24.3	15.872	0.339	0.02	P	3.862	...
202	03:29:12.03	+31:25:48.9	14.878	0.040	0.03	P	1.010	-32.62
204	03:29:12.37	+31:27:23.1	14.738	0.056	0.02	P	0.816	-20.38

Table 3.3—Continued

FMO ^a	R.A. (J2000.0)	Dec. (J2000.0)	K_s^b	$\sigma_{K_s}^c$	Mass ^d [M_\odot]	Class ^e	X-ray ^f [cnts ks ⁻¹]	BD ^g	Stetson Index	Slope ^h [deg]
125	03:29:12.41	+31:14:56.3	11.814	0.018	0.10	3.617	14.78
126	03:29:12.79	+31:20:07.9	13.314	0.039	0.06	...	0.2	W,P	2.235	-21.30
207	03:29:12.90	+31:23:29.3	12.061	0.035	0.11	II	5.618	-40.93
127	03:29:12.95	+31:18:14.5	13.961	0.091	...	I	4.2	...	5.342	...
212	03:29:14.42	+31:22:36.2	13.012	0.029	0.07	...	0.8	W,S,P	3.359	-43.73
213	03:29:15.60	+31:22:42.7	15.805	0.185	0.03	P	1.437	12.07
214	03:29:16.54	+31:21:02.5	12.429	0.021	0.12	2.300	-33.46
216	03:29:16.59	+31:23:49.4	11.183	0.044	0.26	II	3.3	...	16.402	-5.21
217	03:29:16.81	+31:23:25.2	13.679	0.057	0.05	II	...	W,P	5.316	1.04
218	03:29:17.50	+31:24:54.9	15.360	0.110	0.05	P	1.338	-4.61
223	03:29:18.65	+31:20:17.8	14.819	0.075	0.05	II	...	P	1.989	19.74
226	03:29:20.04	+31:24:07.6	12.235	0.100	1.04	II	0.8	...	5.276	-12.05
235	03:29:21.52	+31:25:12.9	11.685	0.014	0.14	2.386	-2.04
236	03:29:21.54	+31:21:10.5	11.404	0.017	0.14	II	1.9	...	2.891	-18.79
238	03:29:22.04	+31:24:15.3	10.982	0.017	0.19	...	2.2	...	2.918	-12.89
243	03:29:23.14	+31:20:30.4	11.235	0.058	0.17	II	0.1	...	24.859	-24.14
246	03:29:23.24	+31:26:53.2	12.182	0.027	0.10	II	...	W	3.672	-27.75
249	03:29:23.49	+31:23:31.0	11.351	0.020	0.16	...	17.8	...	4.356	-8.60
250	03:29:23.70	+31:25:09.6	12.295	0.017	0.10	...	0.4	W	1.788	-28.33
252	03:29:24.07	+31:19:57.7	13.650	0.035	0.05	II	...	W,P	2.089	-9.77
253	03:29:24.83	+31:24:06.3	13.348	0.018	0.05	...	0.3	W,P	0.679	-16.34
264	03:29:27.60	+31:21:10.0	13.076	0.017	0.07	P	-0.094	-21.29
273	03:29:29.77	+31:21:02.7	11.194	0.042	0.19	II	0.8	...	10.035	-46.10
276	03:29:30.84	+31:23:53.1	11.182	0.022	0.21	3.527	-5.87
278	03:29:31.54	+31:25:27.9	15.553	0.115	0.02	I	...	P	1.807	-20.65
279	03:29:32.56	+31:24:37.1	11.574	0.083	0.18	II	22.339	30.30

Note. — The right ascension units are hours, minutes, and seconds. The declination units are degrees, arcminutes, and arcseconds. The Table is sorted by R.A. and Dec. columns.

^aFan Fountain Observatory NGC 1333 infrared sources ID number.

^bAverage magnitude over the total period of observation.

^cObserved RMS.

^dMass derived from the K_s vs. $H-K_s$ color-magnitude diagram using 1 Myr isochrones (Baraffe et al. 1998; Chabrier et al. 2000; Baraffe et al. 2003) and the interstellar reddening law (Cohen et al. 1981) (§ 3.3.2).

^eYSO classification based on 2MASS near-IR and *Spitzer* mid-IR photometry (Gutermuth et al. 2008); The arabic numerals are for the Oasa et al. (2008) classification.

^f*Chandra* X-ray (0.5-8.0 keV band) count rate (Getman et al. 2002).

^gBrown dwarf candidates – W (Willing et al. 2004) and S (Scholz et al. 2009), studied with infrared spectroscopy; P, presented in this paper.

^hLinear regression best-fit slope of the variation on the K_s vs. $H-K_s$ color-magnitude diagram (§ 3.4.2).

Chapter 4

Preliminary Results of the Near-Infrared Variability Study in the Embedded Cluster NGC 7129

Article in preparation

Abstract

Preliminary results of long term near-infrared, J , H , and K_s , photometric monitoring of the embedded cluster NGC 7129 is presented in this Chapter. The data were obtained with *FanCam*, a near-infrared camera at Fan Mountain Observatory near Charlottesville, VA, from November 2005 to October 2007, including 31 epochs of observation. The Stetson variability index and reduced χ^2 methods are employed to identify variable objects. About 35% of the detected point sources, 166 out of 480, are variable, which rate is lower than NGC 1333 (55%) but still much higher than previ-

ous variability studies in other clusters (e.g., the Orion Nebula cluster, Chamaeleon I cluster, ρ Ophiuchi cluster). Color-magnitude and color-color diagrams demonstrate that the median age of the NGC 7129 member stars are older than NGC 1333. Light curves in all three bands are well correlated in general. No periodicities are evident. Based on color-magnitude variability trends, accretion-driven variability predominates over extinction-driven variability; $\sim 85\%$ (119 of 139) of the stars become bluer as they fade, showing negative slopes in the K_s vs. $H-K_s$ diagram. The spatial distribution of variable stars shows a strong correlation with the cavity of the neutral gas distribution (Matthews et al. 2003) while non-variable stars are evenly spread over the whole field of view. 35 out of 41 *Spitzer*-2MASS-identified IR excess YSOs (Gutermuth et al. 2004), 85%, are variable, including 1 Class 0, 5 Class I, 34 Class II, and 1 Class III stars. A total of 131 variable stars were not detected in the previous infrared excess source survey. The statistics of K_s vs. $H-K_s$ color-magnitude diagram slope shows more numbers of positive slopes than NGC 1333 but much less than Trapezium cluster or ρ Ophiuchi cluster.

4.1 Introduction

The embedded cluster NGC 7129 is featured by its kidney-shaped filamentary structure luminous at optical and near-infrared wavelengths. The reflective structure coincides with the cavity wall of a thick molecular cloud in the constellation Cepheus (Matthews et al. 2003; Ridge et al. 2003). The distance estimate to NGC 7129 ranges from 0.9 kpc to 1.25 kpc (e.g., Racine 1968; Shevchenko & Yakubov 1989; Ábrahám et al. 2000), but commonly 1 kpc has been adopted by many authors, same as in this study. Stelzer & Scholz (2009) confirmed the age of the NGC 7129 embedded cluster to be ~ 3 Myrs by interpreting their computation of disk fraction in the cluster. We chose this as the median age of the cluster members, although it is clear from the presence of protostellar objects reported by Gutermuth et al. (2004) and other studies that there are much younger stars present in this region.

The monitoring campaign for NGC 7129 embedded cluster was performed in parallel with NGC 1333 at the same period and with the same strategy. The important data reduction part has been done but the analysis and interpretation parts are on the progress by the time of this thesis prepared. I present my current results and work status of this program in the remaining sections of this Chapter.

4.2 Data

All data were obtained with *FanCam*, a near-infrared camera based on a 1024×1024 Teledyne Imaging Sensors (formerly Rockwell Scientific) HAWAII-1 $2.5\text{-}\mu\text{m}$ cutoff HgCdTe array. The camera features $8.7' \times 8.7'$ field of view and $0.51''\text{pixel}^{-1}$ plate scale. The average system gain and the read noise are measured to be $4.6 e^- \text{ADU}^{-1}$ and $17 e^- \text{rms}$. Typical flux limits for a point source detection in 10σ 15 minutes

integration time are 61, 98, and 160 μJy (or, 18.5, 17.5, and 16.5 mag) in J , H , and K_s bands, respectively. The detailed description of the instrument is provided by Kanneganti et al. (2009). *FanCam* is operated by the University of Virginia on the 31-inch Tinsley reflector telescope at Fan Mountain Observatory.

4.2.1 Observations

Observations of NGC 7129 were conducted from November 11, 2005 through August 12, 2007. The observed field is centered at R.A. (J2000.0) = $21^h42^m58^s$ and Dec. (J2000.0) = $+66^\circ06'35''$. The stacked *FanCam* image of NGC 7129 is shown in Figure 4.1. Each night's observation consisted of 15 minutes of on-source integration in each of the two fields divided into individual 30 or 60 second exposures. Flat field observations consisted of exposures on twilight sky. Flats were obtained either at dusk or dawn every observing night when conditions permitted. Median filtered spatially dithered observations of a field approximately $30'$ from the cluster provided sky images for background subtraction. These reference fields are free from nebulosity and bright sources. Five minutes of sky data were collected between each set of integrations on the cluster in order to minimize the time between source and sky observation. Most of the sky frames were taken within 10 minutes of object observation. Dithering on target permitted the replacement of bad pixels with good data. The frame to frame dither was $\sim 20''$, several times the FWHM. In total, 31 night's data were obtained but I decided to exclude one epoch (January 8, 2006) because of temporal instrumental instability. Table 4.1 provides the observation log of NGC 7129.

4.2.2 Data Reduction

For each night the J -, H -, and K_s -band images were reduced independently by band with a series of standard Image Reduction and Analysis Facility (IRAF) procedures (e.g., McLean 1997). Five 60 sec or ten 30 sec dithered sky images were median-combined to establish a single master sky background frame. We then subtracted this sky background from each object image, which corrects non-uniform background level and fringe patterns generated by airglow emission through the optics system. The sky-subtracted object images were then divided by the normalized flat image. The master flat image was made by combining eight twilight flat frames, and subtracting a master dark image to cancel out the dark current component, although it is only a few counts, compared with typical 6000 counts of sky background at H and K_s bands and 1000 counts at J band. *FanCam* saturation is $\sim 30,000$ ADU. A single master image was produced for each J , H , and K_s band per night, by combining 15 or 30 object frames with “average” as the type of combine operation. Dithered images were shifted into a reference frame using interpolation type “drizzle”, formally known as Variable-Pixel Linear Reconstruction algorithm (Fruchter & Hook 2002), with the pixel fraction parameter [0.5] for both of x and y directions. If pixels are undersampled, drizzle works to improve the image resolution via combining multiple dithered images. For *FanCam* images, which are well sampled, drizzle just maintains spatial resolution while shifting an image. Outlying pixels were rejected from the image combine using the sigma clipping algorithm with 3σ lower and upper limits. One or two of the worst images, for example due to bad tracking, were excluded from the stacking procedure.

Photometric magnitudes and uncertainties were extracted with Point Spread Function (PSF) photometry in the IRAF/DAOPHOT package. The photometric system

of *FanCam* is almost identical with 2MASS system, which is based on the calibrated spectrum of Vega (Cohen et al. 1992). Zero magnitude fluxes of the 2MASS J , H , and K_s bands are 1594 ± 27.8 , 1024 ± 20.0 , and 666.7 ± 12.6 Jy, respectively (Cohen et al. 2003). We use 2MASS magnitudes of non-variable stars to perform the instrumental zero-point correction for *FanCam* photometry. The source match radius $1.0''$ was used. Figure 4.2 shows the differences between *FanCam* and 2MASS magnitudes. Dispersion in these plots most likely arises from photometric variability. However, the broader faint-end dispersions originate from 2MASS uncertainties since the 2MASS data reaches its limiting magnitude ~ 2 mag earlier than *FanCam*. Stars between 11 mag and 15 mag are used for the calibration. The bright end of this range avoids saturation in the *FanCam* data while the faint end avoids significant uncertainty in the 2MASS magnitudes. All nights were referenced, photometrically, to a single epoch – 2005 November 12.

4.2.3 Point Source List

This *FanCam* data set was obtained in various observing conditions, different seeing and different sky background level. Typical seeing disk sizes span from $1.2''$ to $2.5''$. Most of the data were observed during winter season which provides lowest near-infrared thermal background. The limiting magnitudes of a typical night were estimated at 18.7, 17.1, and 16.3 mag at 10σ detection level for J , H , and K_s bands, respectively (Figure 4.3). At the 10σ level or above, a total of 627 point sources were extracted at J , H , or K_s from the reference master images. 147 of these sources were subsequently removed as they proved to be filter glints, persistence, extragalactic extended sources, unresolved double stars, etc. Some bright sources were also excluded because they are close to the saturation limit of the camera system. Table 4.2 gives

the photometric properties of the final 480 objects, brighter than the defined 10σ limiting magnitudes in at least one band. The magnitudes in the table are the mean values of all the observed epochs for each source. The RMS of the ensemble measurements are listed in the neighboring columns – in many cases inflated by source variability.

4.2.4 Photometric Integrity

The observed RMS in our time-series photometry was derived from the individual magnitudes (m_i) and photometric uncertainties (σ_i) with the same of Equation 3.1. The photometric uncertainty of an individual star originates from random fluctuations due to the photon statistics of the sky, which dominates to the read-noise of the detector. We estimate the empirical signal-to-noise ratio of the photometry using the computed observed RMS. Figure 4.4 shows the distribution of the observed RMS as a function of magnitude. The individual outstanding points above the main body of the distribution are due to intrinsic variability. The observed RMS values range from a minimum of ~ 0.015 mag for bright stars, dominated by photometric systematics, to ~ 0.10 for stars near the sensitivity limits described above. The observed RMS floor of 0.015 mag for bright stars is interpreted as the minimum photometric repeatability for our data set, and consequently a minimum photometric uncertainty of 0.015 mag has been imposed on all of the photometric measurements.

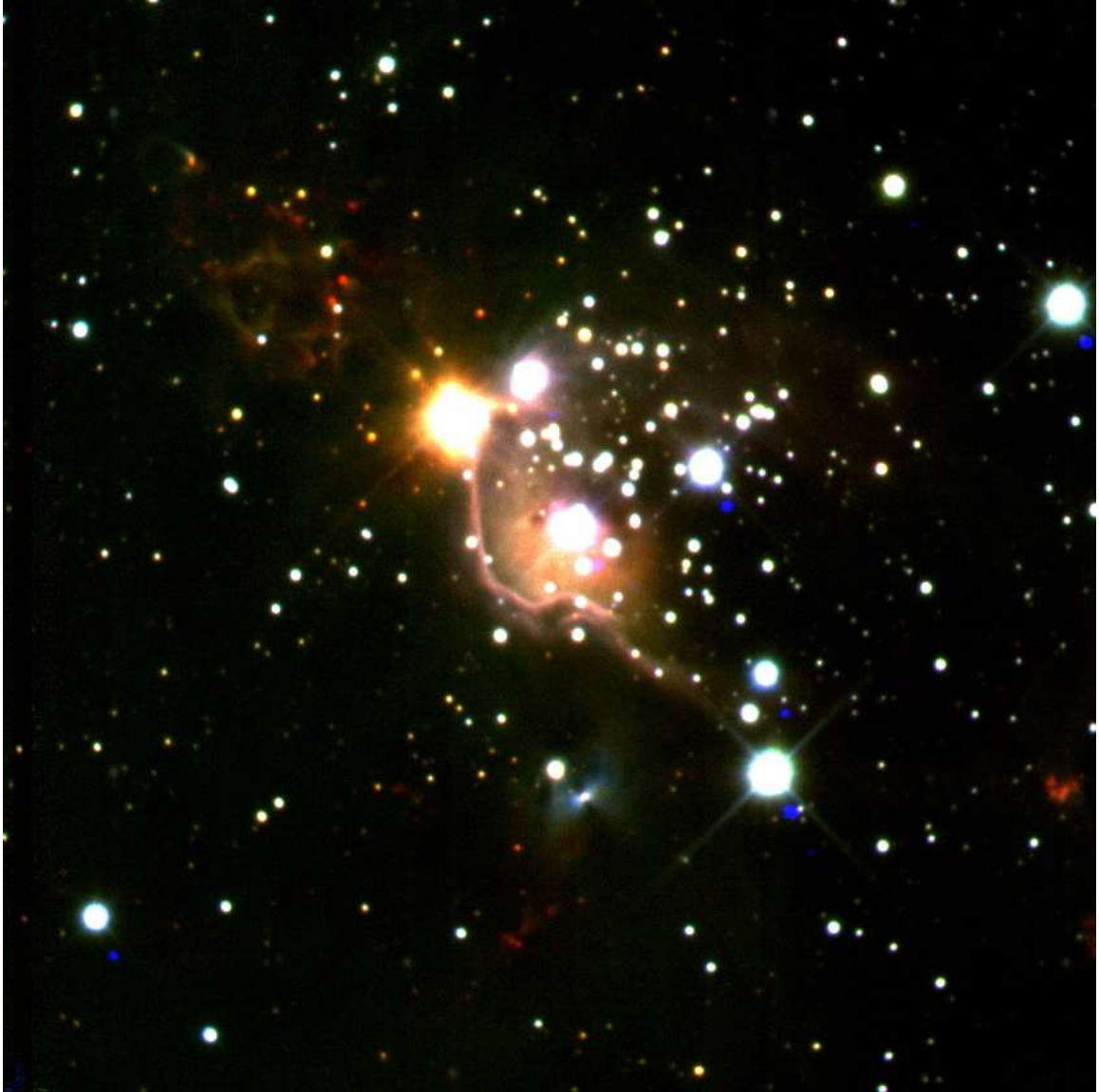


Fig. 4.1.— Color-mosaic image of the embedded cluster NGC 7129, composed of *FanCam J*, *H*, and *K_s* – blue, green, and red colors were assigned respectively. The total integration time is ~ 2.5 hours in each band. Coordinates of the central point are R.A.(J2000.0)= $21^h 42^m 58^s$ and Dec.(J2000.0)= $+66^\circ 06' 35''$. The array plate scale is $0.51''\text{pixel}^{-1}$. The sky seeing spans from $1.2''$ to $2.5''$.

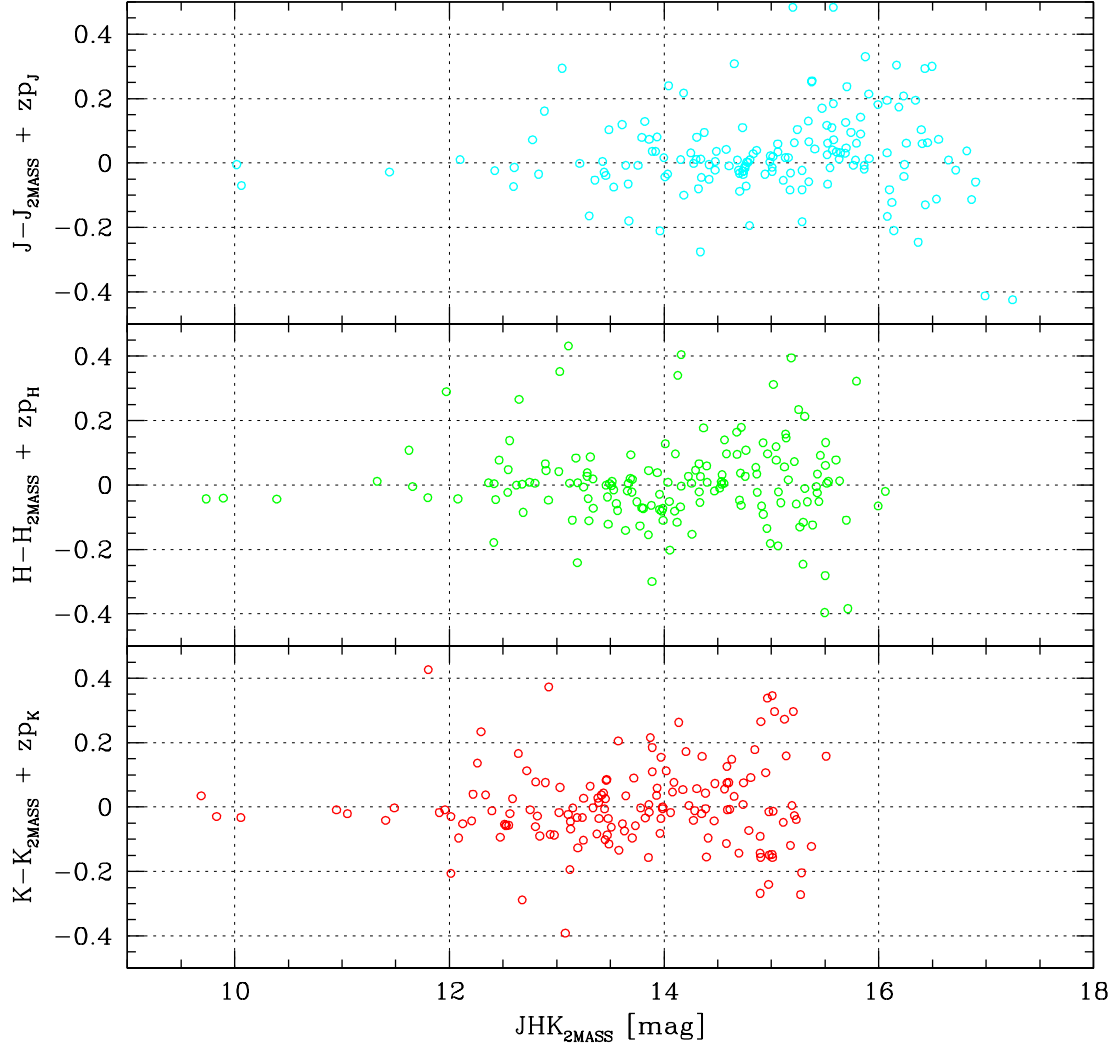


Fig. 4.2.— Magnitude differences between 2MASS and *FanCam* PSF photometry NGC 7129. Instead of observing independent standard stars, a statistical method with 2MASS point-source catalog was used to determine the instrumental offsets of each filter system. General dispersions likely come from stellar variability itself. The broader faint-end scatterings originate from 2MASS magnitude uncertainties near its survey sensitivity limits.

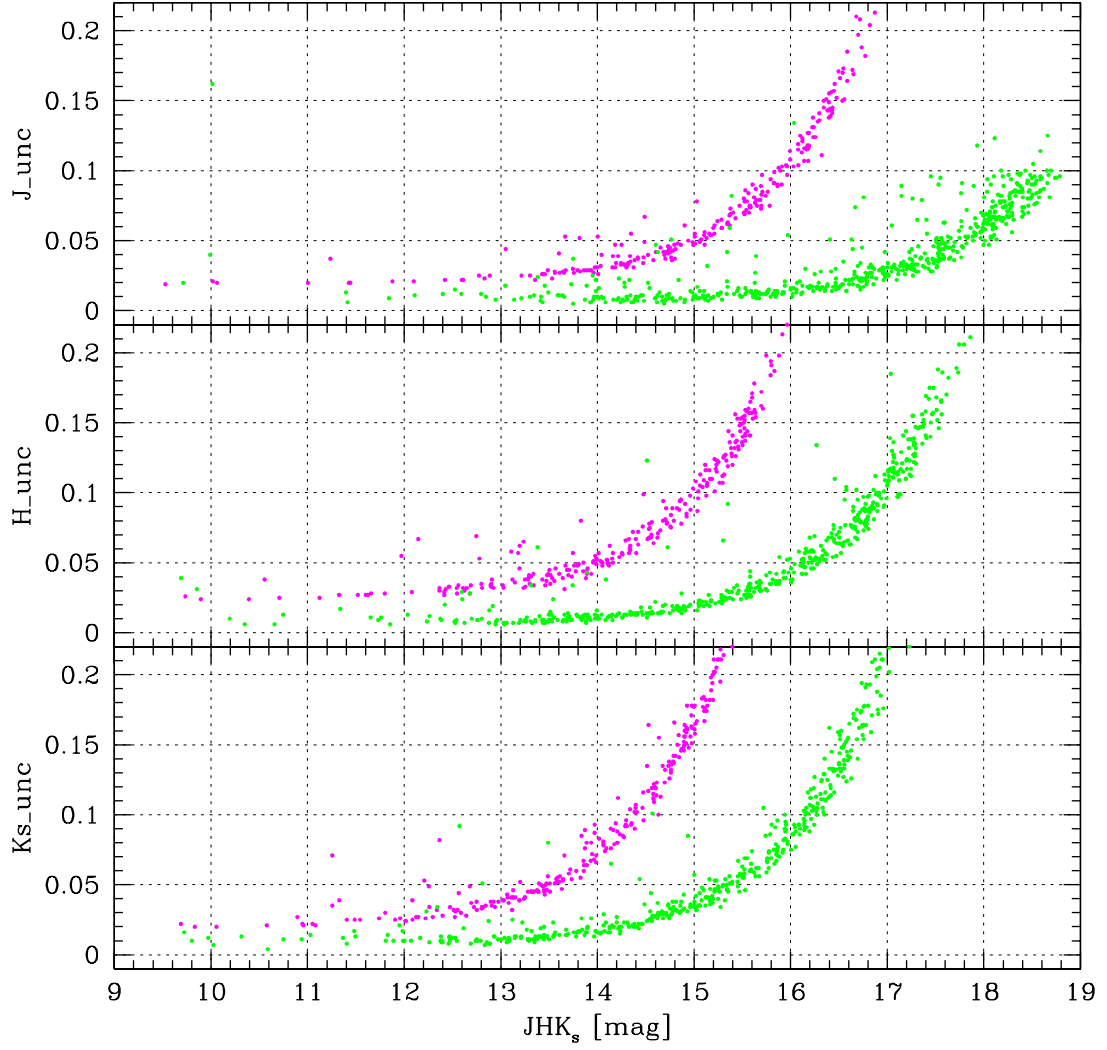


Fig. 4.3.— Photometric uncertainty; *FanCam* NGC 7129 (lower) and 2MASS archive (upper) for comparison. *FanCam* photometry in this study reaches up to 18.7, 17.1, and 16.3 mag for J , H , and K_s , respectively with signal-to-noise ratio 10, which is ~ 2 mag deeper than 2MASS survey.

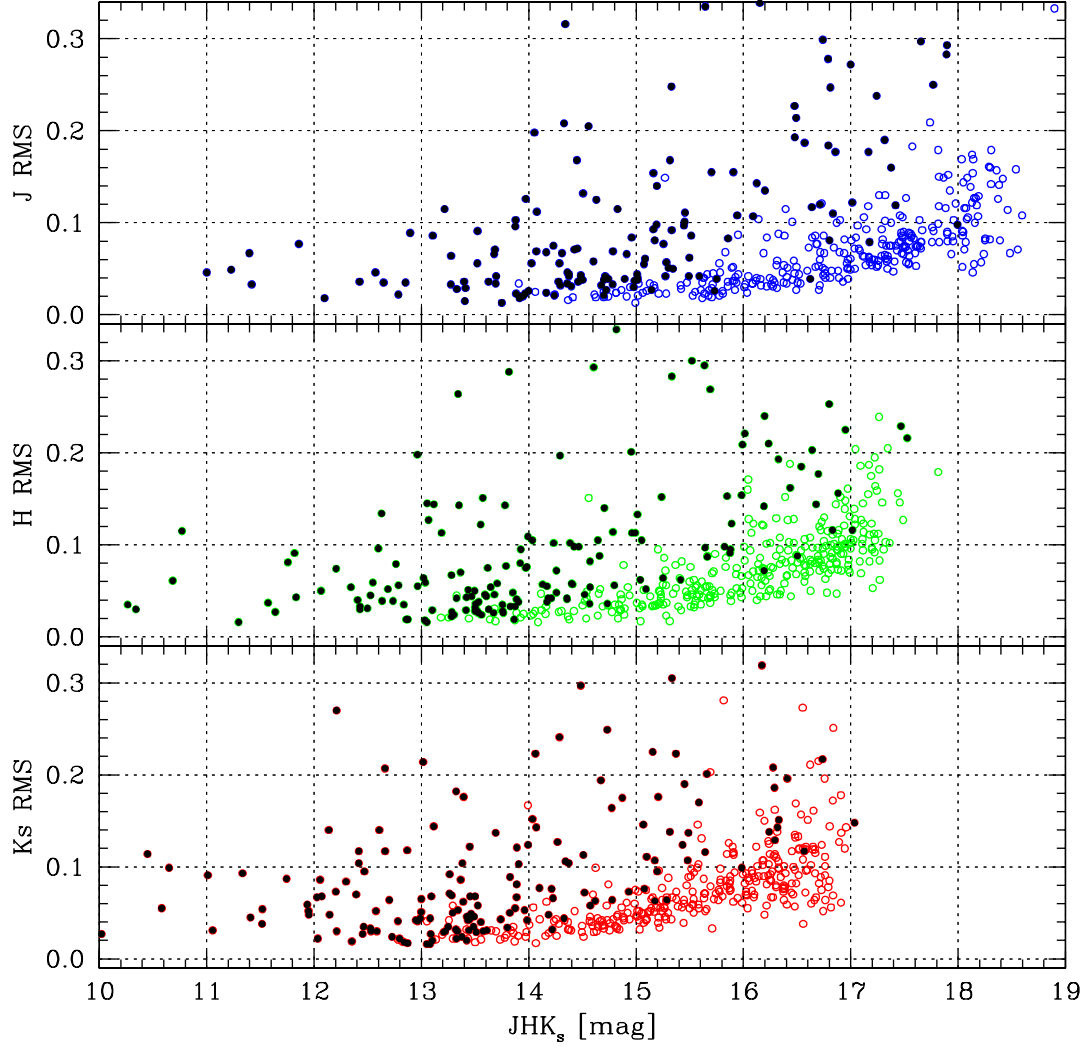


Fig. 4.4.— Observed photometric RMS for variables (solid) and non-variables (open). RMS of the ensemble measurements was computed to estimate the signal-to-noise ratio in our photometry. The observed RMS ranges from ~ 0.015 mag for bright stars to ~ 0.10 for stars near the sensitivity limits of this study. The values correspond to SNRs of ~ 70 and ~ 10 , respectively. We interpret the RMS bottomline 0.015 mag as the photometric repeatability of our data set.

4.3 Results

4.3.1 Identification of Variable Stars

Following the arguments in Carpenter et al. (2001), we use the Stetson variability index (Stetson 1996), S , as the primary statistical tool for variable source selection. Since the Stetson statistic correlates photometric fluctuation in multiband photometry, it has two major advantages over simple RMS-based methods. First, the Stetson statistic will mitigate the significance of a single-band outlying measurement. Second, it multiplies the common-mode signal between bands enhancing the detectability of low-amplitude variables. For each star the index, S , was computed with the same methods as § 3.3. Figure 4.5 presents the Stetson variability index, S , for all the stars in the point-source list as a function of H magnitude. Non-variable stars will scatter symmetrically around zero, while true physical variables show some positive offset depending on their degree of variability. Table 4.3 summarizes the properties of each variable star in the NGC 7129 region.

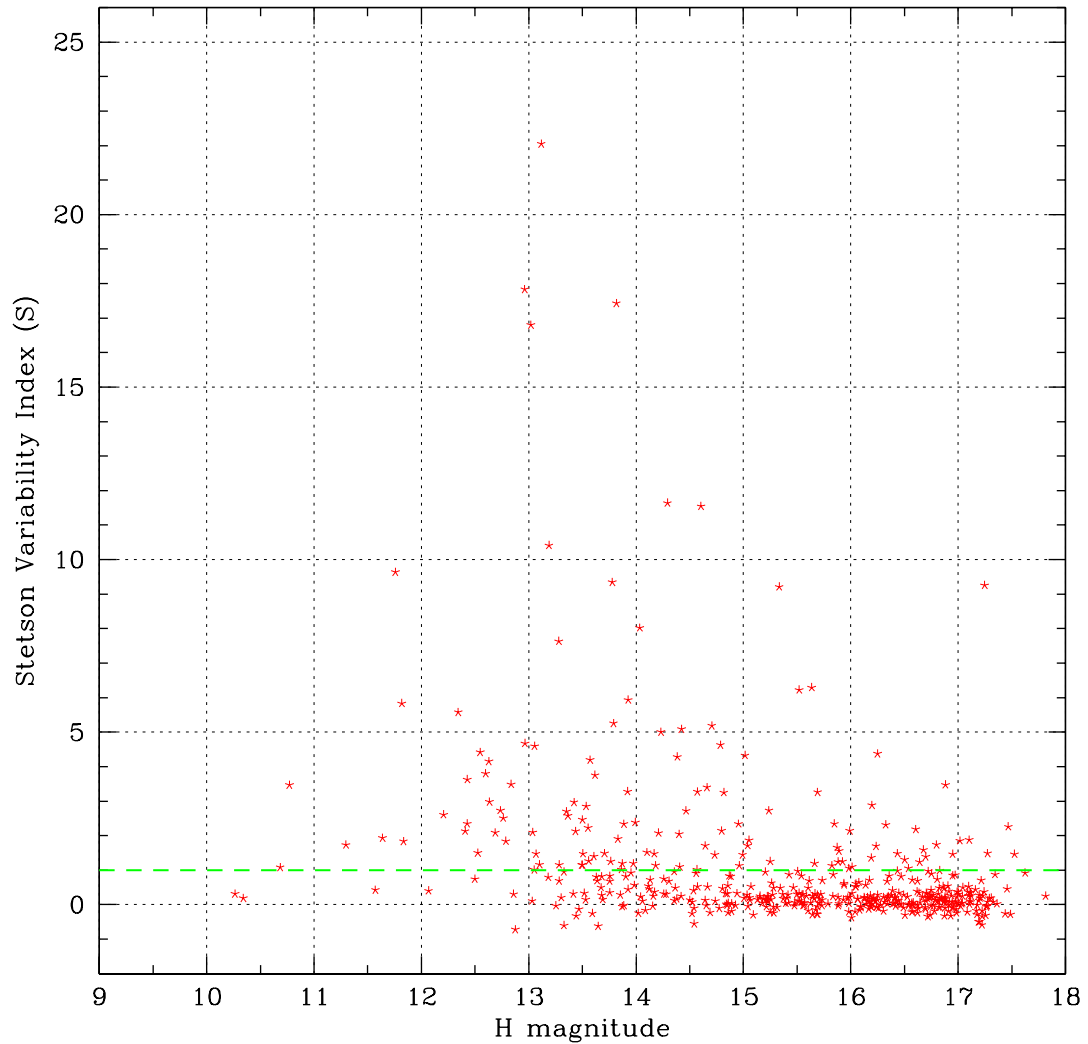


Fig. 4.5.— Stetson variability index (Stetson 1996) of NGC 7129 point sources. Non-variable stars tend to scatter around the parallel zero line symmetrically while true variables show some positive offsets. We identify a point source with $S \geq 1$ as a variable star.

4.3.2 Mean Colors and Magnitudes

The average colors and magnitudes of the variable and non-variable stars are displayed in a color-magnitude diagram (Figure 4.6) and a color-color diagram (Figure 4.7). These diagrams provide insight into the mass and age of the observed cluster and its members. In the K_s vs. $H-K_s$ color-magnitude diagram, the filled circles and the star symbols represent 166 variable and 314 non-variable stars, respectively. Small solid squares on the left hand side represent a mid-age open cluster NGC 2420. It is ~ 2 Gyr old and visual extinction is less than 0.02 mag, therefore we plot it for a reference distribution of an unreddened ZAMS (Lee et al. 1999).

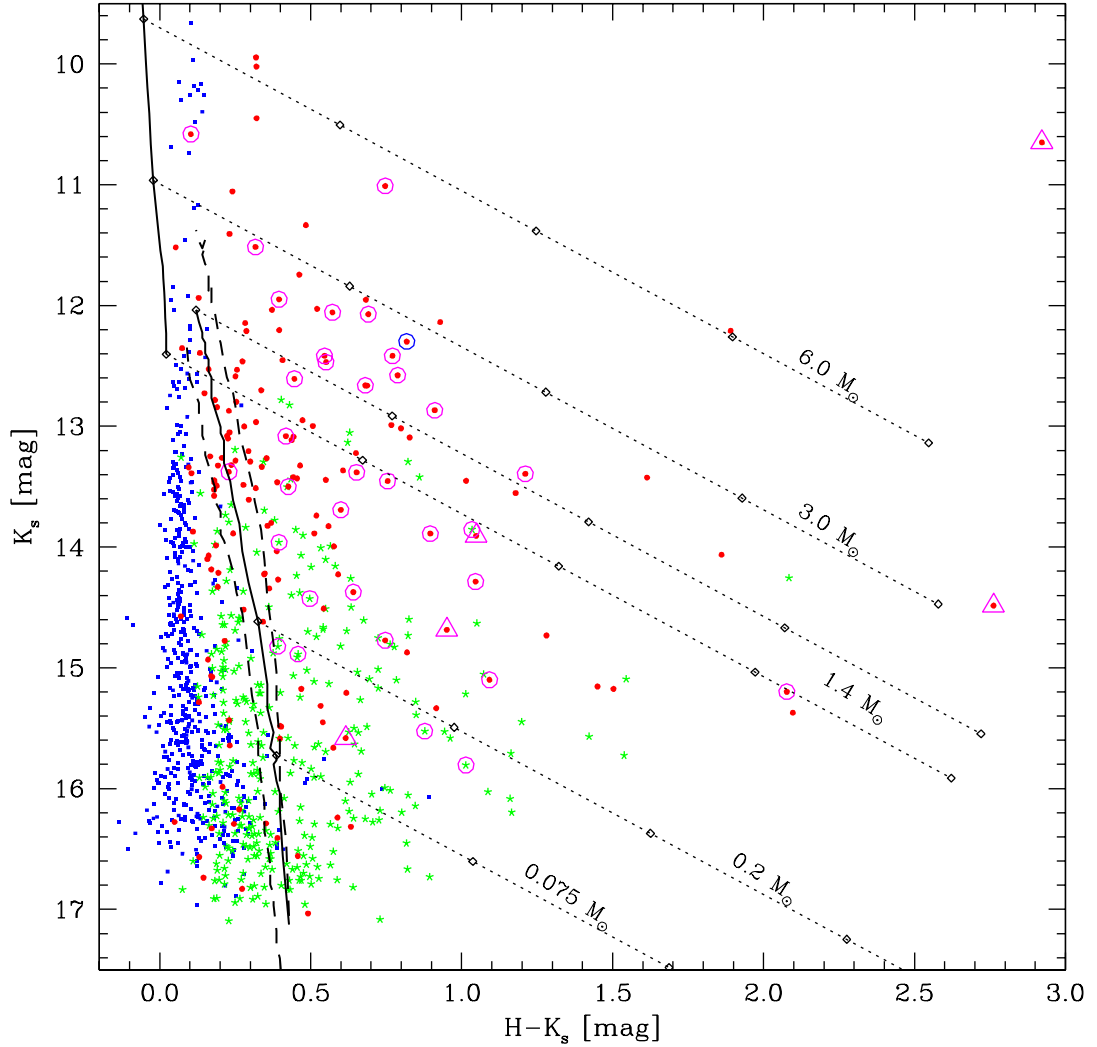


Fig. 4.6.— K_s vs. $H-K_s$ color-magnitude diagram for all point sources; 166 variable stars with small filled circles and 314 non-variables with asterisks. Infrared excess sources (Gutermuth et al. 2004) 5 Class I (triangles) and 34 Class II (open circles) YSOs are marked over. The lower solid line is 3 Myr isochrone of the NextGen model (Baraffe et al. 1998) covering mass from $0.03 M_\odot$ to $1.4 M_\odot$, the upper solid line is 3 Myr isochrone of the Padova group (Marigo et al. 2008) covering mass from $1.4 M_\odot$ to $7 M_\odot$. The upper dashed line is 1 Myr isochrone of the NextGen model covering mass from $0.03 M_\odot$ to $1.4 M_\odot$, the lower dashed line is 10 Myr isochrone of the same model and same mass coverage. The dotted diagonal lines represent the direction and magnitude of the reddening vector (Cohen et al. 1981); the slope is 1.35. The rhombi along the reddening lines are marked for the visual extinction A_V of 10 interval.

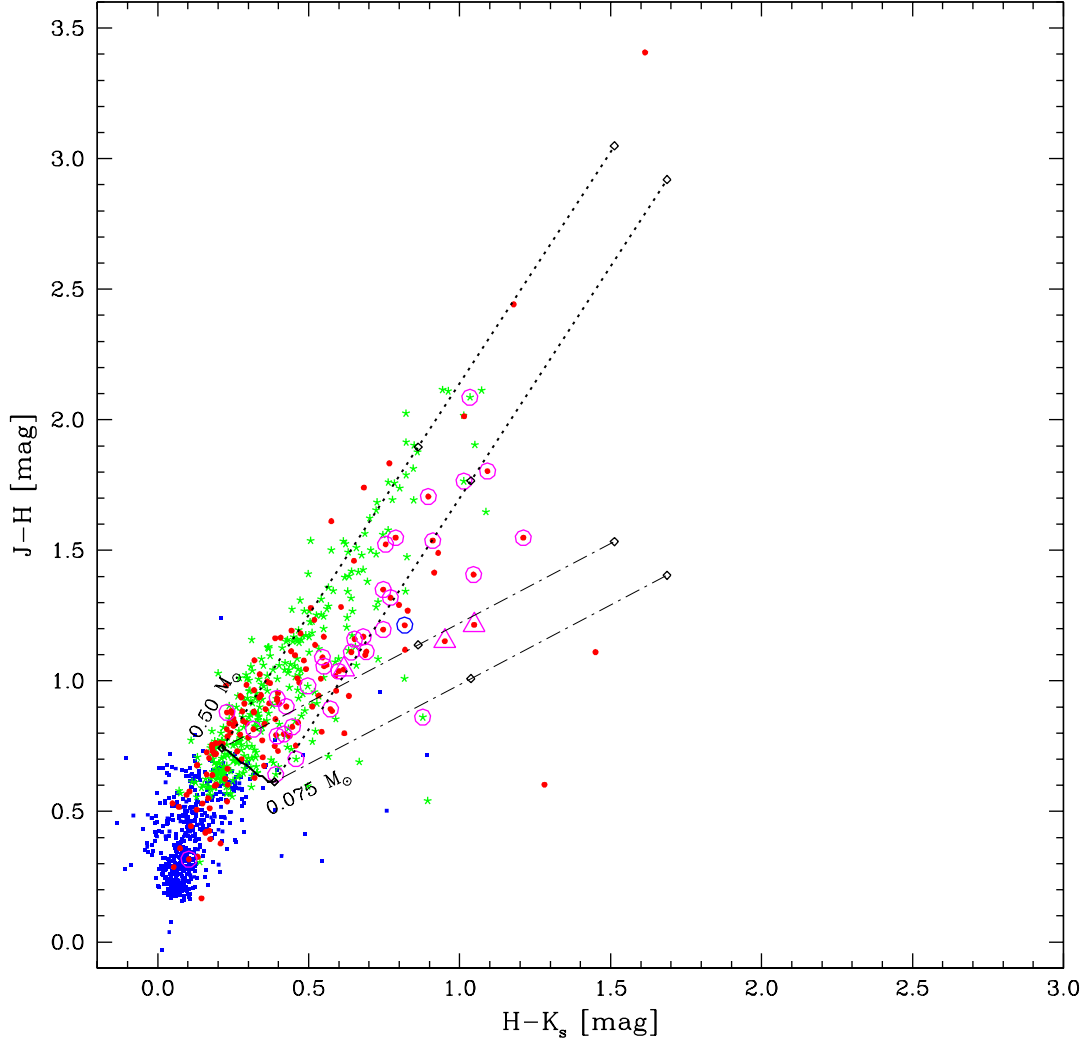


Fig. 4.7.— $J-H$ vs. $H-K_s$ color-color diagram for all point sources; 166 variable stars with small filled circles and 314 non-variables with asterisks. Infrared excess sources (Gutermuth et al. 2004) 5 Class I (triangles) and 34 Class II (open circles) YSOs are marked over. Several variable sources are unseen in the C-C diagram due to their unmeasured J band brightness. The lower left corner solid line is 3 Myr isochrone of the NextGen model (Baraffe et al. 1998) covering mass from $0.075 M_{\odot}$ to $0.5 M_{\odot}$. The dotted diagonal lines represent the direction and magnitude of the reddening vector (Cohen et al. 1981); the slope is 1.35. The rhombi along the reddening lines are marked for the visual extinction A_V of 10 interval.

4.3.3 Light Curves and Color Variations

Figure 4.8 shows J -, H -, and K_s -band time-series photometry for star 366, one of the 166 variable stars identified in this study. Gutermuth et al. (2004) classified this star as a Class II YSO. The abscissa represents the elapsed time since the first day of this monitoring campaign (2005 Nov 11 UT, or, JD 2453685.5). We assumed all the observations of each night were done at midnight local time, allowing ± 0.15 days uncertainty. The full x-axis data (639 days) will be available in the electronic form of this paper, while we use in this figure only first 4 months for the sake of clarity. The plots show non-periodic fluctuations that are well correlated in all three bands. The J and H plots are better correlated with each other than with the K_s light curve, which is consistent with the view that the origin of K_s -band variability is more sensitive to accretion luminosity than the J and H bands. Figure 4.9 shows another example of JHK_s light curves. The object FMO 270 is classified as a Class II YSO and a variable point source. We do not see any characteristic difference between light curves of Class I and Class II pre-main-sequence objects.

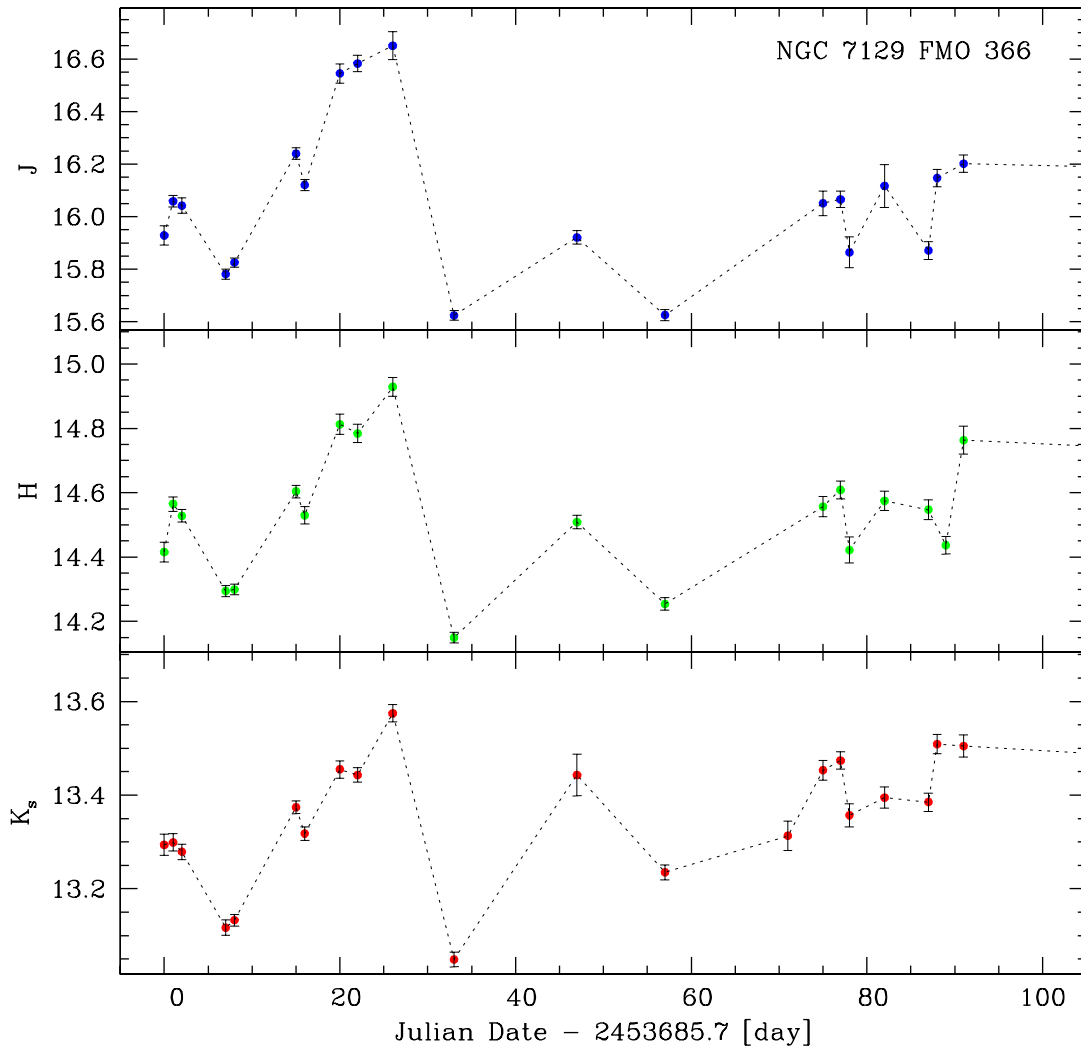


Fig. 4.8.— Example of J , H , and K_s light curves of a Class II pre-main-sequence star; FMO 366 in NGC 7129. Fluctuations are apparently non-periodic but well correlated in all three bands.

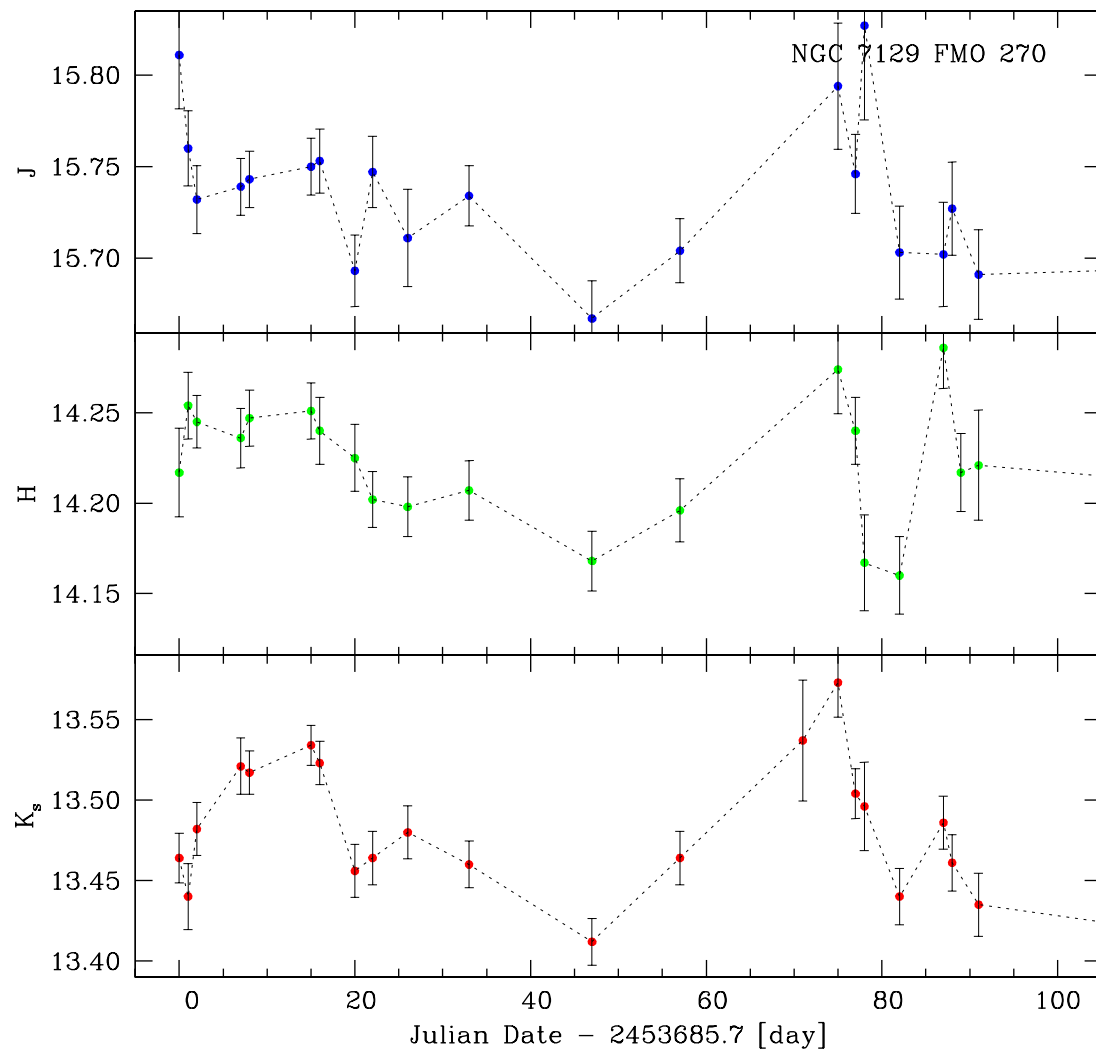


Fig. 4.9.— Example of J , H , and K_s light curves of a Class II pre-main-sequence object; FMO 270 in NGC 7129. Fluctuations are apparently non-periodic but well correlated in all three bands.

NGC 7129 FMO 366

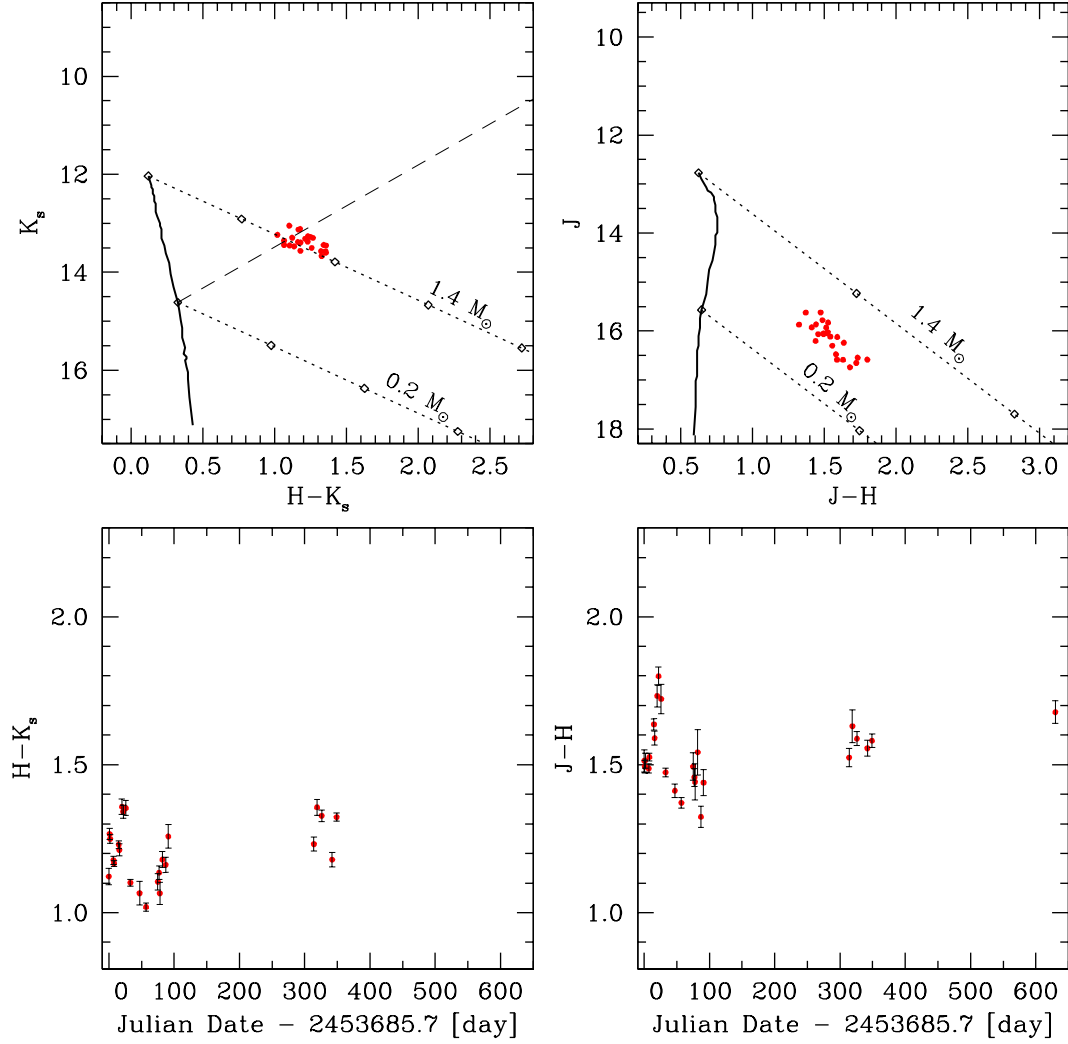


Fig. 4.10.— Color variability of a Class II pre-main-sequence star; FMO 366 in NGC 7129. The upper panels are color-magnitude correlations between K_s vs. $H-K_s$ and J vs. $J-H$. The lowers are time-variations of $H-K_s$ and $J-H$ colors. The K_s vs. $H-K_s$ color-magnitude diagram shows a positive linear-regression slope, or the color becomes redder as the K_s gets fainter, which is consistent with extinction dominant variability. The isochrones in the color-magnitude diagrams are for 3 Myr tracks from Baraffe et al. (1998).

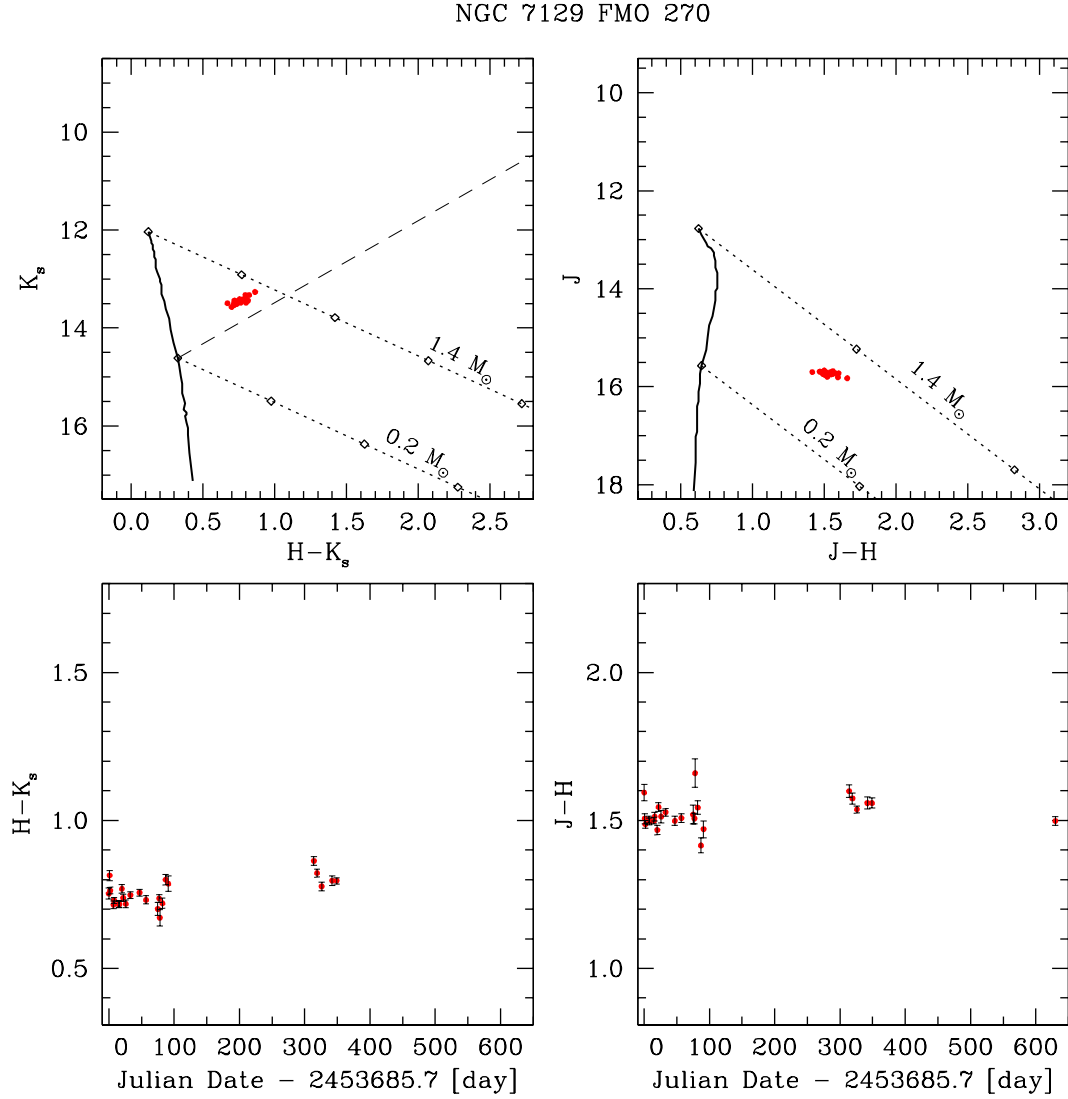


Fig. 4.11.— Color variability of a Class II pre-main-sequence star; FMO 270 in NGC 7129. Each panel represents the same as Figure 4.10. It is an example of a star that becomes redder when it lights up, producing a negative slope in K_s vs. $H-K_s$ relation. The dashed line represents the Classical T Tauri star locus (Meyer et al. 1997), characteristic of disk activity in pre-main-sequence stars.

4.4 Discussion

Using a similar approach as performed in Chapter 3, we investigated a plot of K_s vs. $H-K_s$ for each variable star and produced a histogram of the slope statistics of the linear-regression fit in Figure 4.12. Seven of the 166 variable sources are excluded from the statistics due to high uncertainty in their gradient and missing photometric data (no H band measured). 119 variable stars in NGC 7129 have slope angles $-90^\circ < \theta < -10^\circ$, 20 variable stars have angles $10^\circ < \theta < 90^\circ$, and the remaining 20 have angles $-10^\circ < \theta < 10^\circ$ (colorless variability).

The definition of slope angle follows from Carpenter et al. (2001) and Alves de Oliveira & Casali (2008). The slope of an individual star can be useful for distinguishing the various mechanisms causing photometric variability of the source since different physics result in different trends of color-magnitude correlation (cf. § 3.4.1). Furthermore, the slope statistics of an entire cluster might be meaningful to get an overview of its evolutionary stage since the dominance of each variability mechanism may change with the age of a star-forming cluster. Unlike the NGC 1333 slope histogram, NGC 7129 shows a good possibility of bimodal distribution in its K_s vs. $H-K_s$ histogram (See Figure 3.21). It is more like the previously studied clusters of ρ Ophiuchi (Alves de Oliveira & Casali 2008) and Trapezium (Carpenter et al. 2001), although it is tantalizing yet. A larger sample of embedded cluster variable slope statistics will provide a more definitive correlation between the cluster evolutionary stage and the mode of the histogram distribution.

While some possibility to find brown dwarfs in NGC 7129 exists, the fraction of the substellar objects is much lower than NGC 1333, most likely due to the cluster's larger distance and older age. A dozen of faint variable sources are located under the hydrogen burning limit in the color-magnitude diagram (Figure 4.6). It will be

worthwhile to do further investigation with spectroscopic studies on those possible substellar objects.

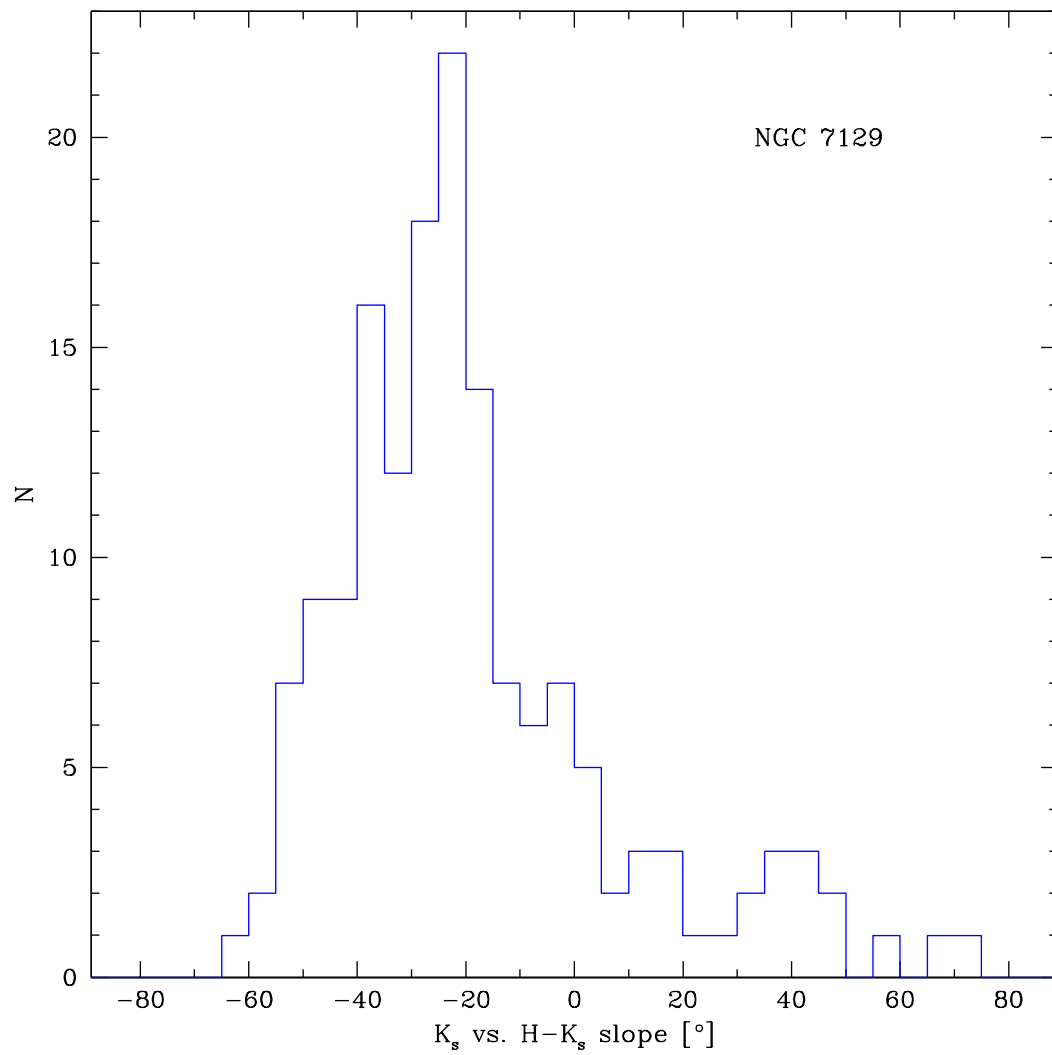


Fig. 4.12.— Histograms of the slopes derived from the K_s vs. $H-K_s$ diagrams in NGC 7129.

Table 4.1. Log of Observations of NGC 7129

UT Date	<i>J</i>	<i>H</i>	<i>K_s</i>	JD−2453685.7 ^a
2005 Nov 11	X	X	X	0
2005 Nov 12	X	X	X	1
2005 Nov 13	X	X	X	2
2005 Nov 18	X	X	X	7
2005 Nov 19	X	X	X	8
2005 Nov 26	X	X	X	15
2005 Nov 27	X	X	X	16
2005 Dec 01	X	X	X	20
2005 Dec 03	X	X	X	22
2005 Dec 07	X	X	X	26
2005 Dec 14	X	X	X	33
2005 Dec 28	X	X	X	47
2006 Jan 07	X	X	X	57
2006 Jan 08	X	X	X	58
2006 Jan 21	X	71
2006 Jan 25	X	X	X	75
2006 Jan 27	X	X	X	77
2006 Jan 28	X	X	X	78
2006 Feb 01	X	X	X	82
2006 Feb 06	X	X	X	87
2006 Feb 07	X	...	X	88
2006 Feb 08	...	X	...	89
2006 Feb 10	X	X	X	91
2006 Sep 21	X	X	X	314
2006 Sep 26	X	X	X	319
2006 Sep 28	X	321
2006 Oct 03	X	X	X	326
2006 Oct 19	X	X	X	342
2006 Oct 26	X	X	X	349
2007 Aug 03	X	X	...	630
2007 Aug 12	X	639
Total Obs #	27	27	29	

^aThe Julian Date for 2005 November 11 05:00:00.0 UT is 2453685.70833.

Table 4.2. Point-Source List of NGC 7129

FMO ^a	R.A. (J2000.0)	Dec. (J2000.0)	J^b	σ_J^c	H^b	σ_H^c	K_s^b	$\sigma_{K_s}^c$	J	N_{obs}^d H	K_s	Stetson Index
030	21:42:14.59	+66:06:31.4	15.891	0.051	15.279	0.056	15.154	0.067	12	09	07	0.48
033	21:42:14.83	+66:07:13.0	14.461	0.036	13.706	0.058	13.526	0.058	13	09	08	1.48
035	21:42:15.06	+66:10:08.4	15.751	0.039	14.992	0.113	14.777	0.064	10	09	04	1.44
038	21:42:15.63	+66:06:40.7	16.703	0.027	16.048	0.067	15.816	0.281	07	08	05	0.51
042	21:42:15.92	+66:06:39.8	16.843	0.073	16.216	0.101	16.040	0.055	08	10	04	0.18
044	21:42:16.04	+66:05:04.1	16.762	0.049	16.093	0.123	15.785	0.098	18	13	10	-0.07
048	21:42:16.75	+66:08:49.3	17.288	0.093	16.720	0.116	16.492	0.082	12	08	04	0.96
049	21:42:16.91	+66:08:12.8	13.999	0.026	13.436	0.051	13.340	0.053	21	17	17	2.12
051	21:42:17.24	+66:03:23.9	15.926	0.041	15.371	0.053	15.242	0.077	21	19	18	0.17
052	21:42:17.44	+66:08:46.5	15.935	0.035	15.248	0.057	14.986	0.060	21	19	17	-0.22
053	21:42:17.52	+66:10:04.3	15.783	0.046	14.883	0.078	14.623	0.099	20	20	17	0.81
054	21:42:17.68	+66:08:40.5	16.716	0.364	15.520	0.300	14.773	0.164	19	20	19	6.22
055	21:42:17.75	+66:09:14.0	14.676	0.032	14.258	0.048	14.100	0.077	21	20	19	0.31
056	21:42:17.80	+66:03:47.2	17.651	0.079	16.771	0.099	16.450	0.082	15	11	08	-0.02
057	21:42:17.86	+66:04:45.2	17.287	0.064	16.504	0.081	16.231	0.128	15	17	09	-0.30
058	21:42:18.17	+66:09:32.1	15.014	0.038	14.130	0.057	13.887	0.067	22	21	20	0.71
064	21:42:18.70	+66:05:42.3	14.278	0.036	13.680	0.046	13.491	0.046	24	24	22	0.26
065	21:42:18.92	+66:02:03.5	15.161	0.093	14.644	0.105	14.574	0.058	08	07	07	1.70
066	21:42:19.01	+66:06:48.5	16.404	0.041	15.477	0.045	15.142	0.065	22	25	21	0.06
067	21:42:19.06	+66:10:06.0	17.127	0.063	16.250	0.102	15.918	0.094	20	20	16	0.13
068	21:42:19.07	+66:06:44.4	17.601	0.067	16.954	0.098	16.757	99.000	14	13	03	-0.07
069	21:42:19.07	+66:05:29.7	14.782	0.033	14.356	0.042	14.185	0.048	25	25	23	0.11
070	21:42:19.35	+66:07:07.5	17.085	0.070	16.393	0.081	16.098	0.067	23	18	16	0.03
072	21:42:19.47	+66:03:18.8	17.758	0.079	16.976	0.078	16.700	99.000	14	11	03	0.03
073	21:42:19.49	+66:04:37.9	17.482	0.106	16.710	0.072	16.600	0.151	19	14	07	0.18
074	21:42:19.54	+66:05:37.5	17.907	0.152	16.944	0.139	16.581	0.119	16	17	14	0.07
076	21:42:19.78	+66:06:20.2	15.166	0.032	14.524	0.039	14.335	0.042	25	26	24	0.07
077	21:42:19.88	+66:09:20.7	16.117	0.037	15.498	0.060	15.287	0.067	25	24	21	0.30
078	21:42:20.07	+66:02:54.0	14.071	0.069	13.495	0.050	13.390	0.062	25	26	24	1.14
081	21:42:20.31	+66:03:56.2	18.185	0.107	17.271	0.062	16.744	0.052	13	06	04	0.07
085	21:42:20.52	+66:02:42.2	17.417	0.119	16.539	0.185	16.293	0.129	16	14	08	1.05
087	21:42:20.77	+66:05:11.3	15.855	0.031	15.231	0.046	15.013	0.046	25	26	24	0.09
088	21:42:20.92	+66:05:45.8	17.899	0.088	16.876	0.098	16.584	0.096	14	15	11	0.15
089	21:42:21.03	+66:04:16.4	18.389	0.081	17.439	0.156	16.958	99.000	07	05	02	-0.25
090	21:42:21.22	+66:09:54.9	17.561	0.084	16.786	0.115	16.487	0.169	16	16	08	0.12
092	21:42:21.54	+66:02:04.5	14.426	0.071	13.983	0.076	13.873	0.055	10	10	11	0.56
093	21:42:21.84	+66:05:03.1	17.902	0.080	17.040	0.122	16.705	0.082	12	13	04	0.05
094	21:42:21.90	+66:03:30.1	17.607	0.074	16.868	0.081	16.677	0.067	16	13	05	0.09
096	21:42:21.96	+66:06:35.0	16.290	0.035	15.587	0.046	15.375	0.065	25	26	25	0.25
097	21:42:22.45	+66:04:45.6	17.467	0.080	16.622	0.079	16.372	0.076	19	18	17	-0.23
098	21:42:22.66	+66:04:19.5	16.700	0.053	15.645	0.054	15.337	0.067	24	26	26	0.24
099	21:42:22.83	+66:07:52.9	13.966	0.023	13.416	0.029	13.249	0.035	26	26	27	0.31

Table 4.2—Continued

FMO ^a	R.A. (J2000.0)	Dec. (J2000.0)	J^b	σ_J^c	H^b	σ_H^c	K_s^b	$\sigma_{K_s}^c$	J	N_{obs}^d H	K_s	Stetson Index
100	21:42:22.92	+66:06:56.2	16.307	0.054	15.465	0.049	15.141	0.055	25	26	26	0.49
101	21:42:23.08	+66:06:04.3	15.194	0.140	14.034	0.105	13.382	0.104	26	26	27	8.02
102	21:42:23.14	+66:06:42.5	15.625	0.040	14.856	0.046	14.642	0.044	23	25	26	0.55
104	21:42:23.34	+66:04:43.5	16.374	0.035	15.659	0.055	15.428	0.056	25	24	27	0.17
105	21:42:23.42	+66:08:47.4	14.359	0.034	13.628	0.030	13.447	0.043	26	26	27	0.80
106	21:42:23.47	+66:06:40.4	16.457	0.038	15.673	0.042	15.443	0.039	20	24	22	-0.14
107	21:42:23.49	+66:02:38.6	17.197	0.054	16.388	0.152	16.120	0.122	20	21	16	0.41
108	21:42:23.63	+66:03:53.0	15.916	0.037	15.231	0.042	15.028	0.042	26	26	26	0.24
109	21:42:23.65	+66:09:49.7	15.718	0.045	15.071	0.051	14.866	0.056	26	25	27	0.52
112	21:42:24.06	+66:04:34.7	17.923	0.135	17.216	0.112	16.891	0.127	14	06	04	0.70
113	21:42:24.08	+66:10:11.0	16.679	0.077	15.835	0.076	15.540	0.094	21	21	22	0.23
114	21:42:24.15	+66:07:11.0	16.570	0.187	16.192	0.072	15.984	0.099	18	24	20	-0.07
115	21:42:24.18	+66:04:59.5	17.331	0.075	16.706	0.120	16.484	0.132	21	20	12	0.31
117	21:42:24.20	+66:02:04.9	16.327	0.088	15.665	0.088	15.471	0.080	10	10	07	0.31
118	21:42:24.44	+66:07:59.6	16.869	0.100	16.306	0.129	16.131	0.101	19	19	16	0.21
119	21:42:24.55	+66:07:45.3	17.376	0.160	16.698	0.177	16.567	0.117	14	09	06	1.38
120	21:42:24.68	+66:04:54.9	15.211	0.023	14.502	0.034	14.281	0.038	26	26	27	0.13
121	21:42:24.80	+66:06:21.3	13.411	0.029	12.498	0.031	12.211	0.030	26	26	27	0.74
122	21:42:25.26	+66:10:08.9	15.010	0.044	14.407	0.057	14.213	0.076	25	26	26	1.09
123	21:42:25.30	+66:03:31.5	17.321	0.130	16.752	0.130	16.511	0.133	18	14	06	0.89
124	21:42:25.36	+66:05:49.2	17.953	0.080	17.107	0.101	16.652	0.161	10	08	07	0.01
129	21:42:26.23	+66:06:56.3	14.813	0.024	14.161	0.033	13.978	0.029	26	26	27	0.24
130	21:42:26.56	+66:06:06.3	18.130	0.122	17.196	0.097	16.730	0.124	08	09	06	0.27
131	21:42:26.59	+66:04:19.2	18.085	0.149	17.043	0.204	16.622	99.000	08	11	03	0.50
132	21:42:26.67	+66:06:16.9	15.707	0.029	14.803	0.035	14.566	0.041	26	26	27	0.46
133	21:42:26.77	+66:05:27.0	17.459	0.108	16.448	0.083	16.177	0.107	20	20	14	0.33
135	21:42:26.96	+66:08:46.4	16.896	0.068	16.250	0.052	16.033	0.069	24	17	17	0.28
139	21:42:27.86	+66:07:11.1	17.659	0.079	16.696	0.088	16.391	0.093	18	15	09	-0.12
140	21:42:27.89	+66:06:29.5	15.637	0.023	15.006	0.037	14.787	0.043	26	26	28	0.18
141	21:42:28.11	+66:07:58.3	15.645	0.335	15.251	0.064	15.077	0.076	23	24	26	1.25
142	21:42:28.26	+66:07:22.9	16.687	0.077	16.063	0.094	15.904	0.115	22	23	20	0.16
143	21:42:28.41	+66:04:08.6	15.018	0.021	14.421	0.028	14.188	0.028	26	26	28	0.24
144	21:42:28.53	+66:01:50.5	16.748	0.086	16.040	0.160	15.909	0.113	07	05	05	-0.20
145	21:42:28.57	+66:10:20.8	17.516	0.074	16.750	0.104	16.552	0.273	15	13	10	0.41
146	21:42:28.85	+66:04:38.7	17.537	0.055	16.527	0.085	16.231	0.091	17	16	15	0.23
147	21:42:28.94	+66:05:48.6	18.147	0.055	17.225	0.105	16.917	99.000	07	04	02	-0.33
149	21:42:29.02	+66:07:21.7	17.178	0.057	16.425	0.103	16.247	0.114	21	17	16	0.12
151	21:42:29.05	+66:07:09.8	16.940	0.082	15.938	0.053	15.636	0.071	25	24	25	0.61
152	21:42:29.14	+66:05:46.5	16.469	0.059	15.836	0.086	15.639	0.071	26	23	21	0.87
153	21:42:29.22	+66:08:34.4	18.091	0.106	17.162	0.155	16.816	0.056	09	09	06	0.44
154	21:42:29.31	+66:04:00.5	18.117	0.139	17.175	0.082	16.910	0.061	07	07	04	-0.28
155	21:42:29.34	+66:08:27.4	16.276	0.038	15.520	0.046	15.243	0.052	24	25	26	0.33

Table 4.2—Continued

FMO ^a	R.A. (J2000.0)	Dec. (J2000.0)	J^b	σ_J^c	H^b	σ_H^c	K_s^b	$\sigma_{K_s}^c$	J	N_{obs}^d H	K_s	Stetson Index
156	21:42:29.39	+66:02:01.1	15.514	0.086	15.092	0.052	14.932	0.073	10	09	11	-0.29
157	21:42:29.51	+66:09:06.0	17.771	0.091	16.917	0.106	16.327	0.099	14	10	12	0.07
158	21:42:29.64	+66:05:20.7	16.671	0.052	15.988	0.053	15.786	0.086	26	22	24	0.22
159	21:42:29.68	+66:04:33.0	17.497	0.075	16.810	0.087	16.622	0.211	19	14	07	0.11
160	21:42:29.77	+66:05:58.0	16.974	0.060	16.315	0.046	16.101	0.070	26	17	17	0.07
161	21:42:29.81	+66:07:50.2	17.064	0.097	16.470	0.102	16.306	0.110	19	12	12	0.81
162	21:42:29.94	+66:04:57.9	16.595	0.048	15.972	0.048	15.779	0.073	26	26	22	0.20
163	21:42:30.00	+66:02:07.8	14.230	0.075	13.468	0.044	13.262	0.071	13	13	13	-0.13
164	21:42:30.01	+66:01:58.5	17.006	0.081	16.414	0.127	16.225	99.000	05	05	03	0.20
165	21:42:30.08	+66:10:02.3	16.315	0.059	15.612	0.060	15.301	0.088	23	25	25	0.69
166	21:42:30.14	+66:01:47.2	15.950	0.087	15.203	0.095	14.993	0.075	07	04	07	0.94
167	21:42:30.22	+66:02:03.3	16.609	0.073	15.937	0.075	15.611	0.131	07	09	08	0.57
169	21:42:30.97	+66:08:28.2	17.516	0.057	16.830	0.085	16.447	0.072	21	15	07	-0.07
170	21:42:31.28	+66:08:04.7	15.777	0.021	15.152	0.033	14.939	0.043	23	26	26	0.19
172	21:42:31.45	+66:07:00.0	17.320	0.102	16.569	0.060	16.372	0.073	21	18	09	0.00
173	21:42:31.93	+66:07:08.5	13.929	0.020	13.304	0.024	13.081	0.016	26	26	28	0.20
174	21:42:32.10	+66:06:40.8	17.947	0.085	17.194	0.123	16.944	0.120	14	09	04	0.11
176	21:42:32.38	+66:04:28.7	16.996	0.061	16.340	0.079	16.120	0.084	22	20	18	0.02
177	21:42:32.41	+66:04:59.0	15.676	0.021	15.034	0.031	14.845	0.032	26	26	27	0.28
178	21:42:32.51	+66:01:52.8	16.091	0.107	15.415	0.062	15.285	0.064	08	08	08	0.28
180	21:42:32.85	+66:04:06.2	17.623	0.075	16.747	0.074	16.380	0.101	16	14	10	-0.03
181	21:42:32.98	+66:07:44.5	16.312	0.029	15.555	0.039	15.298	0.050	26	24	27	-0.02
183	21:42:33.57	+66:03:06.1	18.038	0.091	17.204	0.053	16.801	0.085	12	05	04	0.19
184	21:42:33.64	+66:07:40.6	17.492	0.066	16.845	0.101	16.516	0.119	17	14	09	0.17
186	21:42:33.82	+66:08:02.2	14.624	0.019	13.638	0.019	13.294	0.022	26	26	28	0.69
187	21:42:34.03	+66:08:59.9	17.621	0.075	17.005	0.102	16.790	99.000	19	08	03	0.30
189	21:42:34.26	+66:02:33.9	17.654	0.072	16.702	0.081	16.375	0.080	18	13	10	0.33
190	21:42:34.32	+66:03:12.4	14.741	0.020	13.886	0.026	13.650	0.031	26	26	28	-0.02
191	21:42:34.33	+66:07:41.8	18.058	0.071	16.998	0.106	16.648	0.122	09	12	07	0.37
192	21:42:34.34	+66:01:56.3	17.123	0.106	16.305	0.088	15.872	0.074	06	07	06	-0.18
193	21:42:34.60	+66:07:44.8	16.217	0.031	15.521	0.051	15.269	0.046	24	25	28	0.11
195	21:42:34.72	+66:05:18.6	13.945	0.020	13.282	0.022	13.051	0.016	26	26	28	0.68
196	21:42:34.84	+66:02:49.0	17.140	0.054	16.179	0.075	15.877	0.090	23	22	22	-0.04
197	21:42:34.85	+66:06:14.9	17.666	0.092	17.024	0.105	16.754	99.000	18	12	03	-0.04
198	21:42:35.09	+66:04:09.4	15.617	0.018	15.057	0.035	14.885	0.044	26	26	27	0.20
199	21:42:35.13	+66:02:33.9	17.293	0.077	16.493	0.089	16.283	0.112	20	14	13	0.28
200	21:42:35.31	+66:04:14.1	16.882	0.048	15.982	0.043	15.644	0.052	24	24	26	-0.20
201	21:42:35.75	+66:05:49.2	13.915	0.018	13.101	0.029	12.872	0.017	26	26	28	1.16
202	21:42:36.41	+66:08:22.9	17.646	0.074	16.945	0.101	16.763	0.064	14	11	05	-0.09
203	21:42:36.52	+66:07:44.4	17.374	0.075	16.625	0.050	16.329	0.098	19	17	12	-0.10
204	21:42:36.53	+66:06:45.8	15.808	0.023	14.833	0.020	14.397	0.031	26	26	28	0.32
205	21:42:36.57	+66:02:27.6	18.046	0.090	17.256	0.112	16.833	0.172	11	09	04	-0.31

Table 4.2—Continued

FMO ^a	R.A. (J2000.0)	Dec. (J2000.0)	J^b	σ_J^c	H^b	σ_H^c	K_s^b	$\sigma_{K_s}^c$	J	N_{obs}^d H	K_s	Stetson Index
206	21:42:36.80	+66:07:18.3	18.073	0.116	16.949	0.148	16.582	0.122	08	12	08	0.84
207	21:42:36.87	+66:05:55.4	16.669	0.086	16.075	0.113	15.906	0.062	22	22	19	0.65
209	21:42:37.03	+66:02:13.5	14.286	0.056	13.646	0.054	13.465	0.048	20	15	13	-0.62
212	21:42:37.22	+66:06:01.1	17.530	0.070	16.876	0.112	16.661	0.064	18	11	07	0.22
214	21:42:37.42	+66:03:26.2	15.705	0.019	14.857	0.030	14.496	0.029	25	26	28	-0.22
215	21:42:37.59	+66:02:43.0	15.420	0.028	14.776	0.027	14.572	0.046	26	26	26	-0.10
218	21:42:37.81	+66:06:51.9	16.410	0.051	15.544	0.035	15.210	0.045	25	24	27	0.28
219	21:42:37.90	+66:02:29.8	15.127	0.034	14.541	0.042	14.366	0.040	24	23	25	-0.55
220	21:42:37.92	+66:08:49.0	17.504	0.073	16.869	0.047	16.555	0.108	16	11	06	0.46
221	21:42:38.03	+66:09:40.9	17.421	0.075	16.571	0.070	16.239	0.125	14	15	09	0.71
222	21:42:38.08	+66:05:44.4	17.824	0.079	17.119	0.114	16.818	99.000	17	09	03	0.26
224	21:42:38.20	+66:07:51.3	18.173	0.119	17.109	0.106	16.669	0.115	09	11	07	0.11
225	21:42:38.23	+66:04:06.2	13.749	0.013	13.031	0.018	12.841	0.018	26	26	28	0.10
226	21:42:38.25	+66:07:30.0	16.996	0.049	16.169	0.056	15.846	0.079	23	24	20	0.08
227	21:42:38.30	+66:05:59.0	17.558	0.088	16.623	0.084	16.326	0.106	19	13	15	-0.02
228	21:42:38.36	+66:08:28.2	11.420	0.033	10.341	0.030	10.021	0.027	26	23	26	0.18
229	21:42:38.41	+66:05:04.7	17.430	0.070	16.823	0.091	16.596	0.097	18	12	07	0.48
230	21:42:38.44	+66:04:38.2	16.402	0.034	15.541	0.032	15.260	0.057	26	25	25	0.06
231	21:42:38.70	+66:09:41.5	16.188	0.067	15.539	0.062	15.210	0.096	25	24	23	0.83
232	21:42:38.79	+66:09:32.7	17.475	0.067	16.739	0.096	16.462	0.070	20	15	10	0.20
233	21:42:38.82	+66:06:35.9	14.329	0.208	13.116	0.144	12.298	0.084	26	26	28	22.04
235	21:42:38.97	+66:07:08.7	14.026	0.056	12.860	0.019	12.453	0.027	12	10	13	0.30
237	21:42:39.14	+66:07:10.0	12.896	0.089	11.818	0.091	11.334	0.093	22	22	27	5.83
238	21:42:39.15	+66:09:57.8	17.760	0.095	16.938	0.121	16.720	0.089	08	08	05	0.26
239	21:42:39.31	+66:09:19.8	17.334	0.058	16.669	0.080	16.382	0.077	19	15	09	0.21
240	21:42:39.43	+66:06:12.1	18.156	0.100	17.117	0.123	16.804	0.144	10	11	04	0.08
241	21:42:39.45	+66:05:18.7	18.081	0.104	17.325	0.103	17.096	99.000	13	06	03	0.08
242	21:42:39.47	+66:08:42.8	16.017	0.033	15.395	0.033	15.185	0.056	24	25	27	0.03
245	21:42:39.63	+66:05:30.3	16.973	0.051	16.382	0.058	16.237	0.103	23	18	13	0.27
246	21:42:39.68	+66:03:31.6	15.921	0.027	15.177	0.034	15.003	0.047	26	26	27	0.04
247	21:42:39.87	+66:03:44.1	18.043	0.086	17.177	0.111	16.701	0.215	12	08	04	-0.01
248	21:42:39.95	+66:09:56.4	17.074	0.072	16.045	0.171	15.845	0.114	10	16	18	0.52
250	21:42:40.26	+66:04:58.7	17.201	0.060	16.570	0.106	16.305	0.078	21	17	12	-0.21
251	21:42:40.29	+66:05:04.6	16.739	0.051	16.138	0.079	15.987	0.061	23	23	14	0.56
253	21:42:40.33	+66:10:07.3	11.001	0.046	10.684	0.061	10.581	0.055	25	25	27	1.07
254	21:42:40.45	+66:05:35.3	17.608	0.053	16.692	0.097	16.378	0.064	18	15	08	-0.08
255	21:42:40.57	+66:09:52.1	16.789	0.278	15.637	0.295	14.686	0.348	20	25	28	6.29
256	21:42:40.65	+66:09:10.3	17.814	0.099	16.880	0.073	16.557	0.038	17	15	07	0.18
257	21:42:41.20	+66:08:12.2	17.541	0.056	16.699	0.084	16.347	0.089	16	16	11	0.11
258	21:42:41.22	+66:09:42.2	18.131	0.174	16.972	0.161	16.514	0.091	11	12	05	0.86
260	21:42:41.27	+66:05:40.2	17.038	0.050	16.443	0.044	16.216	0.058	23	15	13	0.11
261	21:42:41.27	+66:06:38.2	17.170	0.063	16.348	0.050	16.023	0.070	22	20	18	0.24

Table 4.2—Continued

FMO ^a	R.A. (J2000.0)	Dec. (J2000.0)	J^b	σ_J^c	H^b	σ_H^c	K_s^b	$\sigma_{K_s}^c$	J	N_{obs}^d H	K_s	Stetson Index
262	21:42:41.32	+66:03:33.5	13.405	0.015	12.875	0.019	12.727	0.024	26	26	28	-0.72
263	21:42:41.48	+66:05:14.1	17.482	0.084	16.912	0.099	16.837	0.251	22	13	08	0.38
264	21:42:41.94	+66:09:24.7	15.145	0.027	14.356	0.041	13.961	0.053	26	26	28	0.95
265	21:42:41.97	+66:06:41.0	16.711	0.060	15.691	0.043	15.328	0.043	25	25	26	-0.05
266	21:42:42.03	+66:03:38.2	17.977	0.121	17.170	0.187	16.647	0.119	17	11	11	-0.17
267	21:42:42.17	+66:06:33.7	16.964	0.056	15.880	0.045	15.536	0.050	26	24	23	0.21
268	21:42:42.30	+66:02:46.2	16.476	0.045	15.222	0.037	14.681	0.042	25	25	28	0.23
269	21:42:42.41	+66:09:08.9	17.342	0.050	16.574	0.098	16.304	0.080	18	17	13	-0.01
270	21:42:42.44	+66:07:45.2	15.732	0.026	14.209	0.042	13.454	0.068	26	26	28	2.07
271	21:42:42.60	+66:05:18.2	16.492	0.027	15.566	0.044	15.279	0.043	24	26	27	-0.01
274	21:42:43.35	+66:02:08.5	15.283	0.057	14.521	0.046	14.329	0.044	15	14	13	-0.25
275	21:42:43.47	+66:04:16.0	17.492	0.090	16.621	0.108	16.314	0.138	12	13	12	0.69
276	21:42:43.58	+66:05:00.2	16.728	0.121	16.012	0.083	15.769	0.075	25	23	22	0.33
277	21:42:43.64	+66:04:20.2	15.942	0.108	15.238	0.152	15.068	0.146	16	25	26	2.72
278	21:42:44.07	+66:08:53.4	14.698	0.021	13.673	0.026	13.335	0.030	26	26	28	0.49
279	21:42:44.14	+66:05:48.2	16.744	0.043	16.066	0.058	15.871	0.082	22	21	17	0.15
280	21:42:44.20	+66:08:09.1	18.483	0.067	16.982	0.084	16.277	0.067	07	08	13	-0.13
283	21:42:44.29	+66:10:06.9	15.344	0.050	14.572	0.054	14.226	0.066	25	26	27	0.52
284	21:42:44.51	+66:05:50.7	17.113	0.064	16.458	0.075	16.217	0.081	21	18	11	0.01
285	21:42:44.56	+66:10:15.0	16.715	0.068	15.708	0.051	15.374	0.073	23	23	25	0.05
286	21:42:44.61	+66:01:59.1	17.605	99.000	16.338	0.046	15.836	0.085	03	06	06	0.18
288	21:42:44.78	+66:06:40.4	16.246	0.040	15.508	0.033	15.065	0.049	25	26	28	0.10
289	21:42:44.87	+66:05:03.3	16.477	0.227	15.875	0.091	15.643	0.116	16	18	22	1.65
291	21:42:45.03	+66:07:47.9	15.681	0.027	14.535	0.020	14.067	0.017	26	26	28	0.41
292	21:42:45.05	+66:07:42.9	16.759	0.045	15.476	0.043	14.753	0.031	24	26	28	-0.03
293	21:42:45.31	+66:04:15.9	17.653	0.297	16.799	0.253	16.409	0.196	08	10	07	1.73
294	21:42:45.32	+66:07:04.5	14.978	0.030	13.864	0.019	13.422	0.020	26	26	28	1.01
295	21:42:45.56	+66:06:30.5	15.528	0.021	14.643	0.023	14.366	0.032	26	26	28	0.12
298	21:42:46.04	+66:08:15.4	14.993	0.013	13.924	0.021	13.502	0.018	26	26	28	0.44
300	21:42:46.08	+66:05:56.3	13.883	0.023	13.051	0.016	12.797	0.022	26	26	28	1.00
301	21:42:46.09	+66:10:20.2	15.256	0.077	13.973	0.075	13.366	0.086	24	25	26	1.19
302	21:42:46.22	+66:06:56.5	14.603	0.058	13.421	0.043	12.948	0.042	25	26	28	2.96
304	21:42:46.60	+66:06:33.2	15.617	0.035	14.849	0.029	14.586	0.040	24	26	27	0.32
305	21:42:46.64	+66:06:22.2	15.952	0.044	15.254	0.035	14.878	0.046	24	26	27	0.14
307	21:42:46.86	+66:06:57.5	13.686	0.071	12.548	0.059	12.027	0.067	24	26	28	4.41
308	21:42:47.05	+66:04:57.8	12.098	0.018	11.297	0.016	11.056	0.031	26	26	28	1.73
309	21:42:47.22	+66:05:18.2	16.640	0.084	16.049	0.128	15.863	0.126	06	12	12	0.60
311	21:42:47.25	+66:06:57.5	16.219	0.084	15.261	0.086	14.742	0.081	20	16	23	0.62
312	21:42:47.42	+66:06:34.4	16.122	0.040	15.405	0.064	15.227	0.056	22	26	28	0.19
313	21:42:47.52	+66:07:03.2	14.985	0.037	13.887	0.041	13.432	0.042	26	26	28	2.33
315	21:42:47.79	+66:05:35.1	14.612	0.022	13.952	0.025	13.734	0.021	26	26	28	0.92
316	21:42:47.89	+66:10:15.9	17.325	0.061	16.417	0.094	15.906	0.116	18	16	20	-0.03

Table 4.2—Continued

FMO ^a	R.A. (J2000.0)	Dec. (J2000.0)	J^b	σ_J^c	H^b	σ_H^c	K_s^b	$\sigma_{K_s}^c$	J	N_{obs}^d H	K_s	Stetson Index
317	21:42:47.90	+66:06:53.0	13.398	0.036	12.407	0.040	12.035	0.022	25	26	28	2.13
318	21:42:47.91	+66:06:13.6	17.821	0.118	17.224	0.195	16.727	0.075	17	07	08	-0.17
319	21:42:48.05	+66:05:05.0	17.768	0.250	17.016	0.116	16.559	0.514	11	09	07	1.85
320	21:42:48.12	+66:07:45.9	17.619	0.074	16.492	0.068	16.080	0.074	13	15	16	-0.08
322	21:42:48.19	+66:07:43.1	15.806	0.026	14.841	0.035	14.377	0.032	25	26	28	0.01
323	21:42:48.23	+66:08:00.7	15.316	0.168	13.779	0.143	12.868	0.118	25	26	28	9.34
325	21:42:48.87	+66:06:26.7	14.485	0.043	13.606	0.044	13.377	0.024	15	20	24	1.39
326	21:42:48.94	+66:06:42.5	16.201	0.135	15.663	0.087	15.433	0.124	11	14	16	1.19
327	21:42:48.96	+66:04:51.8	17.866	0.149	17.097	0.127	16.908	0.178	11	08	07	0.52
328	21:42:48.96	+66:09:01.0	18.760	99.000	17.113	0.145	16.026	0.073	01	08	18	0.34
329	21:42:48.99	+66:06:54.7	16.810	0.247	15.691	0.269	14.872	0.175	20	23	26	3.25
330	21:42:49.25	+66:03:16.7	14.697	0.025	14.022	0.023	13.793	0.026	26	26	28	-0.24
331	21:42:49.27	+66:07:44.4	16.821	0.048	15.690	0.045	15.035	0.032	26	25	27	0.27
332	21:42:49.32	+66:07:28.9	16.261	0.033	15.061	0.033	14.511	0.024	26	26	28	0.13
334	21:42:49.43	+66:06:45.1	17.165	0.177	16.435	0.162	16.172	0.319	08	10	06	1.48
336	21:42:49.86	+66:05:42.4	14.944	0.030	14.121	0.029	13.836	0.031	23	25	28	0.45
337	21:42:49.91	+66:02:35.7	16.157	0.039	14.280	0.027	13.420	0.032	25	26	27	0.30
338	21:42:49.96	+66:01:58.0	11.859	0.077	11.572	0.037	11.519	0.054	09	09	11	0.42
339	21:42:49.97	+66:05:54.3	15.274	0.042	14.567	0.036	14.219	0.032	26	26	28	1.01
340	21:42:50.10	+66:05:45.0	15.713	0.033	15.041	0.017	14.823	0.033	22	23	26	-0.05
342	21:42:50.54	+66:08:32.6	16.163	0.032	15.155	0.034	14.758	0.039	26	26	26	0.25
343	21:42:50.58	+66:05:11.1	15.497	0.062	14.797	0.056	14.519	0.072	26	26	28	2.14
344	21:42:50.70	+66:03:31.1	14.699	0.019	14.086	0.016	13.972	0.024	26	26	28	-0.16
345	21:42:50.72	+66:01:48.4	17.157	99.000	16.006	0.098	15.581	0.103	03	05	05	-0.37
346	21:42:50.92	+66:06:03.6	13.692	0.034	12.836	0.035	12.585	0.030	26	26	28	3.49
347	21:42:51.05	+66:03:59.1	16.857	0.177	16.326	0.193	16.277	0.208	21	17	06	2.31
348	21:42:51.21	+66:05:45.1	15.172	0.029	14.866	0.041	14.727	0.058	26	26	28	0.83
349	21:42:51.41	+66:05:56.4	15.329	0.248	14.292	0.197	13.692	0.137	25	25	28	11.64
350	21:42:51.47	+66:05:53.5	16.494	0.052	15.722	0.071	15.510	0.090	24	25	24	0.30
351	21:42:51.61	+66:04:32.9	18.278	99.000	17.269	0.083	16.452	0.117	03	09	06	-0.02
352	21:42:51.66	+66:06:59.8	16.393	0.115	15.507	0.076	15.020	0.073	24	24	25	0.96
353	21:42:51.95	+66:06:33.8	14.310	0.067	13.328	0.042	13.102	0.020	15	20	22	-0.60
354	21:42:51.95	+66:07:22.0	16.938	0.067	15.982	0.066	15.585	0.055	22	25	24	0.04
355	21:42:52.03	+66:09:44.9	14.894	0.039	14.171	0.038	13.985	0.042	26	26	28	0.37
356	21:42:52.09	+66:07:39.8	16.900	0.103	15.425	0.082	14.599	0.070	24	25	28	0.86
358	21:42:52.25	+66:06:24.6	16.455	0.101	15.735	0.090	15.513	0.098	19	24	26	0.70
359	21:42:52.34	+66:05:35.1	14.486	0.041	13.501	0.032	13.207	0.029	26	26	28	2.46
360	21:42:52.34	+66:08:10.5	16.083	0.034	14.738	0.034	14.157	0.025	24	26	28	0.10
361	21:42:52.42	+66:08:29.8	18.774	99.000	17.457	0.146	16.817	99.000	03	08	02	0.46
363	21:42:52.62	+66:06:57.4	13.875	0.096	12.763	0.079	12.072	0.068	26	22	28	2.51
364	21:42:52.88	+66:09:27.0	18.388	99.000	16.978	0.073	16.479	0.097	03	13	11	0.08
365	21:42:53.05	+66:05:13.0	15.452	0.101	14.660	0.088	14.268	0.127	26	25	28	3.39

Table 4.2—Continued

FMO ^a	R.A. (J2000.0)	Dec. (J2000.0)	J^b	σ_J^c	H^b	σ_H^c	K_s^b	$\sigma_{K_s}^c$	J	N_{obs}^d H	K_s	Stetson Index
366	21:42:53.14	+66:07:14.8	16.153	0.339	14.605	0.293	13.394	0.176	26	26	28	11.54
367	21:42:53.15	+66:08:06.4	17.738	0.209	16.174	0.122	15.488	0.089	09	10	17	0.70
368	21:42:53.22	+66:07:20.8	14.053	0.198	12.963	0.198	12.417	0.117	26	26	28	17.83
370	21:42:53.46	+66:09:19.9	16.740	0.299	15.333	0.283	14.287	0.241	25	25	28	9.21
371	21:42:53.50	+66:08:05.4	13.274	0.033	12.428	0.033	12.145	0.048	26	26	28	3.62
372	21:42:53.60	+66:02:38.9	18.670	99.000	16.986	0.101	16.260	0.067	01	08	11	-0.23
373	21:42:53.82	+66:07:06.4	18.416	0.148	17.344	0.205	16.756	0.196	08	09	06	0.87
374	21:42:53.85	+66:02:15.1	17.566	0.086	16.257	0.076	15.785	0.083	13	14	12	-0.10
375	21:42:53.93	+66:06:50.5	14.712	0.042	13.830	0.033	13.512	0.029	26	26	28	1.90
376	21:42:53.96	+66:08:24.2	17.317	0.065	16.143	0.072	15.499	0.055	22	25	26	0.02
378	21:42:54.04	+66:08:14.9	14.411	0.019	13.253	0.021	12.823	0.019	26	26	28	-0.03
380	21:42:54.59	+66:05:20.4	15.456	0.111	14.571	0.082	13.994	0.124	26	25	28	3.27
381	21:42:54.76	+66:06:35.4	14.511	0.378	13.342	0.264	12.661	0.207	26	26	28	29.68
382	21:42:54.80	+66:06:12.2	14.630	0.125	13.789	0.077	13.324	0.182	13	18	15	5.25
383	21:42:54.81	+66:07:27.0	17.892	0.283	16.950	0.225	16.317	0.143	05	05	07	1.46
384	21:42:54.82	+66:06:13.8	15.084	0.061	14.170	0.055	13.801	0.034	09	16	09	1.47
385	21:42:54.91	+66:07:21.3	14.242	0.022	13.183	0.021	12.781	0.021	25	26	28	0.79
387	21:42:54.93	+66:06:31.2	14.700	0.038	13.763	0.026	13.486	0.035	25	26	28	1.25
388	21:42:55.00	+66:09:04.5	17.220	0.060	15.734	0.043	15.011	0.052	19	24	28	0.14
389	21:42:55.29	+66:06:25.4	13.330	0.028	12.688	0.052	12.526	0.033	25	26	28	2.08
390	21:42:55.44	+66:07:25.4	16.834	0.110	15.880	0.095	15.481	0.107	18	20	22	1.24
391	21:42:55.49	+66:10:06.3	17.163	0.118	16.569	0.078	16.259	0.085	15	14	10	0.03
392	21:42:55.49	+66:06:34.2	18.033	0.169	16.903	0.152	16.536	0.157	06	10	08	0.54
393	21:42:55.69	+66:06:44.9	15.703	0.155	14.705	0.140	14.342	0.106	26	26	28	5.18
394	21:42:55.69	+66:10:04.2	17.035	0.072	16.340	0.108	16.078	0.096	16	16	12	0.19
395	21:42:55.80	+66:05:42.7	15.174	0.081	14.423	0.098	14.035	0.152	25	26	28	5.08
396	21:42:55.81	+66:02:52.6	18.358	0.157	16.932	0.090	16.251	0.092	04	13	15	-0.32
397	21:42:55.82	+66:07:50.8	17.347	0.060	15.930	0.068	15.265	0.055	20	23	24	0.14
398	21:42:55.83	+66:06:59.9	18.287	0.161	17.307	0.095	16.956	0.143	06	06	04	0.19
399	21:42:55.92	+66:07:20.9	14.507	0.132	13.188	0.113	12.417	0.104	26	26	28	10.41
400	21:42:56.04	+66:05:39.5	17.049	0.403	16.882	0.156	16.737	0.217	18	06	04	3.47
401	21:42:56.08	+66:06:52.6	18.571	0.391	17.526	0.216	17.035	0.148	11	11	04	1.46
402	21:42:56.19	+66:10:12.7	17.814	0.179	16.619	0.071	16.153	0.159	15	14	15	0.38
403	21:42:56.24	+66:06:02.2	12.425	0.036	11.639	0.027	11.408	0.045	26	26	28	1.93
404	21:42:56.33	+66:07:03.4	16.802	0.081	15.890	0.123	15.488	0.137	25	25	27	1.55
405	21:42:56.38	+66:09:01.6	16.928	0.036	16.202	0.061	15.876	0.085	24	21	23	0.16
406	21:42:56.48	+66:07:09.9	17.573	0.183	16.805	0.079	16.293	0.162	18	12	16	0.73
407	21:42:56.59	+66:06:46.8	18.898	0.333	17.814	0.179	17.084	99.000	05	06	03	0.24
408	21:42:56.76	+66:06:37.3	13.524	0.091	12.599	0.096	12.203	0.073	25	26	28	3.79
409	21:42:56.79	+66:07:23.6	17.375	0.100	16.434	0.188	15.900	0.122	15	18	18	0.98
410	21:42:56.96	+66:06:59.8	18.147	0.127	16.861	0.144	16.295	0.114	12	13	13	0.52
412	21:42:57.20	+66:06:34.7	13.626	0.036	12.787	0.056	12.531	0.030	26	26	26	1.83

Table 4.2—Continued

FMO ^a	R.A. (J2000.0)	Dec. (J2000.0)	J^b	σ_J^c	H^b	σ_H^c	K_s^b	$\sigma_{K_s}^c$	J	N_{obs}^d H	K_s	Stetson Index
413	21:42:57.24	+66:07:24.9	18.166	0.127	17.625	0.344	16.731	0.539	08	05	07	0.92
415	21:42:57.45	+66:07:14.9	14.163	0.024	13.284	0.027	12.965	0.041	26	26	28	1.15
416	21:42:57.50	+66:02:48.7	18.246	99.000	16.230	0.070	15.217	0.034	02	23	26	0.10
417	21:42:57.71	+66:04:23.3	16.169	99.000	14.955	0.201	13.907	0.103	02	17	26	2.34
419	21:42:57.83	+66:05:55.4	16.615	99.000	16.013	0.221	14.732	0.249	01	07	07	1.09
421	21:42:57.93	+66:02:27.0	18.308	0.179	16.888	0.116	16.246	0.086	06	12	10	0.07
422	21:42:58.09	+66:05:54.5	12.852	0.035	12.526	0.045	12.393	0.070	25	26	25	1.49
423	21:42:58.10	+66:07:39.4	14.296	0.032	13.500	0.028	13.082	0.044	26	26	28	1.14
424	21:42:58.22	+66:05:40.2	14.453	0.072	13.618	0.075	13.264	0.092	25	25	27	3.75
425	21:42:58.27	+66:06:52.8	18.250	0.081	17.229	0.164	16.760	0.111	07	08	06	0.26
426	21:42:58.33	+66:07:26.3	14.374	0.042	12.634	0.039	11.951	0.048	25	26	28	2.97
427	21:42:58.35	+66:05:27.4	13.878	0.103	13.054	0.145	12.608	0.140	26	26	28	4.59
428	21:42:58.36	+66:06:16.7	14.341	0.316	13.552	0.122	13.115	0.144	04	10	14	2.22
430	21:42:58.58	+66:05:34.8	17.715	99.000	16.605	0.566	15.155	0.225	02	13	26	2.18
432	21:42:58.64	+66:08:06.5	17.145	0.093	15.567	0.056	14.804	0.036	17	25	27	0.05
433	21:42:58.74	+66:06:36.9	13.678	0.066	12.736	0.039	12.462	0.035	26	26	28	2.73
434	21:42:59.23	+66:06:36.5	15.074	0.055	14.182	0.042	13.825	0.050	25	26	28	1.13
435	21:42:59.32	+66:09:37.6	18.136	0.154	17.040	0.128	16.668	0.093	07	11	06	0.24
436	21:42:59.33	+66:08:59.8	17.486	0.073	16.212	0.044	15.767	0.064	17	23	18	0.14
437	21:42:59.33	+66:08:11.8	16.532	0.034	15.131	0.044	14.497	0.036	23	25	27	0.14
439	21:42:59.60	+66:07:34.3	16.791	0.184	15.848	0.153	15.315	0.138	20	21	21	2.34
440	21:42:59.60	+66:04:33.7	13.106	0.086	11.757	0.081	11.010	0.091	24	26	28	9.63
441	21:42:59.83	+66:07:31.5	15.332	0.092	13.872	0.033	13.222	0.030	25	25	28	1.19
442	21:42:59.96	+66:07:55.6	17.587	0.083	15.683	0.055	14.632	0.030	17	26	27	-0.26
443	21:42:59.98	+66:06:42.4	14.361	0.046	13.534	0.038	13.283	0.069	26	25	28	2.84
444	21:43:00.19	+66:06:46.4	15.107	0.437	13.816	0.288	13.017	0.214	23	23	28	17.42
445	21:43:00.23	+66:06:48.8	15.190	0.098	13.921	0.080	13.093	0.068	23	24	28	3.28
446	21:43:00.24	+66:05:45.8	14.959	0.084	14.232	0.102	14.070	0.143	25	26	25	5.00
447	21:43:00.27	+66:05:19.1	0.000	99.000	17.243	0.159	16.083	0.093	00	06	15	0.37
448	21:43:00.29	+66:09:53.5	15.900	0.037	14.653	0.047	14.103	0.043	25	26	28	-0.02
449	21:43:00.33	+66:06:33.2	16.999	0.272	15.991	0.209	15.451	0.190	25	26	28	2.14
451	21:43:00.40	+66:02:52.9	15.603	0.027	14.850	0.029	14.642	0.035	26	26	28	-0.01
452	21:43:00.76	+66:06:46.6	15.492	0.042	14.258	0.072	13.739	0.043	22	24	28	0.74
453	21:43:00.86	+66:06:15.3	17.048	0.084	16.358	0.084	15.690	0.203	11	15	16	0.83
454	21:43:01.17	+66:08:19.9	17.254	0.054	16.194	0.074	15.536	0.065	20	23	25	0.02
455	21:43:01.35	+66:06:36.7	16.714	0.120	15.983	0.154	15.585	0.170	20	24	24	1.05
456	21:43:01.54	+66:10:18.5	18.585	99.000	16.470	0.128	15.527	0.073	02	16	22	0.00
457	21:43:01.58	+66:07:06.2	15.780	99.000	14.817	0.334	14.226	99.000	02	05	03	3.24
458	21:43:01.62	+66:08:22.1	16.009	0.030	14.892	0.031	14.260	0.025	26	25	28	0.03
459	21:43:01.66	+66:06:32.2	17.342	0.064	16.184	0.121	15.873	0.077	18	19	17	0.26
460	21:43:01.69	+66:07:09.0	11.398	0.067	10.770	0.115	10.449	0.114	24	24	24	3.46
461	21:43:01.81	+66:03:24.5	0.000	99.000	0.000	99.000	15.574	0.146	00	00	19	0.92

Table 4.2—Continued

FMO ^a	R.A. (J2000.0)	Dec. (J2000.0)	J^b	σ_J^c	H^b	σ_H^c	K_s^b	$\sigma_{K_s}^c$	J	N_{obs}^d H	K_s	Stetson Index
462	21:43:01.88	+66:06:44.8	13.277	0.064	12.344	0.054	11.949	0.052	26	26	28	5.57
463	21:43:02.00	+66:04:02.6	0.000	99.000	17.275	99.000	15.198	0.095	00	03	27	1.48
464	21:43:02.10	+66:07:41.4	0.000	99.000	17.263	0.239	15.725	0.065	00	06	23	-0.06
465	21:43:02.34	+66:04:37.3	18.299	0.160	16.739	0.077	15.993	0.092	07	16	22	-0.30
466	21:43:02.49	+66:07:03.8	14.449	0.168	13.350	0.143	12.663	0.117	20	25	24	2.69
467	21:43:02.52	+66:05:34.7	17.897	0.293	17.103	0.371	16.830	99.000	08	05	03	1.87
468	21:43:02.58	+66:07:12.4	15.270	0.149	14.559	0.151	13.993	0.167	12	13	15	0.90
469	21:43:02.65	+66:09:51.0	15.904	0.052	14.924	0.054	14.427	0.052	24	25	27	-0.01
470	21:43:02.87	+66:08:14.4	16.504	0.035	15.419	0.029	14.820	0.035	26	25	27	0.05
471	21:43:02.94	+66:06:56.5	16.479	0.193	14.466	0.098	13.451	0.122	15	25	26	2.72
472	21:43:03.22	+66:04:53.5	15.416	0.032	14.377	0.019	13.903	0.025	26	26	28	0.17
473	21:43:03.42	+66:05:26.4	13.521	0.056	12.629	0.134	12.057	0.086	26	26	28	4.15
474	21:43:03.43	+66:05:39.9	17.014	0.122	16.502	0.088	16.330	0.151	15	14	11	1.30
475	21:43:03.65	+66:06:26.4	17.665	0.512	16.250	0.379	15.334	0.305	15	19	26	4.37
476	21:43:03.77	+66:04:40.7	18.666	99.000	16.877	0.094	16.054	0.085	02	15	19	-0.09
477	21:43:04.31	+66:05:56.4	15.857	0.083	15.052	0.105	14.509	0.113	21	22	24	1.87
478	21:43:04.44	+66:04:31.3	17.298	0.082	15.604	0.051	14.827	0.048	20	26	28	0.48
479	21:43:04.98	+66:06:53.3	13.216	0.115	12.206	0.074	11.744	0.087	22	23	23	2.60
480	21:43:05.12	+66:10:12.4	15.776	0.056	14.666	0.052	14.165	0.062	24	25	25	0.51
481	21:43:05.17	+66:09:29.4	15.856	0.036	15.214	0.050	14.823	0.046	26	26	28	-0.05
482	21:43:05.17	+66:07:34.1	0.000	99.000	16.339	0.095	14.255	0.043	00	22	28	0.68
483	21:43:05.36	+66:04:51.9	16.034	0.024	15.280	0.023	15.071	0.039	26	26	27	-0.06
484	21:43:05.43	+66:06:03.1	14.785	0.069	13.506	0.036	12.999	0.051	26	25	28	1.47
486	21:43:05.55	+66:03:28.2	14.367	0.016	13.690	0.017	13.555	0.021	26	26	28	0.14
487	21:43:05.77	+66:06:29.6	15.302	0.051	14.400	0.058	13.888	0.081	24	26	25	2.04
488	21:43:05.79	+66:09:41.5	18.803	99.000	16.990	0.131	16.143	0.090	02	11	13	0.21
490	21:43:05.99	+66:04:57.2	17.641	0.103	15.884	0.039	15.100	0.043	21	23	27	-0.02
491	21:43:06.03	+66:06:44.7	0.000	99.000	14.101	99.000	12.210	0.270	00	03	10	1.51
493	21:43:06.48	+66:05:49.0	17.848	0.359	16.829	0.116	16.240	0.138	05	09	07	0.98
494	21:43:06.67	+66:05:00.8	16.764	0.040	15.282	0.037	14.606	0.029	26	26	28	-0.24
496	21:43:06.96	+66:06:41.6	0.000	99.000	13.572	0.151	10.650	0.099	00	19	22	4.19
497	21:43:07.07	+66:02:19.1	14.501	0.038	13.755	0.035	13.575	0.030	23	22	22	0.68
498	21:43:07.08	+66:07:02.4	14.557	0.205	13.067	0.127	12.138	0.140	11	12	17	1.46
499	21:43:07.09	+66:09:21.1	16.365	0.046	15.190	0.034	14.700	0.033	24	25	27	0.17
500	21:43:07.24	+66:10:03.0	15.663	0.044	14.540	0.049	14.006	0.037	25	26	26	-0.10
501	21:43:07.57	+66:09:01.3	14.722	0.027	13.530	0.026	13.087	0.027	26	26	28	0.14
502	21:43:07.63	+66:07:04.8	0.000	99.000	15.924	99.000	14.063	0.223	00	03	16	1.24
503	21:43:07.76	+66:04:29.3	16.808	0.040	15.624	0.043	15.113	0.051	25	26	28	0.04
504	21:43:07.84	+66:07:18.5	16.491	0.214	14.785	0.114	13.889	0.121	23	25	28	4.62
505	21:43:08.81	+66:04:38.0	18.461	0.114	17.292	0.146	16.790	0.078	07	07	05	0.18
506	21:43:09.10	+66:06:23.7	0.000	99.000	17.468	0.229	15.371	0.223	00	05	25	2.26
507	21:43:09.13	+66:04:45.7	17.544	0.080	16.277	0.075	15.632	0.066	21	21	25	-0.00

Table 4.2—Continued

FMO ^a	R.A. (J2000.0)	Dec. (J2000.0)	J^b	σ_J^c	H^b	σ_H^c	K_s^b	$\sigma_{K_s}^c$	J	N_{obs}^d H	K_s	Stetson Index
508	21:43:09.53	+66:08:12.9	18.239	0.066	16.126	0.040	15.053	0.050	05	22	28	0.21
510	21:43:09.89	+66:05:48.5	15.473	0.035	14.305	0.028	13.855	0.035	26	26	28	0.68
511	21:43:09.92	+66:05:28.8	18.057	0.116	16.814	0.100	16.187	0.107	11	15	16	0.32
513	21:43:10.45	+66:02:39.3	0.000	99.000	16.645	0.097	15.446	0.064	00	16	24	0.06
514	21:43:10.53	+66:01:45.3	16.140	0.104	14.115	0.047	13.293	0.058	07	07	07	0.53
515	21:43:11.17	+66:04:25.5	17.994	0.098	16.191	0.142	15.099	0.111	08	23	26	1.36
516	21:43:11.19	+66:08:54.6	15.063	0.024	14.156	0.025	13.776	0.023	26	26	28	-0.04
517	21:43:11.24	+66:09:19.6	17.316	0.190	16.641	0.203	16.289	0.186	17	14	12	1.23
518	21:43:11.24	+66:09:01.6	17.937	0.066	17.190	0.175	16.761	0.101	11	06	07	-0.49
519	21:43:11.63	+66:09:11.7	12.648	0.035	11.833	0.043	11.516	0.038	26	25	27	1.83
520	21:43:11.84	+66:03:37.4	16.711	0.032	15.314	0.017	14.695	0.037	24	26	28	-0.08
521	21:43:12.07	+66:06:44.3	18.446	99.000	15.039	0.062	13.425	0.046	03	26	28	1.71
524	21:43:12.26	+66:09:06.5	17.847	99.000	16.235	0.210	15.660	0.201	03	10	14	1.69
525	21:43:12.38	+66:09:55.6	14.828	0.115	13.926	0.095	13.500	0.068	25	26	27	5.93
527	21:43:12.44	+66:06:56.0	0.000	99.000	16.677	0.144	15.174	0.107	00	14	25	1.59
528	21:43:12.58	+66:06:17.6	0.000	99.000	16.638	0.082	15.093	0.075	00	16	27	0.33
529	21:43:12.83	+66:06:48.1	0.000	99.000	16.991	0.070	15.569	0.099	00	10	24	0.36
530	21:43:13.06	+66:09:40.3	17.242	0.052	16.091	0.071	15.644	0.071	21	23	23	-0.04
531	21:43:13.09	+66:05:50.5	14.862	0.027	14.041	0.025	13.695	0.030	26	26	28	0.23
532	21:43:14.15	+66:07:46.2	0.000	99.000	17.247	99.000	14.485	0.297	00	01	28	9.25
533	21:43:14.37	+66:05:54.5	18.539	0.158	16.778	0.048	16.014	0.082	06	17	20	-0.18
534	21:43:14.43	+66:08:59.0	16.046	0.042	15.345	0.047	14.887	0.042	26	26	27	0.48
535	21:43:14.47	+66:07:34.6	15.446	0.097	14.385	0.102	13.826	0.089	26	26	28	4.28
536	21:43:14.49	+66:07:24.0	16.623	0.039	15.824	0.098	15.206	0.176	26	25	27	1.13
537	21:43:14.70	+66:10:13.5	14.375	0.044	13.592	0.046	13.292	0.050	25	25	25	-0.25
538	21:43:14.78	+66:07:37.7	0.000	99.000	0.000	99.000	14.673	0.194	00	00	27	3.10
539	21:43:14.93	+66:10:00.0	16.890	0.040	16.084	0.050	15.742	0.071	21	21	21	-0.15
540	21:43:14.97	+66:09:07.0	14.814	0.024	14.059	0.028	13.869	0.019	26	26	28	0.10
541	21:43:15.02	+66:08:39.2	16.275	0.031	15.604	0.035	15.205	0.039	25	25	24	-0.17
542	21:43:15.30	+66:07:57.2	14.913	0.066	13.365	0.070	12.577	0.052	26	26	28	2.57
543	21:43:15.31	+66:07:16.4	0.000	99.000	17.362	0.102	16.196	0.150	00	08	19	0.02
544	21:43:15.45	+66:05:58.3	17.256	0.059	16.243	0.066	15.694	0.079	22	22	24	-0.05
545	21:43:15.72	+66:06:59.4	17.469	0.089	15.555	0.054	14.732	0.042	19	24	28	0.29
546	21:43:15.83	+66:08:46.5	18.654	99.000	16.544	0.086	15.582	0.059	02	16	27	0.01
547	21:43:16.37	+66:05:22.3	17.363	0.075	16.157	0.044	15.531	0.059	23	22	26	0.10
548	21:43:16.83	+66:05:48.6	14.163	0.068	13.280	0.067	13.000	0.065	26	26	28	7.63
549	21:43:16.99	+66:08:19.9	16.975	0.039	14.889	0.024	13.855	0.028	23	26	28	-0.19
550	21:43:17.53	+66:02:55.8	18.597	0.108	17.096	0.069	16.521	0.120	04	07	10	0.26
551	21:43:17.59	+66:04:18.2	14.913	0.020	13.871	0.018	13.437	0.022	26	26	28	-0.05
552	21:43:17.97	+66:08:15.5	17.823	0.150	16.130	0.065	15.282	0.063	12	21	24	0.18
553	21:43:18.07	+66:05:35.1	14.742	0.039	13.904	0.038	13.609	0.031	26	26	28	0.81
554	21:43:18.53	+66:05:17.4	18.040	0.052	16.867	0.079	16.387	0.079	12	12	10	0.08

Table 4.2—Continued

FMO ^a	R.A. (J2000.0)	Dec. (J2000.0)	J^b	σ_J^c	H^b	σ_H^c	K_s^b	$\sigma_{K_s}^c$	J	N_{obs}^d H	K_s	Stetson Index
556	21:43:18.68	+66:04:12.7	15.280	0.023	13.755	0.028	13.133	0.021	26	26	28	0.34
557	21:43:19.14	+66:04:07.8	18.831	99.000	17.488	0.127	16.667	0.119	02	08	08	-0.28
558	21:43:19.23	+66:05:20.4	17.396	0.047	16.169	0.064	15.657	0.054	21	24	26	-0.11
559	21:43:19.31	+66:09:28.7	15.550	0.025	14.859	0.029	14.593	0.036	25	26	26	0.04
560	21:43:19.33	+66:06:40.4	18.215	0.057	16.912	0.072	16.182	0.102	05	09	16	-0.00
561	21:43:19.37	+66:07:21.6	15.099	0.026	14.364	0.022	14.043	0.056	26	26	28	0.48
562	21:43:20.09	+66:09:40.9	18.307	0.142	17.222	0.092	16.760	0.091	07	07	05	-0.58
563	21:43:20.29	+66:08:20.4	17.175	0.079	14.733	0.036	13.554	0.040	22	26	28	1.44
565	21:43:20.87	+66:03:36.6	14.239	0.021	13.519	0.028	13.326	0.022	26	26	28	0.33
566	21:43:20.89	+66:06:51.9	15.590	0.042	13.757	0.028	12.990	0.044	26	26	28	0.83
567	21:43:21.06	+66:06:22.9	14.396	0.031	13.559	0.024	13.322	0.032	16	16	19	1.27
568	21:43:21.31	+66:06:24.3	14.061	0.025	13.442	0.020	13.193	0.026	16	16	20	-0.32
569	21:43:21.70	+66:02:45.7	12.786	0.022	12.427	0.030	12.353	0.019	26	26	28	2.34
570	21:43:21.74	+66:09:40.9	18.141	0.169	16.239	0.050	15.390	0.057	09	19	28	-0.06
571	21:43:21.91	+66:06:45.8	0.000	99.000	16.872	0.095	15.709	0.033	00	12	22	-0.32
572	21:43:22.70	+66:10:00.8	15.162	0.154	13.993	0.109	13.443	0.031	10	10	09	2.38
573	21:43:22.93	+66:04:07.8	18.622	99.000	17.085	0.082	16.578	0.072	03	09	09	-0.21
574	21:43:22.94	+66:09:58.7	15.024	0.034	13.681	0.031	13.052	0.041	09	13	17	0.81
575	21:43:22.98	+66:10:00.6	13.973	0.126	13.037	0.059	12.701	0.064	16	15	15	2.09
576	21:43:23.09	+66:04:40.0	18.556	0.071	17.198	0.095	16.632	0.060	04	07	10	-0.49
577	21:43:23.20	+66:03:52.6	18.136	0.046	16.910	0.090	16.405	0.059	09	13	13	-0.18
578	21:43:24.03	+66:09:14.2	17.545	0.064	15.891	0.048	15.167	0.051	18	23	27	0.02
581	21:43:24.91	+66:07:04.5	17.241	0.238	16.197	0.240	15.581	0.382	17	22	20	2.88
582	21:43:24.91	+66:04:41.5	17.168	0.062	15.787	0.050	15.092	0.042	22	25	26	0.02
583	21:43:25.26	+66:05:09.0	16.967	0.050	15.691	0.037	15.131	0.052	23	25	28	-0.27
584	21:43:25.47	+66:07:37.9	17.884	0.116	16.730	0.125	16.267	0.095	15	18	17	0.21
586	21:43:25.88	+66:05:54.8	16.519	0.044	15.206	0.036	14.664	0.041	26	25	28	0.14
587	21:43:26.13	+66:09:06.6	18.737	99.000	16.999	0.096	16.197	0.048	01	13	15	0.05
588	21:43:26.19	+66:07:34.0	18.190	0.129	17.032	0.139	16.556	0.120	05	10	09	0.03
589	21:43:26.62	+66:08:20.5	18.584	99.000	16.819	0.073	15.805	0.068	03	15	23	-0.07
590	21:43:26.79	+66:07:27.2	18.253	0.083	16.718	0.083	16.103	0.088	06	14	18	-0.34
591	21:43:26.96	+66:09:36.7	13.697	0.042	12.965	0.055	12.782	0.041	26	26	28	4.67
592	21:43:27.12	+66:10:03.3	17.514	0.127	16.582	0.077	16.189	0.090	19	17	11	0.05
593	21:43:27.31	+66:04:15.5	18.371	0.126	16.748	0.090	16.046	0.088	04	17	17	0.26
594	21:43:27.69	+66:04:30.7	18.382	0.141	17.114	0.094	16.628	0.102	06	07	06	0.35
595	21:43:27.81	+66:06:18.5	16.377	0.054	15.730	0.047	15.446	0.060	26	25	26	-0.02
596	21:43:27.84	+66:07:33.9	17.541	0.089	16.792	0.069	16.480	0.135	21	13	07	0.13
598	21:43:28.33	+66:01:57.0	16.753	0.067	15.708	0.069	15.243	0.064	09	09	10	0.17
599	21:43:28.46	+66:04:52.5	18.070	0.079	16.577	0.066	15.946	0.066	13	15	18	-0.18
601	21:43:28.97	+66:01:46.6	13.907	0.034	13.328	0.045	13.257	0.042	08	08	08	0.95
602	21:43:29.30	+66:05:55.6	16.124	0.143	15.014	0.133	14.373	0.104	26	26	28	4.32
604	21:43:29.49	+66:04:38.7	15.747	0.039	14.689	0.033	14.236	0.041	25	26	28	-0.22

Table 4.2—Continued

FMO ^a	R.A. (J2000.0)	Dec. (J2000.0)	J^b	σ_J^c	H^b	σ_H^c	K_s^b	$\sigma_{K_s}^c$	J	N_{obs}^d H	K_s	Stetson Index
606	21:43:29.91	+66:07:09.0	17.264	0.130	16.403	0.066	15.525	0.059	19	20	26	0.03
608	21:43:30.03	+66:08:37.8	17.899	0.090	17.091	0.186	16.911	0.137	14	09	04	0.36
609	21:43:30.13	+66:08:24.7	17.958	0.103	16.830	0.111	16.466	0.100	18	10	11	0.18
611	21:43:30.47	+66:09:04.1	18.297	0.082	17.266	0.182	16.835	0.069	06	08	04	-0.03
614	21:43:31.18	+66:07:43.4	15.633	0.040	14.940	0.045	14.690	0.036	26	26	28	0.32
615	21:43:31.20	+66:07:23.9	12.572	0.046	12.066	0.050	11.937	0.059	26	26	28	0.40
616	21:43:31.23	+66:09:54.4	11.228	0.049	10.264	0.035	9.945	0.046	24	23	24	0.31
617	21:43:31.73	+66:08:26.4	16.085	0.034	15.224	0.049	14.922	0.050	25	24	28	0.14
618	21:43:31.82	+66:08:50.7	14.076	0.112	13.020	0.064	12.469	0.095	25	26	28	16.79
619	21:43:31.83	+66:04:38.6	17.477	0.086	16.764	0.063	16.478	0.057	18	17	11	0.27
620	21:43:32.34	+66:07:44.7	17.408	0.058	16.156	0.086	15.630	0.087	20	25	28	0.20
621	21:43:32.71	+66:10:11.6	15.015	0.040	13.852	0.048	13.463	0.049	21	25	25	0.28
622	21:43:32.94	+66:07:25.8	15.831	0.068	15.274	0.072	15.028	0.052	22	24	28	0.28
623	21:43:33.73	+66:09:46.1	17.450	0.079	16.407	0.067	16.025	0.093	15	15	19	0.18
624	21:43:33.96	+66:03:30.0	18.048	0.144	16.538	0.094	15.880	0.075	11	15	22	-0.02
625	21:43:34.29	+66:02:04.1	15.907	0.155	14.961	0.113	14.619	0.063	10	13	09	1.13
626	21:43:34.57	+66:04:37.0	16.637	0.117	15.643	0.097	15.174	0.063	21	23	23	-0.28
627	21:43:35.41	+66:04:02.1	16.382	0.086	15.367	0.078	14.912	0.061	18	18	24	0.29

Note. — The right ascension units are hours, minutes, and seconds. The declination units are degrees, arcminutes, and arcseconds. The list is sorted by FMO identification numbers.

^aFan Fountain Observatory NGC 7129 infrared sources ID number.

^bAverage magnitudes over the total period of the monitoring campaign of this study.

^cObserved RMS.

^dNumber of detection in each band.

Table 4.3. *FanCam*-identified Variable Stars in NGC 7129

FMO ^a	R.A. (J2000.0)	Dec. (J2000.0)	K_s^b [mag]	$\sigma_{K_s}^c$ [mag]	χ_J^{2d}	χ_H^{2d}	$\chi_{K_s}^{2d}$	Stetson Index	Slope ^e [deg]
033	21:42:14.83	+66:07:13.0	13.526	0.058	35.9	95.3	26.9	1.487	-18.59
035	21:42:15.06	+66:10:08.4	14.777	0.064	4.5	24.2	3.1	1.440	42.30
049	21:42:16.91	+66:08:12.8	13.340	0.053	91.8	110.1	49.0	2.125	-19.09
054	21:42:17.68	+66:08:40.5	14.773	0.164	263.7	104.4	36.0	6.225	-6.37
055	21:42:17.75	+66:09:14.0	14.100	0.077	20.8	17.2	21.3	0.310	-28.51
058	21:42:18.17	+66:09:32.1	13.887	0.067	22.6	29.1	23.9	0.716	-24.38
064	21:42:18.70	+66:05:42.3	13.491	0.046	46.4	38.0	18.7	0.268	-13.42
065	21:42:18.92	+66:02:03.5	14.574	0.058	48.0	19.3	2.9	1.707	-14.77
069	21:42:19.07	+66:05:29.7	14.185	0.048	22.1	12.5	8.9	0.117	-23.71
078	21:42:20.07	+66:02:54.0	13.390	0.062	498.3	90.7	68.0	1.148	-30.21
085	21:42:20.52	+66:02:42.2	16.293	0.129	4.8	6.4	2.0	1.053	10.11
092	21:42:21.54	+66:02:04.5	13.873	0.055	45.0	36.4	6.8	0.562	-21.82
099	21:42:22.83	+66:07:52.9	13.249	0.035	32.9	32.9	23.8	0.310	-28.54
101	21:42:23.08	+66:06:04.3	13.382	0.104	259.8	156.6	136.9	8.021	-19.50
105	21:42:23.42	+66:08:47.4	13.447	0.043	83.2	30.9	31.7	0.803	-34.65
114	21:42:24.15	+66:07:11.0	15.984	0.099	28.2	2.2	1.9	-0.075	-37.94
119	21:42:24.55	+66:07:45.3	16.567	0.117	10.9	5.8	1.2	1.385	-51.89
121	21:42:24.80	+66:06:21.3	12.211	0.030	77.3	55.7	30.6	0.740	-22.27
122	21:42:25.26	+66:10:08.9	14.213	0.076	23.6	18.1	18.0	1.095	-35.16
141	21:42:28.11	+66:07:58.3	15.077	0.076	580.9	7.5	5.1	1.256	-37.32
156	21:42:29.39	+66:02:01.1	14.932	0.073	22.9	3.6	2.8	-0.294	-31.41
163	21:42:30.00	+66:02:07.8	13.262	0.071	82.7	21.7	30.2	-0.134	-32.85
173	21:42:31.93	+66:07:08.5	13.081	0.016	30.9	26.5	5.6	0.204	-19.50
178	21:42:32.51	+66:01:52.8	15.285	0.064	23.0	3.4	1.3	0.285	-29.85
195	21:42:34.72	+66:05:18.6	13.051	0.016	30.5	20.6	6.8	0.689	-23.65
201	21:42:35.75	+66:05:49.2	12.872	0.017	18.8	40.9	7.1	1.160	-25.62
209	21:42:37.03	+66:02:13.5	13.465	0.048	58.4	42.2	12.3	-0.621	-29.07
225	21:42:38.23	+66:04:06.2	12.841	0.018	17.9	23.2	12.1	0.106	-35.51
228	21:42:38.36	+66:08:28.2	10.021	0.027	134.7	52.5	37.0	0.184	-24.67
233	21:42:38.82	+66:06:35.9	12.298	0.084	2101.9	1139.7	385.9	22.049	35.50
235	21:42:38.97	+66:07:08.7	12.453	0.027	23.5	2.7	5.5	0.307	-56.46
237	21:42:39.14	+66:07:10.0	11.334	0.093	205.3	243.6	192.2	5.831	-11.89
253	21:42:40.33	+66:10:07.3	10.581	0.055	58.6	86.1	71.6	1.077	-24.20
255	21:42:40.57	+66:09:52.1	14.686	0.348	122.6	81.8	262.7	6.295	5.11
262	21:42:41.32	+66:03:33.5	12.727	0.024	17.9	21.6	15.2	-0.724	-36.58
270	21:42:42.44	+66:07:45.2	13.454	0.068	4.5	18.5	58.4	2.075	-52.47
274	21:42:43.35	+66:02:08.5	14.329	0.044	22.9	10.5	3.1	-0.255	-25.24
277	21:42:43.64	+66:04:20.2	15.068	0.146	13.6	21.3	15.1	2.729	-17.97
278	21:42:44.07	+66:08:53.4	13.335	0.030	17.8	21.2	15.6	0.497	-25.87
283	21:42:44.29	+66:10:06.9	14.226	0.066	22.6	16.0	13.6	0.521	-22.70
289	21:42:44.87	+66:05:03.3	15.643	0.116	63.2	5.0	3.8	1.659	-15.09
293	21:42:45.31	+66:04:15.9	16.409	0.196	18.2	8.4	4.3	1.737	20.71

Table 4.3—Continued

FMO ^a	R.A. (J2000.0)	Dec. (J2000.0)	K_s^b [mag]	$\sigma_{K_s}^c$ [mag]	χ_J^{2d}	χ_H^{2d}	$\chi_{K_s}^{2d}$	Stetson Index	Slope ^e [deg]
294	21:42:45.32	+66:07:04.5	13.422	0.020	13.0	5.4	4.3	1.019	-31.23
300	21:42:46.08	+66:05:56.3	12.797	0.022	21.3	9.9	12.1	1.008	-41.94
301	21:42:46.09	+66:10:20.2	13.366	0.086	37.0	43.0	45.6	1.193	-17.50
302	21:42:46.22	+66:06:56.5	12.948	0.042	55.5	34.5	26.3	2.963	-19.86
307	21:42:46.86	+66:06:57.5	12.027	0.067	124.5	107.4	141.4	4.418	-17.29
308	21:42:47.05	+66:04:57.8	11.056	0.031	19.0	16.1	44.3	1.731	-29.90
313	21:42:47.52	+66:07:03.2	13.432	0.042	17.1	17.9	14.8	2.335	-28.25
317	21:42:47.90	+66:06:53.0	12.035	0.022	58.5	86.7	16.7	2.130	-4.13
319	21:42:48.05	+66:05:05.0	16.559	0.514	10.3	1.3	20.0	1.851	4.66
323	21:42:48.23	+66:08:00.7	12.868	0.118	385.9	445.0	367.8	9.346	-18.27
325	21:42:48.87	+66:06:26.7	13.377	0.024	9.1	14.7	3.0	1.396	18.27
326	21:42:48.94	+66:06:42.5	15.433	0.124	7.8	3.3	4.5	1.198	-38.50
329	21:42:48.99	+66:06:54.7	14.872	0.175	28.1	29.7	23.7	3.257	26.64
334	21:42:49.43	+66:06:45.1	16.172	0.319	8.1	4.5	12.4	1.481	-70.63
338	21:42:49.96	+66:01:58.0	11.519	0.054	107.7	24.9	37.7	0.426	-33.78
339	21:42:49.97	+66:05:54.3	14.219	0.032	19.4	7.5	3.5	1.016	-25.72
343	21:42:50.58	+66:05:11.1	14.519	0.072	21.4	9.3	8.9	2.140	-49.14
346	21:42:50.92	+66:06:03.6	12.585	0.030	48.3	50.3	25.9	3.490	-27.27
347	21:42:51.05	+66:03:59.1	16.277	0.208	18.5	8.8	4.9	2.316	-36.60
349	21:42:51.41	+66:05:56.4	13.692	0.137	647.5	273.8	120.8	11.641	31.26
353	21:42:51.95	+66:06:33.8	13.102	0.020	23.6	21.0	3.2	-0.601	2.61
355	21:42:52.03	+66:09:44.9	13.985	0.042	41.9	20.2	10.3	0.371	-22.10
359	21:42:52.34	+66:05:35.1	13.207	0.029	42.8	26.2	12.8	2.462	-27.17
363	21:42:52.62	+66:06:57.4	12.072	0.068	79.8	81.0	43.0	2.511	-23.56
365	21:42:53.05	+66:05:13.0	14.268	0.127	33.0	20.7	21.7	3.399	-57.93
366	21:42:53.14	+66:07:14.8	13.394	0.176	320.6	400.4	295.4	11.545	39.39
368	21:42:53.22	+66:07:20.8	12.417	0.117	1461.4	1729.0	350.3	17.832	0.76
370	21:42:53.46	+66:09:19.9	14.287	0.241	159.5	149.4	216.6	9.212	37.05
371	21:42:53.50	+66:08:05.4	12.145	0.048	51.2	53.3	57.0	3.629	-41.46
375	21:42:53.93	+66:06:50.5	13.512	0.029	33.1	14.7	7.9	1.902	-34.46
380	21:42:54.59	+66:05:20.4	13.994	0.124	27.7	19.6	26.3	3.272	-48.40
381	21:42:54.76	+66:06:35.4	12.661	0.207	2500.5	1680.8	975.3	29.684	58.38
382	21:42:54.80	+66:06:12.2	13.324	0.182	105.6	32.4	111.8	5.251	-49.12
383	21:42:54.81	+66:07:27.0	16.317	0.143	13.6	5.0	1.7	1.465	47.82
384	21:42:54.82	+66:06:13.8	13.801	0.034	16.4	9.1	3.5	1.478	0.92
387	21:42:54.93	+66:06:31.2	13.486	0.035	17.1	7.8	8.5	1.252	-37.70
389	21:42:55.29	+66:06:25.4	12.526	0.033	28.8	98.0	24.2	2.085	-7.18
390	21:42:55.44	+66:07:25.4	15.481	0.107	11.1	4.5	3.0	1.241	-36.78
393	21:42:55.69	+66:06:44.9	14.342	0.106	115.2	81.3	28.6	5.184	-7.82
395	21:42:55.80	+66:05:42.7	14.035	0.152	58.4	46.0	60.4	5.087	-52.69
399	21:42:55.92	+66:07:20.9	12.417	0.104	315.0	370.3	277.4	10.413	-40.72
400	21:42:56.04	+66:05:39.5	16.737	0.217	74.1	3.3	2.8	3.475	66.62

Table 4.3—Continued

FMO ^a	R.A. (J2000.0)	Dec. (J2000.0)	K_s^b [mag]	$\sigma_{K_s}^c$ [mag]	χ_J^{2d}	χ_H^{2d}	$\chi_{K_s}^{2d}$	Stetson Index	Slope ^e [deg]
401	21:42:56.08	+66:06:52.6	17.035	0.148	13.9	2.2	0.8	1.463	71.14
403	21:42:56.24	+66:06:02.2	11.408	0.045	44.6	38.5	48.1	1.930	-33.85
404	21:42:56.33	+66:07:03.4	15.488	0.137	8.4	11.1	8.9	1.556	-21.41
408	21:42:56.76	+66:06:37.3	12.203	0.073	215.1	173.9	94.5	3.798	-19.21
412	21:42:57.20	+66:06:34.7	12.531	0.030	25.3	65.0	7.2	1.839	-0.90
415	21:42:57.45	+66:07:14.9	12.965	0.041	18.0	21.6	27.4	1.155	-43.76
417	21:42:57.71	+66:04:23.3	13.907	0.103	0.0	16.9	16.7	2.340	5.80
419	21:42:57.83	+66:05:55.4	14.732	0.249	0.0	5.6	10.7	1.097	-22.02
422	21:42:58.09	+66:05:54.5	12.393	0.070	35.1	29.9	30.6	1.498	-41.41
423	21:42:58.10	+66:07:39.4	13.082	0.044	33.4	16.8	30.6	1.148	-35.57
424	21:42:58.22	+66:05:40.2	13.264	0.092	45.8	56.6	38.5	3.754	-44.31
426	21:42:58.33	+66:07:26.3	11.951	0.048	41.6	85.8	79.4	2.978	-43.64
427	21:42:58.35	+66:05:27.4	12.608	0.140	156.2	178.0	123.9	4.593	-13.60
428	21:42:58.36	+66:06:16.7	13.115	0.144	32.9	7.1	7.1	2.226	-31.34
430	21:42:58.58	+66:05:34.8	15.155	0.225	0.0	43.1	18.5	2.180	-3.94
433	21:42:58.74	+66:06:36.9	12.462	0.035	105.9	48.7	21.6	2.731	-35.78
434	21:42:59.23	+66:06:36.5	13.825	0.050	16.7	9.4	8.2	1.136	-35.38
439	21:42:59.60	+66:07:34.3	15.315	0.138	30.8	14.4	11.3	2.344	-46.65
440	21:42:59.60	+66:04:33.7	11.010	0.091	133.6	222.9	320.3	9.639	-8.48
441	21:42:59.83	+66:07:31.5	13.222	0.030	49.3	13.9	12.1	1.194	-23.52
443	21:42:59.98	+66:06:42.4	13.283	0.069	40.9	23.7	34.7	2.848	-46.69
444	21:43:00.19	+66:06:46.4	13.017	0.214	1147.8	747.3	381.6	17.426	46.93
445	21:43:00.23	+66:06:48.8	13.093	0.068	61.6	48.8	40.8	3.280	-8.02
446	21:43:00.24	+66:05:45.8	14.070	0.143	69.8	58.8	57.7	5.005	-61.40
449	21:43:00.33	+66:06:33.2	15.451	0.190	27.9	16.7	12.1	2.141	-21.47
452	21:43:00.76	+66:06:46.6	13.739	0.043	8.0	22.7	6.4	0.742	-38.53
455	21:43:01.35	+66:06:36.7	15.585	0.170	11.1	9.4	7.0	1.050	-20.14
457	21:43:01.58	+66:07:06.2	14.226	99.000	0.0	12.0	0.0	3.248	43.62
460	21:43:01.69	+66:07:09.0	10.449	0.114	92.6	179.5	113.8	3.468	-30.56
462	21:43:01.88	+66:06:44.8	11.949	0.052	179.5	137.0	80.7	5.576	-39.07
463	21:43:02.00	+66:04:02.6	15.198	0.095	0.0	0.0	7.0	1.483	-21.01
466	21:43:02.49	+66:07:03.8	12.663	0.117	26.4	33.8	22.0	2.697	-45.56
467	21:43:02.52	+66:05:34.7	16.830	99.000	20.2	13.2	0.0	1.878	-52.17
471	21:43:02.94	+66:06:56.5	13.451	0.122	21.2	18.3	23.6	2.722	-46.27
473	21:43:03.42	+66:05:26.4	12.057	0.086	90.6	447.1	153.8	4.153	-1.84
474	21:43:03.43	+66:05:39.9	16.330	0.151	13.2	1.8	2.4	1.306	-51.32
475	21:43:03.65	+66:06:26.4	15.334	0.305	85.4	46.7	41.8	4.376	30.34
477	21:43:04.31	+66:05:56.4	14.509	0.113	14.4	17.6	14.6	1.870	-51.83
479	21:43:04.98	+66:06:53.3	11.744	0.087	63.6	33.9	19.8	2.607	-51.38
484	21:43:05.43	+66:06:03.1	12.999	0.051	26.5	14.4	25.6	1.477	-40.81
487	21:43:05.77	+66:06:29.6	13.888	0.081	13.9	11.4	9.4	2.045	-39.36
491	21:43:06.03	+66:06:44.7	12.210	0.270	0.0	0.0	11.3	1.516	41.73

Table 4.3—Continued

FMO ^a	R.A. (J2000.0)	Dec. (J2000.0)	K_s^b [mag]	$\sigma_{K_s}^c$ [mag]	χ_J^{2d}	χ_H^{2d}	$\chi_{K_s}^{2d}$	Stetson Index	Slope ^e [deg]
493	21:43:06.48	+66:05:49.0	16.240	0.138	31.2	2.0	2.8	0.987	-38.28
496	21:43:06.96	+66:06:41.6	10.650	0.099	0.0	13.4	74.8	4.190	11.62
497	21:43:07.07	+66:02:19.1	13.575	0.030	49.3	19.3	7.1	0.682	-22.73
498	21:43:07.08	+66:07:02.4	12.138	0.140	13.9	9.2	9.9	1.469	-49.58
501	21:43:07.57	+66:09:01.3	13.087	0.027	22.0	24.3	16.3	0.142	-18.43
502	21:43:07.63	+66:07:04.8	14.063	0.223	0.0	0.0	9.6	1.245	15.42
504	21:43:07.84	+66:07:18.5	13.889	0.121	56.5	38.3	42.5	4.628	-1.63
506	21:43:09.10	+66:06:23.7	15.371	0.223	0.0	3.2	18.8	2.261	12.68
515	21:43:11.17	+66:04:25.5	15.099	0.111	2.7	8.4	10.1	1.362	17.16
517	21:43:11.24	+66:09:19.6	16.289	0.186	12.5	5.4	3.1	1.234	-57.71
519	21:43:11.63	+66:09:11.7	11.516	0.038	73.6	88.8	43.1	1.835	-13.83
521	21:43:12.07	+66:06:44.3	13.425	0.046	0.0	9.4	21.5	1.717	-8.68
524	21:43:12.26	+66:09:06.5	15.660	0.201	0.0	5.8	5.9	1.696	-29.96
525	21:43:12.38	+66:09:55.6	13.500	0.068	297.0	163.0	55.4	5.934	-2.40
527	21:43:12.44	+66:06:56.0	15.174	0.107	0.0	4.6	8.7	1.590	-2.49
532	21:43:14.15	+66:07:46.2	14.485	0.297	0.0	0.0	138.6	9.257	0.907
535	21:43:14.47	+66:07:34.6	13.826	0.089	90.4	79.3	28.1	4.283	-34.75
536	21:43:14.49	+66:07:24.0	15.206	0.176	2.3	5.4	12.4	1.132	-46.44
537	21:43:14.70	+66:10:13.5	13.292	0.050	45.1	37.6	26.8	-0.252	-23.66
538	21:43:14.78	+66:07:37.7	14.673	0.194	0.0	0.0	20.1	3.105	99.00
542	21:43:15.30	+66:07:57.2	12.577	0.052	39.3	116.4	64.8	2.572	-5.33
548	21:43:16.83	+66:05:48.6	13.000	0.065	216.7	164.2	88.5	7.635	-21.77
553	21:43:18.07	+66:05:35.1	13.609	0.031	42.4	27.3	9.4	0.812	-18.40
563	21:43:20.29	+66:08:20.4	13.554	0.040	4.2	5.7	16.3	1.444	-27.93
565	21:43:20.87	+66:03:36.6	13.326	0.022	32.0	29.9	9.3	0.334	-20.19
566	21:43:20.89	+66:06:51.9	12.990	0.044	14.8	20.1	57.6	0.832	-29.78
567	21:43:21.06	+66:06:22.9	13.322	0.032	12.9	9.5	6.7	1.270	-25.37
569	21:43:21.70	+66:02:45.7	12.353	0.019	357.1	256.6	47.2	2.346	-20.02
572	21:43:22.70	+66:10:00.8	13.443	0.031	33.8	37.3	5.0	2.385	4.76
575	21:43:22.98	+66:10:00.6	12.701	0.064	116.5	24.9	36.0	2.096	-37.34
581	21:43:24.91	+66:07:04.5	15.581	0.382	19.8	16.4	53.9	2.881	-44.28
591	21:43:26.96	+66:09:36.7	12.782	0.041	370.3	402.6	69.3	4.676	-22.55
602	21:43:29.30	+66:05:55.6	14.373	0.104	72.4	50.2	31.9	4.323	-11.45
615	21:43:31.20	+66:07:23.9	11.937	0.059	79.9	94.4	74.0	0.404	-17.67
616	21:43:31.23	+66:09:54.4	9.945	0.046	85.6	45.8	56.4	0.311	-28.13
618	21:43:31.82	+66:08:50.7	12.469	0.095	1051.9	500.7	732.1	16.799	-31.13
621	21:43:32.71	+66:10:11.6	13.463	0.049	16.6	25.6	17.3	0.284	-29.49
625	21:43:34.29	+66:02:04.1	14.619	0.063	47.6	20.0	4.5	1.131	6.35
626	21:43:34.57	+66:04:37.0	15.174	0.063	22.1	8.0	3.3	-0.286	-10.71

Note. — The right ascension units are hours, minutes, and seconds. The declination units are degrees, arcminutes, and arcseconds. The Table is sorted by R.A. and Dec. columns.

^aFan Fountain Observatory NGC 7129 infrared sources ID number.

^bAverage magnitude over the total period of observation.

^cObserved RMS.

^dReduced χ_ν^2 for each observed band.

^eLinear regression best-fit slope of the variation on the K_s vs. $H-K_s$ color-magnitude diagram.

Chapter 5

Summary and Conclusions

Two embedded clusters NGC 1333 and NGC 7129 were photometrically monitored from November 2005 through October 2007 using a UVa-developed near-infrared camera, *FanCam*, at Fan Mountain Observatory near Charlottesville Virginia. Two separate fields in NGC 1333 and one field in NGC 7129 were targeted with each covering $8.7' \times 8.7'$ field of view. Data sets were reduced and analyzed in the view of variability, cluster membership, and the evolutionary stage of the infant cluster.

We identified 110 variable objects in NGC 1333 and 166 variable stars in NGC 7129, using the Stetson index statistic (Stetson 1996) and a conventional reduced- χ^2 method. Color-magnitude and color-color diagrams composed of J , H , and K_s confirm the ultimate youth of the cluster age and the highly extincted circumstellar environment. The three band light curves are displaying temporally well correlated variability for many of the variable stars. Periodic properties are not determined for most of the sources. The spatial distribution densities of variable stars and IR excess YSOs are highest around the central areas of the clusters while non-variables spread over the field of view.

Spitzer-2MASS-identified IR excess YSOs (Gutermuth et al. 2008, 2004) were

compared with *FanCam* variable sources. 64 of the stars are matched as variable stars, reading 89% variability rate, in NGC 1333 and 35 out of 41 stars in NGC 7129. Of 42 *Chandra*-identified X-ray sources (Getman et al. 2002), 41 objects turned out to be variables in NGC 1333, reading virtually 100% variability rate. We present the 25 unmatched ones as new cluster member candidates in NGC 1333, with 15 brown dwarfs ($M < 0.075M_{\odot}$) and 10 very low-mass stars ($0.075 < M < 0.20M_{\odot}$). A total of 131 variable stars in NGC 7129 were not detected in the previous infrared excess source survey.

The general behavior of the Initial Mass Function of NGC 1333 is well consistent with the previous studies in other embedded clusters. It shows a Salpeter type increase in the low-mass stellar mass regime, reaches a peak at $\sim 0.1\text{--}0.2M_{\odot}$, and declines toward brown dwarf regime. The NGC 1333 IMF also shows a tentative secondary peak at $\sim 0.05M_{\odot}$, which was suggested by Muench et al. (2002) and Slesnick et al. (2004) in Trapezium Cluster and by Levine et al. (2006) in NGC 2024. We computed the substellar-to-stellar mass ratio in NGC 1333 ($R_{ss} = 0.34 \pm 0.07$). It is comparable to several previous works in other clusters within their error ranges but not consistent with all of them, which remains the universality of the brown dwarf formation fraction unresolved and requires more thorough study to make the issue clear.

The slope statistics in the K_s vs. $H-K_s$ color-magnitude diagram shows a single mode distribution peaked at near -20° , suggesting that accretion activity dominate the flux variation in the near-infrared bands. The strongest X-ray sources have the K_s vs. $H-K_s$ slopes between -30° and 0° , which is coincident with the angle of the single peak shown in NGC 1333 CMD slopes. From the comparison of four embedded clusters, we find a clue that the color-magnitude variability pattern may reflect the forming-stars' evolution history in its very early stage of cluster formation.

If we could establish the method with larger number of sample clusters, it will be a sensitive and powerful age-determination tool to understand the early stage evolution of star-forming clusters.

FanCam provides the University of Virginia's 31 inch telescope with a near-infrared observing capability that is relatively unique among small-aperture telescopes. *FanCam* features an $8.7' \times 8.7'$ field of view on a 1024×1024 Teledyne Imaging Sensors HAWAII-1 detector array. Its seeing-limited optical design, optimized for the *JHK* atmospheric bands, includes a field stop at the telescope focus, a doublet collimator, two 8-position filterwheels straddling a Lyot stop, and a doublet reimager. Four fold mirrors wrap the optical path onto a compact optical bench. The entire optical train is encased in a cryogenic dewar cooled by a closed-loop cooling system. Since its first-light observation in December 2004, *FanCam* has been robustly operated in every night weather permitted. It has been productive particularly at various Solar System objects, extragalactic supernova events, variability studies of a binary blackhole OJ 287 and the embedded clusters NGC 1333 and NGC 7129, etc.

Appendix A.

A Hand-held NIR Spectrograph for Earth Observations from Space

Article appears in SPIE Proceedings 6265:62653W, 2006 July

Authors: Kanneganti, Park, Hershley, Smith, Skrutskie, Wilson, Traub, Lam,
& Nelson

Dr. Gregory Olsen's private flight to the International Space Station (ISS) in October 2005 provided an opportunity for scientific work during his seven day stay. Dr. Olsen suggested that the Instrumentation Laboratory of the Astronomy Department at the University of Virginia devise an experiment for the mission that would take advantage of a Sensors Unlimited SU320-M focal plane array camera. Astronomical studies were a research possibility, however the Earth's atmosphere is largely transparent in the $0.86\text{--}1.72\mu\text{m}$ spectral response range of the focal plane and the entire sky has been surveyed from the ground to significant depth ($\sim 15\text{ mag mJy}^{-1}$) with good spatial resolution ($\sim 3''$) at near-infrared wavelengths. Opportunities for original near-infrared astronomical research from the ISS are thus quite limited, particularly if restricted to hand-held equipment.

One astronomical object, uniquely accessible from space and infrequently imaged by astronomers is the Earth itself. At present, the infrared spectrum of the Earth is of great interest due to its applicability in interpreting the spectra of yet-to-be-discovered terrestrial-mass planets orbiting nearby stars. Although an armada of satellites orbit the Earth carrying extensive spectral analysis capabilities, few can produce integrated light spectra that mimic the view of an extraterrestrial “Earth” rotating in the gaze of a powerful space-based interferometer/spectrograph such as TPF-I. To date some of the best representations of the integrated light spectral signature of Earth come from Earth-based observations of the earthshine illuminated Moon at crescent phase (Woolf et al. 2002; Tinetti et al. 2006).

The ISS provides a vantage point approximately 350 km above the Earth surface. Although not a hemispheric view of the Earth, the instantaneous view from the ISS typically encompasses a mixture of terrains and cloud types while orbital motion continuously changes the mix. The 0.86-1.72 μm spectral region is rich in “biomarkers” (Des Marais et al. 2002) containing molecular features of water/ice, methane, oxygen, carbon dioxide, and carbon monoxide. Given the natural match between potential Earth spectroscopic science and the capabilities of a hand-held spectrograph on the ISS, the Virginia Astronomical Instrumentation Laboratory embarked on a project to supply Dr. Olsen with a hand-held near infrared spectrograph that could couple trivially to an SU320-M infrared camera. The small scope of the project lent itself to undergraduate and graduate student involvement and, from the beginning, the project was pursued by a mix of faculty/undergraduate/graduate students. As with any space project, mass and volume were primary constraints. Dr. Olsen requested that the mass of the spectrograph not exceed 1500 grams (independent of the camera) and that the instrument fit in a volume $30 \times 20 \times 15$ cm.

A Hand-held Near Infra-Red Slit Spectrograph for Earth Observations

Srikrishna Kanneganti, Chan Park, Heather Hershley, Aaron Smith, Michael Skrutskie, John Wilson (University of Virginia)
WesTraub (Jet Propulsion Laboratory), Charles Lam and Matthew Nelson (University of Virginia)

Introduction

Dr. Gregory Olsen's private flight to the International Space Station in October 2005 provided an opportunity for scientific work during his 7-day stay and he suggested that the Instrumentation Laboratory at the Astronomy Department at the University of Virginia devise an experiment for the mission that would take advantage of a Sensors Unlimited SU320-M focal plane array camera.

Of all the easily observable astronomical targets, the one object uniquely accessible from space and infrequently imaged by astronomers is the Earth itself. At present, the infrared spectrum of the earth is of great interest due to its applicability in interpreting the spectra of yet-to-be-discovered terrestrial-mass planets orbiting nearby stars. To date some of the best representations of the integrated light spectral signature of Earth (such as would be observed for exo-planets by TPF-I) come from Earth-based observations of the earthshine illuminated Moon at a crescent phase (Woolf et al. (2002) & Tinetti et al. (2006)).

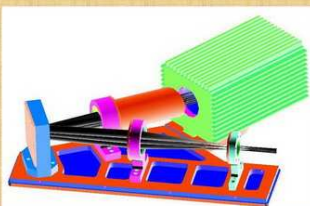
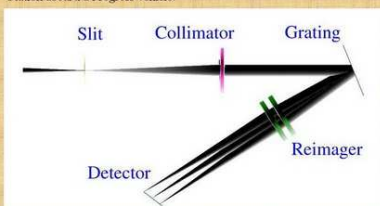
To utilize this opportunity for observing spectral signatures of Earth, we have devised a compact, hand-held, light-weight spectrograph that can be easily assembled to the SU320-M camera and provide an R=200 spectrum in the wavelength range of 0.84 μ m-1.72 μ m. The spectrograph has been space-qualified and one of the three copies was flown to the Space Station aboard a Progress vehicle.

Scientific Motivations and Design requirements

The SU320-M InGaAs 320 x 240 focal plane provided the basic constraint for defining the science possibilities for this experiment. The InGaAs array is sensitive to light in the wavelength range of 0.84 μ m-1.72 μ m. Conveniently, this spans a complete octave of wavelength making first-order grating spectroscopy a natural choice for the instrument. Furthermore, analysis of terrestrial spectra show this spectral range to be rich in molecular signatures with methane bands, a biomarker of keen interest, spanning the entire region. Most of the molecular features in this spectral range are well resolved for spectral resolutions R > 100.

To take advantage of the large second dimension of the array, a "long-slit" configuration has been used in the design of the spectrograph. This would provide an opportunity to perform spatially resolved spectroscopy of large swaths of Earth's surface when observed from the Space Station. An option to obtain "scrambled" spectra of even larger area of the Earth is also retained.

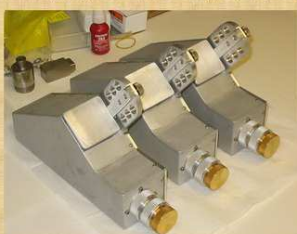
The restrictions on the design included a mass-limit of 1500gm, a constraint on the volume of 12m x 8m x 6 in. The design of the spectrograph also was required to allow accurate alignment and assembly of the spectrograph to an unmodified commercial SU320-M camera. To maintain operability when without the option of adjusting the integration time on the camera, the spectrograph should provide for control of illumination.



Design and Fabrication

The need to fabricate three copies of the spectrograph on a short timescale restricted the optical design to utilizing readily available components only. The optical components had to be mechanically strong and easy to procure at modest cost. As a result, the design was based entirely on commercially available BK7 lenses. Although BK7 is rarely used in the infrared, the material has good transmissive properties in the spectral range of interest. The optical design is shown in the picture above. The dispersive element is a blazed 150 g/mm reflection grating. The design predicts a monochromatic line-width of 10 μ m, comfortably smaller than the 40 μ m-wide pixels on the detector. The telescopic lens helps focus a spectrum of 30km x 1km swath of Earth's terrain onto the slit for spatially resolved spectra, while the diffuser would provide scrambled light from an area of 10,000 km² when observed from the Space Station. The use of solely BK7 lenses has produced a dramatic chromatic focal shift at the array plane. The effect is nearly linear with position on the array, due to the low dispersion and small wavelength range in question, and was effectively countered by a 20° tilt of the focal plane.

The mechanical design of the spectrograph is based on a "workbench" concept wherein all the components are mounted in small modules onto a single surface, making the assembly efficient and relatively tolerant to errors in assembly. To design provides for screw-in modules to hold the telescopic lens and diffuser that can be interchanged readily. Also available are aperture disks that can be used with both the screw-in modules to regulate illumination of the spectrograph. All the machined parts were light-weighted to reduce weight. Additional care was taken in choosing materials, parts, mounting schemes and machining practices to fulfill payload requirements for human-spaceflight. The mechanical design and the spectrograph interior are shown in the top center-right images.



Performance and Results

All three copies of the spectrograph weigh 573g in the flight configuration, shown on the right, and fit in a volume of 6m x 3m x 10m. The spectrographs were tested on ground and found to be identical in performance, ease of assembly and operability. The spectrograph was space-qualified and a copy of it flew to the Space Station on board Progress M-54.

The data from the detector is an NTSC video output which is recorded as digital video using a Sony PD-150 camcorder. The video frames are converted to fits images using the software iMovie, and the ImageMagick package. Despite these numerous transformations, the images retain remarkable consistency. The observing setup is shown on the bottom left with the video directed to a screen for demonstration.



A series of observations of various surfaces in reflected sunlight was carried out near noon on a partly-cloudy, low-humidity day. For each target 100 frames, worth 1.7s of exposure time, were extracted and reduced. Wavelength calibration was provided by an Argon lamp. The calibration is shown in the top panel of the picture on the right. The line-widths are about 1.8 pixels, leaving the resolution of the spectrum Nyquist-limited. Calculated plate-scale of 3.175 μ m/pixel provides a resolution R=206.6, which is a good match to the predicted resolution of 207.

A cleaned spectral image is shown in the middle panel on the right. Many of the spectral features revealed in the spectra in the bottom panel can be recognized in the image. The bottom panel presents initial spectra of various targets. Also included for comparison is an earthshine spectrum from Tinetti et al. (2006).

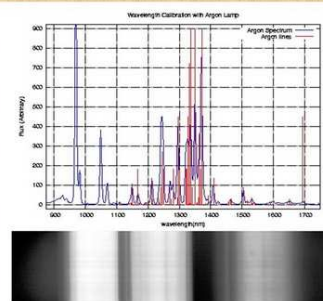


Figure 8. The top panel is a wavelength calibration using an argon gas lamp. The middle panel is a background corrected stacked image of 100 frames, or about 5 seconds of data. The bottom panel is a set of representative spectra. A spectrum from Tinetti et al. (2006) has been included (the dashed black line) for comparison.

References

1. N. J. Woolf et al., 2002, *Astrophysical Journal*, 574, 430
2. D. Tinetti et al., 2006, *Astrobiology*, 6, 34
3. D. J. D. Maras et al., 2002, *Astrobiology*, 2, 153

We acknowledge the generous support of Dr. Greg Olsen for this project. The University of Virginia Authors are also grateful for support from the F. H. Levinson Fund of the Peninsula Community Foundation.

Fig. A.1.— A summary of the Hand-held NIR Spectrograph project (Kanneganti et al. 2006). The poster was presented in SPIE 2006 at Orlando Florida.

Appendix B.

Feasibility of an Infrared Parallax Program using the Fan Mountain Tinsley reflector

Article appears in *New Astronomy* 15:547-553, 2010

Authors: Bartlett, Park, Kanneganti, & Ianna

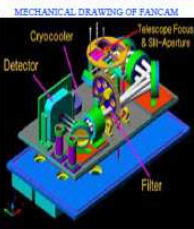
Despite the continuing importance of ground-based parallax measurements, few active programs remain. Because new members of the solar neighborhood tend towards later spectral types, infrared parallax programs are particularly desirable. Therefore, the astrometric quality of the new infrared camera, FanCam, developed by the Virginia Astronomical Instrumentation Laboratory (VAIL) for the 31 inch (0.8 m) Tinsley reflector at Fan Mountain Observatory was assessed using 68 *J*-band exposures of an open cluster, NGC 2420, over a range of hour angles during 2005. Positions of 16 astrometric evaluation stars were measured and the repeatability of those positions was evaluated using the mean error in a single observation of unit

weight. Overall, a precision of $1.3 \pm 0.7 \mu\text{m}$ in x (RA) and $1.3 \pm 0.8 \mu\text{m}$ in y (Dec) was attained, which corresponds to $0.04'' \pm 0.02''$ in each axis. Although greater precision is expected from CCDs in the visual and near-infrared, this instrument can achieve precision similar to that of the ESO NTT infrared parallax program. Therefore, measuring parallaxes in the infrared would be feasible using this equipment. If initiated, such a program could provide essential distances for brown dwarfs and very low mass stars that would contribute significantly to the solar neighborhood census.

The following AAS poster summarizes the infrared parallax feasibility study with *FanCam*.

Jennifer Lynn Bartlett (US Naval Observatory), Chan Park (Korea Astronomy & Space Science Institute/University of Virginia), Srikrishna Kanneganti (University of Virginia), Philip A. Ianna (University of Virginia)

CHARACTERISTICS OF FANCAM		
Parameter	Value	Reference
FPA	Rockwell Scientific HAWAII-1 Hg-CdTe thick, back-illuminated, coated	Ferrie 2002
FOV	8.7 arcmin ²	KCO9
Detector Size	1,024 × 1,024 pixels	Ferrie 2004
Pixel Size	18.5 μm ²	Ferrie 2004
Resolution	0.51° pixel ⁻¹	KCO9
Spectral Response	27.56–μm ²	
Field Curvature	0.85–2.5 μm	
Distortion	–50 μm	KCO9
Distortion	<0.1 pixel over 90% of field	KCO9
Detector Gain	9.3 pixel at corners	
Read Noise	4.6 e DN ¹	KCO9
Read Noise	17 e rms	KCO9
Dark Current	<0.1 e s ⁻¹	Belletti et al. 2003
Wall Capacity	>97 ke	Ferrie 2004
Quantum Eff., K	58.10 %	Ferrie 2004
Operating Temp.	80 K	Ferrie 2004



Frame Batch	X-Cordinate (mm)	Y-Cordinate (mm)	XZ-Averaged (mm)	Comment
All	1.31 ± 0.67	1.34 ± 0.77	1.32 ± 0.72	
Jan. & Nov. Early	1.27 ± 0.80	1.24 ± 0.79	1.24 ± 0.79	Frames within 15 minutes of meridian
Feb. & Nov. Late*	0.73 ± 0.34	1.33 ± 0.43	1.03 ± 0.46	Frames greater than 30 minutes west
Jan. Only	2.02 ± 0.88	1.88 ± 0.88	1.95 ± 0.75	2- and 3- exposures
Feb. Only	1.02 ± 0.57	1.73 ± 0.77	1.38 ± 0.75	Frames greater than 1600 miles west, 5- exposures
Nov. Only*	0.58 ± 0.58	0.83 ± 0.39	0.71 ± 0.32	All frames for November
Nov. Late*	0.57 ± 0.15	0.57 ± 0.15	0.69 ± 0.33	Frames within 15 minutes of meridian
Nov. Early*	0.60 ± 0.16	1.03 ± 0.22	0.82 ± 0.29	Frames greater than 30 minutes west

NOTE: * Astrometric evaluation star 7 dropped from these batches because it saturated in the Nov. frames averaged for a "trail plate."

Program	Average m.e.l. (μ m)		Median m.e.l. (μ m)	
	(μ m)	(max)	(μ m)	(max)
UV's FanCam, all	1.3	40	1.1	30
UV's FanCam, Nov. only	0.7	19	0.6	16
USNO ASTROCAM (Vera 2006)	0.2	3
ESO NIT Soff (1980's)	0.78	12.1

Detector	Pixel Size (μm^2)	Pixel Scale ($" \text{pixel}^{-1}$)
FuCAM (Jorda 2004, ECOO)	18.5	0.51
IRCAM (Vrba 2006)	40	0.54
ASTROCAM (Vrba et al. 2004)	27	0.3654
ESO NTT Soff	18.5	0.28826



Fan Mountain Observatory

- Dark site outside of Charlottesville, VA
- 78° 41.6' E
- 37° 52.7' N
- 556 m elevation
- Operated by UVa since mid-1960s
- Median seeing 1.5"



Results

FanCam infrared parallax program is feasible

- Resulting astrometric precision overall
 - α (α): $1.3 \pm 0.7 \mu\text{m}$ ($0.04'' \pm 0.02''$)
 - γ (δ): $1.3 \pm 0.8 \mu\text{m}$ ($0.04'' \pm 0.02''$)
 - xy-averaged: $\pm 1.3 \mu\text{m}$ ($\pm 0.04''$)
 - comparable w/ ESO NTT program (THOR)
 - better than photographic plates

FauCams could contribute to Solar

Neighborhood Census (25 pc)

- 1,131 stellar systems identified in northern hemisphere
(K. Slater 2009, priv. comm.)
- 3,125 systems expected in northern hemisphere
(K. Slater 2009, priv. comm.)
- New members probably intrinsically faint stars and brown dwarfs.

$\lambda_{\text{peak}} = 0.9 \text{ } \mu\text{m}$
(Drilling & Landolt 2000)

- 752 L and T dwarfs. 86 have parallaxes
(Orlin, Kirkpatrick, & Burgasser 2004)
- 119 northern brown dwarfs are possible solar neighborhood members
(K. Hatten 2009, www.gemini.edu)



31" (0.8-m) TINSLEY REFLECTOR

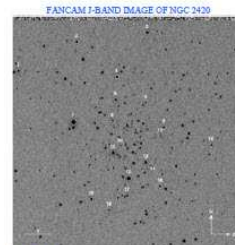
Parameter	Value
Objective Size	0.7810 m 30.73 in
Optics	classical Cassegrain
Focal Ratio	f/15.484
Effective Focal Length	12.19 m 480.0 in
Focal Plane Scale	16.92" mm ⁻¹

1121324C1: Tinsley Lab., 1983

Methods

FanCam mounted on UV's 31" Time reflector

- Observed NGC 2420, open cluster
- 68 I-band frames
- 16 astrometric evaluation stars
- Jan., Feb., & Nov. 2005
- Range of hour angle
- Flattened images: using custom IRA
tasks
- Measured positions using Southern
Parallax Program pipeline
(Sugan, Jara, & Patterson 2010, in prep.)
- Considered various frame
combinations



NGC 3420

Open Cluster for Astrometric Evaluation

- * 10- μ m, 1-band frame on 2005 May 9
- * 2MASS Prototype J filter
 - * Passband 1.105-1.395 μ m
 - * Central wavelength 1.250 μ m
 - * Transmittance 75% (ave)
 - * Limiting magnitude 19.0 (KCO9)
- * Astrometric evaluation stars identified
 - * Star 20 used as parallel star by reduction software used to grade frames and estimate seeing
 - * Stars 1, 2, 3, and 10 dropped because they do not appear in "trail plane"
 - * Star 7 dropped from several batches because it started in some Nova frames
- * FewCam misalignment with focal plane aperture obscures arcstart

REFERENCES

- Devlin, J. J., Park, C., Koenigsmann, B., & Wang, A. P. 2006, *New Astronomical Discoveries*, <http://dx.doi.org/10.1157/na.2006.1>
- Devlin, J. J., & Wang, A. P. 1995, 7022, *High Energy Astrophysical and X-ray Discoveries for Scientists* (Eds. D. A. Dorn & D. A. Helfand) (Bellingham, WA: SPIE) 702018
- Devlin, J. J., & Landolt, A. J. 2010, *IAU Symposium 282*, <http://dx.doi.org/10.1117/1.3364288>
- Drake, J. J. 2004, *Small Satellite Characterization*, <http://www.nasa.gov/pdf/108182main/SSC-04-001.pdf>
- Ennis, B. 2004, *Recovery of Data From Deep-Space Constellation*, CA: Academic (Scientific)
- Ennis, B. C., Karpigian, J. D., & Bergeron, A. J. 2004, *ApJ*, 604, 446, <http://www.astro.ucla.edu/~enris/>
- Ennis, B. C. & Jones, P. A. 1985, *ApJ*, 288, 448, 126
- Koenigsmann, S., Park, C., Shenolik, M. F., Wilson, J. K., Holmes, M. J., Smith, A. W., & Lam, C. 2006, *PASP*, 118, 606 (C1001)
- Torrey, G. C., Hargreaves, A. J., & Karpigian, J. D. 2003, *ApJ*, 593, 1735 (C0003)
- Twiss, R. K. 1998, *Optical Astronomical Telescopes*, Dordrecht, CA: Kluwer
- Tyler, T. 1998, in *Instrumentation in Astronomy XVI* (Eds. L. J. Campbell (Edinburgh, WA: SPIE) 733 (C048)
- Tyler, T. 1999, in *ASP Conf. Ser. 182: Astronomical Data Acquisition Systems and Software* (Eds. B. J. Barlow, B. V. Brakenridge, & J. J. Devlin) (ASP, 17) (BRAF)
- Van, J. 2006, in *IAU Symposium 282: Astronomical Data Acquisition Systems and Software* (Eds. B. J. Barlow, B. V. Brakenridge, & J. J. Devlin) (ASP, 17) (BRAF)
- Wang, A. P. 1995, *IAU Symposium 172*, 209, <http://www.astro.ucla.edu/~enris/>

ACKNOWLEDGEMENTS

The Levinson Fund, UVa Governor's Fellowship and Graduate School of Arts and Sciences, and Hampden-Sydney College funded this research, which used the NASA ADS Bibliographic Services. M. Skrutskie generously made observing time and archival observations available. K. Slattery, who maintains an up-to-date list of the nearest stars in association with the Nearby Star Observers, enthusiastically provided the counts of nearby systems and brown dwarfs. F. Vito graciously shared his experience with the USNO infrared parallax program. K. Riggelman contributed photographs of 31-inch telescope facility on 2009 November 15, which were further processed by J. Bartlett.

FOR MORE INFORMATION

Visit facility webpage at www.astro.virginia.edu/research/observatories/31inch

Fig. B.1.— A quick summary of the infrared parallax feasibility study with *FanCam* (Bartlett et al. 2010a). The poster was presented in AAS 215th 2010 January at Washington DC.

Appendix C.

Theoretical Estimate of FanCam Sensitivity

- Background-limited Equivalent noise electrons (in 10 minutes exposure time)
per pixel

$$\sigma_{eq} = \sqrt{\sigma_R^2 + \sigma_T^2 + \sigma_S^2 + \sigma_A^2} \quad (C..1)$$

where,

σ_R = read noise

σ_T = telescope thermal noise

σ_S = sky background noise

σ_A = airglow emission noise

$$\sigma_R = 30 \text{ electrons} \quad (C..2)$$

$$\sigma_T^2 = \varepsilon \cdot B(\lambda_c, T_T) \cdot \Delta\lambda \cdot \tau \cdot A_{pix} \cdot \Delta\Omega_T \cdot T_\lambda^T \div h\nu_c \quad (C..3)$$

$$\sigma_S^2 = B(\lambda_c, T_S) \cdot \Delta\lambda \cdot \tau \cdot A_{col} \cdot \Delta\Omega_S \cdot T_\lambda^S \div h\nu_c \quad (C..4)$$

$$\sigma_A^2 = N_\lambda^A \cdot \tau \cdot A_{col} \cdot \Delta\Omega_S \cdot T_\lambda^S \quad (C..5)$$

where,

$$A_{pix} = L_{pix} \times L_{pix} \text{ pixel area} \quad (C..6)$$

$$A_{col} = \frac{\pi}{4} \cdot D^2 \text{ collecting area} \quad (C..7)$$

$$\Delta\Omega_T = \frac{\pi}{4} \cdot \frac{D^2}{f^2} \text{ telescope solid angle} \quad (C..8)$$

$$\Delta\Omega_S = \frac{L_{pix}^2}{f^2} \text{ sky solid angle seen by a pixel} \quad (C..9)$$

$$T_\lambda^T = Dw \cdot Ls \cdot Ft \cdot Qe \text{ transmission of telescope emission} \quad (C..10)$$

$$T_\lambda^S = Mr \cdot T_\lambda^T \text{ transmission of sky light} \quad (C..11)$$

$$N_\lambda^A = \text{airglow number of photons } [s \cdot \text{cm}^2 \cdot \text{arcs}^2]^{-1} \quad (C..12)$$

- Input parameters

$$\varepsilon = 20\% = 0.2$$

$$(\lambda_J, \lambda_H, \lambda_K) = (1.25, 1.65, 2.2)\mu m$$

$$(\Delta\lambda_J, \Delta\lambda_H, \Delta\lambda_K) = (0.3, 0.35, 0.4)\mu m$$

$$T_T = 280K$$

$$T_S = 250K$$

$$\tau = 600s$$

$$L_{pix} = 18.5\mu m$$

$$D = 30inch = 76.2cm$$

$$f = 480inch = 1219.2cm$$

$$(Dw, Ls, Ft, Qe, Mr) = (0.95, 0.7, 0.6, 0.8, 0.9^2)$$

$$(N_J^A, N_H^A, N_K^A) = (0.2, 0.8, 0.7) \text{ photons } [s \cdot \text{cm}^2 \cdot \text{arcs}^2]^{-1}$$

- Limiting magnitude corresponding to the equivalent noise electrons

$$m_\lambda = -\frac{5}{2} \cdot \log \left[\frac{F_\lambda}{F_\lambda^o} \right] \quad (\text{C..13})$$

where,

F_λ = minimum flux density to be detected

F_λ^o = normalization flux from Vega

$\left[\frac{S}{N} \right]$ = signal to noise ratio

N_S = seeing disk pixel number

D_S = seeing disk diameter

$\Delta\Omega_S$ = sky solid angle per pixel

$$F_\lambda = \frac{\left[\frac{S}{N} \right] \cdot \sigma_{eq} \cdot \sqrt{N_S} \cdot h\nu_c}{\tau \cdot A_{col} \cdot \Delta\lambda \cdot T_\lambda^S} \quad (\text{C..14})$$

$$N_S = \frac{\pi}{4} \cdot \frac{D_S^2}{\Delta\Omega_S} \quad (\text{C..15})$$

$$(F_J^o, F_H^o, F_K^o) = (1600, 1000, 630) Jy \quad (\text{C..16})$$

$$\left[\frac{S}{N} \right] = 5 \quad (\text{C..17})$$

$$D_S = 2'' \quad (\text{C..18})$$

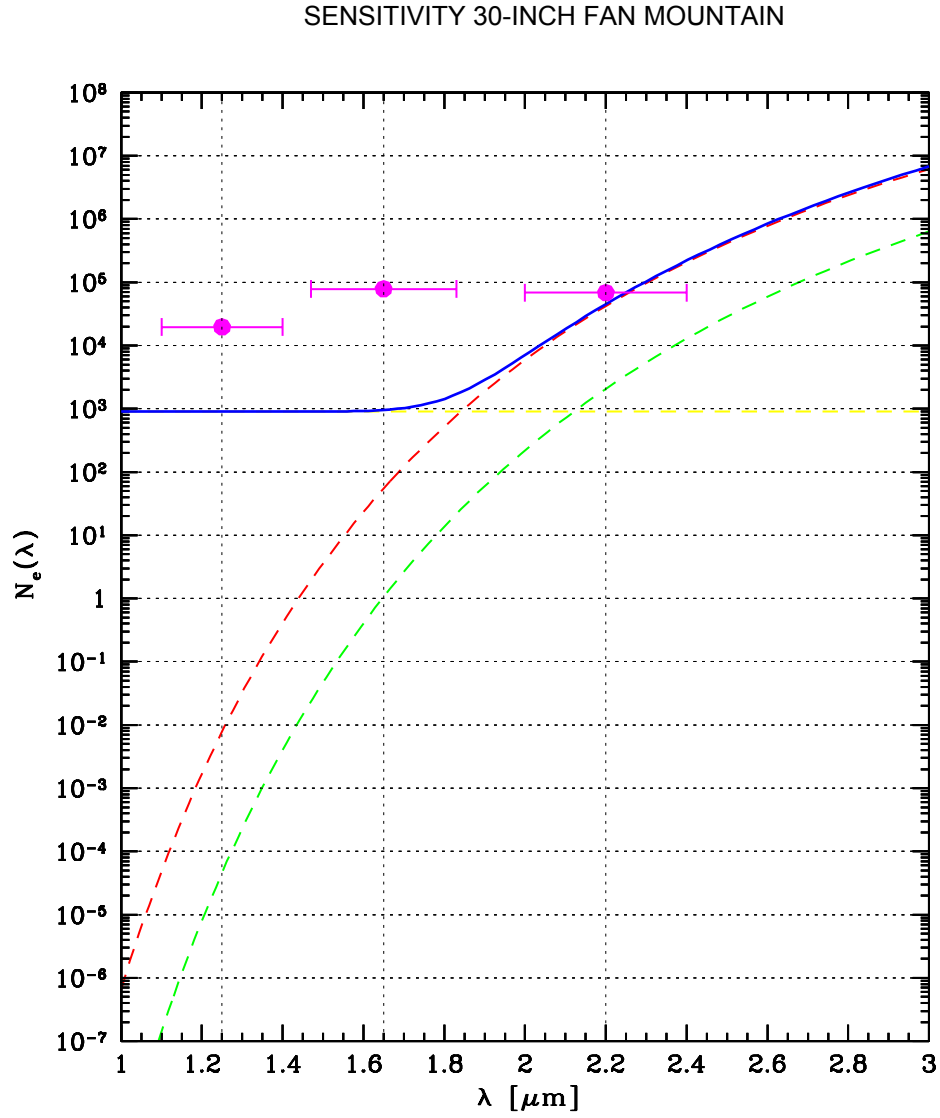


Fig. C..1.— Equivalent noise electrons in 10 minutes exposure for *FanCam*. Lower dashed curve is for sky background, upper one is for telescope thermal noise, and the solid line is for the sum of 2 thermal components and readout noise. Dots with wavelength ranges represent airglow components, which is dominant in *J* and *H* bands. In *K* band, airglow is competing with the sum of other components.

Appendix D.

FanCam Photometric Image Processing

A series of standard IRAF packages were used for *FanCam* data reduction. Several (5-10) dithered sky images were median-combined to establish a single master sky background frame. We then subtracted this sky background from each object image, which corrects non-uniform background level and fringe patterns generated by airglow emission through the optics system. The sky-subtracted object images were then divided by the normalized flat image. The master flat image was made by combining eight twilight flat frames, and subtracting a master dark image to cancel out the dark current component, although it is only a few counts, compared with typical 6000 counts of sky background at H and K_s bands and 1000 counts at J band.

A single master image was produced by combining multiple object frames with “average” as the type of combine operation. Dithered images were shifted into a reference frame using interpolation type “drizzle”, formally known as Variable-Pixel Linear Reconstruction algorithm (Fruchter & Hook 2002), with the pixel fraction parameter [0.5] for both of x and y directions. If pixels are undersampled, drizzle

works to improve the image resolution via combining multiple dithered images. For *FanCam* images, which are well sampled, drizzle just maintains spatial resolution while shifting an image. Outlying pixels were rejected from the image combine using the sigma clipping algorithm with 3σ lower and upper limits. One or two of the worst images, for example due to bad tracking, were excluded from the stacking procedure. Figure D.1 provides quick visual summary of the image processing steps used in this thesis data reduction.

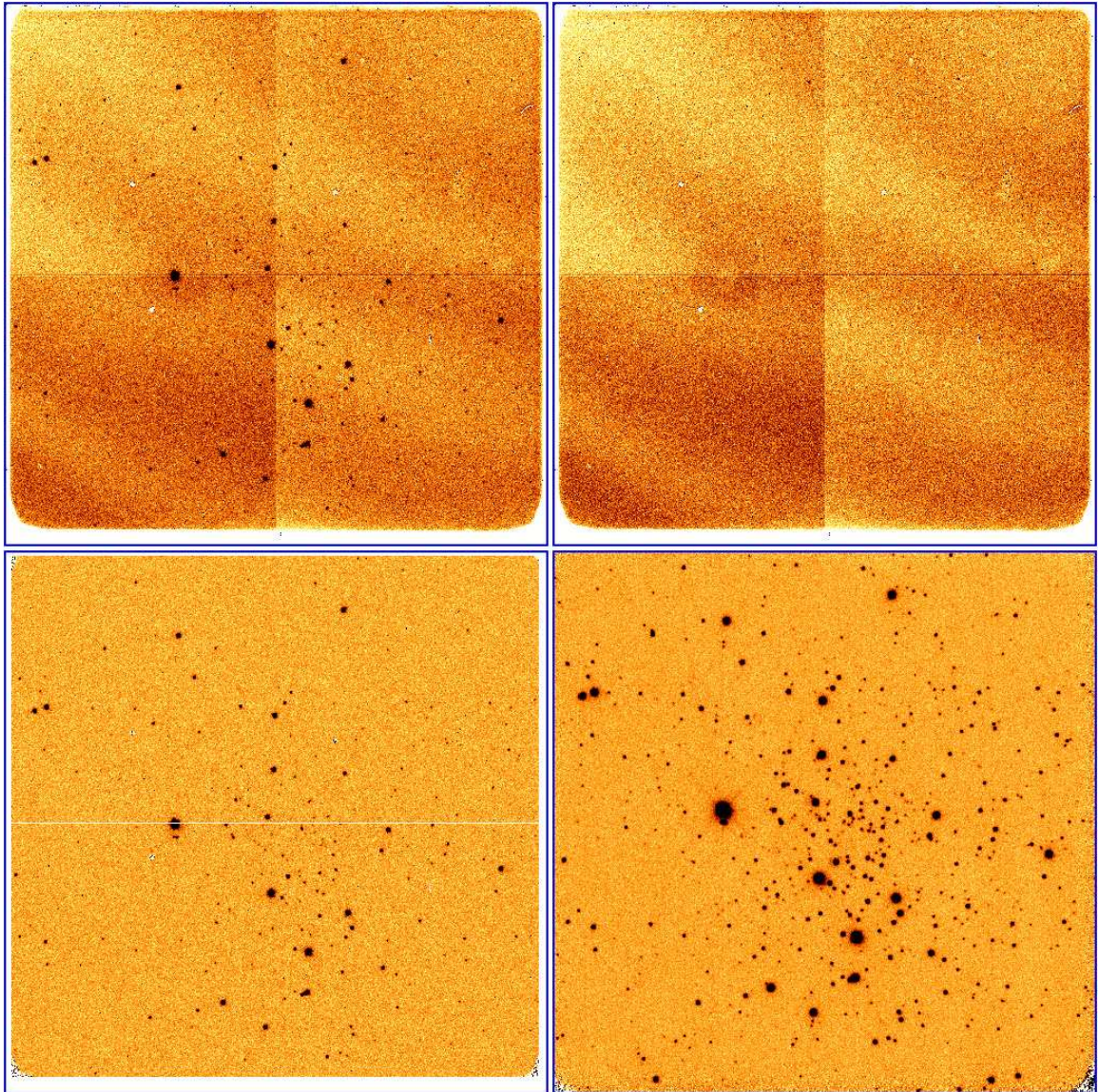


Fig. D..1.— *FanCam* photometric data reduction procedure. (*top left*) Raw image. (*top right*) Median-combined sky image. (*bottom left*) Raw image subtracted by the median-combined sky frame. (*bottom right*) Master object frame, combined 10 individual reduced object image, ready for photometry.

Appendix E.

More Examples of Light Curves and Color-magnitude Variabilities

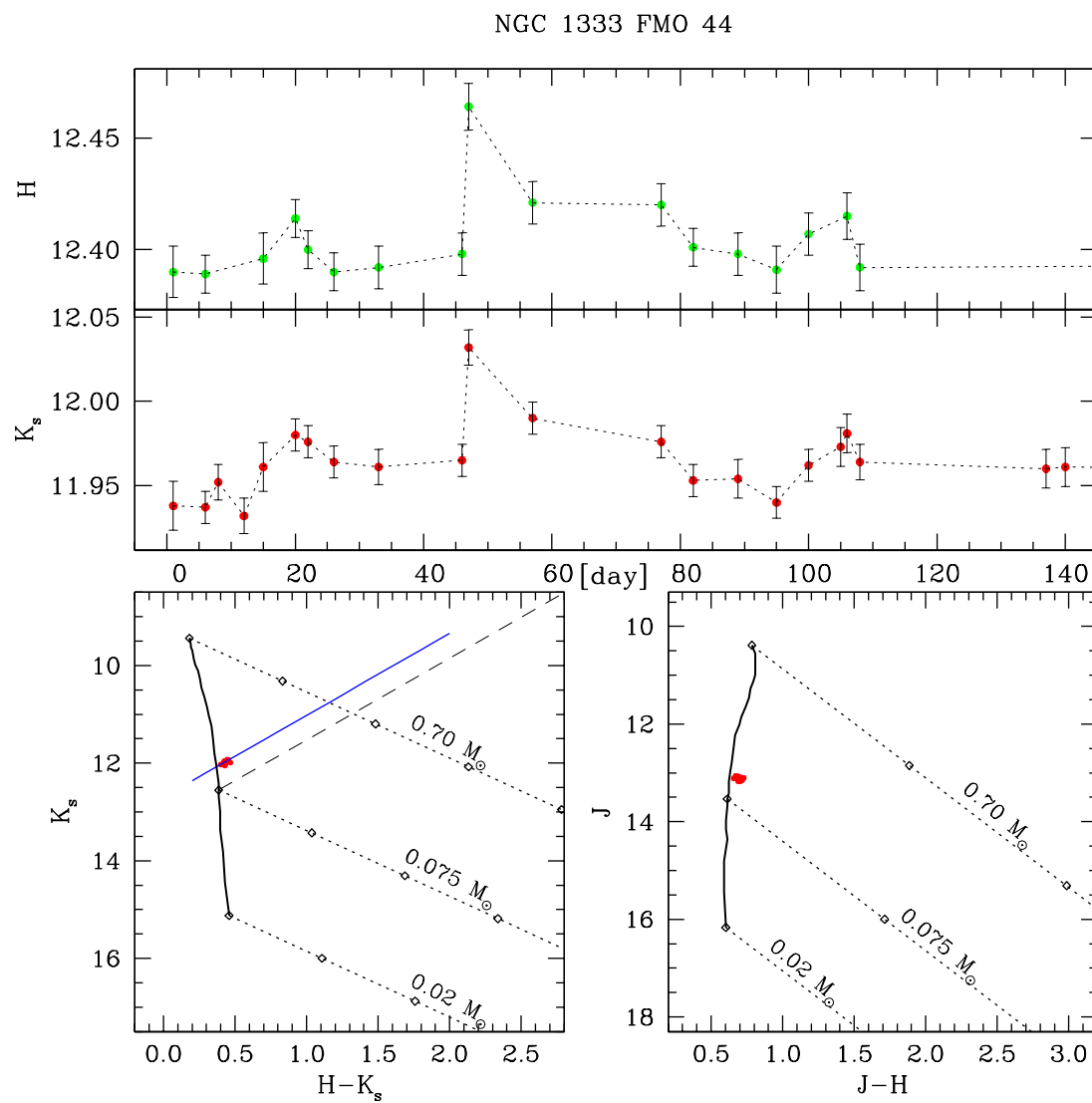
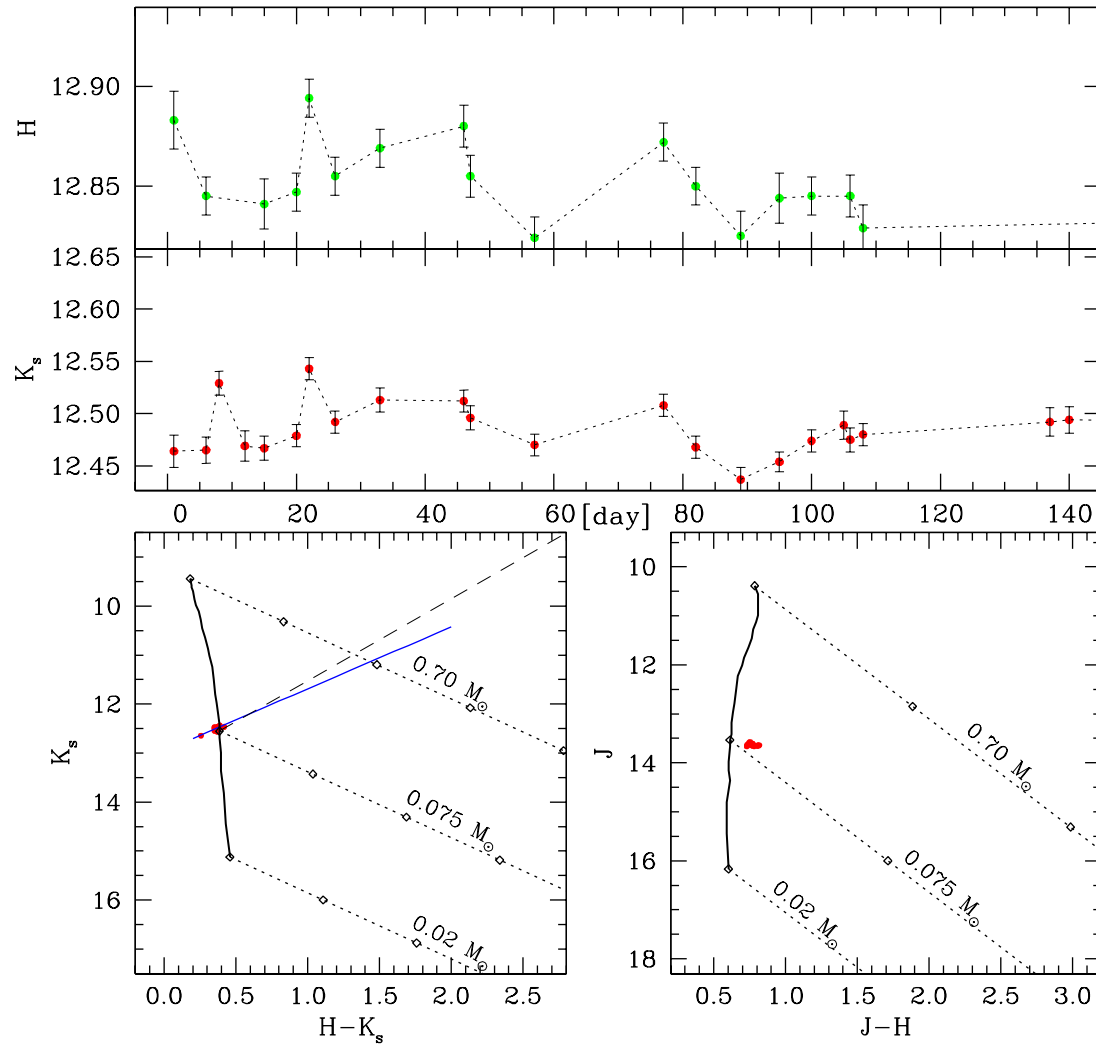
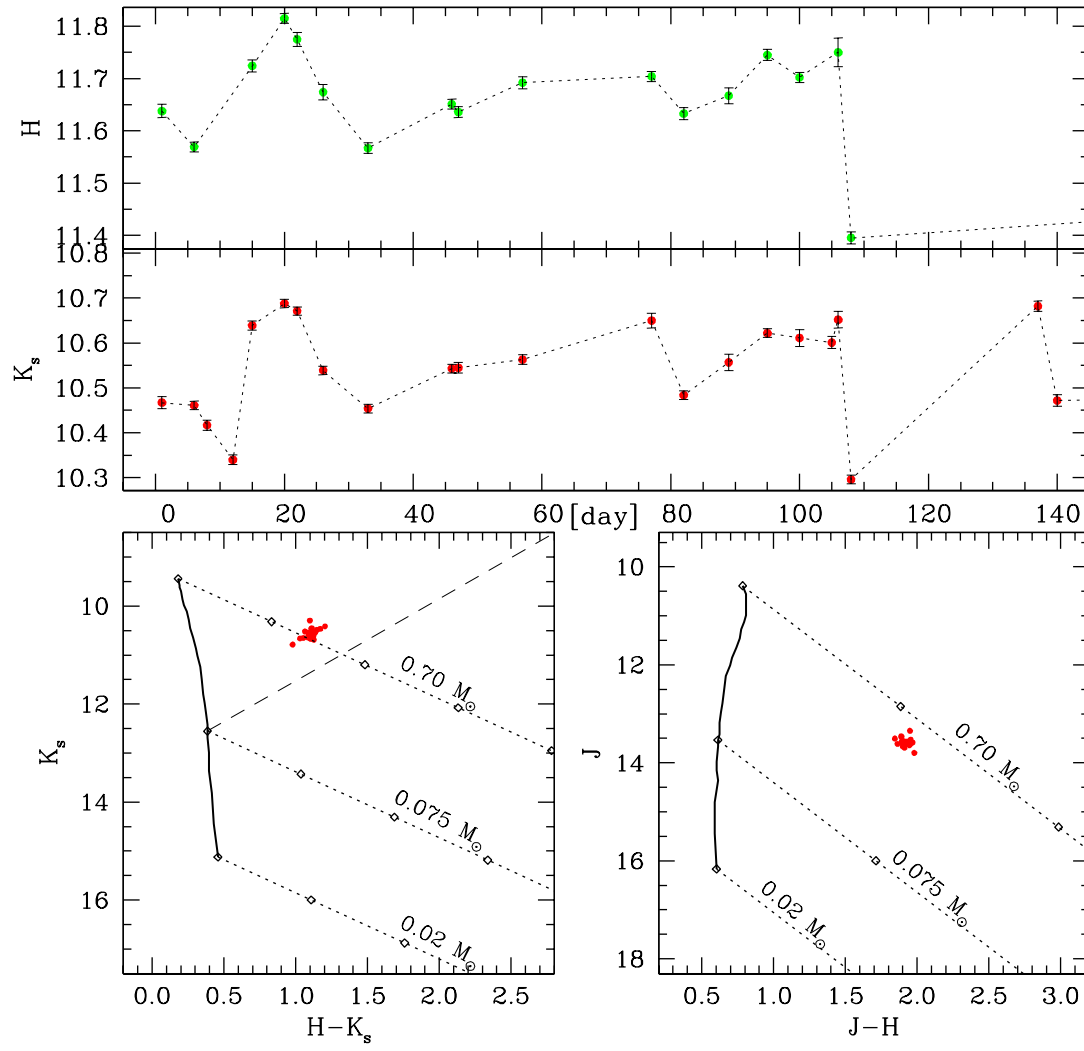


Fig. E.1.— Light curves and color-magnitude correlations for the variable star FMO 44 in NGC 1333.

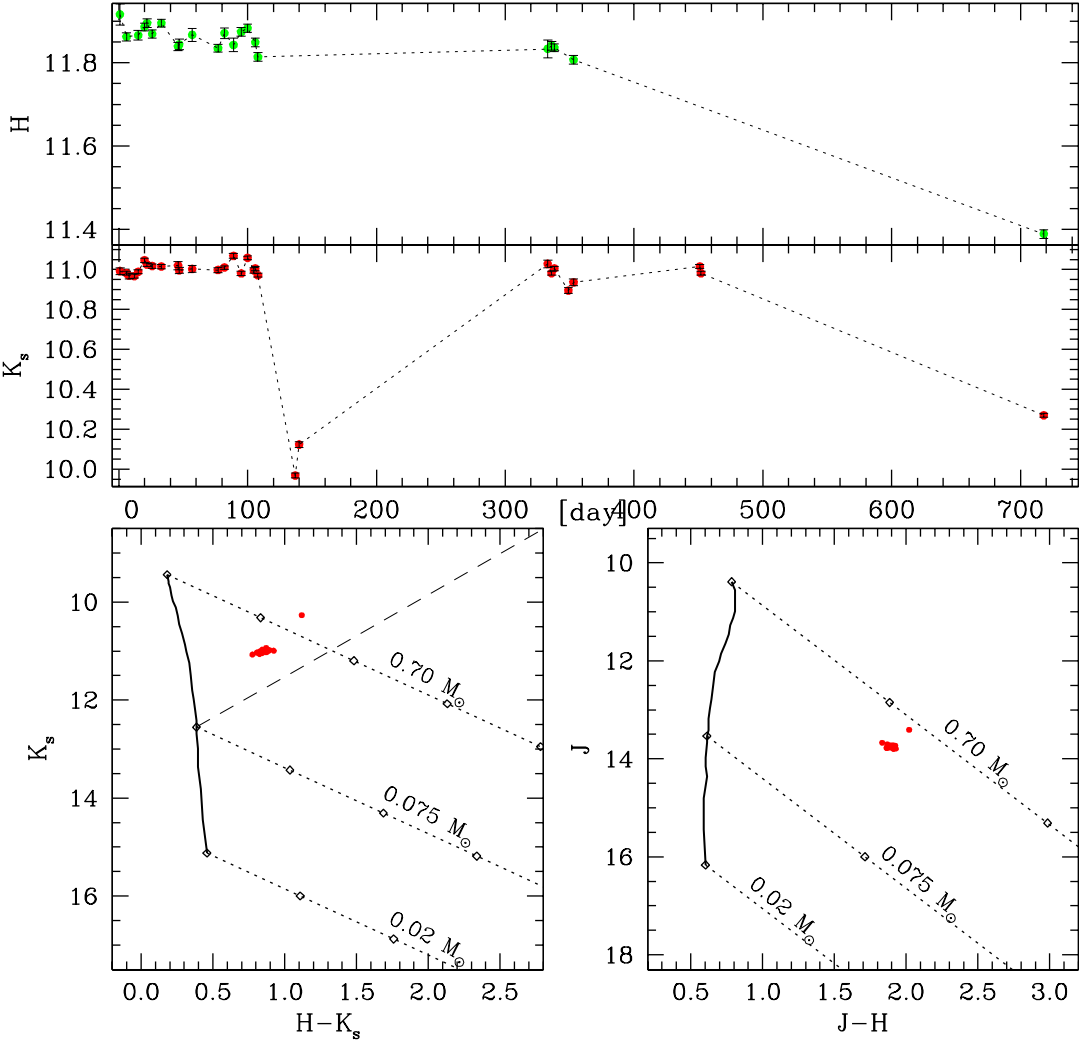
NGC 1333 FMO 46



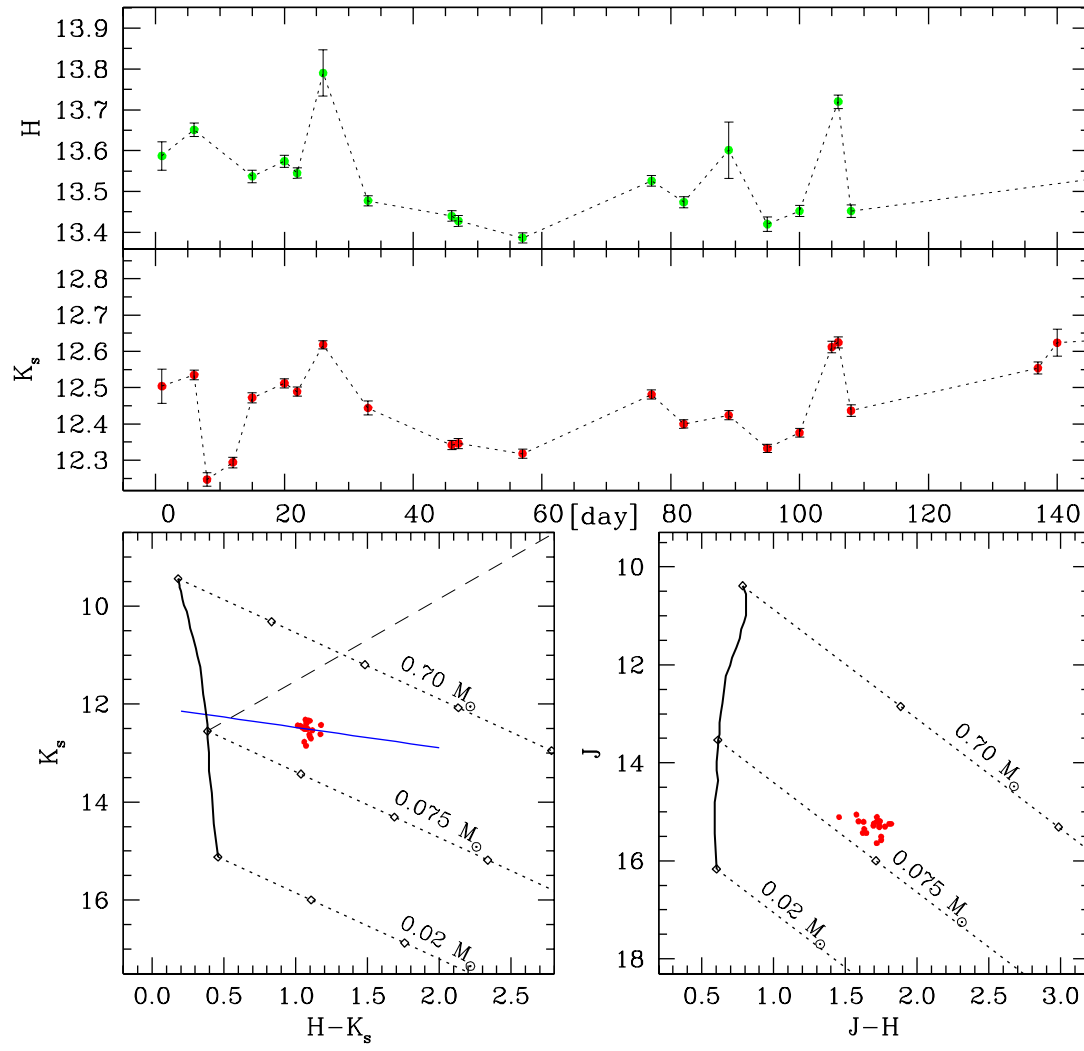
NGC 1333 FMO 52



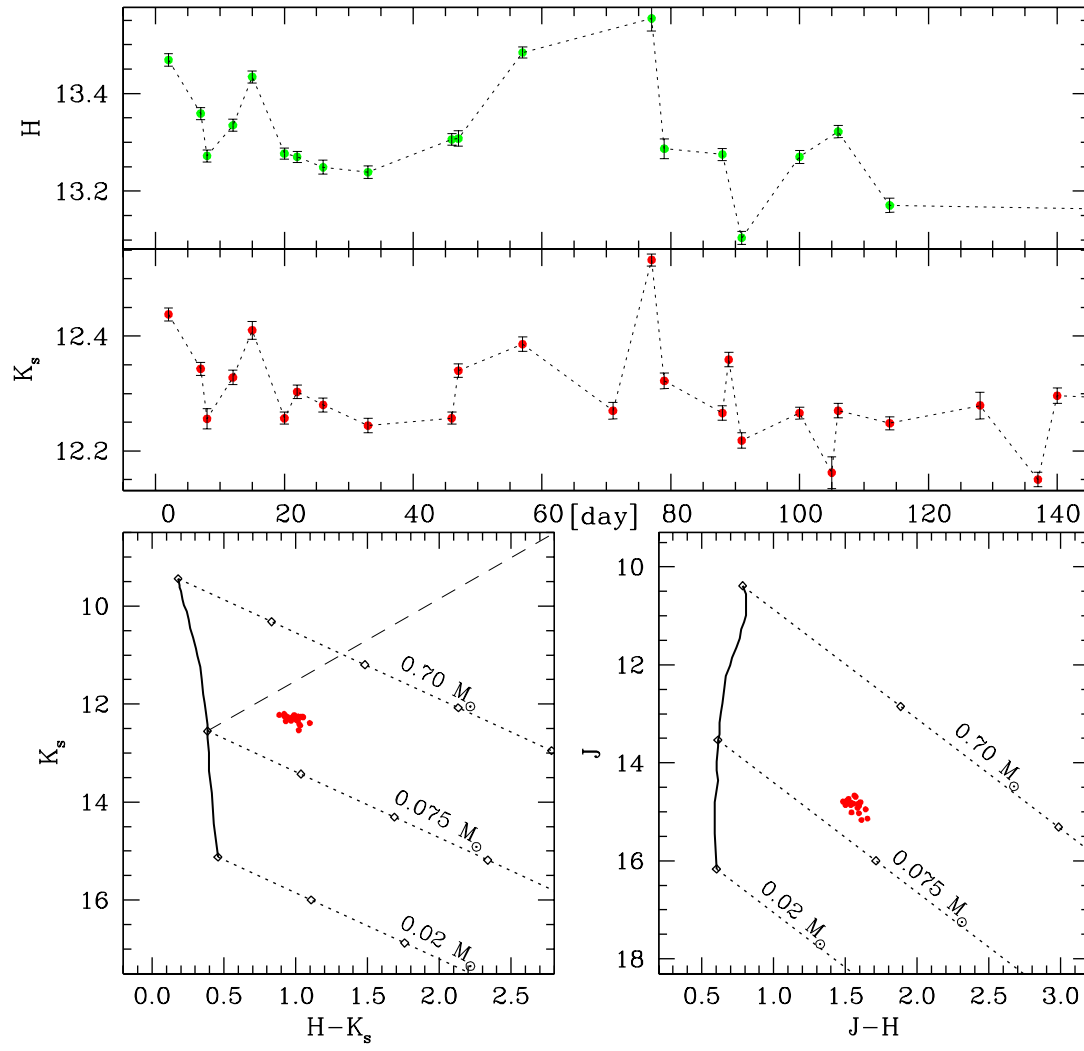
NGC 1333 FMO 68



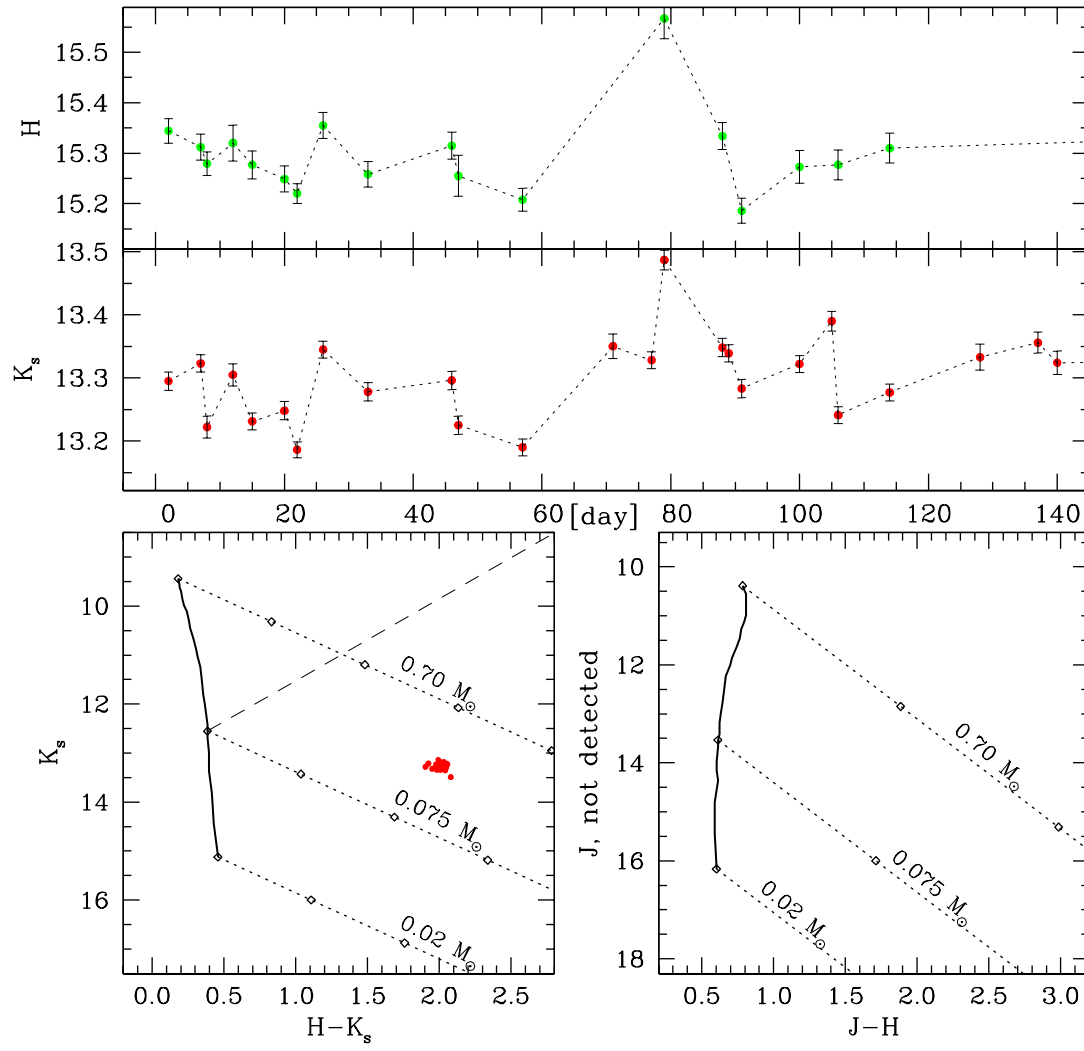
NGC 1333 FMO 109



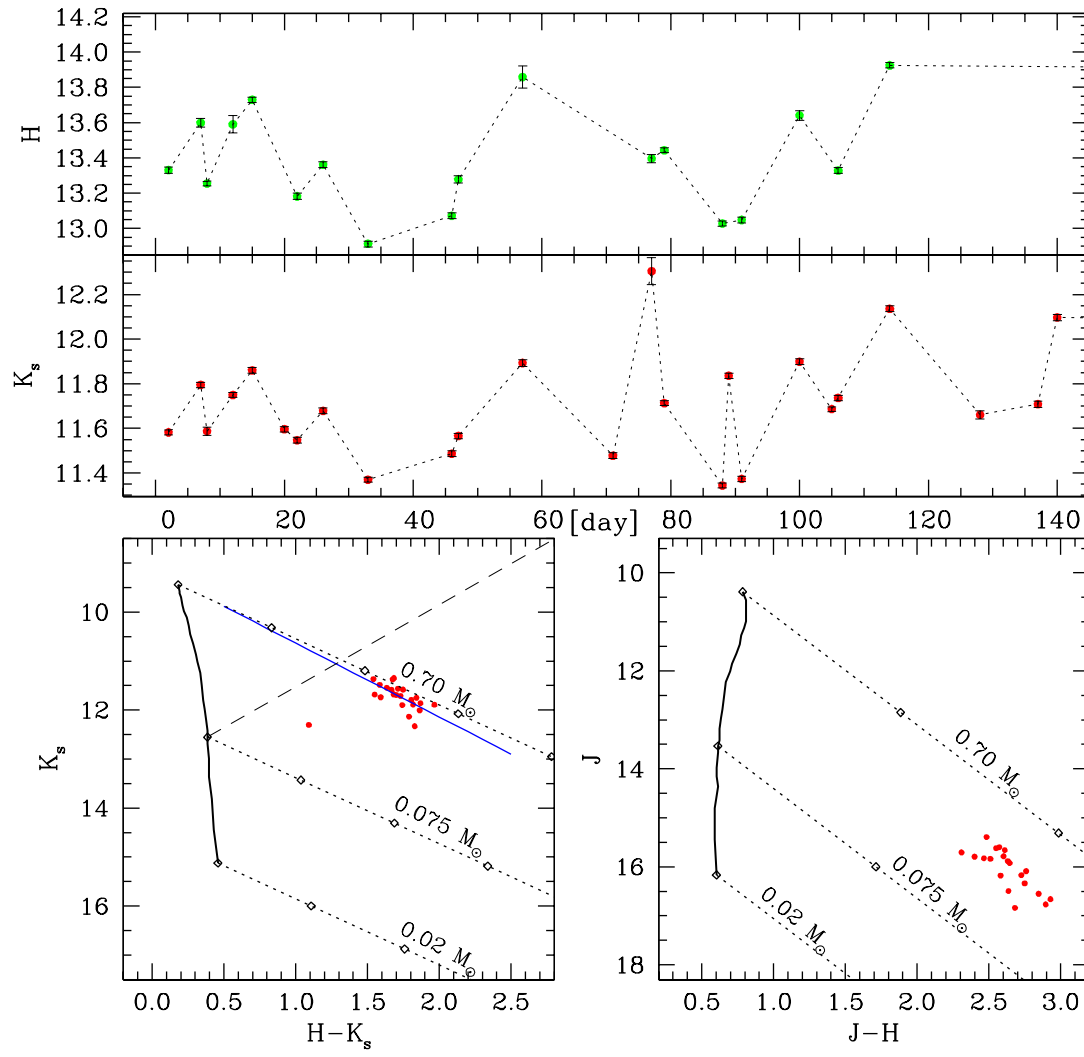
NGC 1333 FMO 135



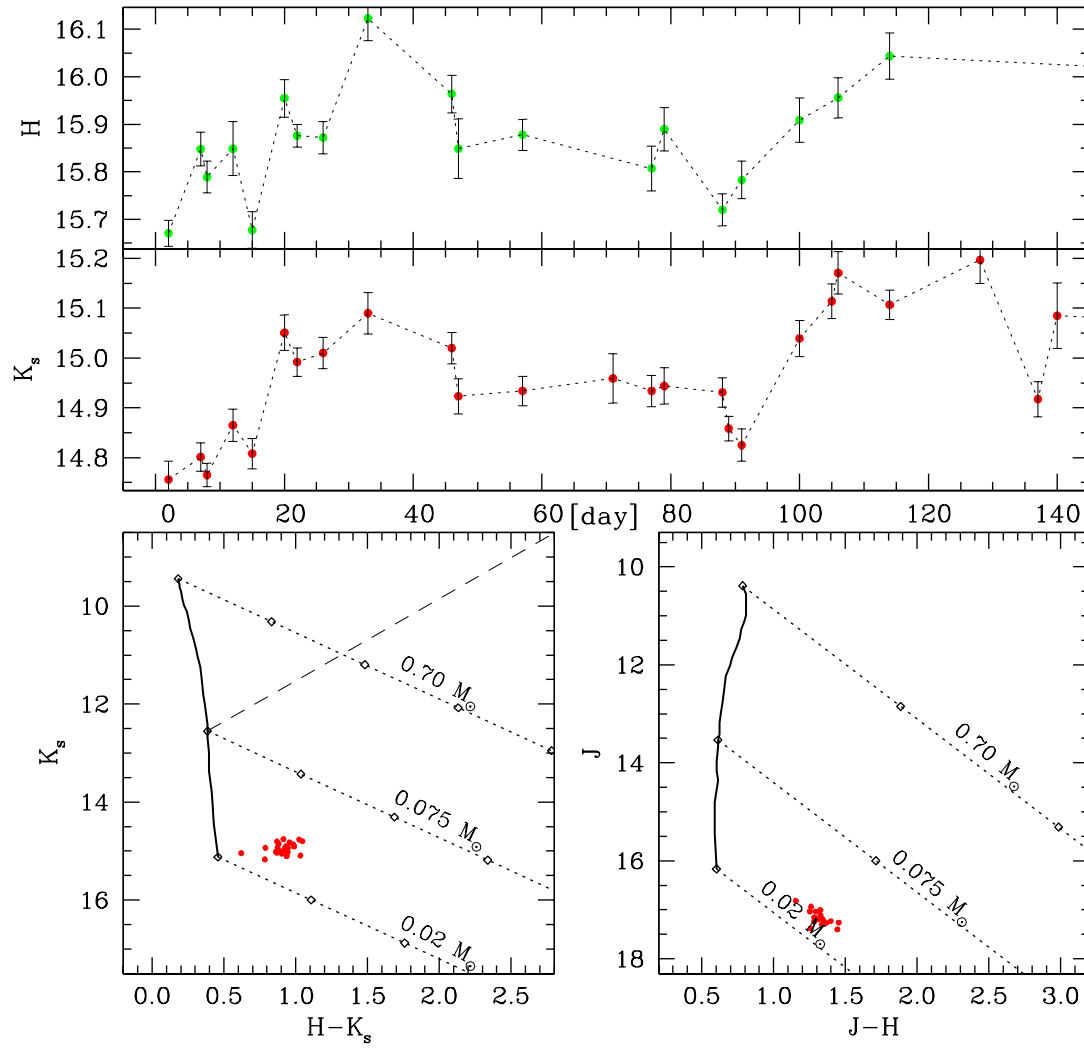
NGC 1333 FMO 168



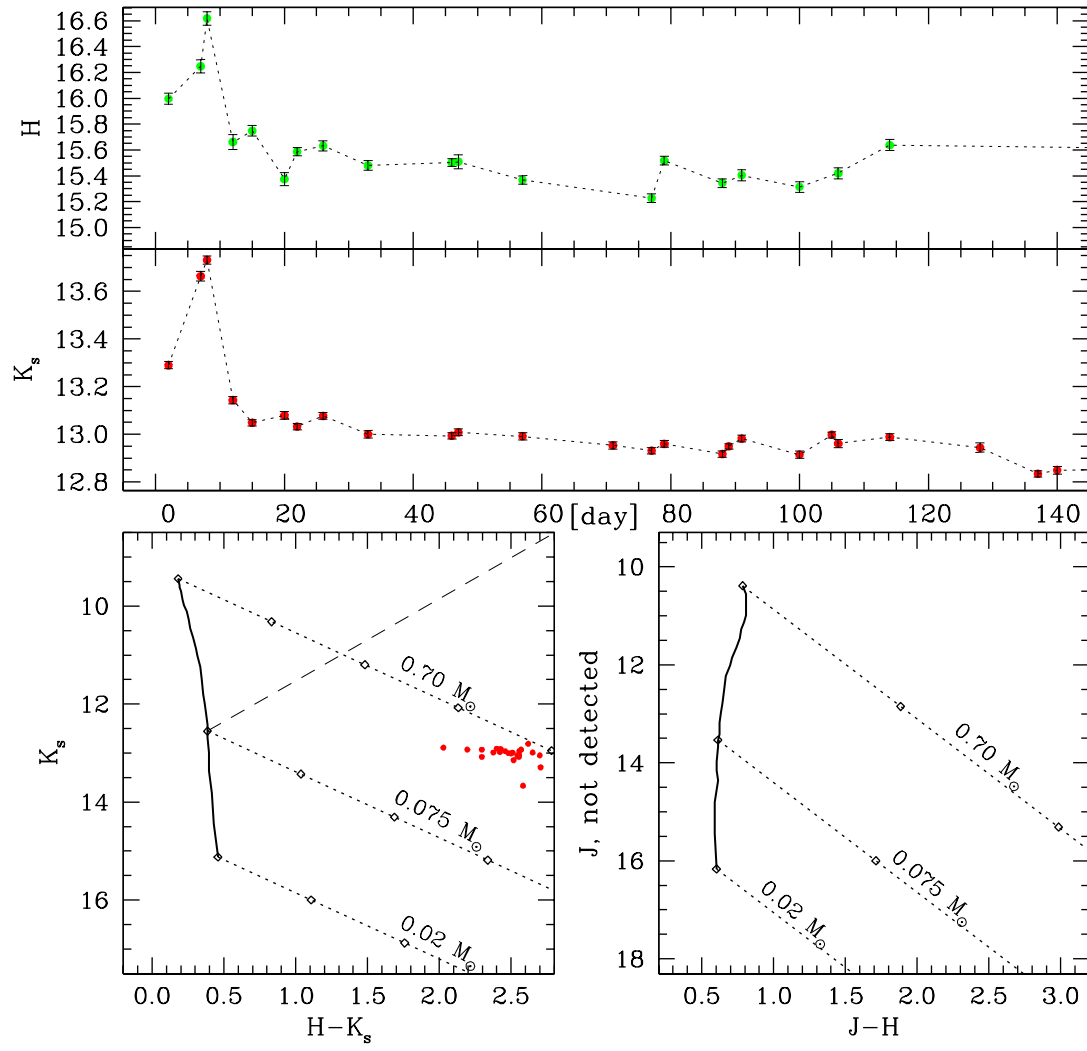
NGC 1333 FMO 179



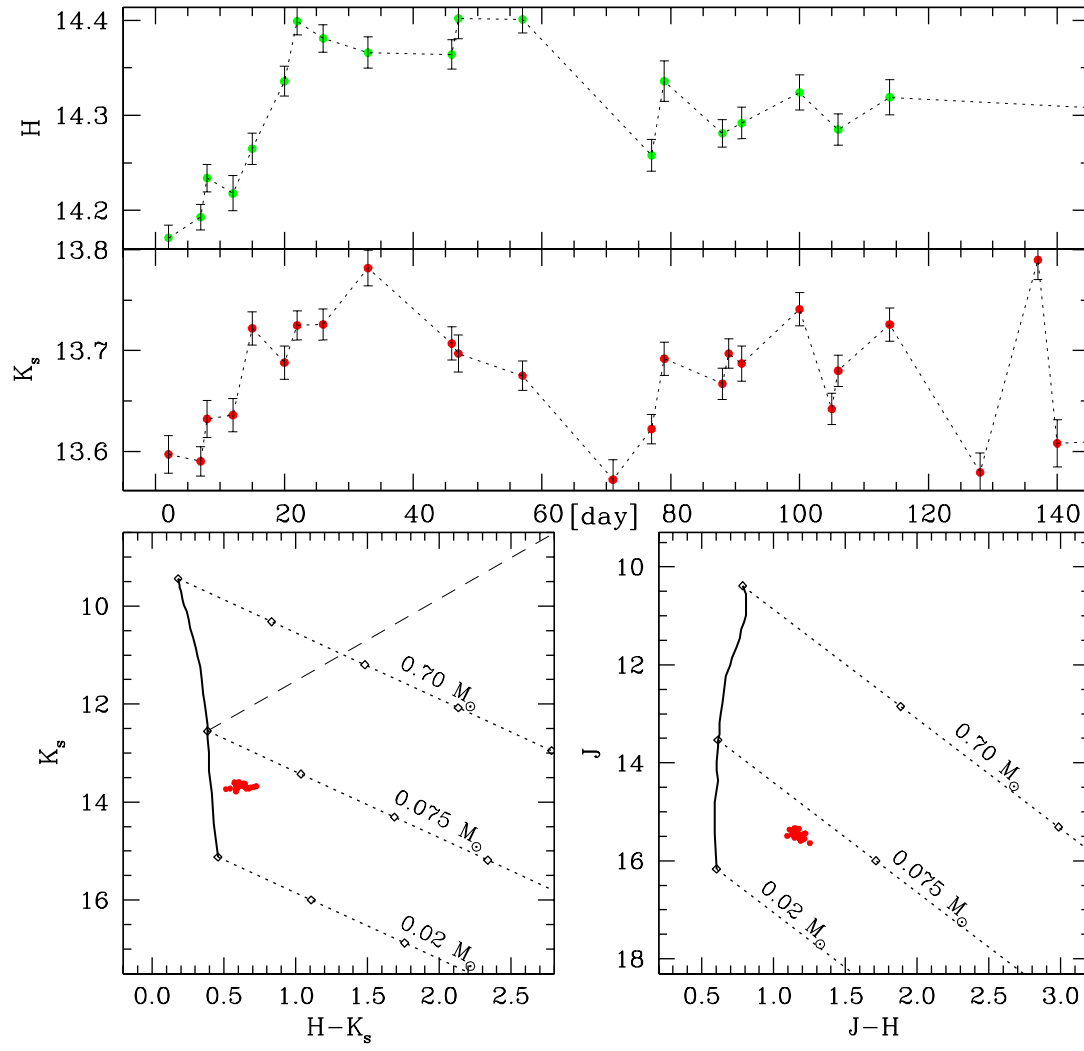
NGC 1333 FMO 197



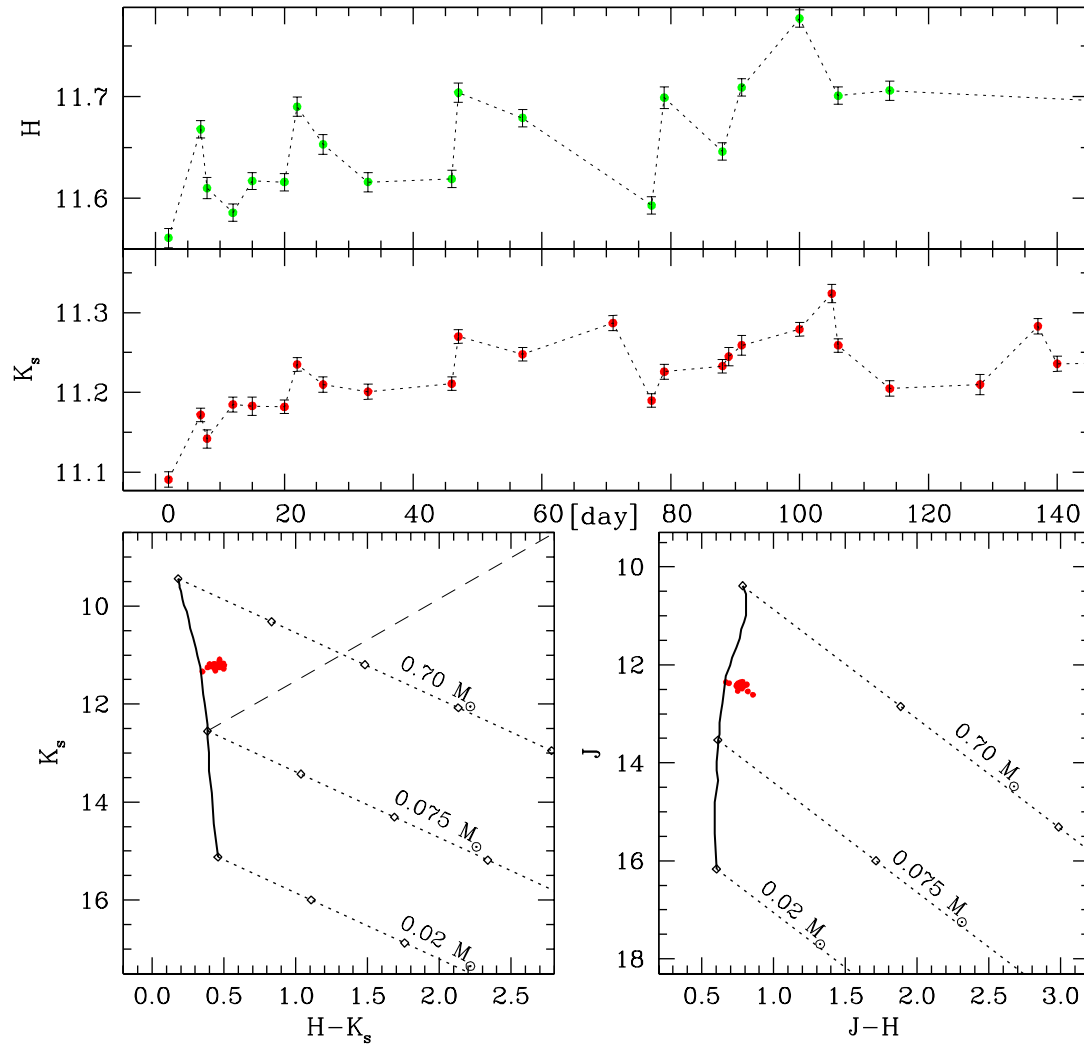
NGC 1333 FMO 200



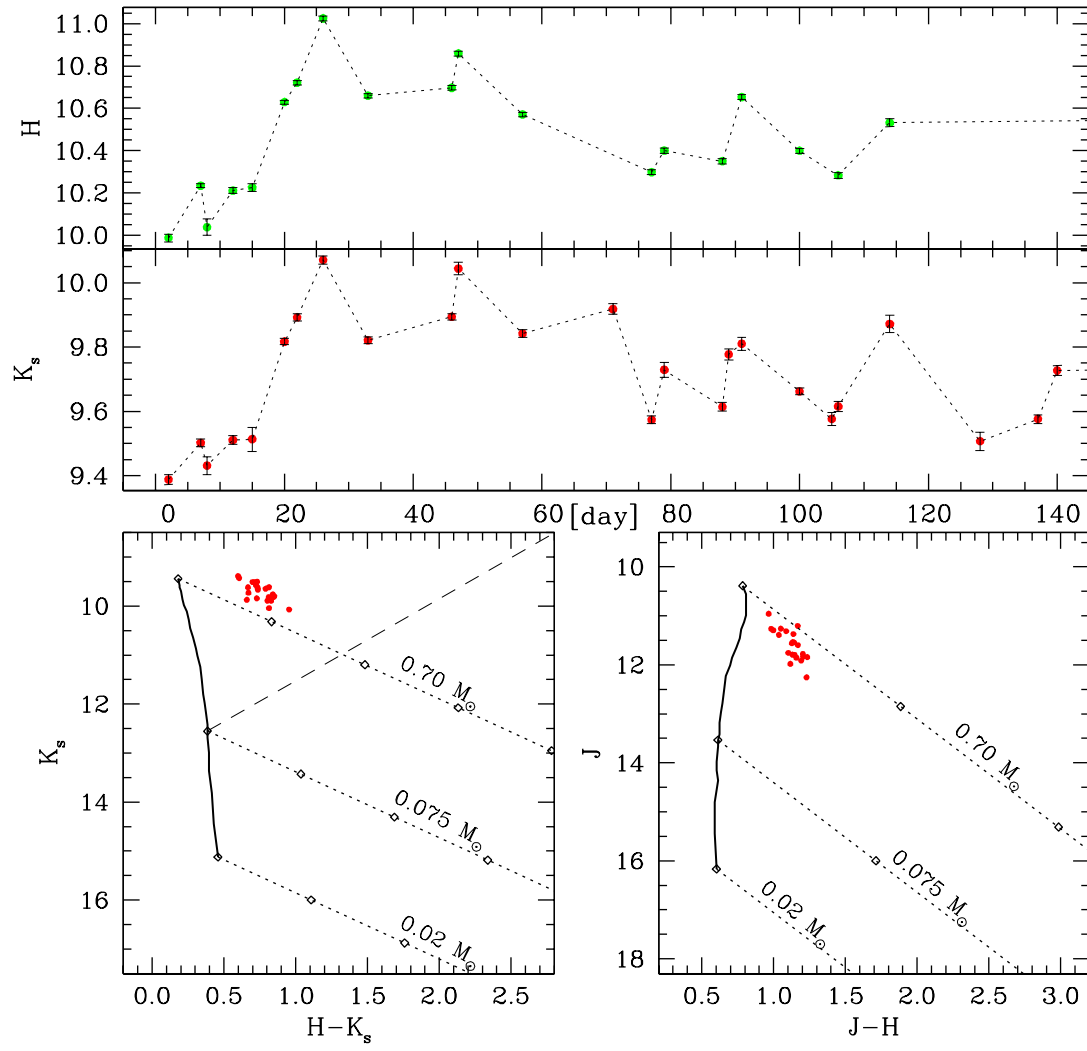
NGC 1333 FMO 217



NGC 1333 FMO 243



NGC 1333 FMO 256



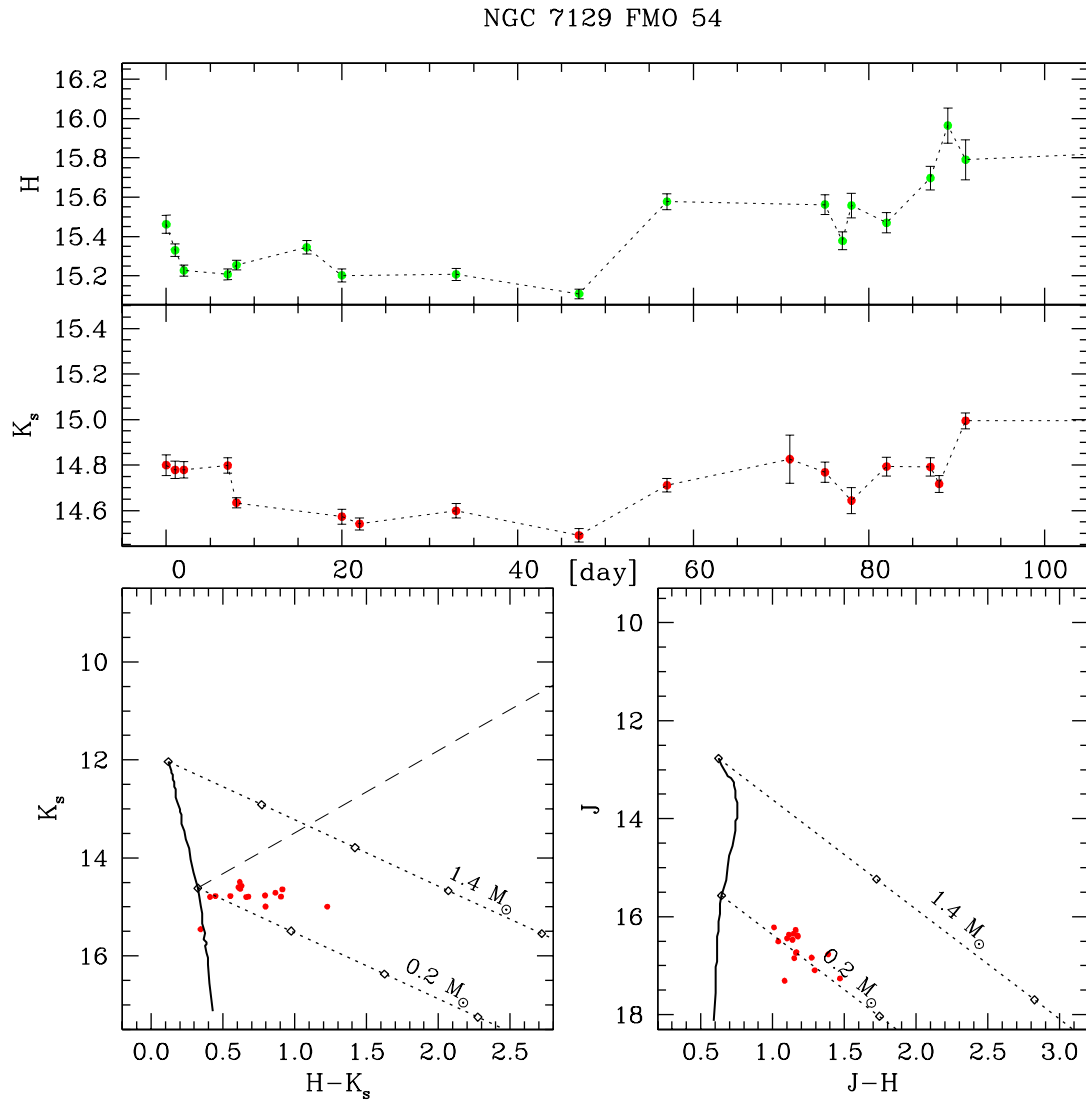
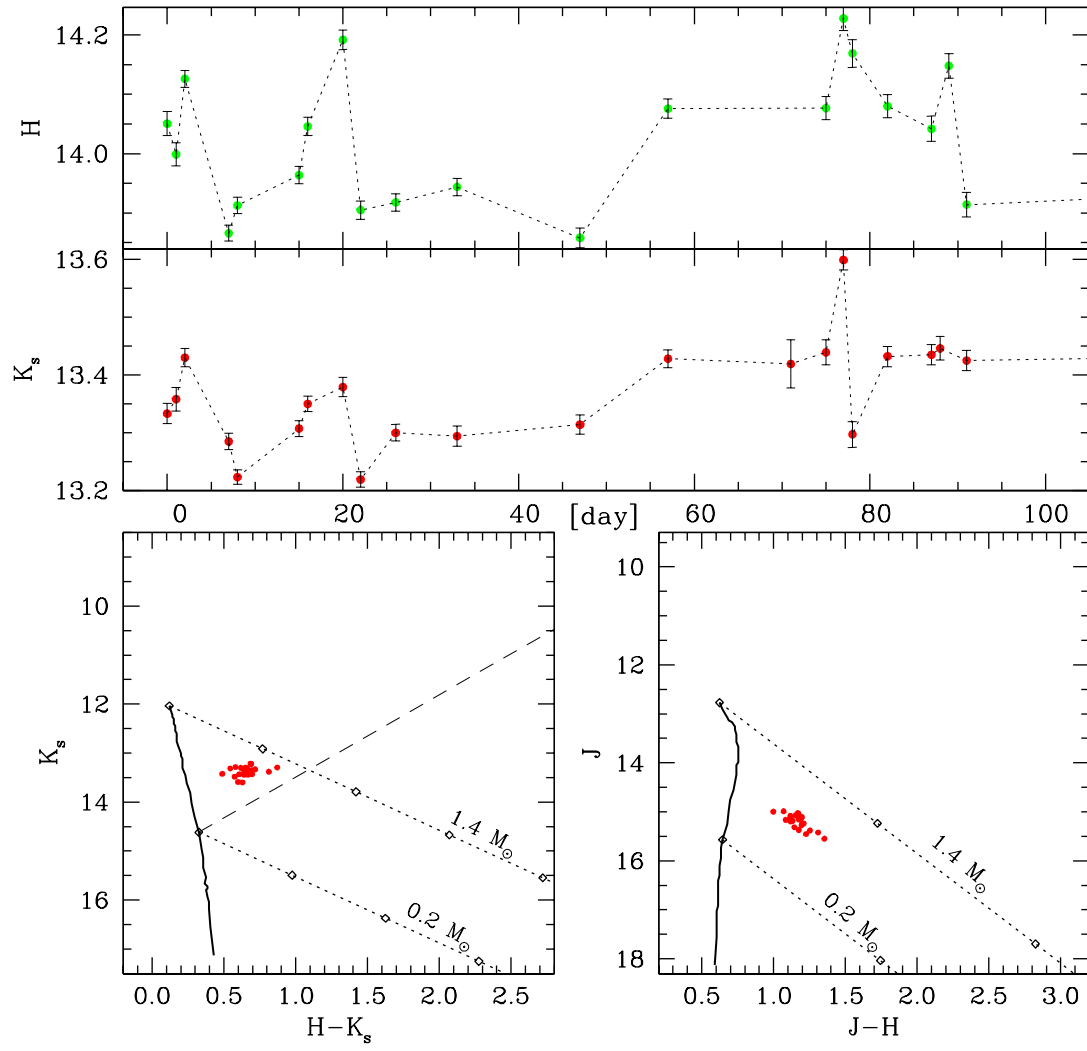
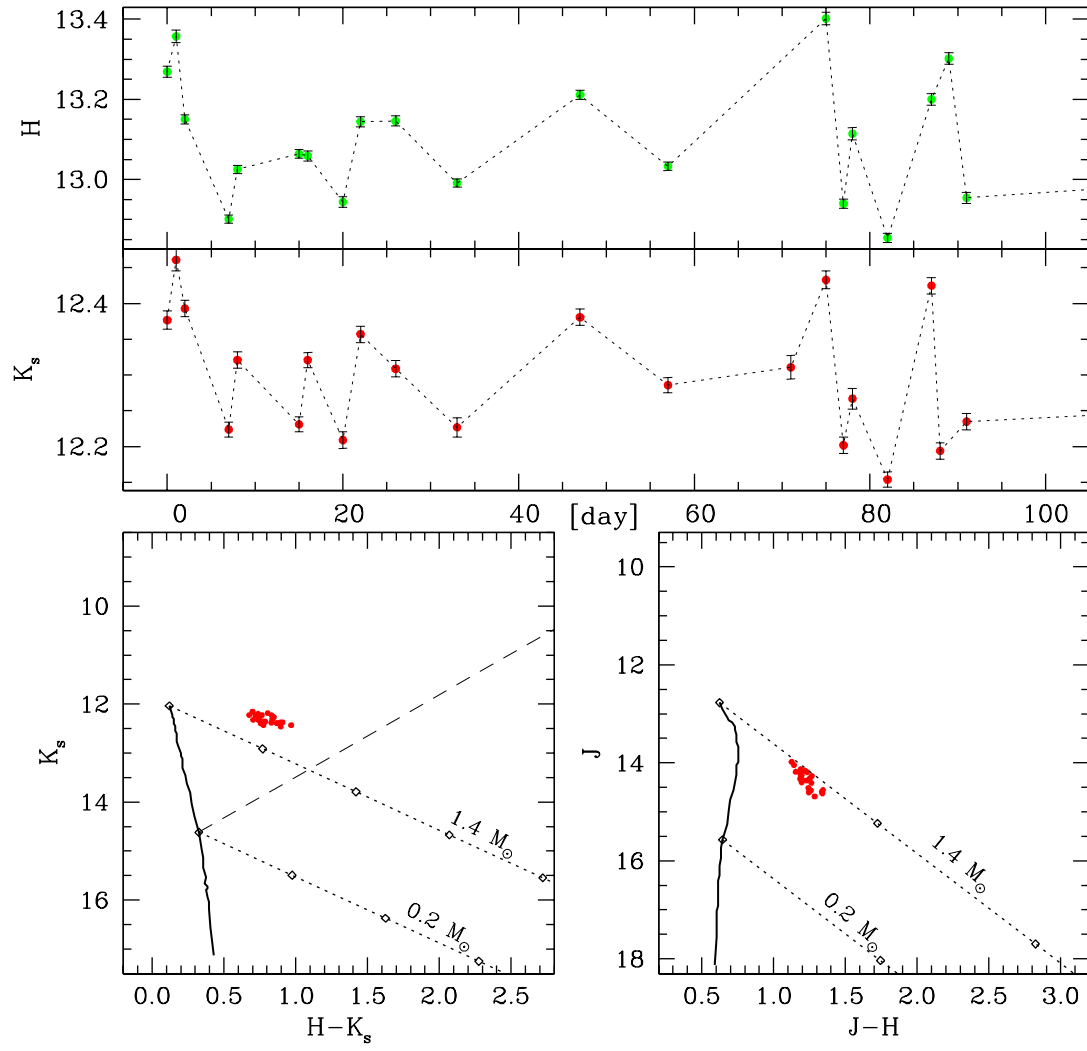


Fig. E.2.— Light curves and color-magnitude correlations for the variable star FMO 54 in NGC 7129.

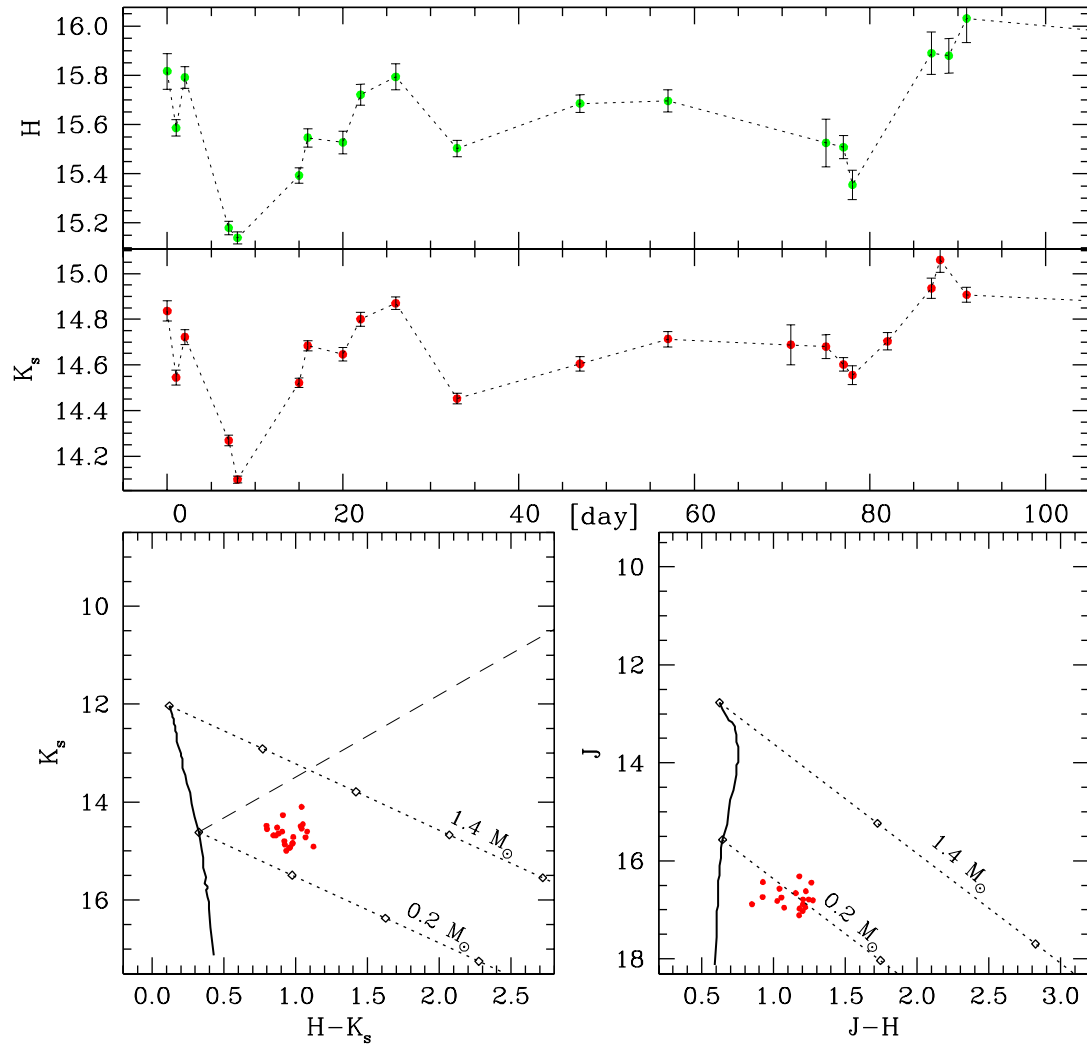
NGC 7129 FMO 101



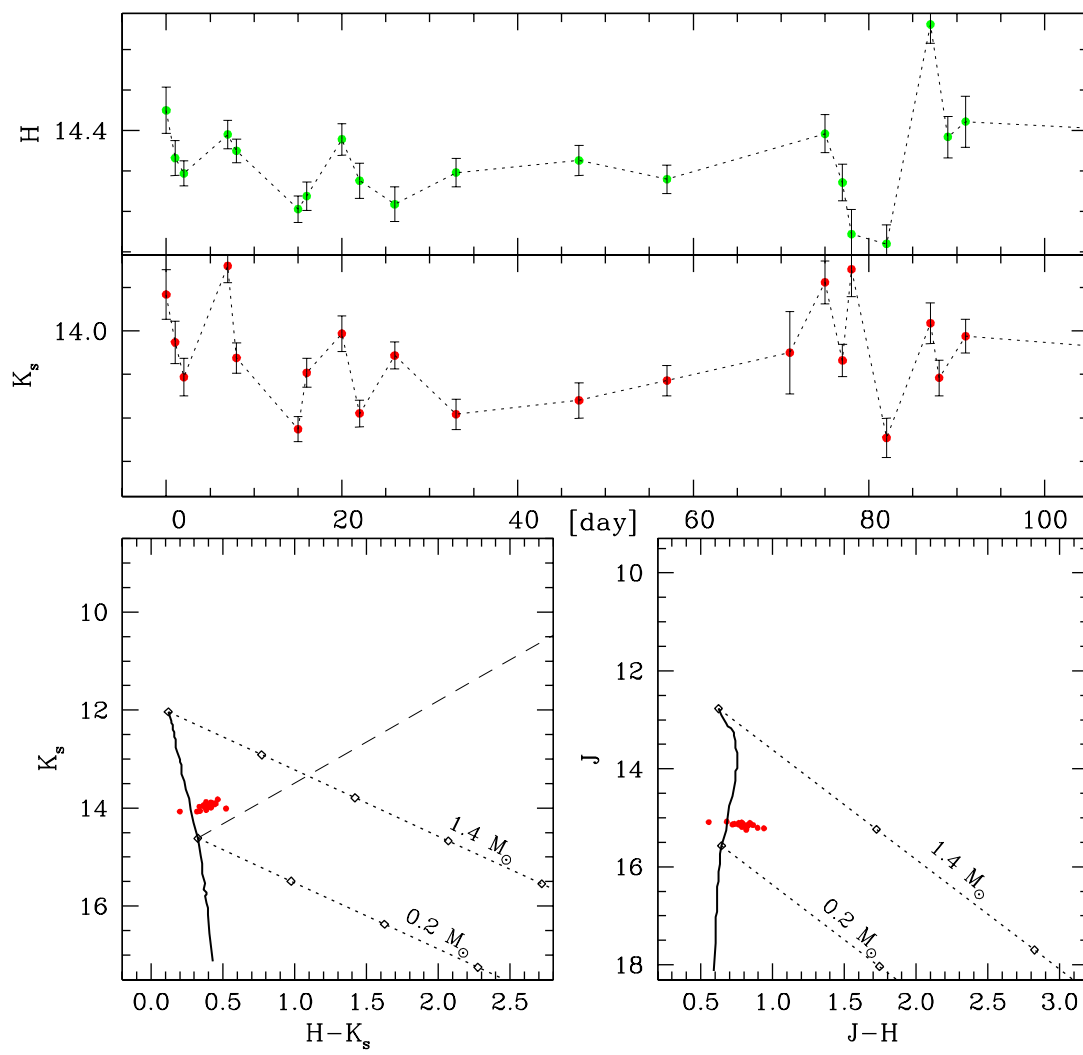
NGC 7129 FMO 233

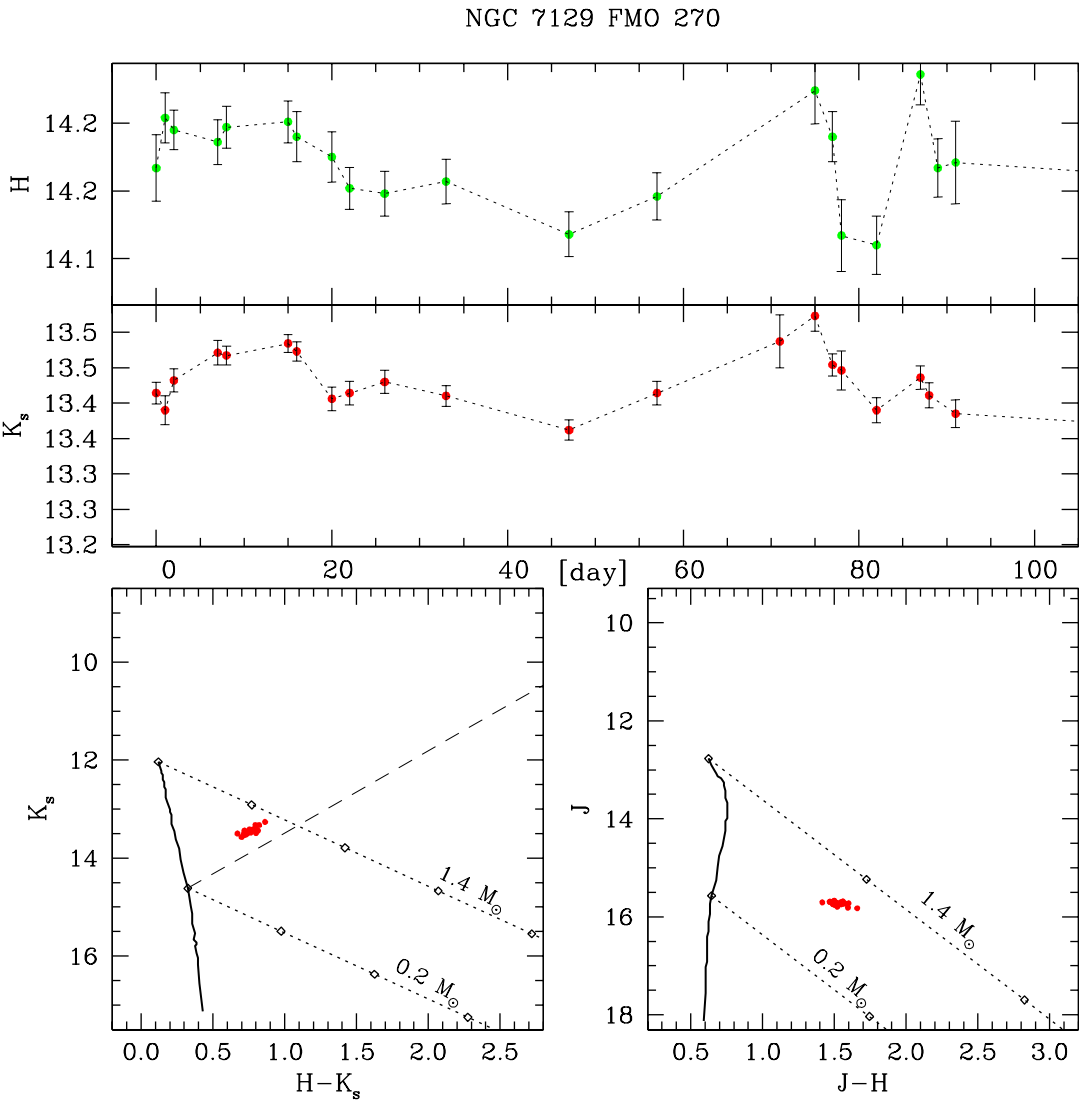


NGC 7129 FMO 255

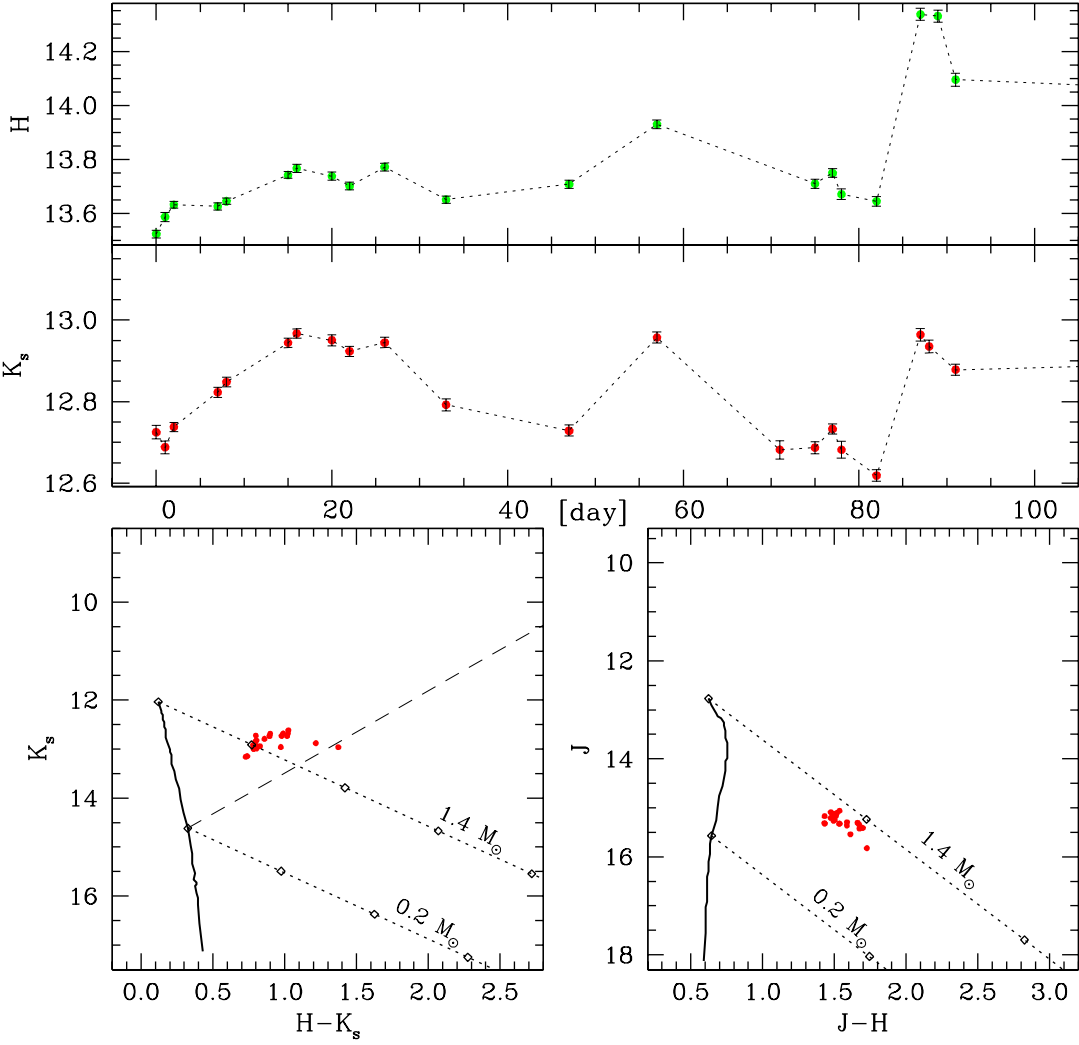


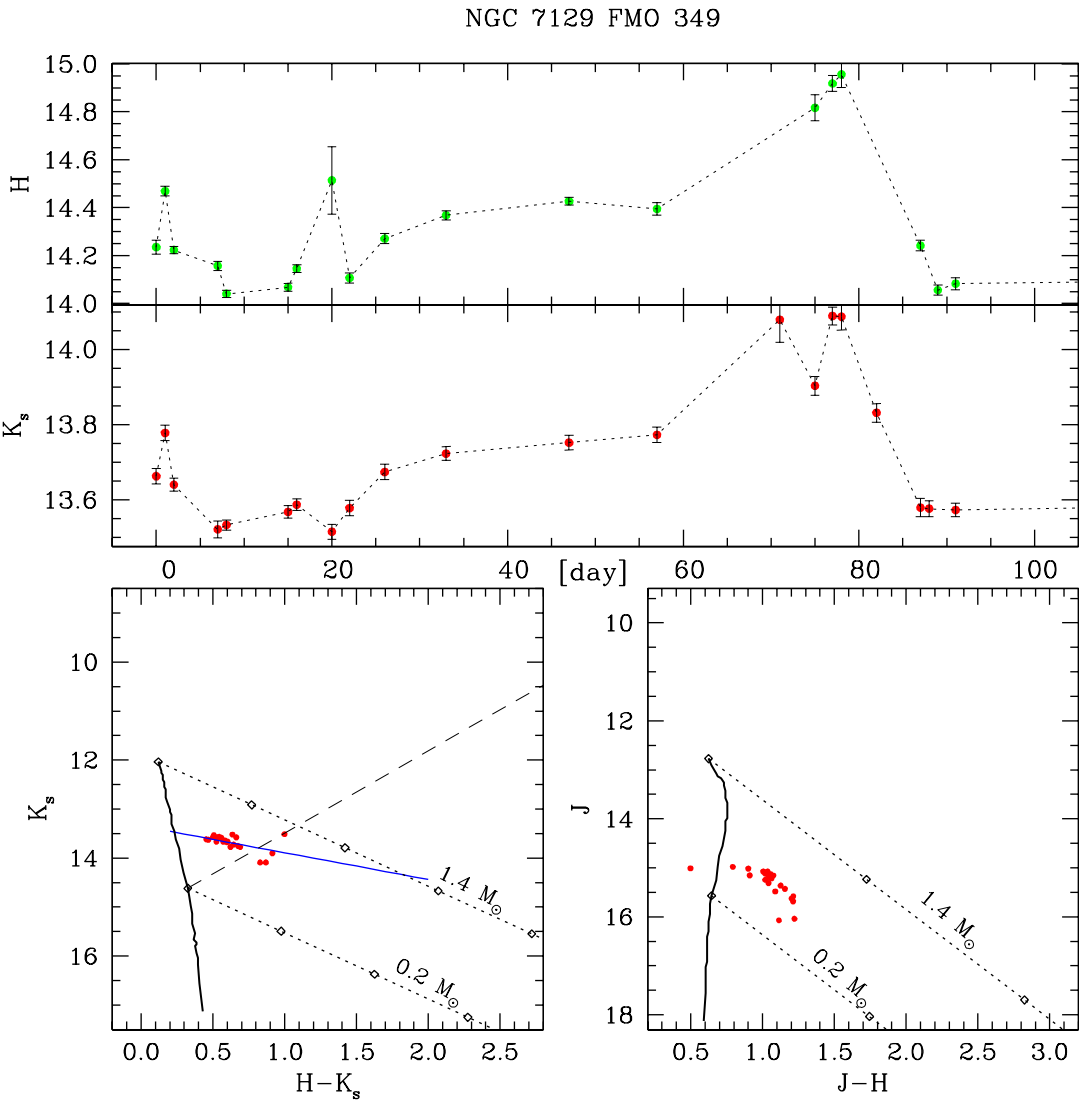
NGC 7129 FMO 264



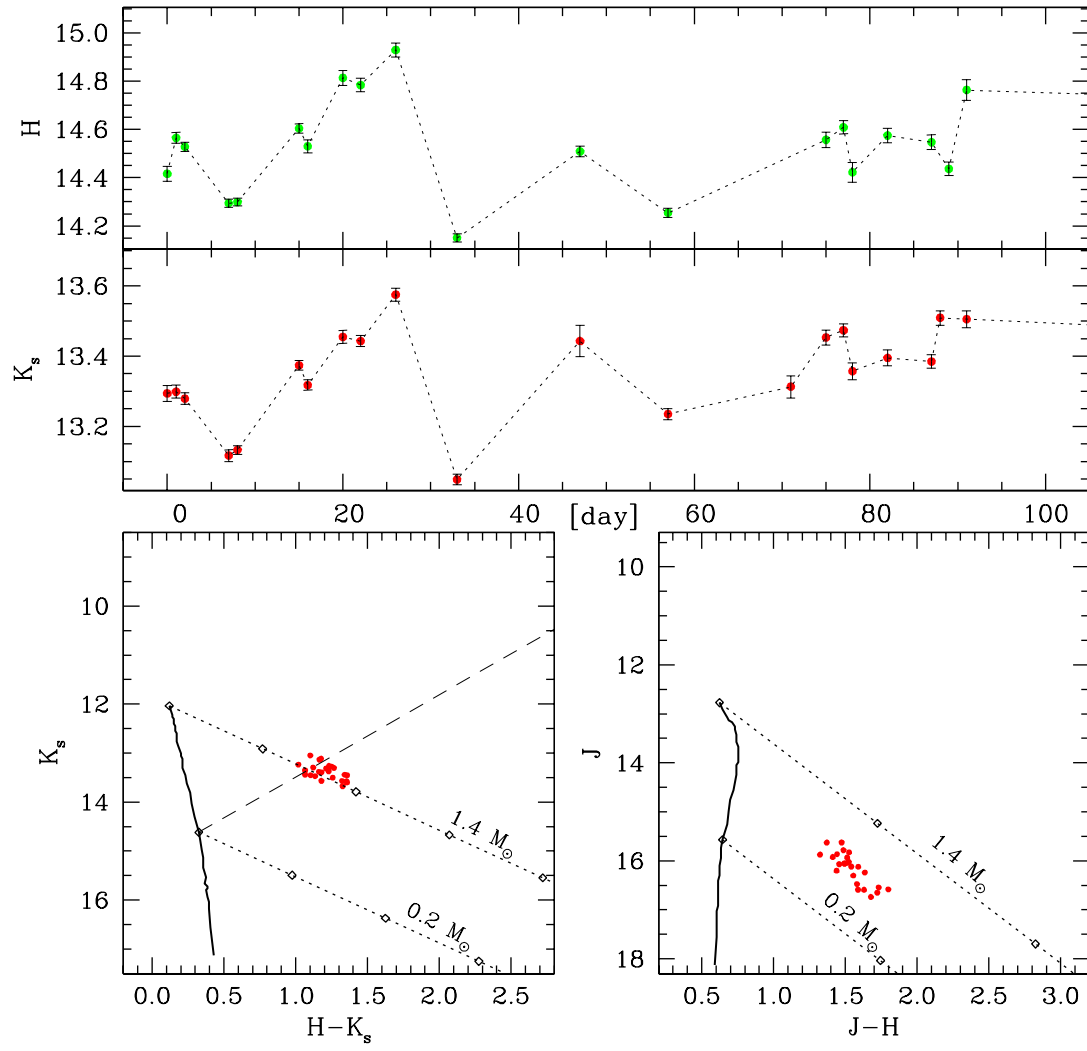


NGC 7129 FMO 323

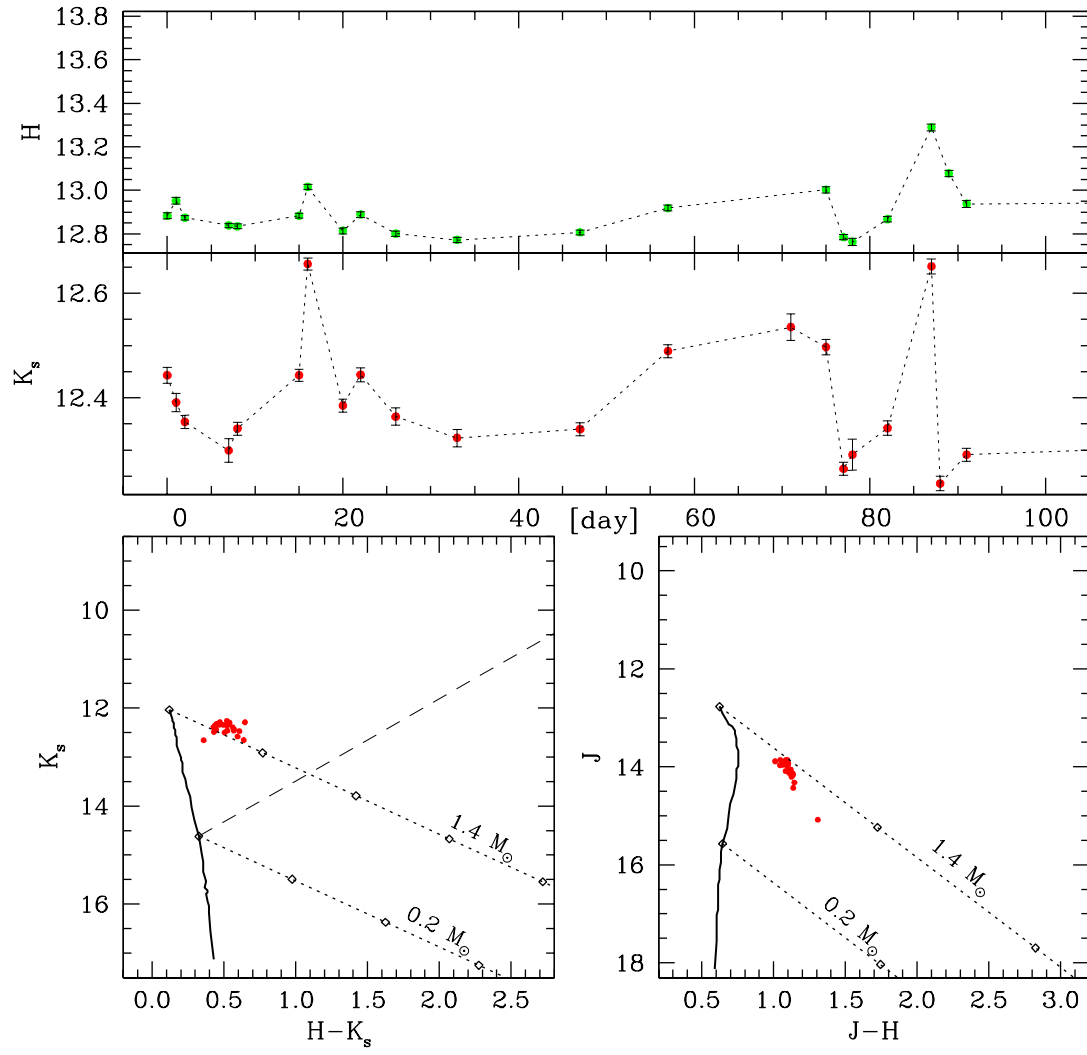




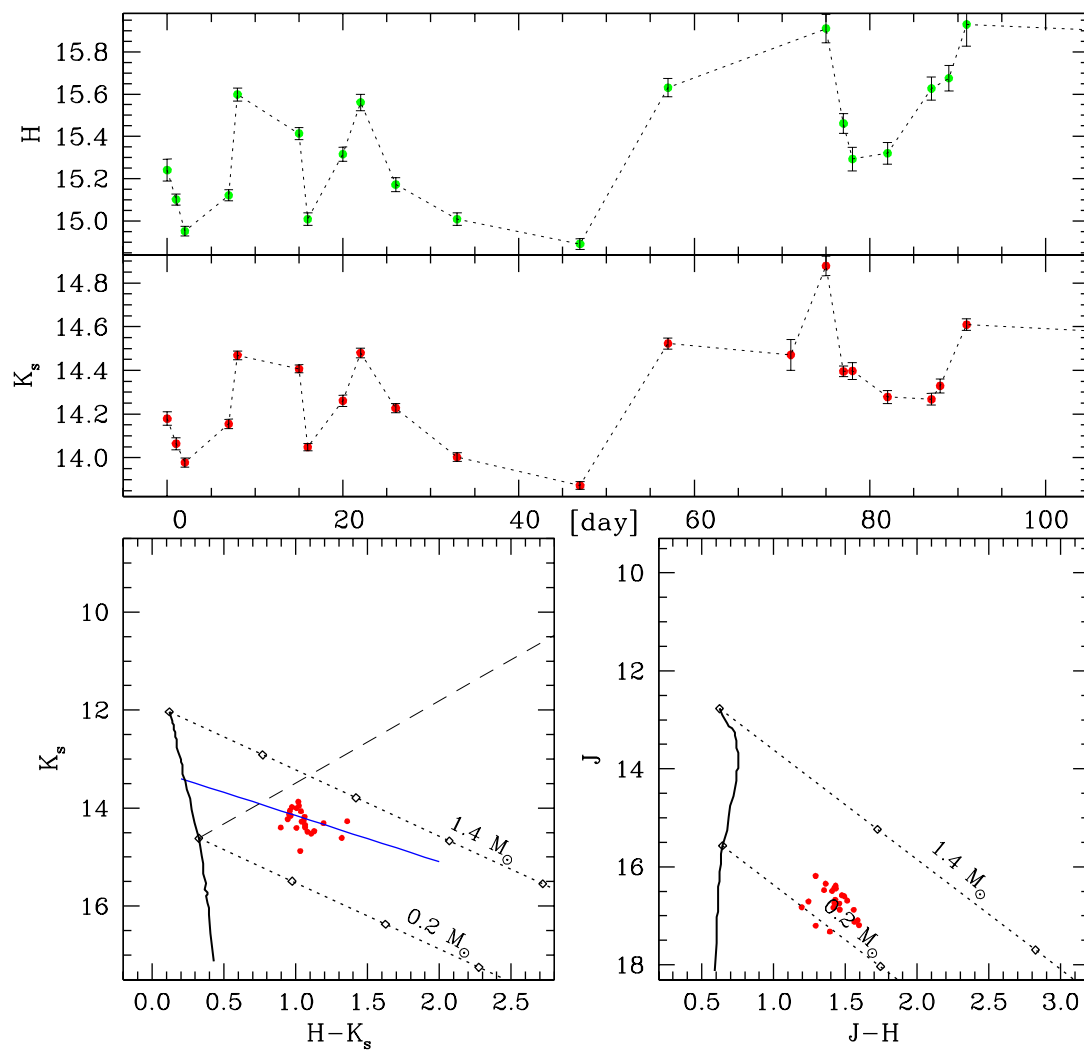
NGC 7129 FMO 366



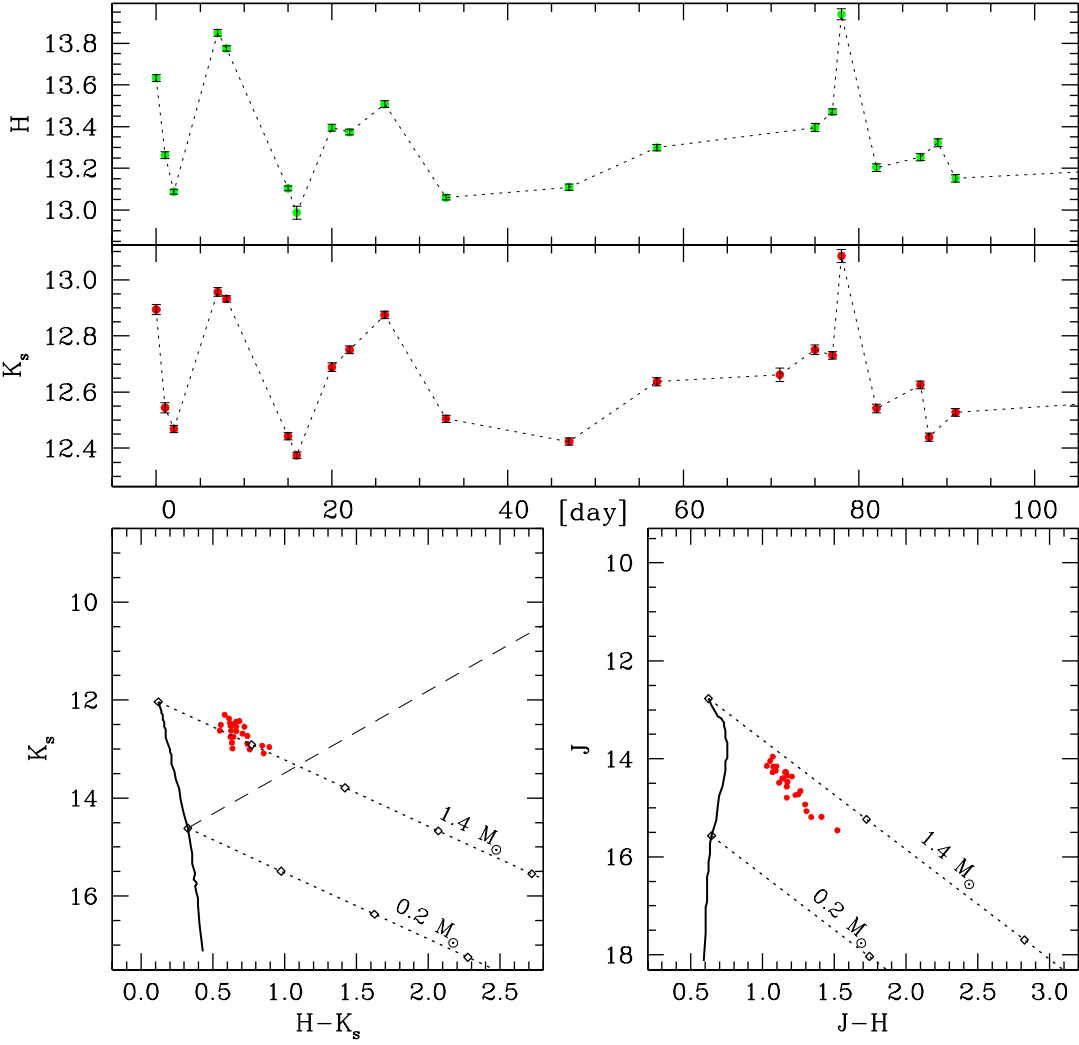
NGC 7129 FMO 368



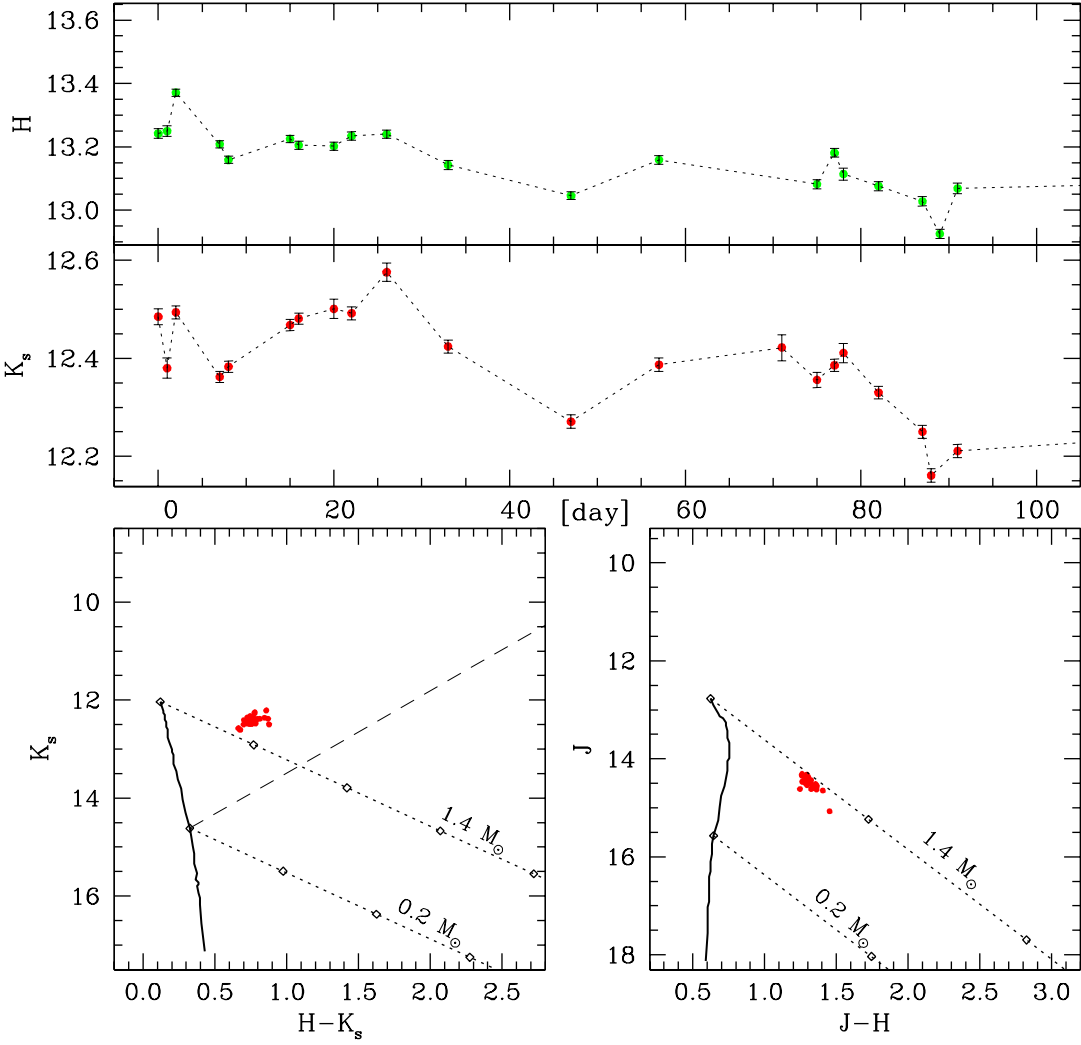
NGC 7129 FMO 370



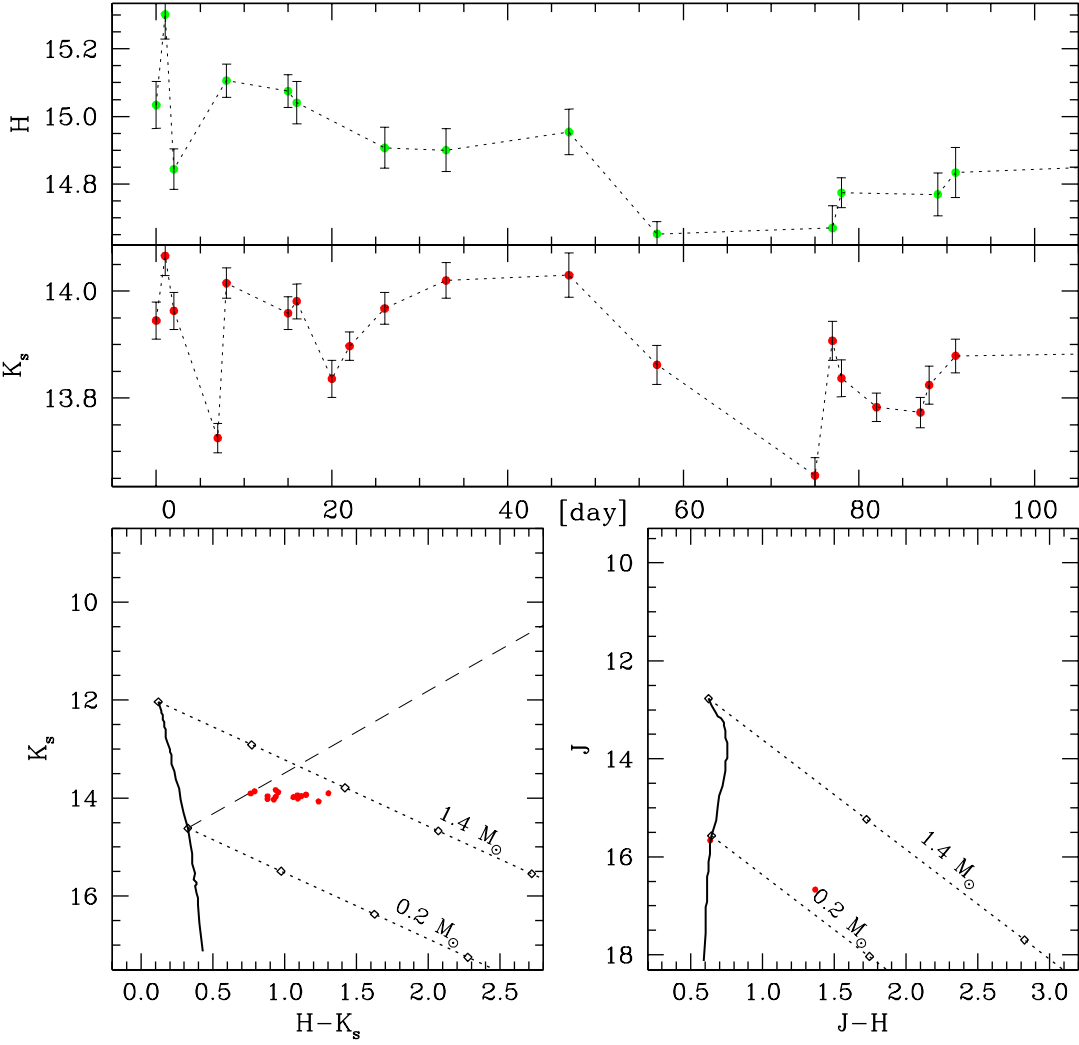
NGC 7129 FMO 381



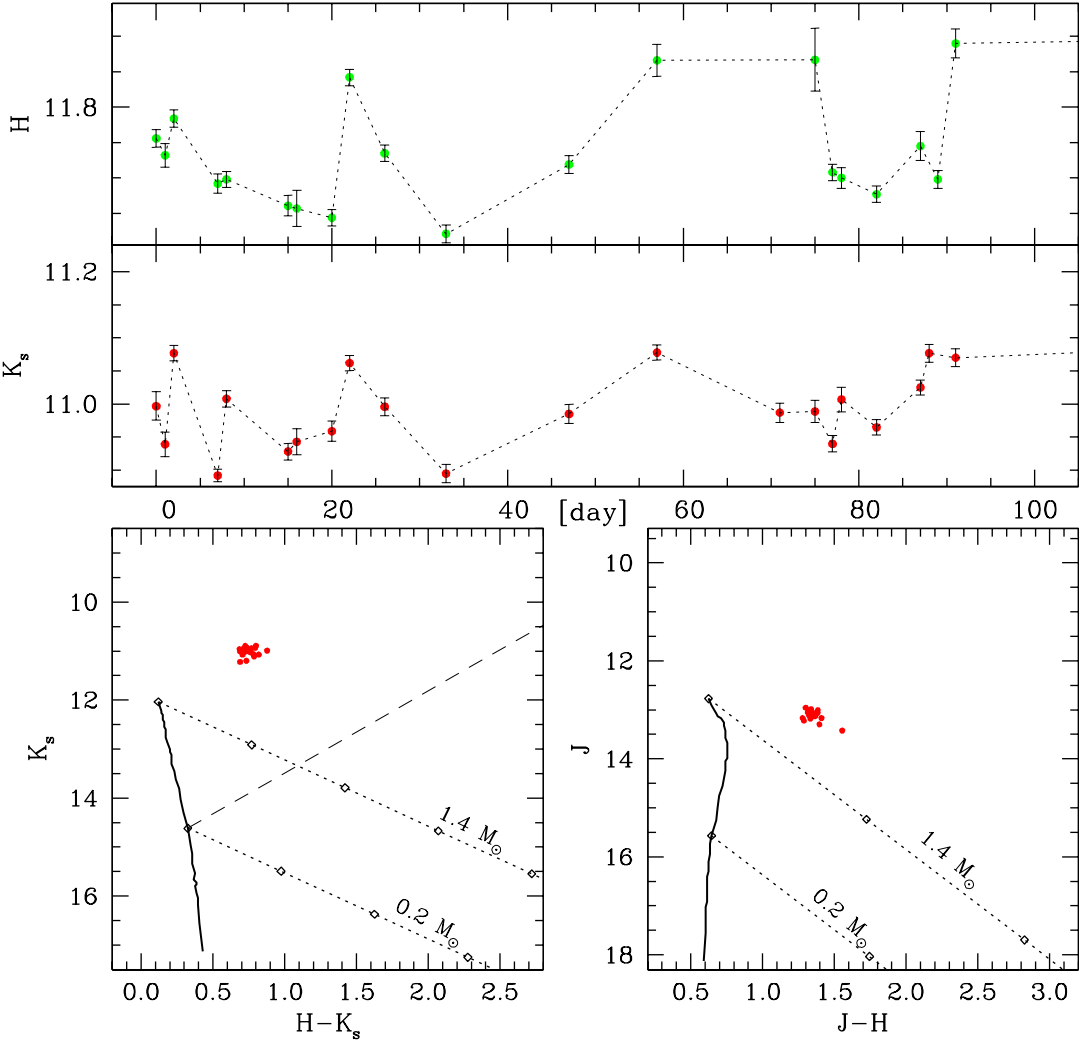
NGC 7129 FMO 399



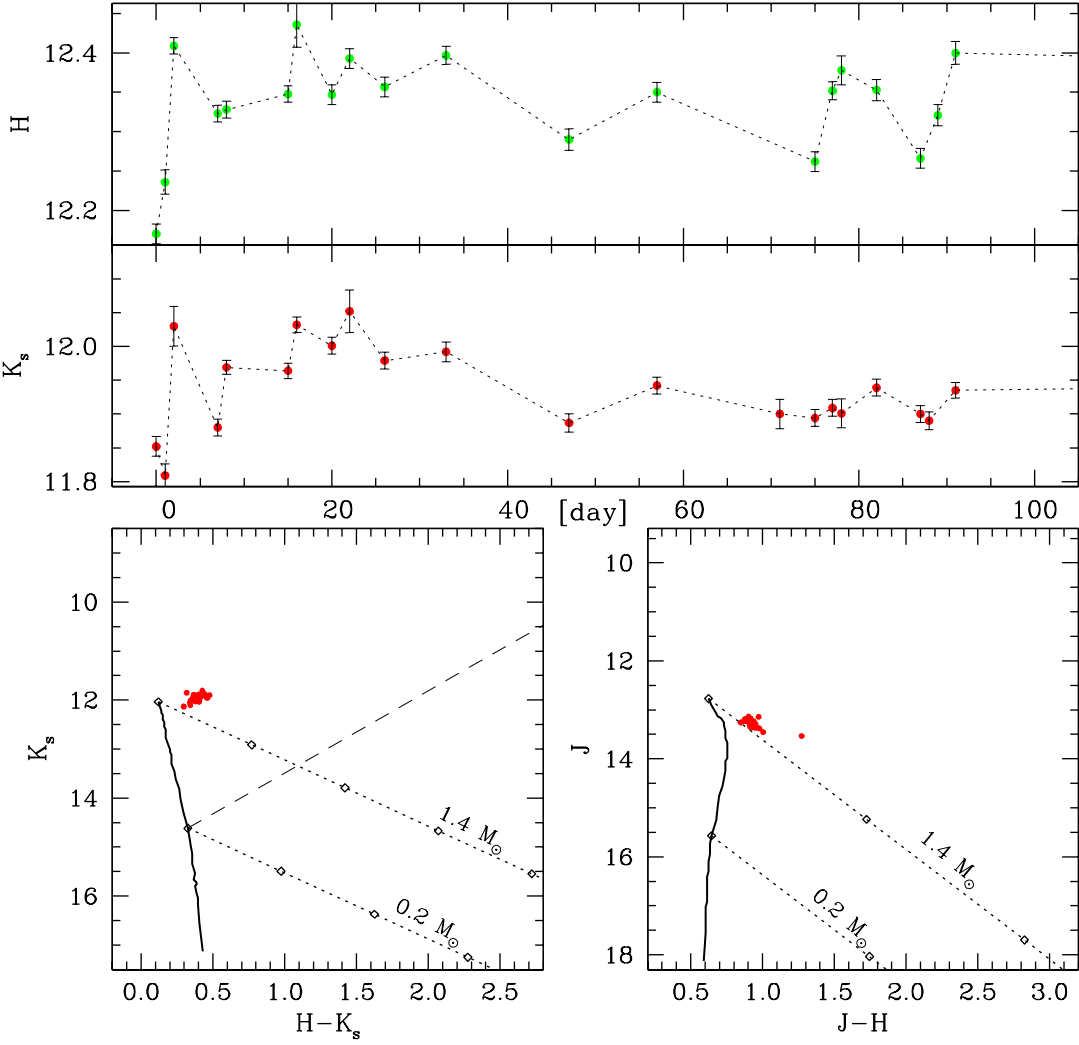
NGC 7129 FMO 417

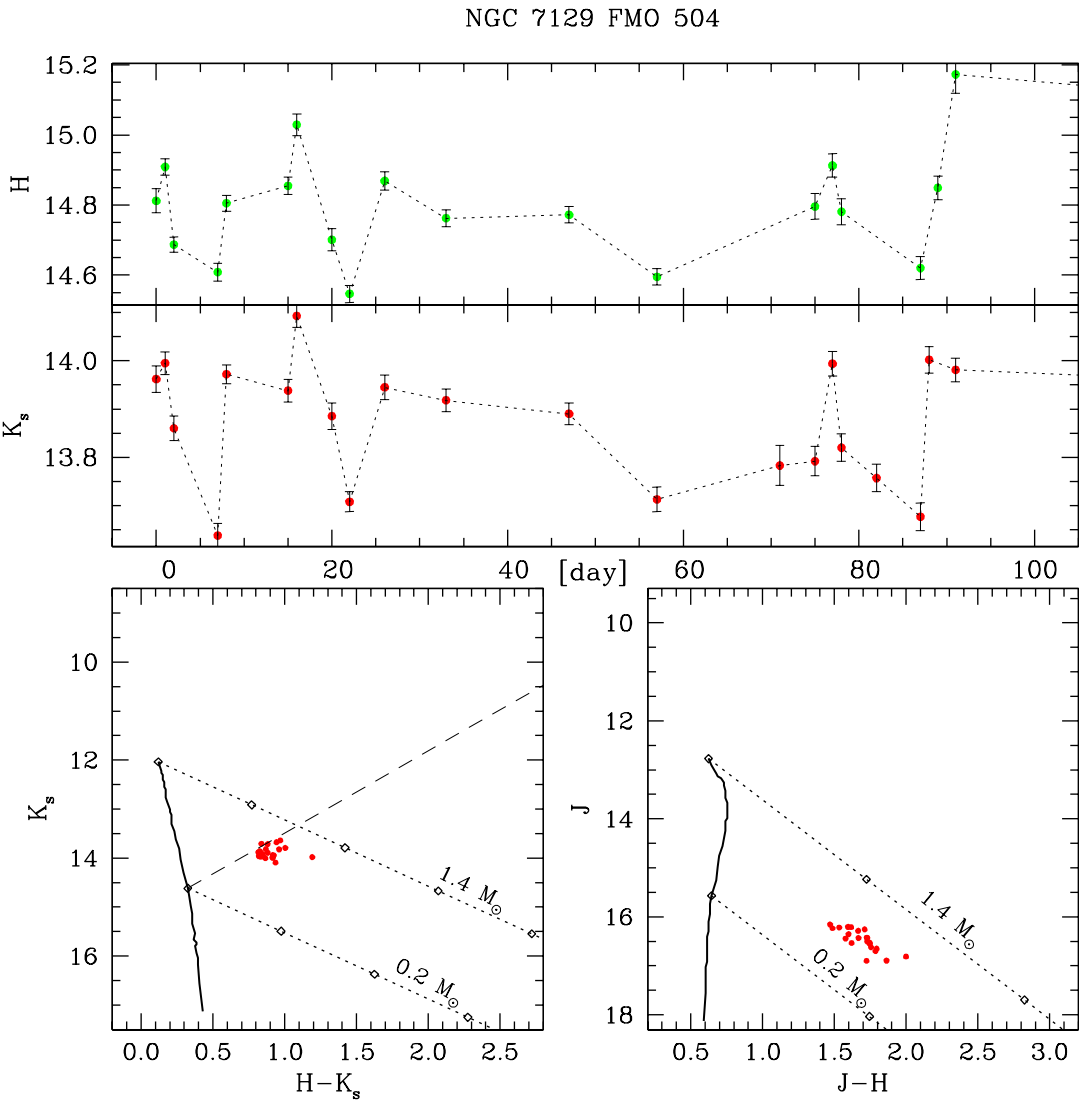


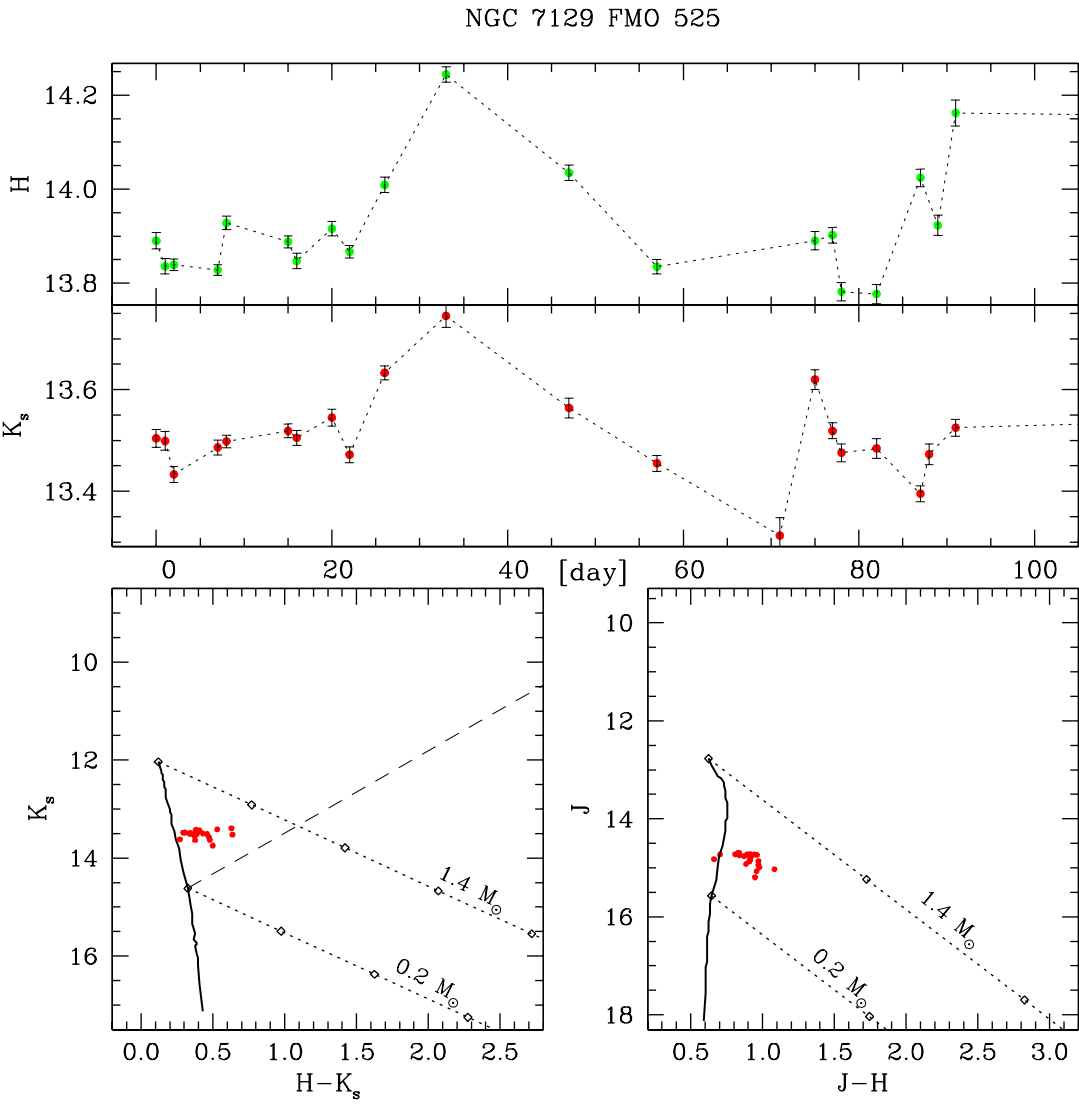
NGC 7129 FMO 440

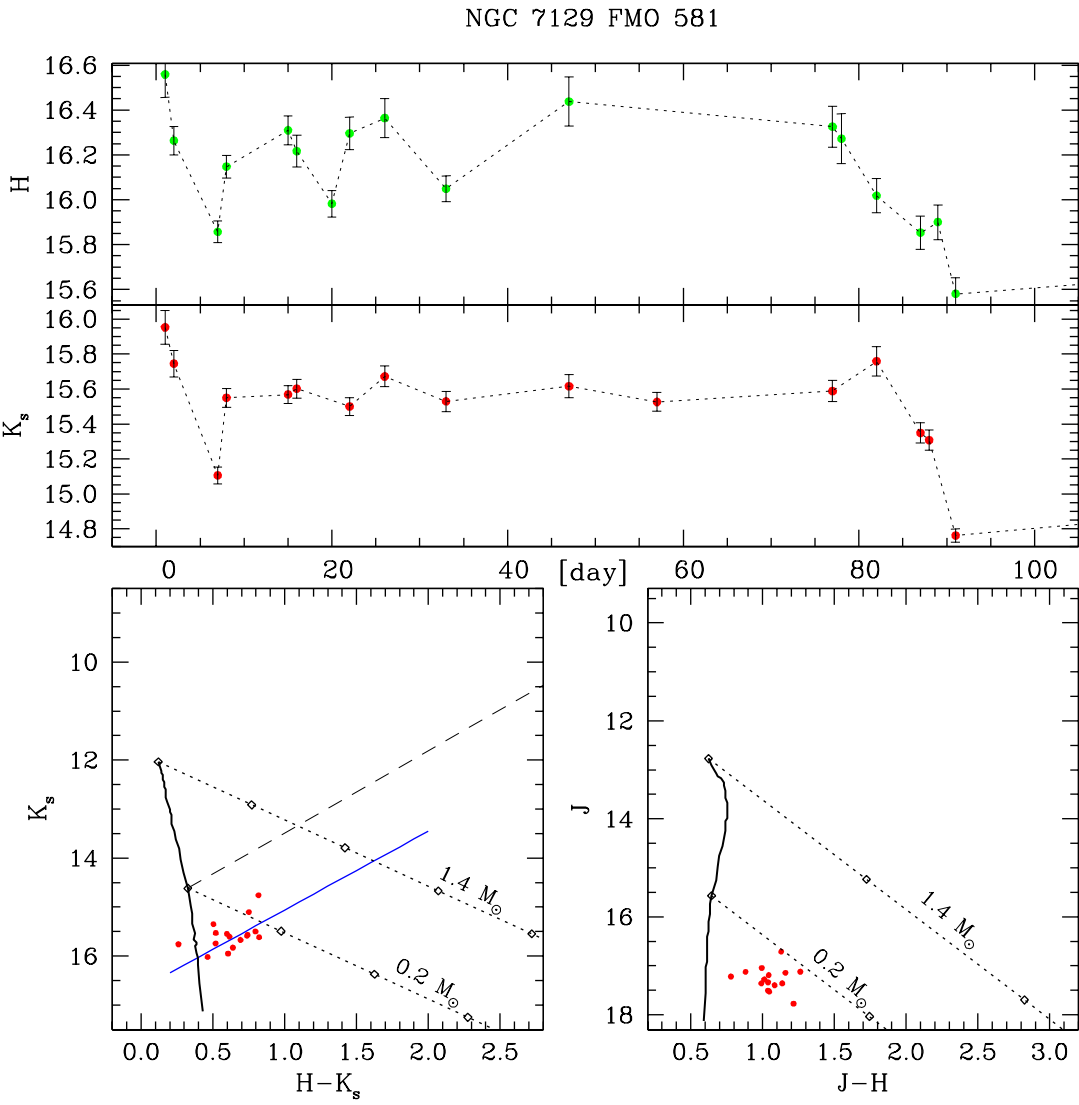


NGC 7129 FMO 462

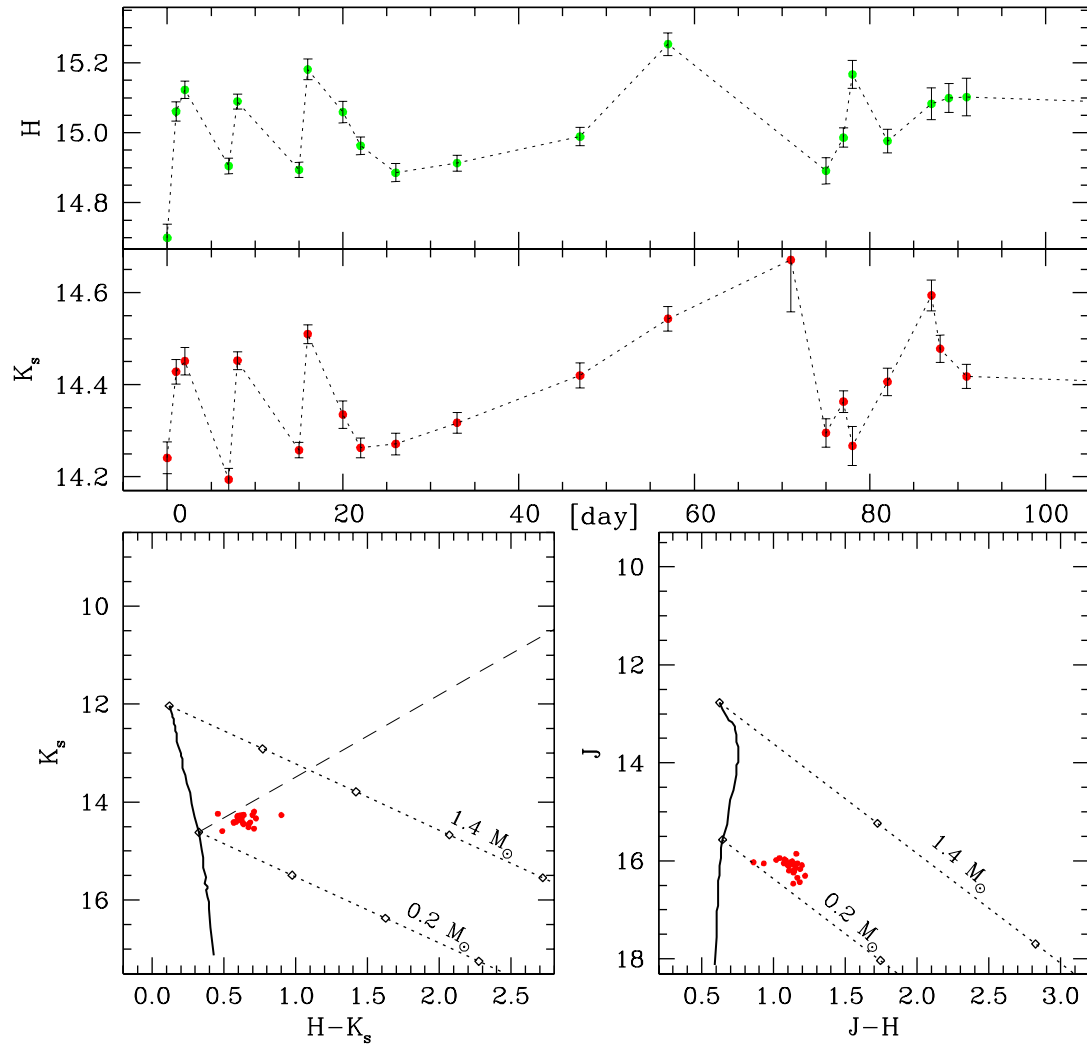




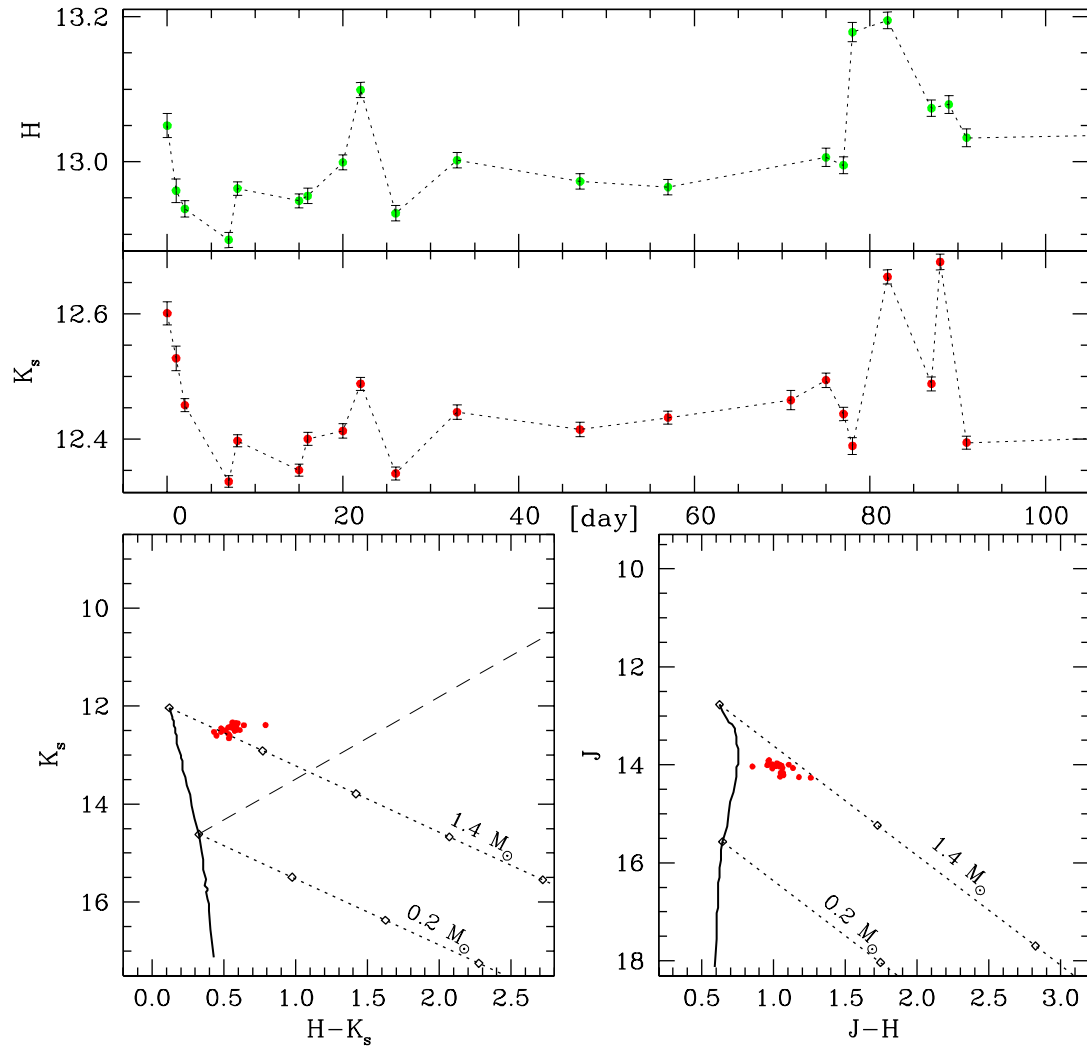




NGC 7129 FMO 602



NGC 7129 FMO 618



References

- Ábrahám, P., Balázs, L. G., & Kun, M. 2000, *A&A*, 354, 645
- Alves de Oliveira, C., & Casali, M. 2008, *A&A*, 485, 155
- Andre, P., & Montmerle, T. 1994, *ApJ*, 420, 837
- Aspin, C., Sandell, G., & Russell, A. P. G. 1994, *A&AS*, 106, 165
- Bachiller, R., Guilloteau, S., Gueth, F., Tafalla, M., Dutrey, A., Codella, C., & Castets, A. 1998, *A&A*, 339, L49
- Bally, J., Devine, D., & Reipurth, B. 1996, *ApJ*, 473, L49
- Bally, J., & Reipurth, B. 2001, *ApJ*, 546, 299
- Baraffe, I., Chabrier, G., Allard, F., & Hauschildt, P. H. 1998, *A&A*, 337, 403
- Baraffe, I., Chabrier, G., Barman, T. S., Allard, F., & Hauschildt, P. H. 2003, *A&A*, 402, 70
- Bary, J. S., Matt, S. P., Skrutskie, M. F., Wilson, J. C., Peterson, D. E., & Nelson, M. J. 2008, *ApJ*, 687, 376
- Bartlett, J. L., Park, C., Kanneganti, S., & Ianna, P. A. 2010, *New Astronomy*, 15, 547

- Bartlett, J. L., Park, C., Kanneganti, S., & Ianna, P. A. 2010, *Bulletin of the American Astronomical Society*, 41, 404
- Beichman, C. A., Chester, T. J., Skrutskie, M. F., Low, F. J. & Gillett, F., 1998, *PASP*, 110, 480
- Bessell, M. S., & Brett, J. M. 1988, *PASP*, 100, 1134
- Bevington, P. R., & Robinson, D. K. 2003, *Data reduction and error analysis for the physical sciences*, 3rd ed. (Boston, MA: McGraw-Hill)
- Belikov, A. N., Kharchenko, N. V., Piskunov, A. E., Schilbach, E., & Scholz, R.-D. 2002, *A&A*, 387, 117
- Birney, D. S., 1966, *S&T*, 31, 210
- Briceño, C., Luhman, K. L., Hartmann, L., Stauffer, J. R., & Kirkpatrick, J. D. 2002, *ApJ*, 580, 317
- Burrows, A., et al. 1997, *ApJ*, 491, 856
- Carpenter, J. M. 2001, *AJ*, 121, 2851
- Carpenter, J. M., Hillenbrand, L. A., & Skrutskie, M. F. 2001, *AJ*, 121, 3160
- Carpenter, J. M., Hillenbrand, L. A., Skrutskie, M. F., & Meyer, M. R. 2002, *AJ*, 124, 1001
- Cernis, K. 1990, *Ap&SS*, 166, 315
- Chabrier, G., Baraffe, I., Allard, F., & Hauschildt, P. 2000, *ApJ*, 542, 464
- Chini, R., Ward-Thompson, D., Kirk, J. M., Nielbock, M., Reipurth, B., & Sievers, A. 2001, *A&A*, 369, 155

- Choi, M., Hodapp, K. W., Hayashi, M., Motohara, K., Pak, S., & Pyo, T.-S. 2006, ApJ, 646, 1050
- Cohen, J. G., Frogel, J. A., Persson, S. E., & Elias, J. H. 1981, ApJ, 249, 481
- Cohen, M., & Schwartz, R. D. 1976, MNRAS, 174, 137
- Cohen, M., Walker, R. G., Barlow, M. J., & Deacon, J. R. 1992, AJ, 104, 1650
- Cohen, M., Wheaton, W. A., & Megeath, S. T. 2003, AJ, 126, 1090
- D'Antona, F., & Mazzitelli, I. 1997, Memorie della Societa Astronomica Italiana, 68, 807
- D'Antona, F., & Mazzitelli, I. 1998, Brown Dwarfs and Extrasolar Planets: ASP Conference Proceedings, 134, 442
- Des Marais, D. J., et al. 2002, Astrobiology, 2, 153
- de Zeeuw, P. T., Hoogerwerf, R., de Bruijne, J. H. J., Brown, A. G. A., & Blaauw, A. 1999, AJ, 117, 354
- Feigelson, E. D., Casanova, S., Montmerle, T., & Guibert, J. 1993, ApJ, 416, 623
- Feigelson, E. D., Broos, P., Gaffney, J. A., III, Garmire, G., Hillenbrand, L. A., Pravdo, S. H., Townsley, L., & Tsuboi, Y. 2002, ApJ, 574, 258
- Feigelson, E. D., & Montmerle, T. 1999, ARA&A, 37, 363
- Flynn, T. M., *Cryogenic Engineering*, Second Edition, Dekker, 2005
- Fox, O., et al. 2009, ApJ, 691, 650
- Fruchter, A. S., & Hook, R. N. 2002, PASP, 114, 144

- Guieu, S., Dougados, C., Monin, J.-L., Magnier, E., & Martín, E. L. 2006, *A&A*, 446, 485
- Getman, K. V., Feigelson, E. D., Townsley, L., Bally, J., Lada, C. J., & Reipurth, B. 2002, *ApJ*, 575, 354
- Greissl, J., Meyer, M. R., Wilking, B. A., Fanetti, T., Schneider, G., Greene, T. P., & Young, E. 2007, *AJ*, 133, 1321
- Gutermuth, R. A., Megeath, S. T., Muzerolle, J., Allen, L. E., Pipher, J. L., Myers, P. C., & Fazio, G. G. 2004, *ApJS*, 154, 374
- Gutermuth, R. A., Myers, P. C., Megeath, S. T., Allen, L. E., Pipher, J. L., Muzerolle, J., Porras, A., Winston, E., & Fazio, G. 2008, *ApJ*, 674, 336
- Hatchell, J., Richer, J. S., Fuller, G. A., Qualtrough, C. J., Ladd, E. F., & Chandler, C. J. 2005, *A&A*, 440, 151
- Herbig, G. H., & Jones, B. F. 1983, *AJ*, 88, 1040
- Herbst, W., Herbst, D. K., Grossman, E. J., & Weinstein, D. 1994, *AJ*, 108, 1906
- Hillenbrand, L. A., & Carpenter, J. M. 2000, *ApJ*, 540, 236
- Hodapp, K.-W. 1994, *ApJS*, 94, 615
- Hodapp, K. W., Hora, J. L., Hall, D. N., Cowie, L. L., Metzger, M., Irwin, E. M., Keller, T. J., Vural, K., Kozlowski, L. J. & Kleinhans, W. E., 1995, *Proc. SPIE*, 2475, 8
- Kaas, A. A. 1999, *AJ*, 118, 558

- Kanneganti, S., Park, C., Hershley, H., Smith, A., Skrutskie, M., Wilson, J., Traub, W., Lam, C., & Nelson, M. 2006, *Proc. SPIE*, 6265
- Kanneganti, S., Park, C., Skrutskie, M. F., Wilson, J. C., Nelson, M. J., Smith, A. W., & Lam, C. R., 2009, *PASP*, 121, 885
- Kenyon, S. J., et al. 1994, *AJ*, 107, 2153
- Kenyon, S. J., & Hartmann, L. 1995, *ApJS*, 101, 117
- Knee, L. B. G., & Sandell, G. 2000, *A&A*, 361, 671
- Kolesnik, L. N., & Metreveli, M. D. 1985, *Kinematika i Fizika Nebesnykh Tel*, 1, 53
- Lada, C. J., Alves, J., & Lada, E. A. 1996, *AJ*, 111, 1964
- Lada, C. J., & Lada, E. A. 2003, *ARA&A*, 41, 57
- Lee, S. H., Kang, Y.-W., & Ann, H. B. 1999, *Publication of Korean Astronomical Society*, 14, 61
- Lesh, J. R. 1969, *AJ*, 74, 891
- Levine, J. L., Steinhauer, A., Elston, R. J., & Lada, E. A. 2006, *ApJ*, 646, 1215
- Liseau, R., Lorenzetti, D., & Molinari, S. 1992, *A&A*, 253, 119
- Looney, L. W., Mundy, L. G., & Welch, W. J. 2000, *ApJ*, 529, 477
- López-Chico, T., & Salas, L. 2007, *Revista Mexicana de Astronomia y Astrofisica*, 43, 155
- Loren, R. B. 1976, *ApJ*, 209, 466
- Luhman, K. L., Rieke, G. H., Lada, C. J., & Lada, E. A. 1998, *ApJ*, 508, 347

- Luhman, K. L. 1999, *ApJ*, 525, 466
- Luhman, K. L., Stauffer, J. R., Muench, A. A., Rieke, G. H., Lada, E. A., Bouvier, J., & Lada, C. J. 2003, *ApJ*, 593, 1093
- Lynds, B. T. 1969, *PASP*, 81, 496
- Marigo, P., Girardi, L., Bressan, A., Groenewegen, M. A. T., Silva, L., & Granato, G. L. 2008, *A&A*, 482, 883
- Matthews, H. E., Purton, C. R., Roger, R. S., Dewdney, P. E., & Mitchell, G. F. 2003, *ApJ*, 592, 176
- McDavid, D. A., Kanneganti, S., Park, C., Skrutskie, M. F. & Wilson, J. C., 2006, *Proc. SPIE*, 6269, 166
- McLean, I. S. 1997, *Electronic imaging in astronomy: Detectors and instrumentation*, (Chichester, UK Wiley)
- Meyer, M. R., Calvet, N., & Hillenbrand, L. A. 1997, *AJ*, 114, 288
- Muench, A. A., Lada, E. A., Lada, C. J., & Alves, J. 2002, *ApJ*, 573, 366
- Oasa, Y., Tamura, M., Sunada, K., & Sugitani, K. 2008, *AJ*, 136, 1372
- Oliva, E., 1997, *A&AS*, 123, 589
- Oliva, E. & Gennari, S., 1995, *A&AS*, 114, 179
- Oliva, E. & Gennari, S., 1998, *A&AS*, 128, 599
- Oliva, E., Gennari, S., Vanzi, L., Caruso, A. & Ciofini, M., 1997, *A&AS*, 123, 179
- Park, C., Skrutskie, M. F., & Kanneganti, S., in prep

- Persson, S. E., West, S. C., Carr, D. M., Sivaramakrishnan, A. & Murphy, D. C., 1992, PASP, 104, 204
- Persson, S. E., Murphy, D. C., Gunnels, S. M., Birk, C., Bagish, A. & Koch, E., 2002, AJ, 124, 619
- Preibisch, T. 2003, A&A, 410, 951
- Preibisch, T., & Zinnecker, H. 2001a, AJ, 122, 866
- Preibisch, T., & Zinnecker, H. 2001b, From Darkness to Light: ASP Conference Proceedings, 243, 791
- Racine, R. 1968, AJ, 73, 233
- Ramírez, S. V., et al. 2004, AJ, 127, 2659
- Ren, D. & Allington-Smith, J. R., 1999, Opt. Eng. 38(3), 537
- Rieke, G. H., & Lebofsky, M. J. 1985, ApJ, 288, 618
- Ridge, N. A., Wilson, T. L., Megeath, S. T., Allen, L. E., & Myers, P. C. 2003, AJ, 126, 286
- Rydgren, A. E. 1971, PASP, 83, 656
- Rydgren, A. E., & Vrba, F. J. 1983, AJ, 88, 1017
- Salpeter, E. E. 1955, ApJ, 121, 161
- Sandell, G., Aspin, C., Duncan, W. D., Russell, A. P. G., & Robson, E. I. 1991, ApJ, 376, L17
- Sandell, G., & Knee, L. B. G. 2001, ApJ, 546, L49

- Sandell, G., Knee, L. B. G., Aspin, C., Robson, I. E., & Russell, A. P. G. 1994, *A&A*, 285, L1
- Sargent, A. I. 1979, *ApJ*, 233, 163
- Scargle, J. D. 1989, *ApJ*, 343, 874
- Scholz, A., Geers, V., Jayawardhana, R., Fissel, L., Lee, E., Lafreniere, D., & Tamura, M. 2009, *ApJ*, 702, 805
- Schultheis, M., et al. 2000, *A&A*, 362, 215
- Scurlock, R. G. & Saull, B., 1976, *Cryogenics*, 16, 303
- Shevchenko, V. S., & Yakubov, S. D. 1989, *Soviet Astronomy*, 33, 370
- Shu, Q. S., Fast, R. W. & Hart, H. L., 1986, *Cryogenics*, 26, 671
- Skrutskie, M. F., Meyer, M. R., Whalen, D., & Hamilton, C. 1996, *AJ*, 112, 2168
- Skrutskie, M. F., et al. 2006, *AJ*, 131, 1163
- Slesnick, C. L., Hillenbrand, L. A., & Carpenter, J. M. 2004, *ApJ*, 610, 1045
- Stelzer, B., & Scholz, A. 2009, *A&A*, 507, 227
- Stetson, P. B. 1996, *PASP*, 108, 851
- Stochl, R. J., 1974, *NASA Technical Note*, D-7659
- Strom, S. E., Grasdalen, G. L., & Strom, K. M. 1974, *ApJ*, 191, 111
- Strom, S. E., Vrba, F. J., & Strom, K. M. 1976, *AJ*, 81, 314
- Sung, H., Bessell, M. S., & Chun, M.-Y. 2004, *AJ*, 128, 1684

- Tinetti, G., Meadows, V. S., Crisp, D., Fong, W., Fishbein, E., Turnbull, M., & Bibring, J.-P. 2006, *Astrobiology*, 6, 34
- Tokovinin, A., 2002, *PASP*, 114, 1156
- Treister, E., et al. 2006, *ApJ*, 640, 603
- Wainscoat, R. J., Cohen, M., Volk, K., Walker, H. J., & Schwartz, D. E. 1992, *ApJS*, 83, 111
- Walsh, A. J., Myers, P. C., Di Francesco, J., Mohanty, S., Bourke, T. L., Gutermuth, R., & Wilner, D. 2007, *ApJ*, 655, 958
- Welch, D. L., & Stetson, P. B. 1993, *AJ*, 105, 1813
- Wiling, B. A., Meyer, M. R., Greene, T. P., Mikhail, A., & Carlson, G. 2004, *AJ*, 127, 1131
- Winston, E., et al. 2009, *AJ*, 137, 4777
- Woolf, N. J., Smith, P. S., Traub, W. A., & Jucks, K. W. 2002, *ApJ*, 574, 430
- Xu, Y., Reid, M. J., Zheng, X. W., & Menten, K. M. 2006, *Science*, 311, 54